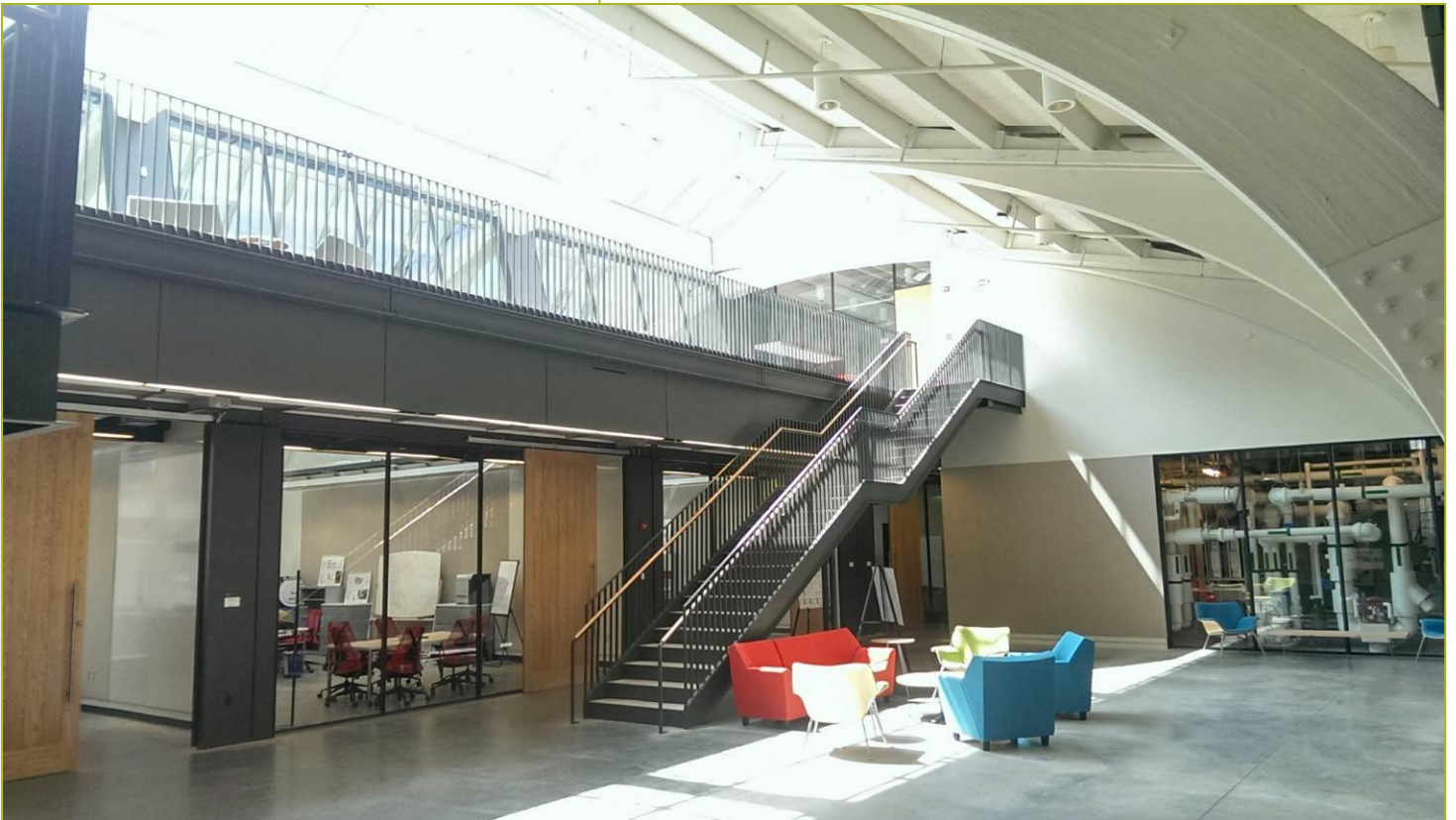


Title: Cost Effective Building Retrofit through Robust Control and Scalable Algorithms

Report Date: January 2013

Report Author(s): (See Report)



CBEi was referred to as the Energy Efficiency Buildings HUB at the time this report was developed.



Report Abstract

CBEI developed and demonstrated a set of tools and approaches for generating and implementing building-specific control algorithms that minimize energy consumption and energy costs while maintaining occupant comfort. The general approach involves the use of model-based predictive control (MPC) with reduced-order models and inverse (data-driven) models for the building envelope, indoor environment, and plant.

Contact Information for Lead Researcher

Name: James E. Braun

Institution: Purdue University

Email address: jbraun@purdue.edu

Phone number: 765-494-9157

Acknowledgement

This material is based upon work supported by the Consortium for Building Energy Innovation (CBEI) sponsored by the U.S. Department of Energy under Award Number DE-EE0004261.

Disclaimer

This report was prepared as an account of work sponsored by an agency of the United States Government. Neither the United States Government nor any agency thereof, nor any of their employees, makes any warranty, express or implied, or assumes any legal liability or responsibility for the accuracy, completeness, or usefulness of any information, apparatus, product, or process disclosed, or represents that its use would not infringe privately owned rights. Reference herein to any specific commercial product, process, or service by trade name, trademark, manufacturer, or otherwise does not necessarily constitute or imply its endorsement, recommendation, or favoring by the United States Government or any agency thereof. The views and opinions of authors expressed herein do not necessarily state or reflect those of the United States Government or any agency thereof.



Cost Effective Building Retrofit through Robust Control and Scalable Algorithms

Authors (in alphabetical order):

James E. Braun, Jie Cai, Donghun Kim, Vamsi Putta
Purdue University

Trevor Bailey, Miroslav Baric, Pengfei Li, Zheng O'Neill, Satish
Narayanan, Draguna Vrabie
United Technologies Research Center

Jeffrey Borggaard, John A. Burns, Eugene Cliff, Serkan Gugercin
Virginia Tech

Task 4.2

Final Report

Budget Period 2
(February 1st 2012 to January 31st 2013)

Table of Contents

Executive Summary	3
Reduced-Order Building Modeling	4
Coupled Indoor-Air Model	5
Inverse Building Modeling	9
Data-Driven Model from System Identification	11
Building 101 Simulation Based MPC Study	13
Evaluation of MPC Strategies for Purdue Living Lab case study	16
Scalable and Cost Effective Implementation of Optimal Building Control	16
1. Introduction.....	21
2. Control Oriented Model Development	23
2.1 Introduction.....	23
2.2 Reduced Order Model.....	23
2.3 Coupled Indoor- Air Model	41
2.4 Inverse Model for Building Envelope and Equipment.....	52
2.5 Data-Driven Model.....	74
3. Optimal Supervisory Control.....	85
3.1 Introduction.....	85
3.2 Building 101 Simulation Based MPC Study	85
3.3 Purdue Living Lab Simulation Based MPC Study	98
3.4 MPC Approaches and Algorithms.....	108
3.4.1 Optimal Control Formulations.....	108
3.4.2 Comparative Evaluation of MPC Strategies for Purdue Living Lab Case Study	119
3.5 Scalable and Cost Effective Implementation of Optimal Building Control	129
3.5.1 Introduction and Motivation	129
3.5.2 Preliminary Study on the Hierarchical Control Architecture	130
3.5.3 Automatic Differentiation.....	132
3.5.4 State Estimation from Sensed Data (Optimal Sensor Placement)	133
4. Summary and Future Work.....	137
Appendix.....	138
Appendix 2.2.....	138
Appendix 2.5.....	140
Appendix 3.2.....	145
Appendix 3.4.....	146

Appendix 3.5..... 171

Subtask 4.2: Cost Effective Building Retrofit Through Robust Control and Scalable Algorithms

Deliverable #18: Demonstration of prototype building control algorithms that provide guaranteed performance

Brief Summary: In BP2, researchers from Purdue University, United Technologies Research Center, and Virginia Tech developed and demonstrated a set of tools and approaches for generating and implementing building-specific control algorithms that minimize energy consumption and energy costs while maintaining occupant comfort. The general approach involves the use of model-based predictive control (MPC) with reduced-order models and inverse (data-driven) models for the building envelope, indoor environment, and plant. The models could be generated from either detailed physical models (e.g., TRNSYS for the building and plant, CFD for the indoor environment) or using measurements from short-term (e.g., two-week normal operational data and/or functional test data) monitoring at the site. The models are utilized in combination with an integral cost function that considers the cost of energy and impacts on comfort. The primary goals of this subtask are to develop and demonstrate a process, tools and algorithms that can significantly reduce the development and commissioning time/cost to implement optimal supervisory control for retrofits in buildings. Accomplishments in the BP2 have included 1) development of control-oriented models along with case study demonstration results, which covers reduced-order and inverse (data-driven) models for building envelope, indoor-air, and HVAC equipment; 2) development, comparisons and implementation of MPC approaches and algorithms along with case study results, which covers simulation-based studies for both Building 101 and the Purdue Living lab; and 3) scalable and cost effective implementation of optimal building control, which covers preliminary study on the hierarchical control architecture, state estimation from sensed data and efficient algorithms for optimal control with meaningful cost models.

Executive Summary

In the United States, the buildings sector (commercial & residential) accounts for nearly 41 percent of the primary energy consumption. A significant amount of energy in buildings is consumed by their heating, ventilation, and air-conditioning (HVAC) systems. Efficient and automatic building control algorithms could help improve the energy efficiency of HVAC systems and thus reduce the overall energy consumption in buildings. Traditionally, building control algorithms are based on ad-hoc and heuristic rule-based approaches that typically require significant effort in the tuning process during the commissioning and retro-commissioning processes. Furthermore, the tuned control approaches may not be close to the optimal solution and control performance cannot be guaranteed if the actual operational conditions have drifted from these trial-and-error based tuning ranges. Recently, model-based optimal control has been investigated for the control of full scale (or partially) HVAC systems and thermal mass in buildings. Among possible approaches, model predictive control (MPC), an optimization-based control strategy, has gained a lot of attention for application to building automation and controls because of significant potential for energy consumption and/or energy cost savings. MPC utilizes

dynamic building and HVAC equipment models and input forecasts to estimate future energy usage and employs optimization to determine control inputs that minimize an integrated cost function for a specified prediction horizon.

In Budget Period 2 (BP2), researchers from Purdue University, United Technologies Research Center, and Virginia Tech within the EEB task 4.2 developed and demonstrated a set of tools and approaches for generating and implementing building-specific control algorithms that minimize energy consumption and energy costs while maintaining occupant comfort. The general approach involves the use of model-based predictive control (MPC) with reduced-order models, inverse (data-driven) models for the building envelope, indoor environment, and plant. The models could be generated from either detailed physical models (e.g., TRNSYS for the building and plant, CFD for the indoor environment) or using measurements from short-term (e.g., two-week normal operational data and/or functional test data) monitoring at the site. The models are utilized in combination with an integral cost function that considers the cost of energy and impacts on comfort. The primary goals of this subtask are to develop and demonstrate a process, tools and algorithms that can significantly reduce the development and commissioning time/cost to implement optimal supervisory control for retrofits in buildings.

Accomplishments in the BP2 have included 1) development of control-oriented models along with case study demonstration results, which covers reduced-order and inverse (data-driven) models for building envelope, indoor-air, and HVAC equipment; 2) development, comparisons and implementation of MPC approaches and algorithms along with case study results, which covers simulation-based studies for both Building 101 and the Purdue Living lab; and 3) scalable and cost effective implementation of optimal building control, which covers preliminary study on the hierarchical control architecture, state estimation from sensed data and efficient algorithms for optimal control with meaningful cost models. In the following sections, an executive summary is provided for these accomplishments.

Reduced-Order Building Modeling

Computationally efficient building models are needed for practical and scalable implementation of model-based predicted control (MPC) in buildings. In this project, a methodology has been developed, demonstrated, and evaluated for generating a reduced-order building model from a detailed description of a multi-zone building. The methodology has been demonstrated and evaluated for a 59-zone building (Building 101 at the Navy Shipyard, Philadelphia, PA).

The first step of the methodology involves using a building description to create a full-order, linear-time-invariant (LTI), state-space representation of the whole building dynamic behavior. The overall system of equations is then broken down into smaller subsystems of equations and balanced truncation is applied to each subsystem separately to create reduced-order models. Solving a number of smaller model-order reduction problems dramatically reduces the computational requirements as compared with solving a single model-order reduction problem for the entire building. The subsystem reduced-order models are then assembled in a complete building model and an additional step of model-order reduction is applied.

Comparisons between reduced-order model (ROM) and TRNSYS predictions were performed over a whole year for all 59 zones of Building 101 for both open-loop and closed-loop response of zone air temperatures. In general, the agreement is excellent. Sample comparisons for open-

loop response between TRNSYS and the ROM for a zone on the 3rd floor are shown in Figure 1 for several days. These represent the “worst” case results that were obtained and yet the agreement is very good. The solid line (T_{TRN}) and dashed line (T_r) represent zone air temperature profiles generated by TRNSYS and reduced-order models, respectively.

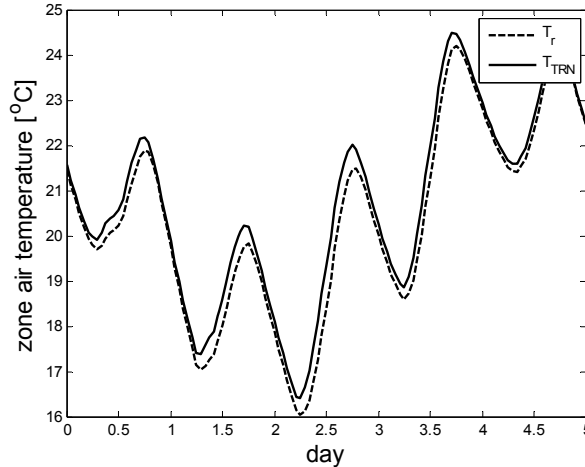


Figure 1 Open-loop response model comparisons between TRNSYS and reduced-order models (8th zone on the 3rd floor, May)

Compared to TRNSYS, the computation was reduced by about a factor of 100 for the 59-zone simulation as demonstrated in Table 1. These data were determined for one-year simulations with a 3.10 GHz (32 bit) computer. Based on these results, the ROM is more appropriate for use in optimization, optimal control or any high level control than existing modeling approaches. The time required to generate the ROM was also evaluated and was an order of magnitude less than the TRNSYS one-year simulation time. Therefore, in addition to controls applications, the computational savings associated with application of a ROM indicate that this approach may be useful for general building simulation, particularly when considering parametric studies and optimization for design.

Table 1 Computational time comparison for ROM and TRNSYS with one-year simulation

Time step [min]	TRNSYS [sec]	ROM [sec]
10	876.9	8.7
30	482.6	4.7
60	248.5	3.0

Coupled Indoor-Air Model

Many advanced HVAC components and systems, such as chilled beams and displacement ventilation, rely on vertical temperature gradients for effective operation. Moreover, accurate assessment of environmental-quality must be based on conditions in appropriate occupied zones and not on large-scale averages. In particular, large comfort variations may exist in spaces that have relatively large aspect ratios in combination with large south facing windows. Accordingly, it is appropriate to consider indoor environment models that accurately predict spatially varying

comfort conditions. However, the computational requirements necessary to consider this situation using traditional CFD are too large to be practically applied. As a result, a methodology has been developed for generating a ROM for indoor air using CFD results that is then coupled to a building envelope ROM to enable controls-oriented models that consider spatial comfort variations. The methodology was demonstrated for one of the Purdue Living Laboratory rooms. As indicated in the Figure 2, the Indoor-Air model uses wall surface temperatures from the building envelope as inputs and dynamically determines the resulting wall surface fluxes. We have used FLUENT software to model internal flow including temperature, velocity, pressure, as well as water vapor and CO₂ mass fractions. The resulting input/output data was fit with an ODE model and then further reduced using the IRKA algorithm developed in this project.

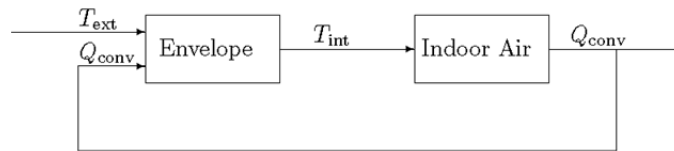


Figure 2 Coupled Envelope/Indoor-air Model

The indoor-air model is realized as an LTI system that approximates specified input-output behaviors observed in computational fluid dynamics (CFD) simulations. A grid for the CFD simulation for the Purdue Living Laboratory is shown in Figure 3 (left). The yellow zones depict (24) locations for student work areas; their numbering is shown on the right. Volumetric source terms are specified in the odd-labeled zones to emulate generation of water-vapor, carbon-dioxide and energy in these zones. In addition, (volume-averaged) human comfort metrics are read from all zones. The brown/green 'cloud' structures support (8) inlet diffusers, and a single air-return is located on the back (North) wall. The bounding surfaces for the VAV-room were decomposed into 19 sections as shown in Figure 4. The first step in developing the coupled ROM is to generate a building envelope ROM as previously described. Steady state outputs from this model at some nominal condition are perturbed and used as inputs to drive a CFD simulation that produces temperature and velocity fields. The CFD results are then used to fit a LTI ROM for the indoor air.

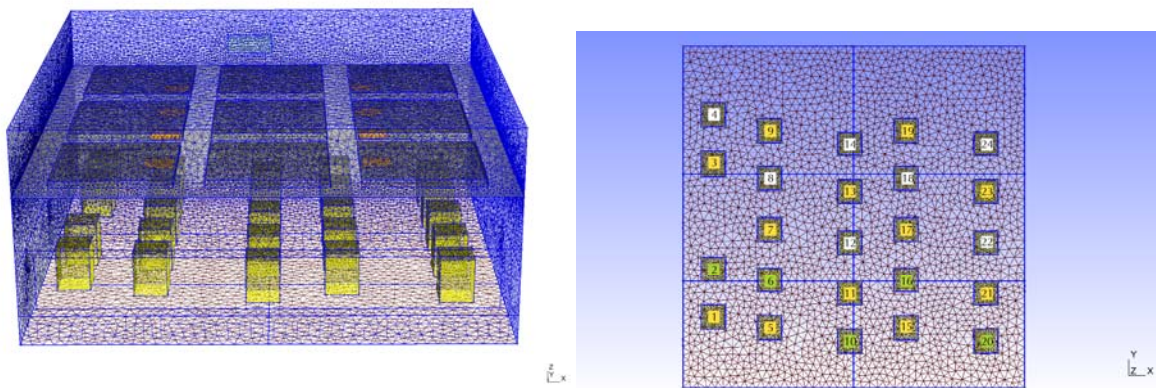


Figure 3 CFD Grid and Occupied Zones for the Purdue VAV Room

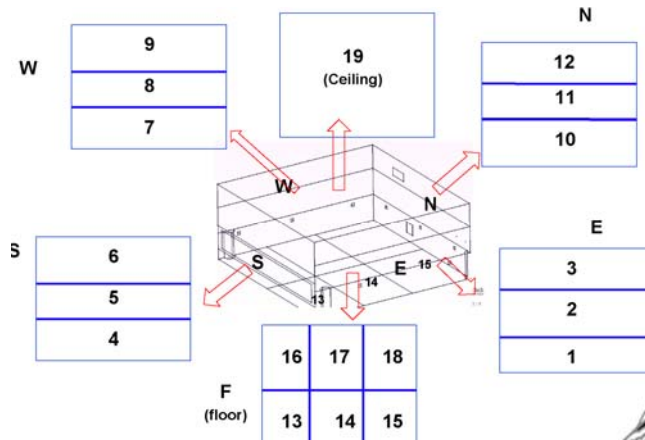


Figure 4 Interior Surfaces for the Purdue VAV Room

The coupled building/indoor air ROM model was used to assess variability in comfort conditions and the importance of thermostat location on comfort conditions and cooling requirements for the Purdue Living Lab 3. Figure 5 shows time histories of comfort conditions for a well-mixed room model and three locations for the ROM coupled model. The coupled model predicts dramatic spatial differences in the comfort conditions (much higher air and mean radiant temperatures near the window (oz_{15}); higher air velocities and lower temperatures near diffusers (oz_{18})). The well-mixed model predicts conditions within the middle of the values determined for the coupled model. This is because the average room temperature was used for feedback control for the coupled model. For this case, the cooling requirement for the coupled/indoor air model was close to that for a fully-mixed zone model. However, it is unrealistic to use the average zone air temperature for feedback control. Results were also generated for the same day with a thermostat located near the south windows (average of zones 1, 5, 10, 15, and 20). In this case, peak temperatures in all local zones were lower by 2 to 3 °C compared to control based on room average temperature. This led to an increased heat extraction rate for the coupled model compared to the well-mixed model as shown in Figure 6.

Figure 7 demonstrates the importance of thermostat location on the overall comfort as represented using predicted mean vote (PMV). The right plot shows PMV for the sensor located near the south window. In this case, the conditions are slightly warm near the window during the middle of the day but cold in other locations. Moving the thermostat away from the windows to zone 2 improves comfort in most of the space except near the windows where the conditions become quite warm.

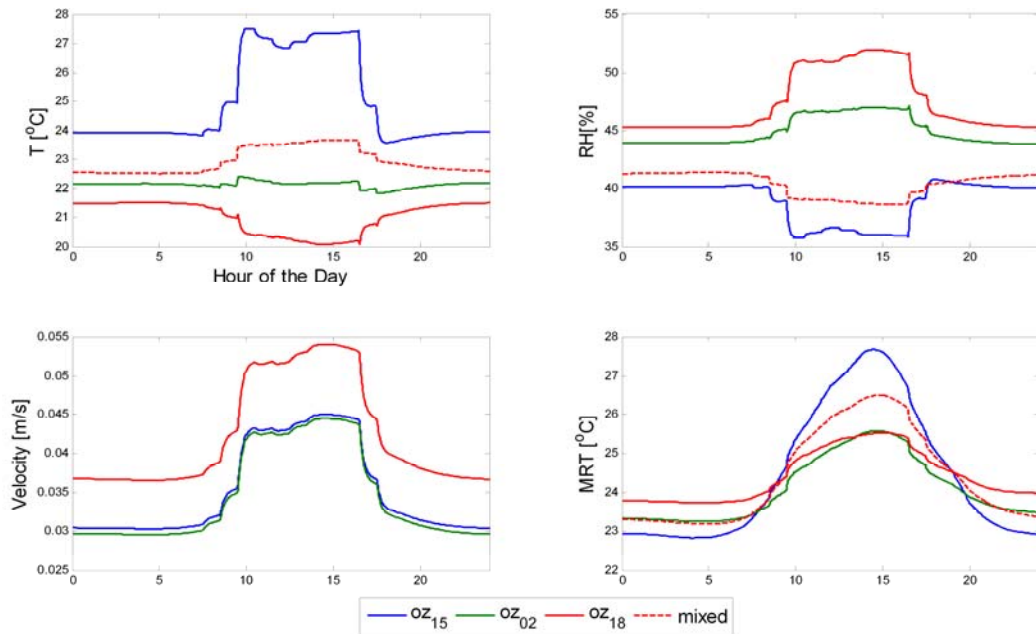


Figure 5 Indoor environmental metrics based on feedback control using average room temperature (oz_{15} = average of zones nearest south window (zones 1, 5, 10, 15, and 20); oz_{02} = occupied zone 2, on west end of second row in Figure 6; oz_{18} = occupied zone 18, near back of room away from windows)

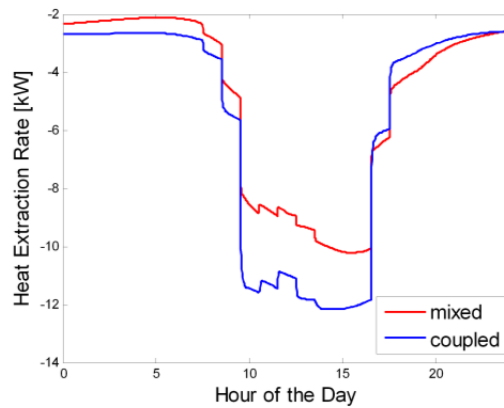


Figure 6 Heat extraction rate based on feedback control using the average of zones 1, 5, 10, 15, and 20 (oz_{15} , CFD-coupled model) as compared with well-mixed mode

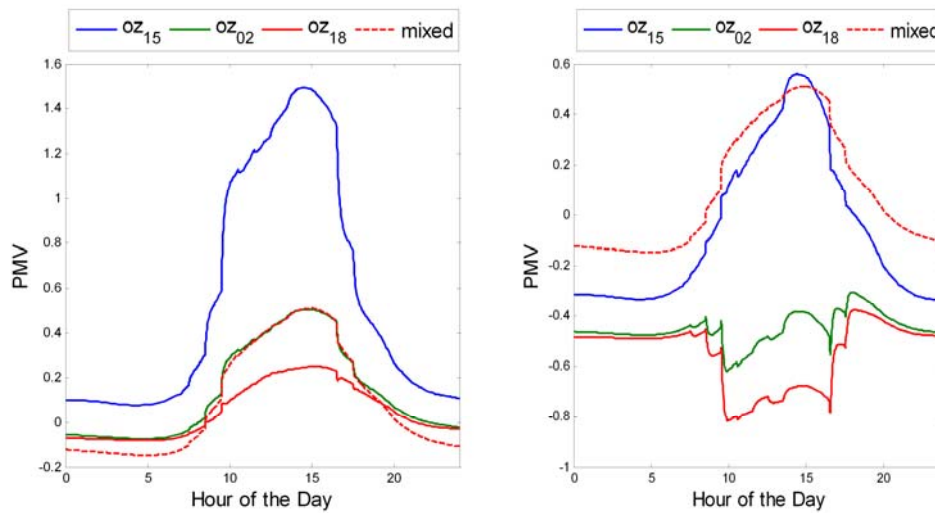


Figure 7 Comparison of PMV variations for well-mixed model with CFD-coupled model assuming feedback based on zone 2 (left plot) and the average of zones 1, 5, 10, 15, and 20 (right plot)

Inverse Building Modeling

Building envelope inverse model

An alternative to reduced-order modeling based on a physical description is to train an inverse model using measurements. Both approaches are important as tools for applying model-based predictive control on a widespread basis. The inverse modeling considered in this study extends previous work to allow scalability to large multi-zone buildings and is based on a thermal network representation. A robust training approach was developed that breaks the large multi-zone training process into a number of smaller problems that are loosely coupled. The training method was first tested using simulation data and then applied to data from Building 101.

Figure 8 shows example predictions of zone temperatures compared to measurements for three zones located in the north wing on the second floor of Building 101 given measured inputs for solar radiation, ambient temperature, internal gains, and zone cooling. The model captures the zone temperature response reasonably well. It is believed that the model for Zone 8 was more accurate because information for initial parameter estimates were obtained from an on-site inspection, whereas the parameters for the other two zones were taken from the inputs to a TRNSYS model. Also, zonal internal heat gains were estimated using area ratios and total heat gains.

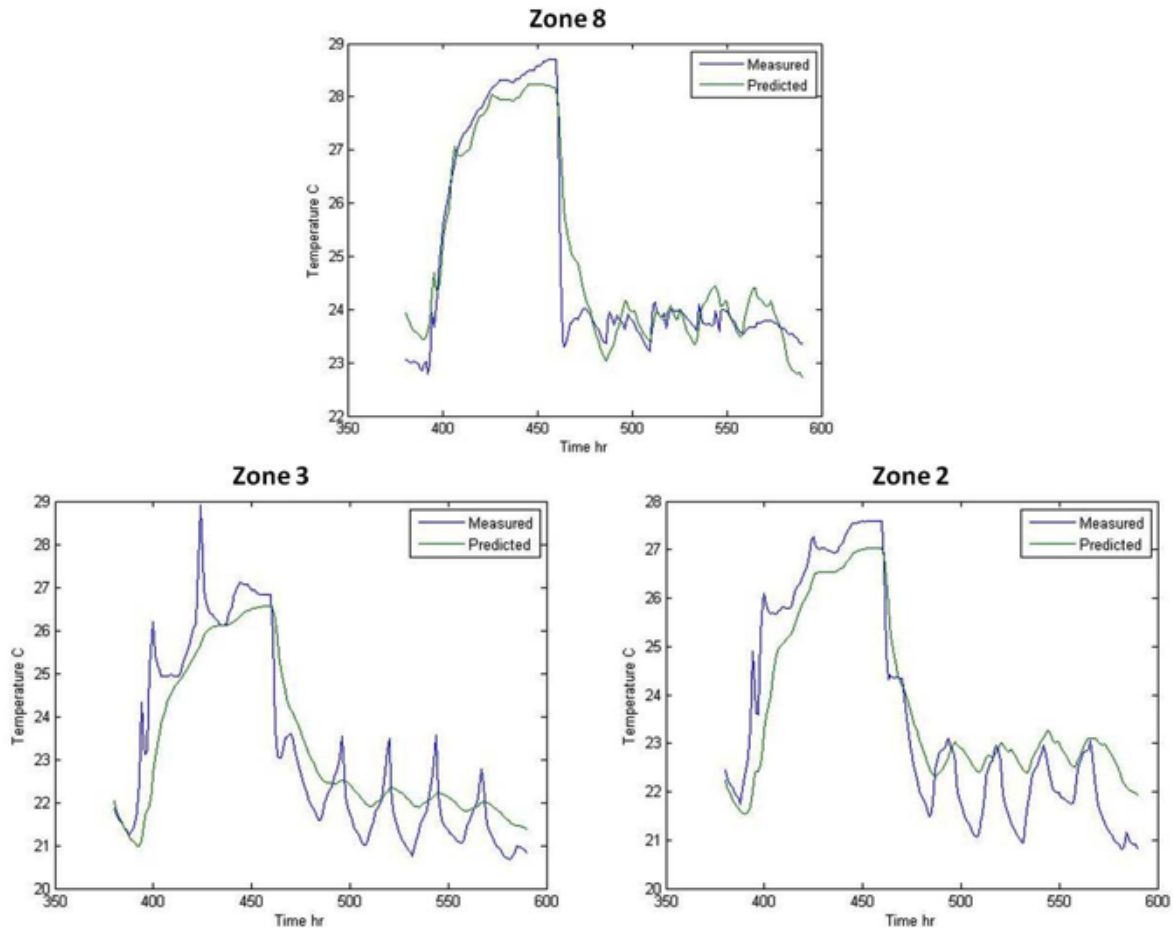


Figure 8 Performance of estimated model from measured data.

Equipment inverse model

A method was developed for learning the performance of vapor compression cooling equipment using limited measurements. The methodology is based on a gray-box modeling approach that utilizes basic physics for the components of the equipment (e.g, compressor, heat exchangers) along with empirical parameters that are trained using data. The model can predict total cooling rate, sensible heat ratio, compressor power, condenser fan power, and supply fan power as a function of supply air temperature setpoint and air flow, return temperature, and ambient temperature. The method was applied to the multi-stage direct expansion (DX) system and VAV air-handling unit (AHU) that serves the north wing of Building 101. The model was then used to assess the impact of supply temperature setpoint on DX unit power consumption to identify optimal setpoints.

Figure 9 shows example comparisons between measurements and model predictions for total DX unit cooling rate and compressor power consumption. The root-mean square errors are 5% for cooling and 6% for compressor power. In applying the model, it was found that the optimal strategy for supply air temperature setpoints for this system is to use the largest value that will provide the needed moisture removal. Significant energy savings are possible by switching to this strategy from the current control, which uses a relatively low fixed supply air temperature setpoint.

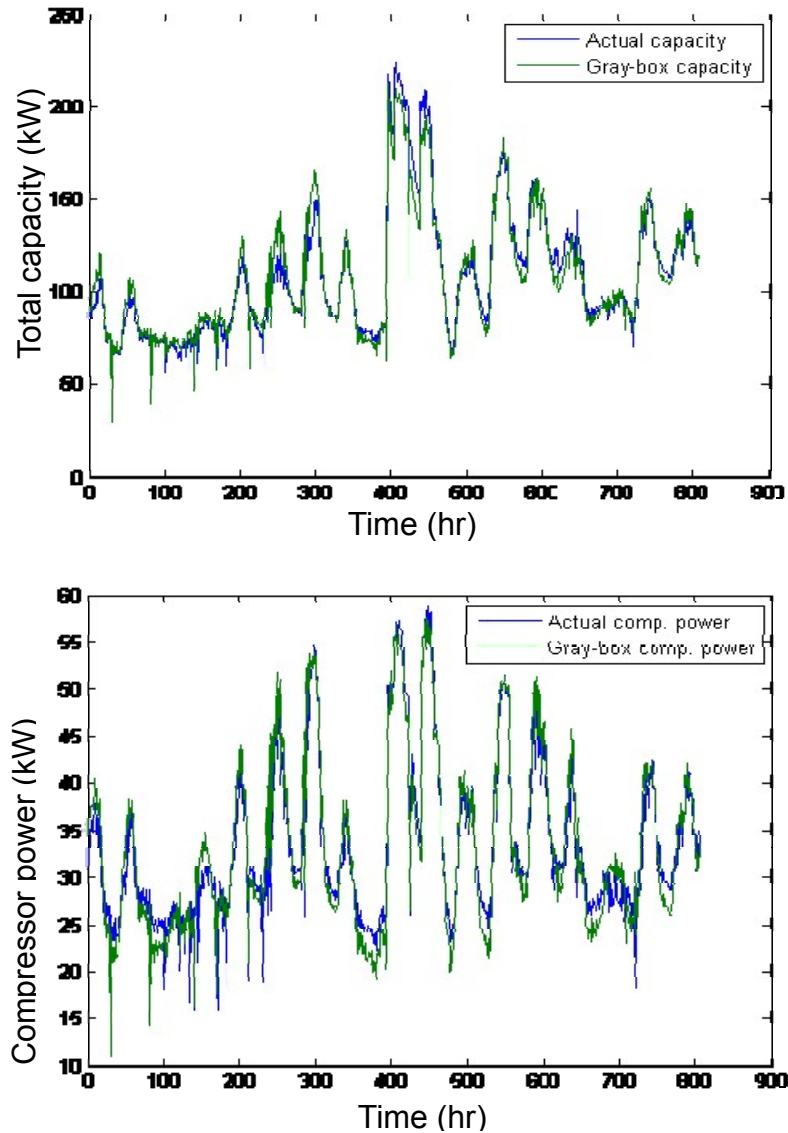


Figure 9 Comparisons of the predicted capacity and compressor power to the actual values

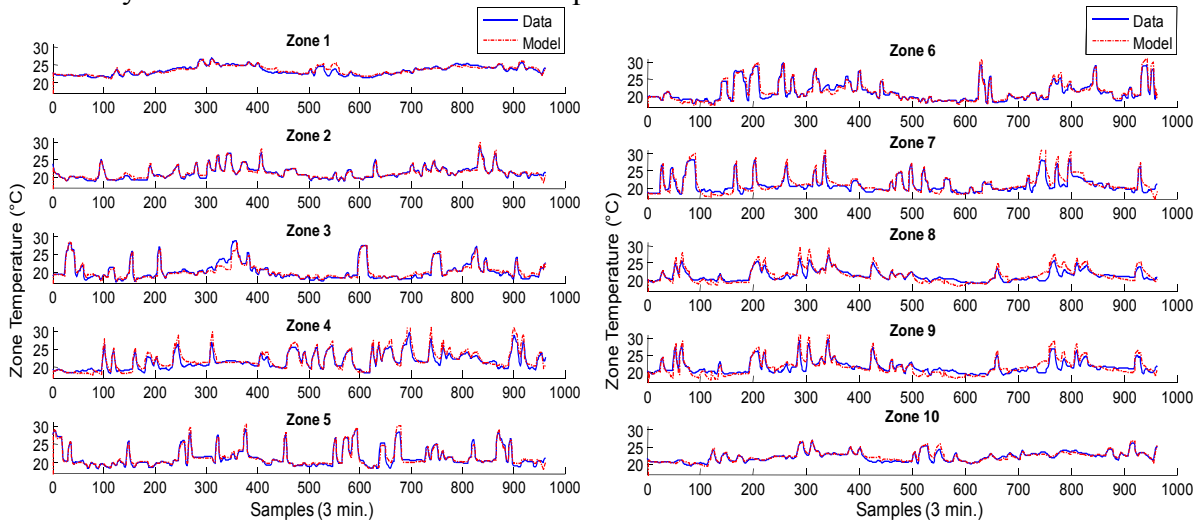
Data-Driven Model from System Identification

Modeling accuracy is a key enabler for effective and robust controller performance. A dynamic model with reasonable prediction performance (e.g., accuracy and simulation speed) is crucial for a practical implementation of MPC. In the BP2, low-order state-space models are identified from the designed input-output responses of thermal zones with disturbances from ambient conditions and internal heat gains. A high-fidelity TRNSYS model of an office building (i.e., Building 101) was used as a virtual testbed to generate data for system identification, parameter estimation, and validation of the proposed model structures.

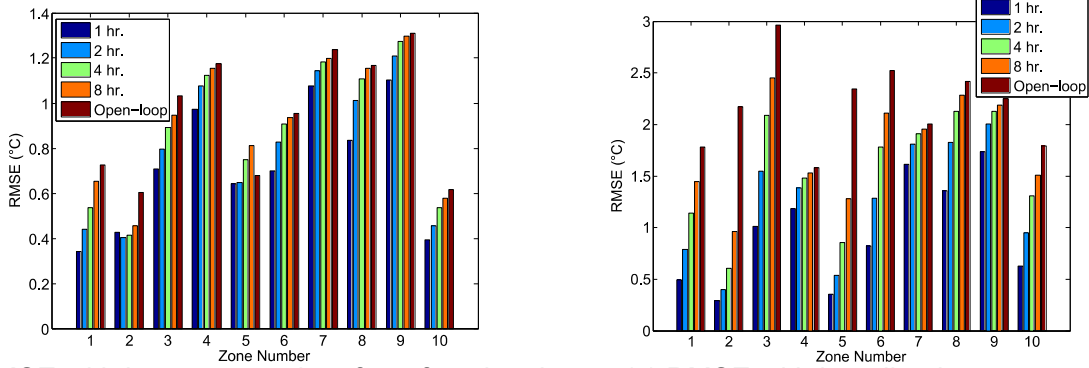
Figure 10(a) shows comparisons of 2nd order state-space model predictions with data for all 10 zones served by AHU3 based on validation data. To evaluate the effectiveness of model performance for MPC implementation, Figure 10(b) and 10(c) show comparisons of root mean

squared error (RMSE) for the 10 zones with predictions of 1 hr., 2 hr., 4 hr., 8 hr., and open-loop scenarios based on functional test and TRNSYS baseline input-output data, respectively. The scenarios for predicting 1 hr., 2 hr., 4 hr., and 8 hr. ahead were realized by reinitializing the system states every 1hr., 2 hr., 4 hr., and 8 hr., respectively. The open-loop scenario did not involve any reinitialization of system states.

Note that we performed very aggressive functional tests to fully excite the system dynamics with predictive results in Figure 10(b) that appear to be quite good for control design. For the additional model validation results in Figure 10(c), baseline feedback controllers were implemented within the TRNSYS testbed. The TRNSYS zone air flow rates and supply air temperatures were then fed into the simplified model to determine the zone temperature responses that were compared with TRNSYS zone temperatures. Overall errors in the zone temperature predictions for this test case are presented in Figure 10(c). This control input scenario is much different than that employed during the model training periods. Overall, the model yielded much worse results for both short-term and long-term predictions than those presented in Figure 10(b). The degraded model performance under this validation scenario is probably due to the fact that the effects of solar radiation and internal loads become more important relative to the control inputs (zone supply air flow rate and temperature), as compared with the validation scenarios based on functional test data. Future study will be conducted to address the aforementioned limitations. In particular, better models may be needed to approach optimal MPC performance in the presence of variable utility rates and demand charges because longer prediction horizons are required. Uncertainty analysis for internal and solar heat gain predictions should be carried out before these gains are added as inputs to the predictive model. Future study will be conducted to address this problem.



(a) Zone model validation (functional tests, 2 hr. prediction)



(b) RMSE with input-output data from functional tests (c) RMSE with baseline input-output data
 Figure 10 Validation results for 10 zones in Building 101

Building 101 Simulation Based MPC Study

A Modeling Language for Mathematical Programming (AMPL (Fourer et al., 1987)) was selected to be used as an optimization platform. Figure 11 illustrates the software architecture for optimization-based building control which integrates

- TRNSYS as a virtual testbed,
- MATLAB® as a data acquisition and organization interface and
- AMPL® for solving optimization based control problem.

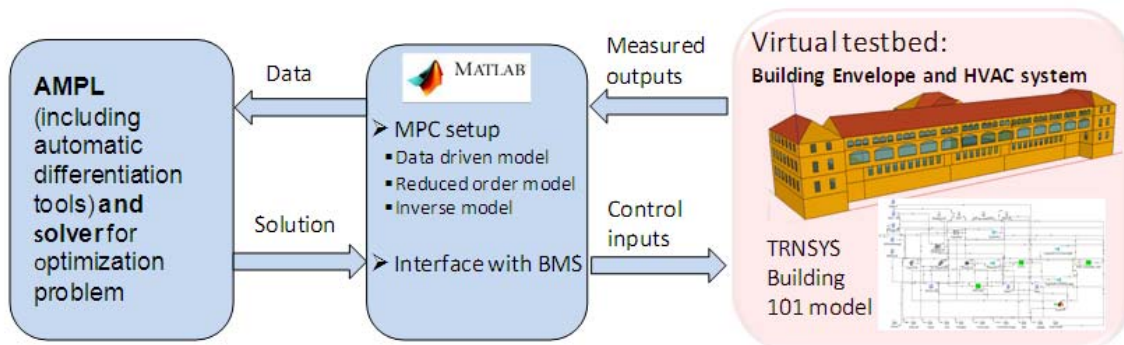


Figure 11 Integrated tool chain for optimization based building control algorithm development, testing and performance evaluation in simulation

Figure 12 presents a schematic representation of the integration of building and HVAC system models with the MPC algorithm. Specifically, the MPC algorithm receives “measurements” of the zone temperatures and outside air temperature (uncontrolled disturbance) and uses optimization tools to calculate the control inputs based on an internal representation of the system dynamics, i.e. building and HVAC equipment models. The control objective considered herein is to minimize energy consumption used for air conditioning such that the occupant’s thermal comfort is satisfied.

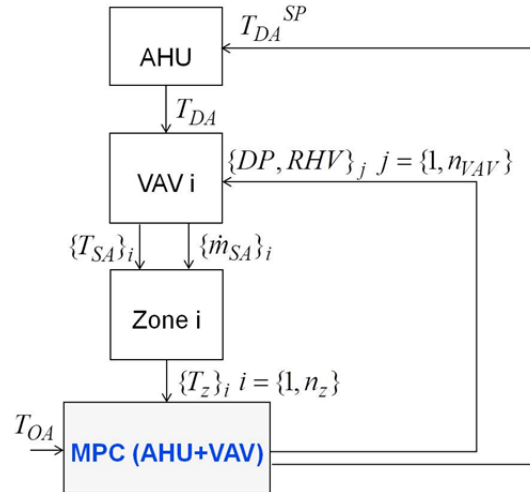


Figure 12 Control integration with building system

Simulation studies were conducted to evaluate the effectiveness of the proposed centralized MPC controller. The high-fidelity TRNSYS model was adopted as our virtual testbed. A summer period was considered for the case study. A TRNSYS simulation was performed over five weekdays in the first week of August, 2012. Similar to the study of the data-driven modeling approach, the virtual weather data from 2011 was used in the simulation.

Figure 13 presents the temperature profile of each zone controlled by the baseline and the MPC, respectively. As can be observed, the centralized MPC controller is trying to regulate the temperature in each zone tightly around the upper bound of the thermal comfort region (dashed lines in Figure 13) and meanwhile exploiting the trade-offs of DX coil discharge air temperature (DAT) setpoint, VAV flow rate setpoint, and VAV reheat coil valve positions to optimize the combined energy-and-comfort based costs.

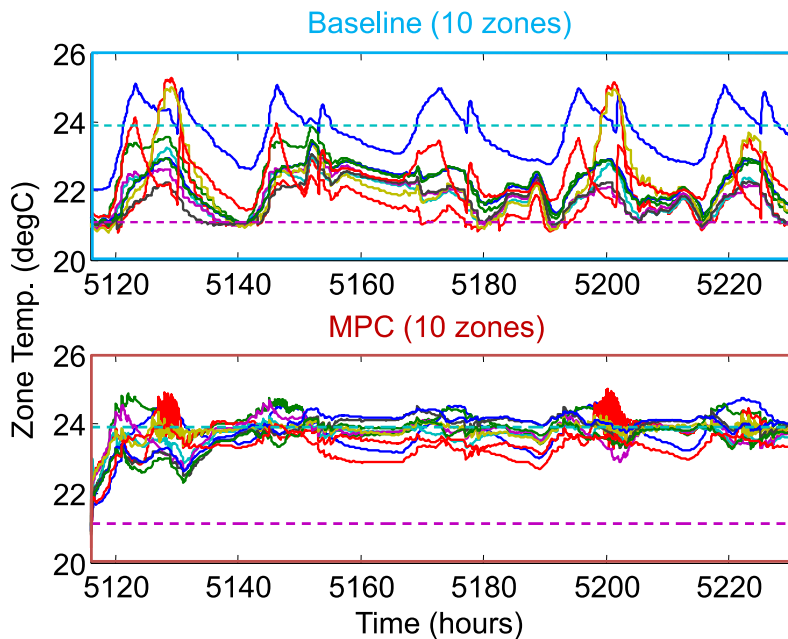


Figure 13 Comparisons of zone temperature profiles between baseline and MPC

Figure 14 shows comparisons of energy consumption breakdowns between the baseline control and the MPC. The system with the proposed MPC strategy demonstrated ~17.5% energy savings for the HVAC system. It can be observed that most of the energy savings come from reduced electrical energy savings for the compressors within the DX unit.

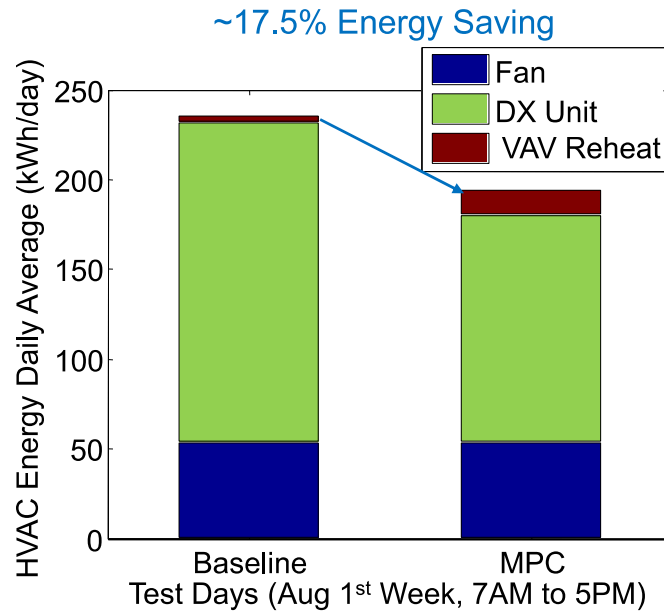


Figure 14 Comparisons of energy consumption breakdown between baseline and MPC

Figure 15 illustrates the main reasons for energy savings brought by the MPC. Compared to the baseline control, the discharge air temperature (DAT) setpoint is higher during the whole test week, which brought significant savings for the direct expansion (DX) unit power, as shown in the lower subplot of Figure 15.

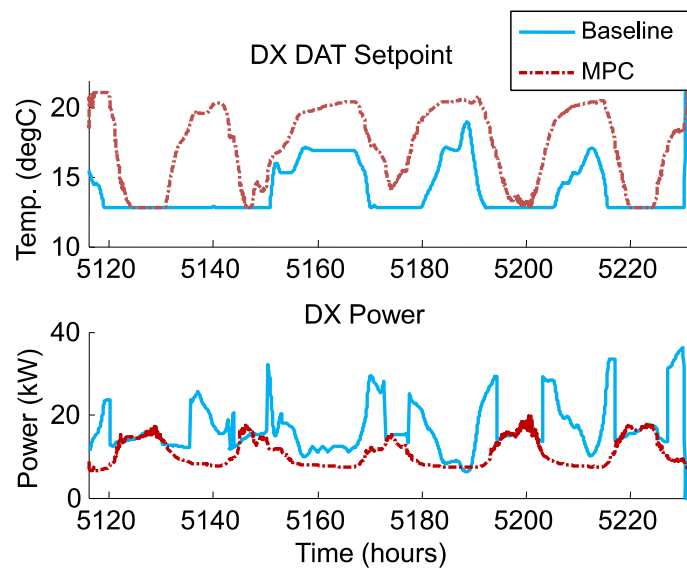


Figure 15 Comparisons of DAT setpoints and DX unit power between baseline and MPC

Evaluation of MPC Strategies for Purdue Living Lab case study

The computational requirements for MPC are a major concern for practical implementation, especially when considering the complexities associated with large multi-zone buildings. Therefore, simplifying assumptions are often made when formulating a problem that can result in loss in optimality. There is a need to understand the tradeoffs between computational requirements and optimal performance when considering alternative formulations and optimization solvers. With this in mind, a simulation tool was developed and applied to a case study for the Purdue Living Laboratory in order to evaluate alternative MPC formulations and solvers. The different optimal control solutions were compared to a conventional night setup control strategy to provide the baseline operating costs from which the cost savings were measured.

Table 2 summarizes the performance of the three different solvers that were studied. The Quadratic Programming (QP) solver approximates the nonlinear energy cost function with a quadratic in order to make the computation of the optimal control tractable. Sequential quadratic programming (SQP) extends that idea by iteratively approximating the cost function as a quadratic and the search direction is chosen to be the corresponding minimizer. Move blocking refers to the reduction in the degrees of freedom (number of control inputs to be optimized) by restricting a fixed number of changes in the control inputs. The greatest cost savings (9%) relative to conventional control were realized using the QP approach. However, a significant fraction of these savings were realized using the move blocking solution with an order of magnitude less computing cost. Additional case studies for more complicated problems with other solution approaches will be considered in future work.

Table 2 Comparison of MPC solvers

<i>Solver</i>	<i>Mean AHU Energy Costs (per day)</i>	<i>Computational Costs(sec/decision) Intel Core2Duo 2.1Ghz</i>
Conventional(Setback based)	1.409 \$ (baseline)	Realtime (no optimization involved)
Quadratic Programming (QP)	1.278 \$ (9.3 % saving)	4.5 sec (24 hour lookahead)
Move blocking (12 degrees of freedom)	1.306 \$ (7.3 % saving)	0.65 sec (24 hour lookahead)
Sequential Quadratic programming based solver	1.300 \$ (7.7 % saving)	4.55 sec (24 hour lookahead)

Scalable and Cost Effective Implementation of Optimal Building Control

Preliminary Study on the Hierarchical Control Architecture

During the BP2, while developing and evaluating the technical approach we noted the following challenges associated with the potential implementation of a control retrofit using the MPC algorithmic approach

- High commissioning cost – due to time required for model selection and calibration

- Maintenance of the control solution – due to the fact that the model parameters can exhibit high variability for different operating points
- Computational scalability – large computation power and time required

To alleviate the above mentioned difficulties, we proposed an approach that can be implemented and tested as part of the efforts planned for the BP3. The proposed approach has been developed based on the divide and conquer idea, and makes use of optimization tools to achieve optimal coordination between the HVAC equipment. Specifically, the proposed approach may use the following sequence of decisions at different levels in the hierarchy:

- For each zone using available measured data one computes current expected demand (to compensate for the effects of the thermal load disturbances) based on a
 - Simplified nominal model of thermal zone dynamics and
 - Online uncertainty/load estimation
- Propagate the expected optimal air conditioning demand (heating or cooling) as a request to the AHU level where decision will be made on using optimization on the AHU (air flow and discharge air temperature),
- Given the received discharge air temperature received from AHU, at the VAV level an optimization problem can be again solved to provide optimal zone inputs supply air flow and supply air temperature.
- Demand for energy can be further propagated to cooling/heating plant level where a new optimization based control problem can be formulated and solved.

Figure 16 presents the obtained optimal decision maps for supply air temperature setpoint and supply mass air flow setpoint for a zone, calculated at the VAV level, given a fixed discharge air temperature provided at the level of the AHU. The figures show the values of the optimal control inputs setpoints with respect to the value of the estimated uncertainty and the value of the measured zone temperature.

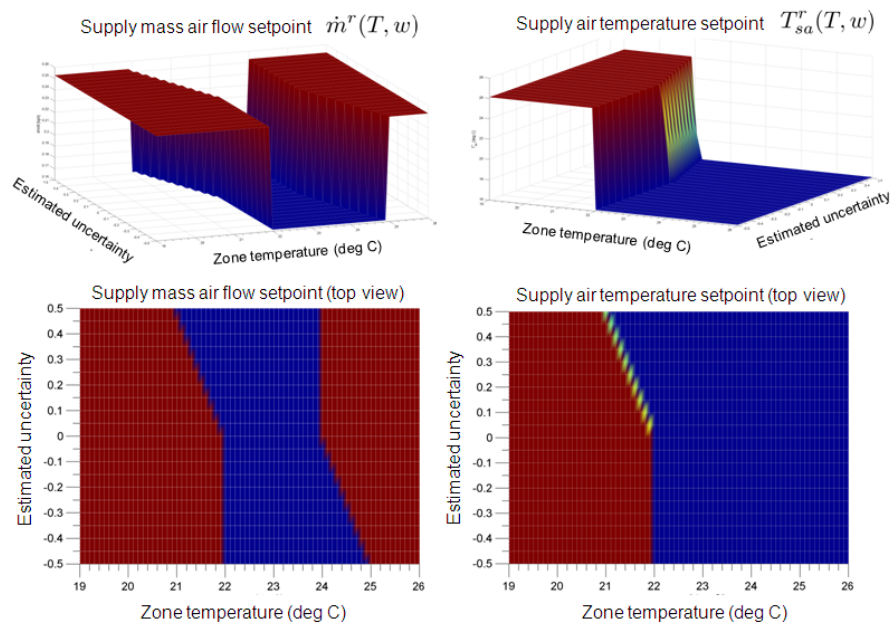


Figure 16 Optimal decision maps for supply air temperature setpoint and supply mass air flow setpoint at VAV level

The preliminary results indicate that the on a local level one can optimally calculate the supervisory control setpoints that will result in zone temperature control with minimal energy consumption. We note that these preliminary results, calculated using optimization, present a similar switching pattern with the VAV control inputs often observed in common practical implementations. In fact one notes that the calculated optimal control inputs present a on/off behavior and the switching boundary, correlated with the zone thermal comfort setpoint band of [21.1, 23.89] deg C, can be optimally selected based on the value of the estimated uncertainty and the present zone temperature measurement.

The features that will characterize the hierarchical control approach are summarized as the following

- Hierarchical architecture: amenable for parallel and distributed implementation,
- Minimal modeling efforts of building envelope,
- Adaptive to model parameters/load variations.

The implementation of the hierarchical control architecture will result in an overall increased scalability of the control development and deployment, and increased robustness to unmeasured and uncertain disturbances. This will ultimately translate into reduced control commissioning time and will allow for continuous adaptation of a control strategy to respond to continuously variable loads associated with changing weather conditions, occupant behavior, etc. Additionally, enabled by the hierarchical approach to building control, the control retrofit strategy will become highly scalable to implementation on a heterogeneous set of buildings.

The hierarchical architecture offers high flexibility to an integration with model based predictive control approach that has been developed in the BP1 and the BP2 to exploit the advantages offered by prediction coupled with the storage capability offered by the building envelope.

State Estimation from Sensed Data

It is well known that the performance of MPC deteriorates because of the estimation error. In order to study and quantify the robustness an output feedback MPC, it is necessary to choose a suitable strategy for the state estimation. We focus on the Kalman Filter (KF) since it is the most popular tool used in modern control and there is a rigorous proof of the stability with error bounds. Recently, new (local) error estimates have been obtained for the Extended Kalman Filter (EKF) which will be essential for Nonlinear MPC (NMPC) that is the basis for the Task 4.2 work. To illustrate the potential practical benefits of the sensor location tool, consider the results obtained on the test room as shown in Figure 17 below.

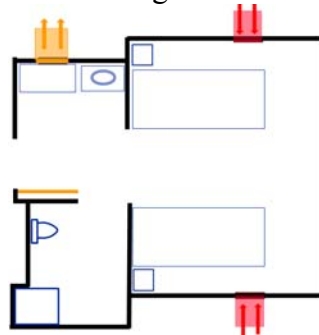


Figure 17 Hospital Suite

The test case is a suite with one zone devoted to a bed area and the remaining zones are bath and dressing areas as depicted in the Figure above. There are two inlet diffusers and one outflow return vent, which is the only outflow when the door is closed.

The estimation error is based on employing a Kalman Filter for state estimation and given by

$$J(\bar{\mathbf{q}}) = \mathbb{E} \left(\int_0^{+\infty} \|z_e(s, \bar{\mathbf{q}}) - z(s)\|^2 ds \right) = Tr(\Sigma(\bar{\mathbf{q}})),$$

where $\bar{\mathbf{q}}$ is the sensor location, $\mathbb{E}(\mu)$ denotes the expected value of the random variable μ and $Tr(\Sigma(\bar{\mathbf{q}}))$ denotes the trace of the state estimation covariance operator $\Sigma = \Sigma(\bar{\mathbf{q}})$. Consequently, the optimal sensor location problem is to find an optimal location $\bar{\mathbf{q}}^{opt}$ such that $J(\bar{\mathbf{q}}) \triangleq Tr(\Sigma(\bar{\mathbf{q}}))$ is minimized.

In Figure 18 below we plot the values of $\rho(\bar{\mathbf{q}}) = Tr(\Sigma(\bar{\mathbf{q}}))$ as the sensor location $\bar{\mathbf{q}}$ moves around the wall in the right room. Here, “upper” refers to the upper wall, “right” refers to the right wall, “lower” is the bottom wall, and “left” is the left wall of the bed area.

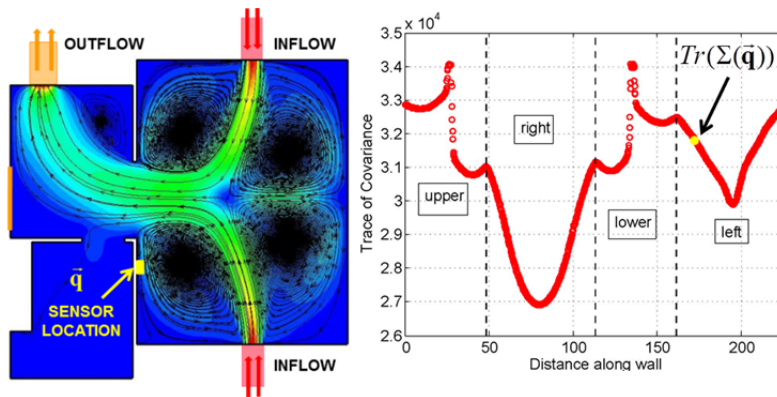


Figure 18 Flow (left) and cost function

We have demonstrated that estimation error can be sensitive to sensor location and demonstrated an approach to sensor placement that minimizes the estimation error.

Efficient Algorithms for Optimal Control with Meaningful Cost Models

MPC implementation relies on rapid, accurate solution of an underlying optimization problem. During BP2 we applied optimal control theory to several formulations of efficient cooling problems. For example, in one class of problems that included a cost function dependent on peak power use we developed a computable optimality condition that characterized the unknown peak-power level. We also developed an approximation framework, wherein the infinite-dimensional optimal control problem was replaced by a finite-dimensional nonlinear programming problem (NLP). In this framework the dynamical equations are approximated by collocation constraints in the NLP.

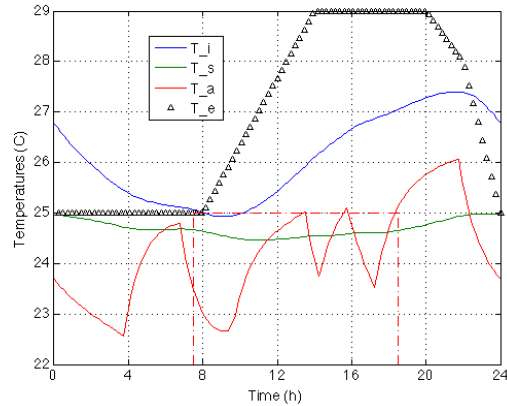


Figure 19 State (temperature) time histories for an NLP formulation

As shown in Figure 19, there are five cooling periods including one at the beginning (approximately [00, 04]) and one at the end (approximately [22, 24]). The control switches in the late afternoon tend to keep the air-temperature near its upper bound (dashed-red line), and the zone-air temperature exceeds the upper-bound just as the occupied period ends at 1800 h. Note that solution of the NLP can be enhanced by accurate derivative information provided by the Automatic Differentiation software which is currently under development in subtask 4.2.

The collaborative effort in the BP2 will continue in the BP3 and will involve further development and application of the tools. There are three collaborative activities in this subtask. UTRC is focusing on implementation and demonstration for a centralized solution in Building 101 and West Chester University. Purdue is addressing automatic model generation and evaluating the benefits of distributed versus centralized solutions. VT is tackling some of the numerical approaches for obtaining models and solving the optimization problems. This subtask will start to categorize optimal control strategies for different building and systems types with potential energy savings range. This will facilitate building owners, operators and energy managers to screen, identify and select the appropriate strategies for their buildings.

1. Introduction

The realization of energy efficient building design and operation is possible by integrating on-site, combined heat and power with energy storage systems, ventilation and cooling systems with occupancy behavior. This requires a more substantial base in the system design methods and tools. The integration of subsystems that have historically been designed, sold, installed and operated in isolation raise risks that can only be reduced by investing in a more substantial base in the design science for systems.

Flexible modeling environments for use in design and operation are lacking, and are critical to moving designs involving controls, diagnostics implementation with consistency and accuracy from conceptual to detailed design and verification. The development of reduced-order building models amendable to controls design is essential. The models must address heterogeneity involving multi-scale dynamics in buildings, couplings between building envelope, mechanical system, equipment and controllers. A modular modeling platform is being developed with reusable component libraries to capture the multi-scale dynamics of buildings and for assembly of heterogeneous components. The modeling platform is critical to enable a highly automated process usable by designers and operators that will be scalable to the entire building stock. Automation is the key to reduce design cycle time and cost. Using models to quantify uncertainty is critical for system robustness and ensuring the persistence of energy savings throughout a life cycle of the building operation.

Nonlinear Model Predictive Control (NMPC) has its roots in the mathematical theory of optimal control (OC). The fundamental idea is use a dynamic model to forecast system behavior, and then to optimize the forecast and compute the best decision - the control to use at the current time. As time and the system's response evolves, the forecast-optimize cycle is repeated to determine the best control. Whereas this concept has a long history, progress in computational-speed and in algorithmic power now makes the approach technically and economically practical.

It's clear that accurate dynamic models are enabling for any NMPC implementation. The feedback nature of the implementation provides some tolerance for modeling errors, however, model errors almost certainly degrade achievable performance. Accordingly, a significant amount of the BP2 effort has been devoted to developing scalable modeling procedures. In order to make precise the notion of forecasting system behavior it is necessary to specify the time horizon for the forecast. In the case of building energy control the time has to be sufficiently long to capture the important dynamics in the buildings thermal behavior. For example, stored thermal energy in the building envelope can be used to shape energy consumption and reduce peak-demand requirements. Longer time horizons increase computational complexity in the underlying optimization cycle and this requires informed trade-offs in the NMPC implementation.

In a general sense, optimal supervisory control involves minimization of a cost function (e.g., energy cost) with respect to control setpoints (e.g., chilled water and air supply temperatures) and subject to constraints (e.g., comfort and equipment capacities). More specifically, model predictive control (MPC) involves minimization of an integrated cost (e.g., daily) and employs building and equipment models as key elements in enabling adaptive and predictive control in response to time varying inputs. Generating models, constraints, and appropriate cost functions

for a new application can be time consuming and expensive and has been a limiting factor for widespread application of optimal control. The primary goals of this subtask are to develop and demonstrate a process, tools and algorithms that can significantly reduce the development and commissioning time/cost to implement optimal supervisory control for retrofits in buildings. This approach involves automating generating models, cost functions, and constraints needed to minimize energy costs. The goal is to provide algorithms that are scalable and that could be deployed across commercial buildings.

During the BP2, this subtask is focusing on the following deliverables:

- 1) Adaptive and optimal control algorithms that can adapt and optimize performance with changing environmental and building usage conditions. Model-predictive controls to compensate loads in a predictive fashion while respecting state and actuation constraints.
- 2) Control-oriented models (i.e., reduced-order model and inverse (data-driven) model) which capture the relevant physics and dynamics of the building sub-systems and the indoor environment and are suitable for advanced supervisory and terminal control design. The models will be easily replicable and scalable to multiple building configurations and locations, reducing the effort required for control design and optimization.
- 3) Supervisory level control algorithms to generate optimal set points for lower level controllers, accounting for outdoor and indoor disturbances.

2. Control Oriented Model Development

2.1 Introduction

Modeling accuracy is a key enabler for effective and robust controller performance. Compared to the process industry, where the effectiveness and benefits of MPC have been successfully demonstrated [1], models for building HVAC systems have larger uncertainties due to cost constraints that limit the number and quality of sensors that are available for model training or tuning. MPC utilizes dynamic building and HVAC equipment models and input forecasts to estimate future energy usage and employs optimization to determine control inputs that minimize an integrated cost function for a specified prediction horizon. A dynamic model with reasonable prediction performance (e.g., accuracy and simulation speed) is crucial for a practical implementation of MPC. One modeling approach is to use whole-building energy simulation programs such as EnergyPlus, TRNSYS and ESP-r, etc. However, the computational and set up costs for these models are significant and they do not appear to be suitable for on-line implementation.

According to ASHRAE [2], modeling approaches can be classified within two categories: 1) forward (classical) modeling, and 2) data-driven (inverse) modeling. Forward modeling approach typically starts from exploiting physics of the system. For example, a very detailed physics-based building envelope model could be built by inputting information for building geometry, physical parameters of each wall (internal/external surfaces) and windows, and their connectivity graphs. One of the drawbacks of this approach is that it would require a large number of parameters to be determined, which may not be easy to obtain from existing measurements in practice. Data-driven (inverse) modeling approaches, on the other hand, typically start from processing measurement data from the system. However, some inverse modeling approaches utilize a physics-based model structure, e.g., thermal-network, where the data is mainly used to train the model parameters. The major advantage of the forward modeling approach is that it can be applied to systems in the design phase prior to construction [2]. On the other hand, a data-driven modeling approach is easier to apply for an existing system and is often more accurate in terms of predicting system responses compared to forward models [2].

In this section, the following modeling methods are presented:

- Reduced order model
- Couple reduced order indoor-air model
- Inverse model
- Data driven model based on system identification

2.2 Reduced Order Model

For the last two decades there has been a growing interest in applying Model-Based Predictive Control (MPC) for reducing energy use and costs for operation of buildings. The application of MPC to buildings could have high computational requirements depending on the number of control variables, the time horizon for the optimization, the discretization for control decisions and model solution, and the complexity of the models.

Reducing model complexity and computational requirements, while retaining prediction accuracy, is the goal when considering reduced-order modeling. Many different model order reduction (MOR) methods have been developed in computational fluid dynamics, very large

scale integration and control. These include state aggregation methods, balanced realization approaches, singular perturbation methods and moment matching approximation based on the Krylov subspace method.

Various approaches have been developed and applied for building envelope systems in order to cope with high dimensionality that results from a spatial discretization of the partial differential equations (PDE) that model heat conduction in walls. Gouda [3] categorized the MOR methods for building applications into three groups.

- Polynomial reduction methods
- Parameter estimation
- State-space transformation-based techniques.

In this section, we will restrict our attention to state-space based methods. E. Palomo et al. [4] investigated several state transform methods for building applications and suggested a guide to select a reduction technique for thermal models. The authors also applied the reduced-order models (ROM) to investigate control strategies such as PID and optimal controllers [5]. In their approach, a reduced-order linear time invariant (LTI) model for a multi-zone building was developed from a detailed description of the wall dynamics based on a finite volume or finite difference method. A full-order model is assembled for each wall and MOR is applied. The procedure to generate a reduced-order model is described as “complete-assembled-reduced” or simply c-a-r according to Ménézo’s notations [6].

C. Ménézo et al [6] proposed application of a state aggregation method to each wall and then assembly of all the reduced models with a zone air balance and surface boundary conditions to construct a lower order multi-zone model. Additional MOR can be applied to the assembled model. In comparison to c-a-r, this approach can be described as “reduced-assembled (r-a) or reduced-assembled-reduced (r-a-r)”. In the study, comparisons of results for a single-zone case study were provided for the c-a, c-a-r, r-a and r-a-r approaches.

S. Goyal and P. Barooah [7] also started from a simplified wall model for wall dynamics described as 3R2C (three resistances and two capacitances) in order to obtain a reduced-order zone model. A multi-zone is constructed from the simplified wall models and then a balanced truncation method is applied to further reduce the dimension. A model-order reduction method to treat nonlinearities appearing from water vapor balance equations was also presented.

K. Deng et al. [8] proposed a method to reduce complicated thermal networks by aggregating a number of nodes into “super-nodes”. The proposed method is based on model reduction of Markov chains.

Many approaches have been suggested for the building system, but the previous researches focused on the model reduction technique itself, thereby the comparisons of the reduced order model were restricted to their original models. However, to the building system simulation field, the most fundamental questions on the MOR method might be the applicability and reliability of the lower order model, not the model reduction technique itself. Unfortunately, none of them compared their ROMs to experimental data or reliable models which are validated to experiment, such as Energy plus [9] and TRNSYS [10], thereby left the essential questions of the usability of

the reduced order model.

The previous case studies for reduced-order modeling were limited to a relatively small number of zones, e.g. four zones, and there were no comparisons of computational requirements with more traditional simulation models. These limited results lead to a question on the applicability of MOR methods to a commercial size of building.

This section presents a general approach for generating a ROM from a detailed representation of the dynamics of commercial sized multi-zone buildings and provides comparisons of predictions and computational requirements with a commercial building simulation tool. The proposed method utilizes balanced truncation [11] for subsystem model reduction.

A general and systematic methodology for converting the complex thermal network of a multi-zone building into a linear time invariant model is developed in Section 2.2.1. In Section 2.2.2, we review balanced truncation and introduce the subsystem model reduction method with summaries of the advantages when it is applied to a building system. Case study results are presented for an existing 59-zone building in Section 2.2.3. In this section, the performance of the approach is also compared with a TRNSYS model in terms closed and open-loop responses, as well as computational requirements.

2.2.1. Mathematical Modeling

State-Space Representation of a Thermal Building Model

The key feature of our modeling approach is a hierarchical, modular treatment of a large number of temperature nodes in a multi-zone building envelope system. Following this multi-level approach, a systematic method for generating a LTI model for the complex thermal network of a multi-zone building is presented.

The structure of the states is summarized as follows.

T_j^i = temperature at j^{th} node in i^{th} wall in a single zone

\vec{T}_j = set of all j^{th} temperature nodes of walls in a single zone, i.e. $\vec{T}_j = \left[T_j^1 \quad T_j^2 \quad \dots \quad T_j^{Nw} \right]^T$

\vec{T}_w^I = set of all node temperatures of walls and windows in I^{th} zone, i.e.

$$\vec{T}_w^I = \left[\vec{T}_1^T \quad \vec{T}_2^T \quad \dots \quad \vec{T}_n^T \right]$$

\vec{T}_w = set of all temperatures nodes of walls in multiple zones, i.e. $\vec{T}_w = \left[(\vec{T}_w^1)^T \quad \dots \quad (\vec{T}_w^{Nz})^T \right]^T$

In this section, the term zone is used to represent a unit or module of the thermal network of a room. A multi-zone representation is a group of thermal network units. The state-space model of a building system starts from a module (network unit) and extends to constructing more complex multi-zone models. A detailed formulation is described in this section. Some of the important assumptions used to construct the network unit are:

- The temperature of each surface or surface segment and of its cross section is uniform.
- Each zone is well mixed.
- Each wall emits or reflects diffusely and is gray and opaque.
- Air is a nonparticipating media with respect to radiation.

- Heat transfer is one dimensional.
- Conduction between each window and window frame is neglected (1-D assumption).

The main approach to treating the complex thermal network for a multi-zone building is to linearize long-wave radiation exchange and group the states (temperatures) and fundamental equations in the form of a state-space representation to facilitate model-order reduction.

Conduction through Walls

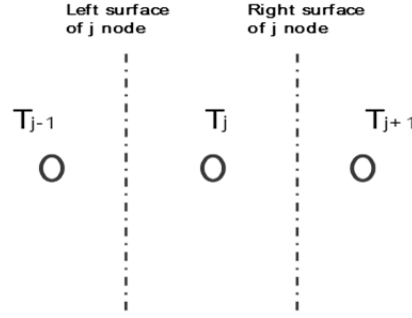


Figure 2.2.1 Notation for conduction through walls.

A finite volume formulation is used to describe the heat conduction through walls and is depicted in Figure 2.2.1. For any j^{th} node in a wall except the first and last nodes, an energy balance leads to

$$\rho_j^i C_j^i w_j^i \frac{dT_j^i}{dt} = h_{cd}^L |j^i T_{j-1}^i - (h_{cd}^L |j^i + h_{cd}^R |j^i) T_j^i + h_{cd}^R |j^i T_{j+1}^i + q_{gen_j}^i \quad (2.2.1)$$

where $h_{cd}^L |j^i = \frac{k^L |j^i}{w^L |j^i}$ and $q_{gen_j}^i$ is an energy source [W/m^2] inside the j^{th} finite control volume that belongs to the i^{th} wall.

By using the following matrix notation,

$$\vec{q}_j \equiv \begin{bmatrix} q_{gen}^1 \\ q_{gen}^2 \\ \vdots \\ q_{gen}^{Nw} \end{bmatrix}, \quad \tilde{H}_j^L \equiv \begin{bmatrix} h_{cd}^L |j^1 & & 0 \\ & h_{cd}^L |j^2 & \\ 0 & & \ddots \\ & & & h_{cd}^L |j^{Nw} \end{bmatrix}, \quad \vec{T}_j \equiv \begin{bmatrix} T_j^1 \\ T_j^2 \\ \vdots \\ T_j^{Nw} \end{bmatrix}$$

$$\tilde{C}_j \equiv \begin{bmatrix} \rho C w |j^1 & & & 0 \\ & \rho C w |j^2 & & \\ & & \ddots & \\ 0 & & & \rho C w |j^{Nw} \end{bmatrix},$$

equation (2.2.1) can be expressed in the following matrix form.

$$\tilde{C}_j \frac{d\vec{T}_j}{dt} = \tilde{H}_{cd,j}^L \vec{T}_{j-1} - (\tilde{H}_{cd,j}^L + \tilde{H}_{cd,j}^R) \vec{T}_j + \tilde{H}_{cd,j}^R \vec{T}_{j+1} + \vec{q}_j \quad (2.2.2)$$

Note that \vec{T}_j is a group of all of the wall temperature nodes belonging to an individual zone.

Heat Balance at Outside Surface

For any i^{th} outside wall (connected to the external ambient) belonging to an individual zone, the heat balance equation at the surface is

$$\rho_1^i C_1^i w_1^j \frac{dT_1^i}{dt} = h_{cv,ex}^i (T_a - T_1^i) + h_{cd,l}^R |_1^i (T_2^i - T_1^i) + \alpha_1^i q_{SWR}^i + q_{LWR}^i \quad (2.2.3)$$

where T_1^i represents the wall temperature of the first node which is set to be an outside surface of the wall.

With the assumptions that the outside surface is gray and diffuse and the air is a non-participating radiation media, net long wavelength interactions with the environment can be expressed as

$$q_{LWR}^i = \sigma \epsilon_1^i F_{sky}^i (T_{sky}^4 - T_1^{i4}) + \sigma \epsilon_1^i F_{grd}^i (T_{grd}^4 - T_1^{i4})$$

Using a linear approximation of the long-wave heat exchange term gives

$$\rho_1^i C_1^i w_1^j \frac{dT_1^i}{dt} = -(h_{cv,ex}^i + h_{cd,l}^R |_1^i + h_{rad,ex}^i) T_1^i + h_{cd,l}^R |_1^i T_2^i + q_1^i \quad (2.2.4)$$

where

$$h_{rad,ex}^i = 4\sigma \epsilon_1^i (F_{sky}^i \bar{T}_{sky}^3 + F_{grd}^i \bar{T}_{grd}^3),$$

$$q_1^i = h_{cv,ex}^i T_a + 4\sigma \epsilon_1^i (F_{sky}^i \bar{T}_{sky}^3 T_{sky} + F_{grd}^i \bar{T}_{grd}^3 T_{grd}) + \alpha_1^i q_{SWR}^i$$

$$\bar{T}_{sky} = \frac{T_{sky} + T_1}{2}, \quad \bar{T}_{grd} = \frac{T_{grd} + T_1}{2}$$

The mean temperatures for long-wave exchange between the surface and sky and surface and ground are assumed to be the same for all outside surfaces.

Equation (2.2.4) can be generalized and written in compact matrix form as

$$\tilde{C}_1 \frac{d\vec{T}_1}{dt} = -(\tilde{H}_{cd,l}^R + \tilde{H}_{rad,ex} + \tilde{H}_{cv,ex}) \vec{T}_1 + \tilde{H}_{cd,l}^R \vec{T}_2 + \vec{q}_1 \quad (2.2.5)$$

where

$$(\vec{q}_1)_i = h_{cv,ex}^i T_a + 4\sigma \epsilon_1^i (F_{sky}^i \bar{T}_{sky}^3 T_{sky} + F_{grd}^i \bar{T}_{grd}^3 T_{grd}) + \alpha_1^i q_{SWR}^i$$

Heat Balance at Inside Surface

For the i^{th} zone and i^{th} wall, the energy balance equation for the inside surface is

$$\rho_n^i C_n^i w_n^j \frac{dT_n^i}{dt} = h_{cv,in}^i (T_z - T_n^i) + h_{cd,l}^L |_n^i (T_{n-1}^i - T_n^i) - q_{net,rad}^i \quad (2.2.6)$$

where $q_{net,rad}^i$ is net radiative flux out of the inside wall.

The radiosity method is utilized to express the net flux under the assumption that the walls are

gray, diffuse and opaque. The same linearization method used in Equation (2.2.4) is employed leading to

$$\vec{q}_{net,rad} = \tilde{A}^{-1}[\tilde{B}'\vec{T}_n - \vec{h}_o] \quad (2.2.7)$$

where,

$$\tilde{A}_{ij} \equiv \frac{\delta_{ij}}{\epsilon_j} - \frac{\rho_j}{\epsilon_j} F_{ij}$$

$$\tilde{B}'_{ij} = 4\sigma(\delta_{ij} - F_{ij})\bar{T}^3$$

A similar formulation for the treatment of long-wave interactions is shown in [12]. In equation (2.2.7), radiosity does not appear explicitly, which is convenient for building simulation. Since h_o^i represents an external radiative source acting on the i th surface, the effects of internal sources and transmitted solar energy through windows are treated in a consistent manner. For any shaped room, the net radiative flux can be explicitly calculated as a function of surface temperatures if the view factors and the external radiative sources are known.

By letting $\tilde{H}_{rad,in} \equiv \tilde{A}^{-1}\tilde{B}'$ and $\vec{q}_n \equiv \tilde{A}^{-1}\vec{h}_o$,

$$\tilde{C}_n \frac{d\vec{T}_n}{dt} = \tilde{H}_{cd,n}^L \vec{T}_{n-1} - (\tilde{H}_{cd,n}^L + \tilde{H}_{rad,in} + \tilde{H}_{cv,in})\vec{T}_n + \vec{h}_{cv,in} T_z + \vec{q}_n \quad (2.2.8)$$

State-Space Representation of Thermal Network Module

Gathering the system of equations that represent heat balance equations for external to internal wall elements, i.e. equations (2.2.2), (2.2.5) and (2.2.8),

$$\tilde{C}_w \dot{\vec{T}}_w = \tilde{H}_{ww} \vec{T}_w + \tilde{H}_{wz} T_z + \vec{q}_w \quad (2.2.9)$$

where

$$\tilde{C}_w = \begin{bmatrix} \tilde{C}_1 & & & & \\ & \tilde{C}_2 & & & \\ & & \dots & & \\ & & & & \tilde{C}_n \end{bmatrix}, \quad \tilde{H}_{ww} = \begin{bmatrix} -\tilde{H}_1 & \tilde{H}_{cd,1}^R & & & \\ \tilde{H}_{cd,2}^L & -(\tilde{H}_{cd,2}^L + \tilde{H}_{cd,2}^R) & \tilde{H}_{cd,2}^R & & \\ & & \dots & \dots & \\ & & & \tilde{H}_{cd,n}^L & -\tilde{H}_n \end{bmatrix}$$

$$\tilde{H}_1 = (\tilde{H}_{cd,1}^R + \tilde{H}_{cv,ex} + \tilde{H}_{rad,ex})$$

$$\tilde{H}_n = (\tilde{H}_{cd,n}^L + \tilde{H}_{cv,in} + \tilde{H}_{rad,in}) \quad \tilde{H}_{wz} = \begin{bmatrix} \mathbf{0}^T & \mathbf{0}^T & \dots & (\vec{h}_{cv,in})^T \end{bmatrix}^T \quad \vec{q}_w = \begin{bmatrix} \vec{q}_1^T & \vec{q}_2^T & \dots & \vec{q}_n^T \end{bmatrix}^T$$

A tri-diagonal block matrix is formed with parameters that characterize heat transfer due to conduction in the walls (from node number 2 to node number $n-1$) and radiative/convective heat transfer at the boundaries (first and last nodes only). The terms \vec{q}_j , where j is from 2 to $n-1$, vanish if there are no heat flux sources inside the wall such as embedded radiant heating or

cooling.

Because a multi-zone representation is a group of thermal network units, it can be readily developed based on Equation (2.2.9). The coupling parameters between the units are derived from the heat conduction equation in the form

$$\tilde{C}_w \dot{\vec{T}}_w = \tilde{H}_{ww} \vec{T}_w + \tilde{H}_{wz} \vec{T}_z + \vec{q}_w \quad (2.2.10)$$

where the coefficient matrices, \tilde{C}_w , \tilde{H}_{ww} and \tilde{H}_{wz} have block diagonal forms, except for the coupling matrix, consisting of the coefficient matrices for each zone, \tilde{C}_w , \tilde{H}_{ww} and \tilde{H}_{wz} . Each variable also represents the set of all individual variables in all zones. For example, \vec{T}_w is the set of all temperature nodes of walls in multi-zones, i.e., $\vec{T}_w = [(\vec{T}_w^1)^T \dots (\vec{T}_w^{Nz})^T]^T$

State-Space Representation of Zone Air Balance

To complete the state-space representation of a multi-zone building, the dynamics of zone air temperatures need to be included. Heat fluxes to an air control volume within a zone can be categorized as follows.

$$\dot{Q}_{vent}^I = \text{ventilation}$$

$$\dot{Q}_{inf}^I = \text{infiltration}$$

$$\dot{Q}_{cpl}^I = \text{air mixing among rooms}$$

$$\dot{Q}_S^I = \text{convective internal source due to computer, human action and so on,}$$

$$\dot{Q}_{CV}^I = \text{convective heat exchange between a zone air and its surrounding walls}$$

The balance equation for the I^{th} zone is

$$\rho^I C_V^I V^I \frac{\partial T_z^I}{\partial t} = \dot{Q}_{cv} + \dot{Q}_{cpl}^I + \dot{Q}_{inf}^I + \dot{Q}_S^I + \dot{Q}_{vent}^I \quad (2.2.11)$$

A linear state-space form was formulated based on Equation (2.2.11) under the assumption that the inter-zone mixing and infiltration terms are negligible and is expressed as

$$\tilde{C}_z \dot{\vec{T}}_z = \tilde{H}_{zw} \vec{T}_w + \tilde{H}_{zz} \vec{T}_z + \vec{Q}_S + \vec{Q}_{vent} \quad (2.2.12)$$

\tilde{C}_z is a diagonal matrix where the I^{th} element is the I^{th} zone air capacity, i.e. $\rho^I C_V^I V^I$. The terms \vec{T}_z , \vec{Q}_S and \vec{Q}_{vent} are vectors where the I^{th} element is T_z^I , Q_S^I or Q_{vent}^I . \vec{T}_w is defined in Equation (2.2.10). \tilde{H}_{zw} and \tilde{H}_{zz} are block diagonal matrixes where the I^{th} block represents the convective heat exchange between the I^{th} zone air and its surrounding walls.

Final State-Space Representation of Thermal Network

Based on Equations of (2.2.10) and (2.2.12), the state-space representation of the thermal network can be written as

$$\begin{bmatrix} \tilde{C}_W & 0 \\ 0 & \tilde{C}_Z \end{bmatrix} \begin{bmatrix} \dot{\tilde{T}}_W \\ \dot{\tilde{T}}_Z \end{bmatrix} = \begin{bmatrix} \tilde{H}_{WW} & \tilde{H}_{WZ} \\ \tilde{H}_{ZW} & \tilde{H}_{ZZ} \end{bmatrix} \begin{bmatrix} \tilde{T}_W \\ \tilde{T}_Z \end{bmatrix} + \begin{bmatrix} \tilde{q}_W \\ \tilde{Q}_Z \end{bmatrix} \quad (2.2.13)$$

The matrices \tilde{C} and \tilde{H} represent the thermal capacitance and heat transfer coefficients of all wall nodes and zone nodes, respectively. The subscripts W and Z refer to wall and zone.

When constructing the state-space representation in the form of $\dot{x} = Ax + Bu$ from Equation (2.2.13), the size of the B matrix will be the same as the size of a . However, the size of matrix B can be dramatically reduced by introducing a simple transformation denoted by \tilde{T}' in Equation (2.2.14), since the heat sources inside the wall are zero except for the case of radiant floor heating and cooling.

The final standard form is

$$\begin{bmatrix} \dot{\tilde{T}}_W \\ \dot{\tilde{T}}_Z \end{bmatrix} = \begin{bmatrix} \tilde{C}_W & 0 \\ 0 & \tilde{C}_Z \end{bmatrix}^{-1} \begin{bmatrix} \tilde{H}_{WW} & \tilde{H}_{WZ} \\ \tilde{H}_{ZW} & \tilde{H}_{ZZ} \end{bmatrix} \begin{bmatrix} \tilde{T}_W \\ \tilde{T}_Z \end{bmatrix} + \begin{bmatrix} \tilde{C}_W & 0 \\ 0 & \tilde{C}_Z \end{bmatrix}^{-1} \tilde{T}' \tilde{u}$$

$$\tilde{y} = \tilde{C} \begin{bmatrix} \tilde{T}_W \\ \tilde{T}_Z \end{bmatrix} \quad (2.2.14)$$

2.2.2. Model Reduction Method

Balanced Truncation Method

The purpose of model order reduction (MOR) is to derive a lower order model from a high order system preserving the dominant dynamics of the original high order model. The problem definition of MOR for a linear time invariant system is to construct lower order matrices for A_r, B_r, C_r, D_r , Equation (2.2.15), from the original system of Equation (2.2.16).

$$G_r : \begin{cases} \dot{x}_r(t) = A_r x_r(t) + B_r u(t) \\ y_r(t) = C_r x_r(t) + D_r u(t) \end{cases} \quad (2.2.15)$$

$$G_o : \begin{cases} \dot{x}(t) = Ax(t) + Bu(t) \\ y(t) = Cx(t) + Du(t) \end{cases} \quad (2.2.16)$$

where the state $x(t) \in \mathcal{R}^n$, $x_r(t) \in \mathcal{R}^r$ and $r \ll n$.

Note that we want to reduce the state order from n to r while keeping the response error $\|G_o - G_r\|_\infty$ small. ($\|\cdot\|_\infty$ is the H-infinity norm and G_o and G_r are transfer functions of the original and reduced-order systems, respectively.)

Several model order reduction methods are available, but one representative method employed in the current study is the balanced truncation technique originally proposed by B.C. Moore [13].

The main idea of the balanced truncation approach is to truncate states which make little contribution to input and output behavior [14]. The importance of the states can be measured by the singular values of the Hankel operator defined by

$$(\Gamma v)(t) = \int_0^{\infty} C e^{A(t+\tau)} B v(\tau) d\tau \quad (2.2.17)$$

In other words, if one can find the Hankel singular values, denoted by Σ , one can judge the contribution of each of the states.

The first step of the state-space transformation technique is to find a transformation which balances the observability and controllability Gramians, defined by

$$W_c = \int_0^{\infty} e^{A\tau} B B^\dagger e^{A^\dagger \tau} d\tau$$

$$W_o = \int_0^{\infty} e^{A^\dagger \tau} C^\dagger C e^{A\tau} d\tau$$

where the superscript \dagger denotes conjugate transpose.

After balancing the Gramians, one can obtain the Hankel singular value via the well-known formula: $W_c = W_o = \Sigma$.

The second step is to construct and to perform a Galerkin projection based on the singular values of the balanced Gramians [15]. Important features of the approach are the reduced-order model maintains most of the original model properties such as dynamic behavior, observability, controllability and stability [16], thereby providing a more reliable model. Furthermore the truncation of error, $\|G_o - G_r\|_{\infty}$, is bounded by twice the sum of the truncated singular values.

In this study, the balanced truncation method was adopted for constructing a reduced-order model based on the system of Equation (2.2.14). An algorithm to compute the state-space balancing transformation is presented by A.J. Laubi [17].

Subsystem Model Reduction by Balanced Truncation

A natural treatment for considering various numbers of states in the multi-zone building is to start from simplified wall dynamics, such as a 3R2C representation, and to assemble them (r-a or r-a-r). However these “bottom-up” type methods are questionable because the elementary lower order model pre-programs a certain loss in dynamic behavior that may be important when considering a large coupled system with many walls and zones.

Needless to say, it is more systematic and reliable to construct a ROM from the original full order model rather than aggregating approximate models. However the main disadvantage to this approach is the fact that the computational time increases significantly as the number of states increase. For example, computation complexity applying the Lyapunov balancing method increases with the 3rd power of the dimension of state space [18]. The application of the Iterative Rational Krylov Algorithm is included in the Appendix 2.2.

Instead of reducing the entire coupled system or reducing each wall separately, it makes sense to reduce the thermal network unit representing each zone while taking into account its interconnection with other units, and then to reduce the assembled entire lower model (c-a-r-a-r). The procedure is performed on the framework of subsystem model reduction [11] as follows.

A subsystem (thermal network unit for one zone) representation of a coupled LTI system can

have the following general form.

$$\begin{aligned}\dot{x}_j(t) &= A_j x_j(t) + B_j u_j(t) \\ y_j(t) &= C_j x_j(t)\end{aligned}\tag{2.2.18}$$

where $j \in \{1, 2, \dots, k\}$, $x_j(t) \in \mathcal{R}^{n_j}$, $u_j(t) \in \mathcal{R}^{m_j}$, $y_j(t) \in \mathcal{R}^{p_j}$ and the matrices of subsystems with appropriate dimensions.

The ‘‘coupling effect’’ is characterized by the relations

$$\begin{aligned}u_j(t) &= \sum_{i=1}^k K_{ji} y_i(t) + H_j u(t) \\ y(t) &= \sum_{i=1}^k R_i y_i(t)\end{aligned}$$

where $u(t) \in \mathcal{R}^m$ and $y(t) \in \mathcal{R}^p$ represents exogenous inputs and outputs of the entire system and the matrix $[K_{ji}]_{i,j=1}^k$ defines the interactions between the subsystems.

The entire LTI system representation can be readily obtained and is shown below.

$$\begin{aligned}A &= \tilde{A} + \tilde{B} \tilde{K} \tilde{C} \\ B &= \tilde{B} \tilde{H} \\ C &= \tilde{R} \tilde{C}\end{aligned}\tag{2.2.19}$$

where

$$\begin{aligned}\tilde{A} &= \text{diag}(A_1, \dots, A_k) \in \mathcal{R}^{n,n} \\ \tilde{B} &= \text{diag}(B_1, \dots, B_k) \in \mathcal{R}^{n,m_1+\dots+m_k} \\ \tilde{C} &= \text{diag}(C_1, \dots, C_k) \in \mathcal{R}^{p_1+\dots+p_k,n} \\ \tilde{K} &= [K_{ji}]_{i,j=1}^k \in \mathcal{R}^{m_1+\dots+m_k,p_1+\dots+p_k} \\ \tilde{H} &= [H_1^T, \dots, H_k^T]^T \in \mathcal{R}^{m_1+\dots+m_k,m} \\ \tilde{R} &= [R_1, \dots, R_k] \in \mathcal{R}^{p,p_1+\dots+p_k}\end{aligned}$$

$$n = n_1 + \dots + n_k$$

When balanced truncation method is applied to each subsystem of Equation (2.2.18), the reduced model for the coupled system has the same form of Equation (2.2.19). Thus, the original subsystems are replaced with the reduced ones but with preservation of the structure of the interconnections.

The main advantage of following this approach to building envelope system modeling is that the truncation error for the entire ROM can be bounded and stability is guaranteed, because each thermal network unit is asymptotically stable. More rigorous discussion of the approach is provided in [11].

The theoretical bound of the approximation error gives a more reliable reduced-order model than the one constructed by r-a-r approaches. Also, the accumulation of truncated dynamic properties is reduced. Furthermore computational time to construct a ROM is reduced compared to the c-a-r approach. With these advantages, we move our attention to the capability and the performance

tests of the proposed method.

2.2.3. Case Study Results And Discussions

Building description and case study results

For testing the validity of the detailed (full-order) model representation, both steady and dynamic responses were evaluated for various cases. The direct stiffness method (FEM) with the an exact radiosity solution for long-wave radiation was used to check the steady-state behavior. TRNSYS Version 17 was used to compare dynamic response. A case study for the performance test of the full-order and reduced-order models for a single zone is provided in [19].

In BP2, a case study for the Building 101 located at the Philadelphia Navy Yard is presented to demonstrate the accuracy and computational requirements of reduced-order modeling as compared to the TRNSYS model. Figure 2.2.2 shows an external view of the building. Some characteristics uses in the modeling include:

- 55,000 square feet of total floor area
- 3 occupied floors with a basement and attic spaces and a total of 59 zones
- 18 different types of layers used for wall construction that primarily consist of concrete, insulation board, plaster board, and brick
- 6 different types of walls various combinations of the layer types
- ground boundary temperature is modeled as a time varying signal
- TMY2 weather data for Philadelphia
- Values of $17.77[\text{W}/\text{m}^2\text{-K}]$ and $3.05[\text{W}/\text{m}^2\text{-K}]$ were used for convective heat transfer coefficients at the outside and inside surfaces, respectively.

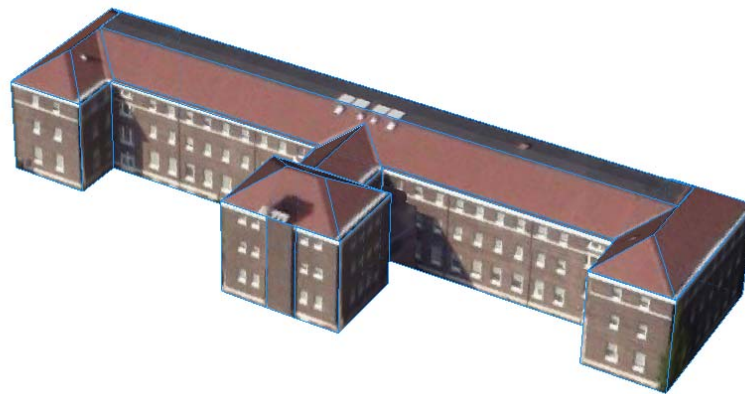


Figure 2.2.2 External view of Building 101 (3D Google Map)

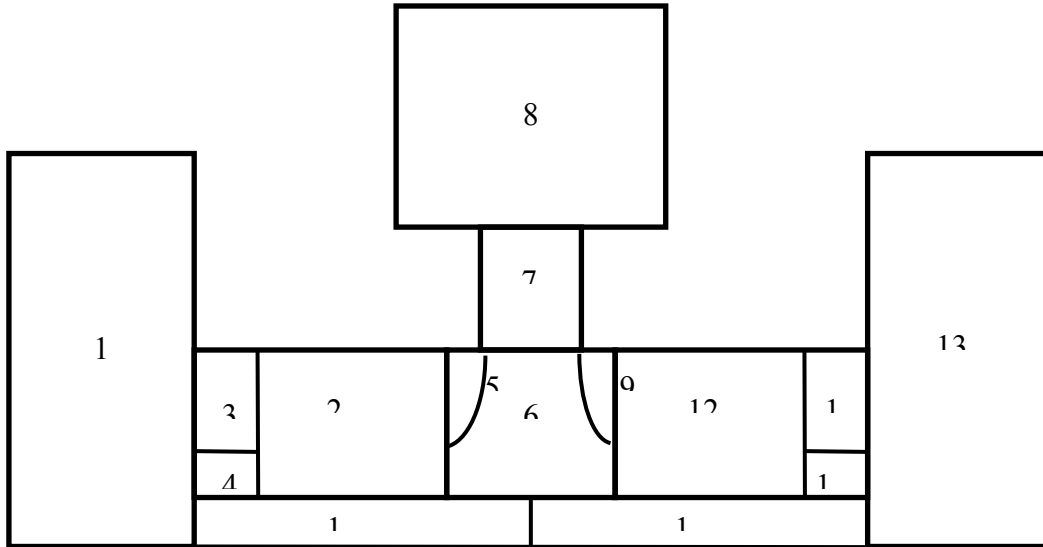


Figure 2.2.3 Zoning of 2nd floor of Building 101

The ground and attic were represented using 11 and 5 zones, respectively. The 1st, 2nd, and 3rd floors used the zoning shown in Figure 2.2.3.

In order to construct a linear time invariant system, average values of effective sky temperature, ground surface temperature and mean external wall temperatures are needed for linearization of the radiation heat transfer coefficient and are determined prior to simulation. The average ground temperature was taken as the average annual air temperature. The average sky and air temperature were determined from the TMY2 weather file, whereas the mean external wall temperature was set to 15°C.

Note that the computational time for solution of differential (difference) equations is highly dependent on the differential (difference) equation solver algorithm. Therefore performance judgments with respect to simulation time relative to TRNSYS are difficult. One of the most important differences between the state-space representation and TRNSYS is that the former is continuous, but the latter is represented using discrete equations. A continuous representation lends itself to variable time step solution algorithms, whereas the TRNSYS representation utilizes fixed time steps.

In order to provide reasonable computational comparisons between the ROM and TRNSYS, first-order hold discretization was performed for the ROM with the same time step used in TRNSYS. Table 2.2.1 and Table 2.2.2 show comparisons of computational time and errors for open-loop variation of zone temperatures for one year for TRNSYS and ROM with a 3.10 GHz (32 bit) computer. The time required for preprocessing in both models was not counted in the Table 2.2.1.

Note that the comparisons are for an entire year. Although there are some deviations at the ground floor and the attic, the ROM provides comparable accuracy overall with 0.74 °C maximum root mean square (RMS) differences. Compared to TRNSYS, the computation was reduced by about a factor of 100. As a result, the ROM is more readily utilized in optimization,

optimal control or any high level control than existing modeling approaches.

The computational time required to generate the reduced-order model is summarized in Table 2.2.3. The total amount of system memory reserved for the MATLAB process was 631 MB. The full-order model had a total of 3664 nodes for the 59 zones. The computational time to generate the entire system matrix was 5.5 sec and the memory required to save the system matrix was 243.4 KB utilizing sparsity of the matrix. The computational time for subsystem model reduction and the assembly process was 9 sec. The number of states was reduced by about a factor 2 from the full-order model for the subsystem model reduction. The computational time for the assembled system MOR was more significant (65.1 sec), but the number of states was reduced by about a factor of 25. In addition to controls applications, the computational savings demonstrated in Table 2.2.1 indicate that this approach may be useful for general building simulation, particularly when considering parametric studies and optimization for design.

Table 2.2.1 Computational time comparison for ROM and TRNSYS with one-year simulation

Time step [min]	TRNSYS [sec]	ROM [sec]
10	876.9	8.7
30	482.6	4.7
60	248.5	3.0

Table 2.2.1 Mean error (°C) and root mean square error (°C) comparison for ROM and TRNSYS with one-year simulation for Building 101

#	Ground Floor		First Floor		Second Floor		Third Floor		Attic	
	ERR	RMS	ERR	RMS	ERR	RMS	ERR	RMS	ERR	RMS
1	0.19	0.29	-0.07	0.22	-0.18	0.32	-0.21	0.39	-0.07	0.62
2	0.44	0.58	0.04	0.34	-0.03	0.31	0.05	0.32	0.22	0.70
3	0.30	0.37	0.10	0.29	0.03	0.29	0.06	0.32	0.52	0.66
4	0.00	0.07	0.02	0.17	0.07	0.32	0.12	0.36	-0.23	0.51
5	0.28	0.36	0.13	0.28	0.06	0.27	0.08	0.31	-0.20	0.67
6	0.28	0.41	0.05	0.31	0.13	0.28	0.22	0.37	-	-
7	0.04	0.35	0.06	0.22	0.01	0.26	0.02	0.35	-	-
8	0.03	0.13	-0.25	0.39	-0.40	0.51	-0.34	0.58	-	-
9	0.31	0.41	0.19	0.31	0.14	0.29	0.11	0.31	-	-
10	0.62	0.74	0.04	0.22	0.07	0.59	0.12	0.59	-	-
11	0.27	0.45	0.10	0.34	0.02	0.50	0.06	0.51	-	-
12	-	-	0.29	0.48	0.41	0.55	0.25	0.39	-	-
13	-	-	-0.06	0.25	-0.23	0.39	-0.33	0.52	-	-
14	-	-	-	-	0.26	0.60	0.11	0.48	-	-
15	-	-	-	-	0.27	0.58	0.09	0.51	-	-

where $ERR[^{\circ}C] = (\sum_k T_r[k] - T_{TRN}[k]) / N$ and $RMS[^{\circ}C] = \sqrt{(\sum_{k=1}^N (T_r[k] - T_{TRN}[k])^2) / N}$.

Table 2.2.2 Computational time for generating ROM for 59 zone building envelope system

	System Matrix [sec]	Subsystem MOR & Assembly [sec]	Assembled System MOR [sec]
Computational time	5.5	9	65.1
Number of states	3664	1954	81

Sample model output comparisons between TRNSYS and the reduced-order model (ROM) for floating zone temperature, driven by weather, for several days are shown in Figure 2.2.4 and Figure 2.2.5. The 1st zone on the 2nd floor and the 8th zone on the 3rd floor are chosen as a “normal” and “worst” case, respectively. The corresponding zone locations can be checked in Figure 2.2.3. The zones in the attic and the ground floors, which are not occupied, were excluded in the selection of “worst” zone. The black solid line (T_{TRN}), blue dashed line (T_r) represents zone air temperature profiles generated by TRNSYS and reduced-order models, respectively.

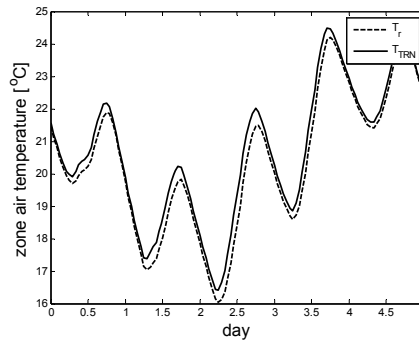


Figure 2.2.4 Open-loop response model comparisons between TRNSYS and reduced-order models (8th zone on the 3rd floor, May)

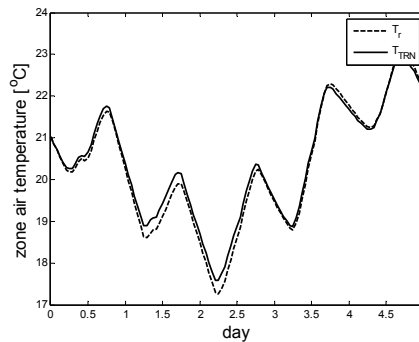


Figure 2.2.5 Open-loop response model comparisons between TRNSYS and reduced-order models (1st zone on the 2nd floor, May)

In order to test closed-loop response of the ROM, the responses under a dual setpoint thermostat controller with saturation points were imposed and the control sequence is shown in Figure 2.2.6. Heating and cooling zone air temperature setpoints of 23°C and 27 °C, respectively, where

utilized. In this test, a 6 kW convective gain was assigned to each zone during the occupied period of 7 am to 6 pm. Example closed loop responses for the TRNSYS and reduced-order models are shown in Figure 2.2.6 and Figure 2.2.7 for the same zones considered in Figures 2.2.4 and 2.2.5.

The computational requirements with 5 minute time steps for a one-year simulation were 3966.2 sec for TRNSYS and 91.4 sec for the ROM model. The mean and RMS differences for the worst case were -0.071 and 0.235°C, respectively. For all of the zones, the mean and RMS differences were 0.0587°C and 0.1724 °C.

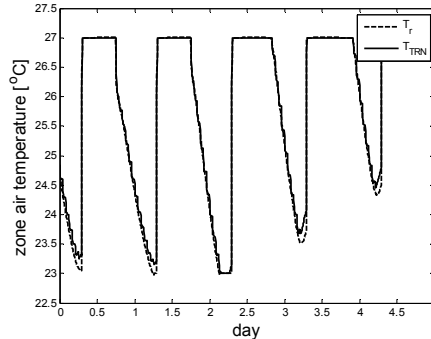


Figure 2.2.6 Closed-loop response model comparisons between TRNSYS and reduced-order models (8th zone on the 3rd floor, May)

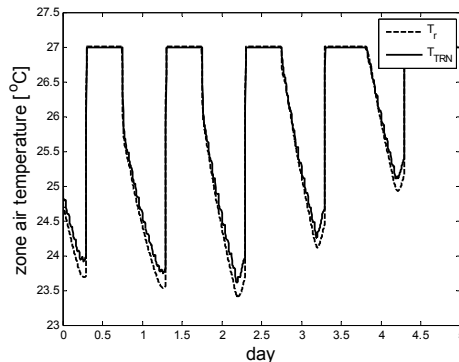


Figure 2.2.7 Closed-loop response model comparisons between TRNSYS and reduced-order models (1st zone on the 2nd floor, May)

The subsystem model reduction method allowed a practical solution to the Lyapunov balance equation for 59 zones in a building initially have 3664 states. Compared to the full-order model, the ROM resulted in about a factor of 50 reduction in state variables (from around 3664 to 81 states) for this specific case study. Compared to TRNSYS, the computation was reduced by about a factor of 100. As a result, the ROM is more readily utilized in optimization, optimal control or any high level control than existing modeling approaches.

2.2.4. Conclusions and future work

Modeling and model order reduction methods to handle commercial size multi-zone buildings were presented. A mathematical representation to describe the thermal network of a building was formulated and applied to generate a reliable reduced-order model using a subspace model reduction technique with balanced truncation. This method is reliable in the sense that the

approximation provides theoretical error bounds.

A case study was carried out for a 59-zone building and results were compared with predictions from a commercially available building energy simulation tool. The lower order model gave results that were close to those predicted by TRNSYS with about one-hundredth the computational requirements. The model has been successfully applied to a Model Predictive Control case study for a single zone building system by D.Kim and J.E. Braun [20].

The physics-based, reduced-order building model lends itself to application of control theory to investigate system properties and to evaluate control performance with the help of control toolkits such as Matlab/Simulink. For example, the system time constant, DC gain under various control inputs, frequency response, stability, controllability and observability can easily be investigated for design of controllers for building systems.

The modeling approach is general for any building geometry (i.e., not restricted to rectangular shapes of walls) because it was developed using the radiosity method that incorporates view factors that can be determined for any geometry. This aspect allows individual wall elements to be divided into separate smaller elements to facilitate coupling to a CFD model for the indoor environment. This spatial discretization of walls is appropriate when the surface temperatures vary significantly due to solar or other non-uniform inputs. A case study for coupling a reduced-order CFD indoor air model with the reduced-order building envelope has been carried out [21].

2.2.5. References

1. Qin, S. J., Badgwell, T. A. 2003. A survey of industrial model predictive control technology. *Control Engineering Practice*, 11(7): 733-764.
2. ASHRAE. 2009. *ASHRAE Handbook-Fundamentals*. Atlanta: American Society of Heating Refrigeration and Air Conditioning Engineers, Inc., pp. 19.1.
3. M. Gouda, S. Danaher, and C. Underwood, Building thermal model reduction using nonlinear constrained optimization, *Building and Environment*, vol. 37, pp. 1255–1265, 2002
4. E. Palomo, Y. Bonnefous, F. Deque, 1997, Guidance for the selection of a reduction technique for thermal models, in: *Proceedings of the IBPSA'97 Building Simulation Conference*, Prague, Czech Republic, 8–10.
5. E. Palomo, G. Lefebvre, P. Behar, N. Bailly, 2000, Using model size reduction techniques for thermal control applications in buildings, *Energy and Buildings*, 33, pp.1-14
6. C. Ménézo, J.J. Rox, J. Virgone, 2002, Modelling heat transfers in building by coupling reduced-order models, *Building and Environment*, 37, pp. 133–144
7. S. Goyal, P. Barooah, 2012, A method for model-reduction of nonlinear building thermal dynamics of multi-zone buildings. *Energy and Buildings*, 47:332–340
8. K. Deng, P. Barooah, P.G. Mehta, S.P. Meyn, 2010, Building Thermal Model Reduction via Aggregation of States, *American Control Conference*. IEEE, 5118–5123
9. EnergyPlus 7.0, 2011, US Department of Energy, <http://apps1.eere.energy.gov/buildings/energyplus/>
10. TRNSYS 17, 2009, Solar Energy Laboratory, University of Wisconsin-Madison
11. T. Reis, T. Stykel, 2008, A survey on model reduction of coupled systems, W.H.A. Schilders, H. van der Vorst, J. Rommes: *Model Order Reduction: Theory, Research Aspects and Applications*, pp. 133-155, *Mathematics in Industry*, Vol. 13, Springer-Verlag, Berlin/Heidelberg
12. Michael F. Modest, *Radiative Heat Transfer*, Second Edition
13. B.C. Moore, 1981, Principal Component Analysis in Linear Systems: Controllability, Observability, and Model Reduction *IEEE transactions on automatic control*. Vol. AC-26, NO. 1

14. S. Skogestad, I. Postlethwaite, 1996, Multivariable Feedback Control, John Wiley & Sons, Chichester
15. S. Lall, J.E. Marsden, S. Glavaski, 2000, A subspace approach to balanced truncation for model reduction of nonlinear control system, International Journal of Robust and Nonlinear control, 12, pp 519-53
16. M. Green, D.N. Limebeer, 1995, Linear Robust Control, Prentice hall information and system science series
17. A.J. Laubi, M.T. Heath, C.C. Paige, R.C. Ward, 1987, Computation of System Balancing Transformations and Other Applications of Simultaneous Diagonalization Algorithms, IEEE Transactions on automatic control, vol. AC-32, No. 2
18. S. Gugercin, A. Antoulas, 2004, A survey of model reduction by balanced truncation and some new results. Int J Control, 77(8): 748–766
19. D. Kim, J.E. Braun, 2012, Reduced-Order Building Modeling For Application To Model-Based Predictive Control, Simbuild 2012
20. D. Kim, J.E. Braun, 2012, Model-Based Predictive Control for Buildings with Decoupling and Reduced-Order Modeling, 2nd International High Performance Buildings Conference at Purdue
21. D.Kim, J.E. Braun, E. Cliff, J. Borggaard, S. Gugercin, Coupled CFD/Building Envelope Model for the Purdue Living Lab, 2nd International High Performance Buildings Conference at Purdue
22. W.H.A. Schilders, H.A. van der Vorst, and J. Rommes, 2008, Model Order Reduction: Theory, Research Aspects and Applications, Springer (Series Mathematics in Industry, Vol. 13), ISBN 978-3-540-78840-9

2.2.6. Nomenclature

\tilde{A}_{ij} = (i,j) components of a matrix \tilde{A}

\tilde{A}^T = transpose of a matrix \tilde{A}

C_V^I = Ith zone air thermal capacity(constant volume specific heat) [J/kg-K]

$h_{cv,in}$ = convective heat transfer coefficient at an internal wall [W/m²K]

$h_{cv,ex}$ =convective heat transfer coefficient at the outside surface of a wall[W/m²K]

h_o^i = external radiative source term acting on ith surface [W/m²K]

\tilde{I} = identity matrix

$k^L|_j^i$ = thermal conductivity at left surface of the jth node in ith wall

$nnod$ = number of nodes in a wall

Nz = number of zones (or rooms)

Nw = number of walls in a zone (or a room)

q_{LWR} = net long wavelength radiation exchange with environment [W/m²]

q_{SWR} = short wavelength solar irradiation [W/m²]

q_{gen} = energy source term [W/m²]

$(\vec{q})_i$ = ith component of a vector \vec{q}

$q_{net,rad}$ = net radiative heat flux out of an internal surface [W/m²]

\dot{Q} = heat flow rate [W]

\bar{T} = mean temperature [K]

\vec{T}_w = set of all temperatures nodes of walls in multiple zones, $\vec{T}_w = \left[\vec{T}_1^T \ \vec{T}_2^T \ \dots \ \vec{T}_n^T \right]$

\vec{T}_j^I = set of all node temperatures of walls and windows in Ith zone, $\vec{T}_w = \left[\vec{T}_1^T \ \vec{T}_2^T \ \dots \ \vec{T}_n^T \right]$

\vec{T}_j = set of all jth temperature nodes of walls in a single zone, $\vec{T}_j = \left[T_j^1 \ T_j^2 \ \dots \ T_j^{N_w} \right]^T$

T_j^i = temperature at jth node in ith wall

\vec{T}_z = set of all zone air temperatures nodes in multiple zones

T_z^I = Ith zone air temperature [K]

V^I = Ith zone air volume [m³]

w_j^i = width of control volume of jth node in ith wall [m]

w_j^L = distance from the "j-1"th node to the jth node in ith wall [m]

δ_{ij} = Kronecker delta

Σ = Hankel singular value

ρ_j^i = density at jth node in ith wall

ρ^I = Ith zone air density [kg/m³]

Γ = Hankel operator

W_c = Controllability gramian

W_o = Observability gramian

$\|\cdot\|_\infty$ = Hardy infinity norm (or H_∞ norm)

2.3 Coupled Indoor- Air Model

Many advanced HVAC components and systems, such as chilled beams and displacement ventilation, rely on vertical temperature gradients for effective operation. Moreover, accurate assessment of environmental-quality must be based on conditions in appropriate occupied zones and not on large-scale averages. In particular, large comfort variations may exist in spaces that have relatively large aspect ratios in combination with large south facing windows. Accordingly, it is appropriate to consider indoor environment models that accurately predict spatially varying comfort conditions.

In this section we develop a procedure for coupling a building envelope model to a CFD-based model for the indoor air environment. The formulation retains spatially varying features such as water-vapor content and enables calculation of comfort metrics at various occupied locations.

2.3.1 Introduction

Whereas energy-efficiency in buildings is enhanced by improved components such as low-emissivity glass, high-resistance insulation and improved-efficiency compressors, there is evidence that significant energy savings requires a more coordinated control approach. With control-design as an objective, we seek mathematical models of the building system that capture the important physics but that are computationally tractable.

In the present study we examine coupling between the building envelope and the indoor air. To this end it is useful to consider the coupled system as the cascade shown in Figure 2.3.1.

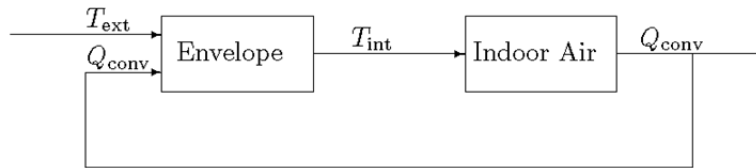


Figure 2.3.1 Cascaded Building-Envelope and Indoor-Air Blocks

In this view the building envelope is driven by external convective and radiative loads, which result in a distribution of interior surface temperatures. These surface temperatures are inputs for the indoor-air model (along with internal and HVAC loads); among the outputs of the indoor-air model are heat loads on the bounding surfaces. In section 2.3.2 we discuss a building envelope model that incorporates conductive and radiative heat transfer among its components. In section 2.3.3 we briefly discuss a standard model for a single, well-mixed zone and then describe our model driven by data from CFD simulations. Our model is based on the Purdue Living Laboratory #3, a facility being designed and constructed at Purdue University. Some details of the facility are provided in section 2.3.4 along with a case study of the closed-loop system response.

2.3.2 Building Envelope Modeling

A reduced-order building envelope model was formulated based on procedures described in section 2.2. A finite-volume formulation is used to describe the heat conduction through walls. On the external walls an energy balance is applied considering convective heat, solar radiation and long wavelength interactions. The radiosity method is utilized to express the net flux under the assumption that the walls are grey, diffuse and opaque. The long-wave interaction terms were linearized and fixed convective heat transfer coefficients were assumed to construct a linear time

invariant model (LTI) for the building thermal network. The final form of the state-space building envelope system is:

$$\begin{aligned}\dot{x}(t) &= Ax(t) + B_u u(t) + B_w w(t) \\ y(t) &= Cx(t)\end{aligned}\tag{2.3.1}$$

where the input (u) represents the convective heat flux between walls and the zone air, and the input (w) represents several exogenous terms, including the heat flow due to solar radiation, long-wave interaction between sky/ground and exterior walls. The output (y) is chosen to be the inside wall temperatures.

The main features of this work are:

- The modeling approach is general for any shaped building (i.e. not restricted to rectangular shaped walls) because it is developed using the radiosity method that incorporates view factors that can be determined for any geometry.
- Individual wall elements can be divided into sub-elements to facilitate coupling to a CFD model for the indoor environment. This is appropriate when surface temperatures along a wall vary significantly due to solar or other non-uniform inputs.
- The system of equations is continuous in time and is not restricted to a fixed time step.

Variable time-step algorithms can be employed, which is helpful in handling different time scale problems that are inherent for building systems.

Based on the compact state-space representation (2.3.1) various model reduction techniques can be readily utilized to construct a reduced-order building model. A balanced truncation method is applied to the representation to generate a reduced-order model. The reduced-order model preserves significant input/output properties of the original system.

2.3.3 Indoor-air Model

The Standard Model

Energy exchange between a bounding surface and the adjacent indoor-air is typically modeled in terms of a convective film coefficient as

$$q(t) = h(T_{wall}(t) - T_{zone}(t))\tag{2.3.2}$$

where $q(t)$ is the instantaneous flux (W/m^2), and h is a film coefficient. The latter may be based on experimental results and depends on surface finish and orientation. Evolution of the zone temperature (T_z) is commonly modeled as

$$C \frac{dT_z(t)}{dt} = \sum_{j=1}^m q_j(t) + S_z(t)\tag{2.3.3}$$

where C is the thermal capacity of the well-mixed air (J/K), there are m wall segments, and $S_z(t)$ represents source terms in the zone.

If we identify system inputs (u) with the segment temperatures (T_i), and the outputs (y) with the segment heat fluxes (q_j), then the standard system (2.3.2, 2.3.3) is an LTI system and in the usual first-order system form (A, B, C, D) we can identify

$$A = \frac{-\sum_{k=1}^m h_k}{C} \text{ (a scalar), } B = \frac{C^T}{C}, C = \begin{bmatrix} h_1 \\ h_2 \\ \vdots \\ h_m \end{bmatrix}, \text{ and } D = \begin{bmatrix} h_1 & 0 & \cdots & \cdots & 0 \\ 0 & h_2 & 0 & \cdots & 0 \\ 0 & 0 & \ddots & \cdots & 0 \\ \vdots & \vdots & \vdots & \ddots & 0 \\ 0 & 0 & 0 & 0 & h_m \end{bmatrix} \quad (2.3.4)$$

Note that (2.3.4) does not account for the $(m+1)^{\text{th}}$ input (S_z).

The Standard Model transfer function from the inputs (segment temperatures (T)) to the outputs (the segment loads (Q)) is given by

$$H^{std}(s) = \frac{-CC^T}{(C_s + \sum h_k)} + D \quad (2.3.5)$$

where the arrays C, D depend on the wall-segment convective parameters h_i as given in display (2.3.4).

Note that the transfer function H^{std} is not strictly proper ($D \neq 0$).

CFD-Based Model

Our indoor-air model is realized as an LTI system that approximates specified input-output behaviors observed in computational fluid dynamics (CFD) simulations. A grid for our CFD (Fluent) simulation is shown in Figure 2.3.2 (left). The yellow zones depict (24) locations for student work areas; their numbering is shown on the right. Volumetric source terms are specified in the odd-labeled zones to emulate generation of water-vapor, carbon-dioxide and energy in these zones. In addition, (volume-averaged) human comfort metrics are read from all zones. The brown/green 'cloud' structures support (8) inlet diffusers, and a single air-return is located on the back (North) wall.

The bounding surfaces for the VAV-room were decomposed into 19 sections as shown in Figure 2.3.3. The building envelope model was coupled to a Standard Model for the indoor-air and subjected to fixed loads. The resulting steady surface temperatures were enforced as Dirichlet boundary conditions and the Fluent simulation was run to a nominal steady-state. Some features of the resulting temperature/velocity fields are shown in Figure 2.3.4. In the right view (a mid-room slice) it can be seen that near the west wall (left) and the east wall (right) the flow is vertically upward. With a steady flow solution in hand we then subjected the CFD model to a step-like change in each of the surface temperature ($+10^\circ\text{C}$). Responses of the west wall fluxes to a change in the temperature on the middle section of the west wall are shown in Figure 2.3.5. Note that the initial response on the middle section (west 2) is a rapid increase; this is due to the direct coupling term $hT_w(t)$ (see equation 2.3.2). As the local air temperature increases, the flux value relaxes somewhat. In contrast, the response of the flux on the upper section (west 3) displays a significant decrease as the heated air rises. The effect on the lower wall flux (not

shown) is much smaller.

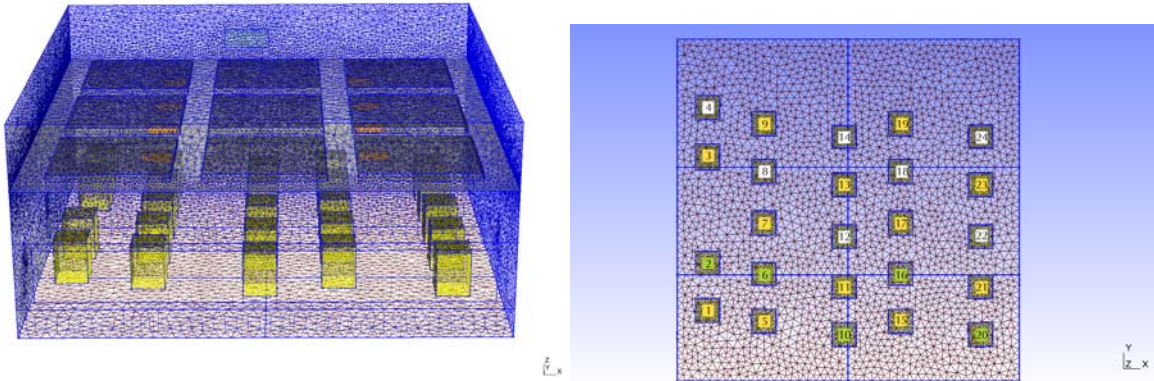


Figure 2.3.2 CFD Grid and Occupied Zones for the Purdue VAV Room

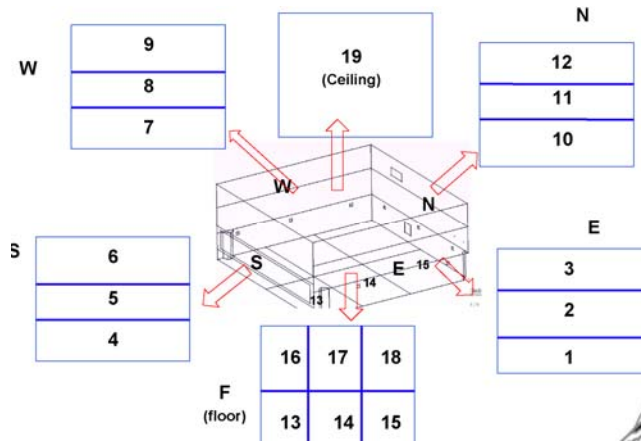


Figure 2.3.3 Interior Surfaces for the Purdue VAV Room

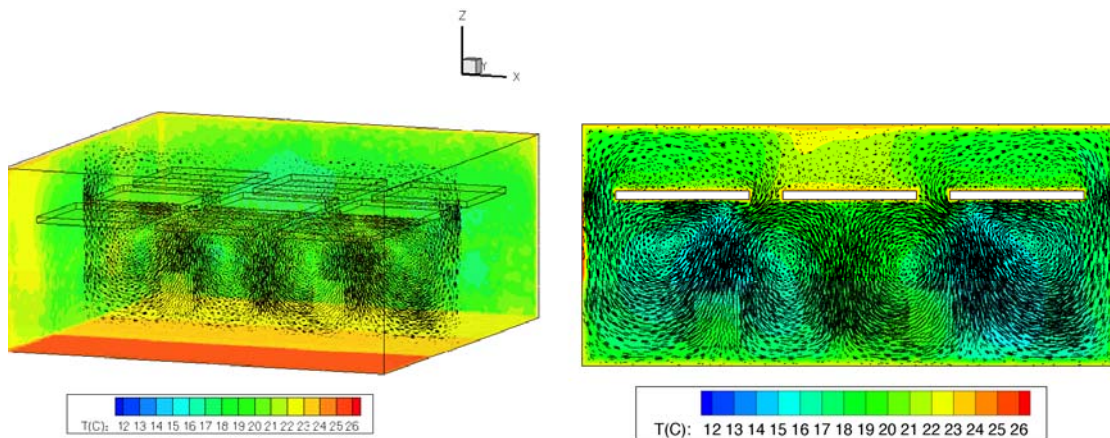


Figure 2.3.4 Volume (left) and Y -plane (right) of Steady CFD Solution

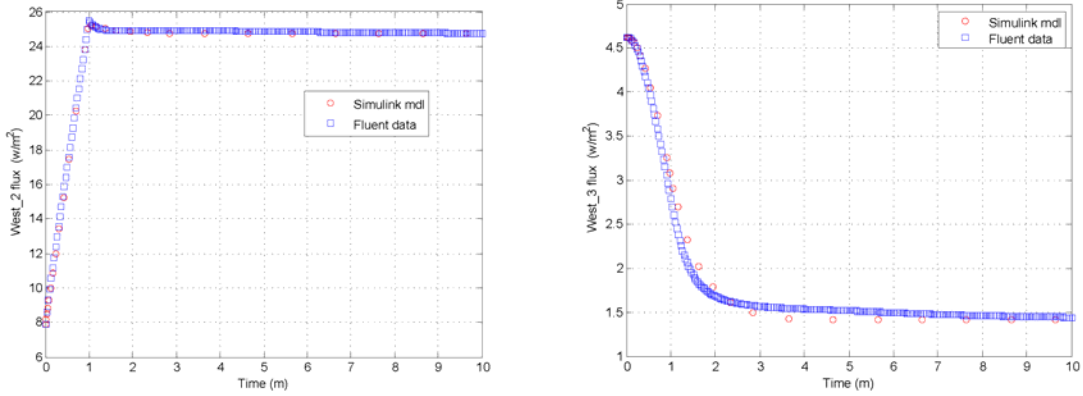


Figure 2.3.5 Flux responses on west wall segments due to ΔT on west 2

In addition to the (19) surface temperatures we subjected the CFD model to perturbations in the supply air mass-rate and temperature, and to a change in occupancy load(s). In addition to the (19) required surface fluxes, we recorded responses in return air temperature, water-vapor and CO₂ levels and to environmental quality metrics in various occupied zones (CO₂, water-vapor, temperature and mean velocity). In all 40 output quantities were recorded.

Fitting the Data

For each input (u_j) we hypothesize an LTI model of the form

$$\dot{x}_j(t) = -\frac{1}{\tau_j} x_j(t) + u_j(t) \quad (2.3.6)$$

$$y^j(t) = C^j x_j(t) + D^j u_j(t) \quad (2.3.7)$$

where x_j is a scalar state, and the column matrices $C^j, D^j \in \mathbb{R}^{40}$. Based on the Standard Model (2.3.2) we have $D^j = h_j$, the film coefficient for j^{th} surface. This value is extracted from the nominal steady CFD solution.

The building envelope model exhibits more than ten eigenvalues (time constants) that are slower than 800 seconds. As seen in Figure 2.3.5 the indoor air time constants are typically much faster. (Indoor air time constants for perturbations in the supply air or the occupant loads are of the order of 800 seconds.) For this reason we insist that the asymptotic response of the model exactly match the data. For a unit-step input this implies that

$$C^j = \frac{y_{ss}^j - D^j}{\tau_j}$$

Thus, under the constraint that the steady-state output of the model exactly match the data, we have a single free parameter (τ_j). This single parameter is found as a solution of a least-squares minimization problem;

$$\min_{\tau} J(\tau) \triangleq \sum_k \|y_{model}(t_k; \tau) - y_{data}(t_k)\|^2$$

This minimization was done using Matlab's `fminsearch` procedure. Some results are shown in Figure 2.3.5, where the red circles represent model responses.

2.3.4 The Coupled Model: A Case Study

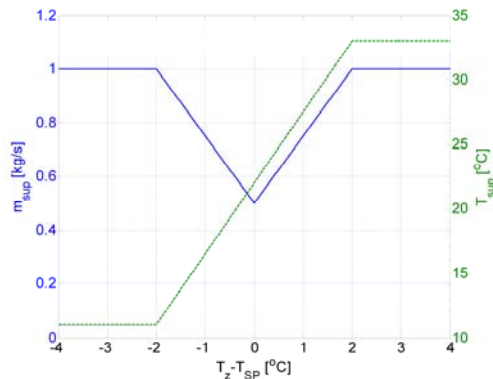
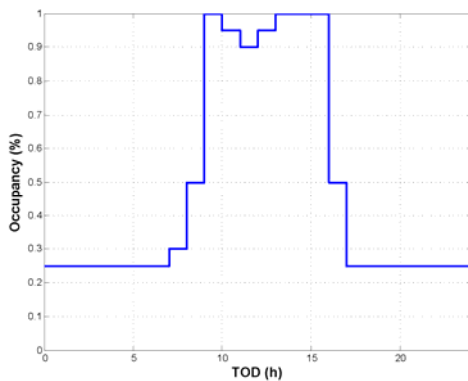
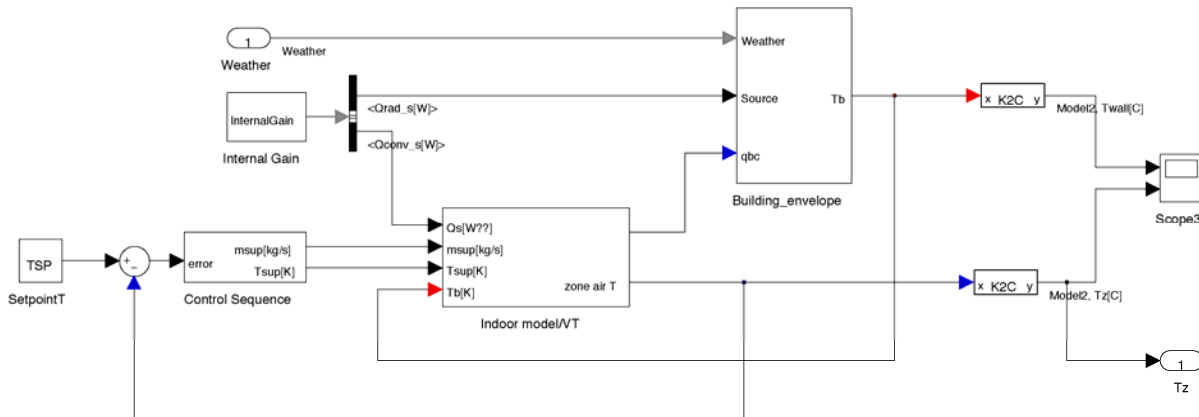


Figure 2.3.6 Simulink diagram, occupancy schedule and feedback control sequence used in the study

We consider a case study based on the Purdue Living Lab 3. A Simulink diagram of the coupled envelope/indoor-air system is shown in the top of Figure 2.3.6. Some parameters employed in the modeling include:

- The size of the building: 32 ft for width and depth and 14.5 ft height
- The materials for wall construction consist of concrete, insulation board, stucco, gypsum board, and double glazed windows.
- The east wall and floor are adjacent to other rooms that are assumed to be at a fixed air temperature of 22°C.
- TMY2 weather data in Indianapolis for the summer season (July) was used.
- A constant value of 17.77 W/m²-K was used for the convective heat transfer coefficient at the outside surface of walls and windows. For the well-mixed case, a coefficient of 3.05 W/m²-K was used for inside surfaces.
- Sensible energy gains for each occupant were: 65 W for activity level (seated/writing), 230 W for office equipment (computer/monitor), and 32 W for lighting. The lighting gains were assumed to be 40% convective and 60% radiative, whereas the other internal gains were assumed to be all convective. In addition, each occupant was assumed to generate 18 mg/s of moisture gain as a latent load and 0.25 L/min of CO₂ production. The

left-hand bottom of Figure 2.3.6 shows the occupancy schedule for simulation case study with full occupancy corresponding to gains associated with 24 people.

- A proportional controller is assumed to manipulate the supply air mass flow rate and its temperature as illustrated in Figure 2.3.6. Both quantities can become saturated due to capacity limitations for the air-handling unit (AHU). The bounds are 1 kg/s for maximum supply air flow rate and 11°C for minimum supply temperature. In the feedback control sequence shown in Figure 2.3.6 the x-axis represents the deviation of zone air temperature from a setpoint (22°C in this case study) and m_{sup} and T_{sup} represent discharge air mass flow rate and temperature, respectively.

The predicted mean vote (PMV) is a comfort level metric that incorporates many different indoor environmental parameters. Fanger (1972) developed a PMV model that uses six input variables: zone air temperature, relative humidity, relative air velocity, mean radiant temperature, activity level, and insulation value of the clothing. PMV values range from -3 (cold), to +3 (hot) with zero as the desirable value. Fanger also related the percent of people dissatisfied (PPD) to PMV.

The PMV-PPD model is widely used and accepted for design and field assessment of comfort conditions. In calculating PMV within this study: 1) a value 0.5 clo was used for clothing/ensemble insulation which is appropriate for summer dress with trousers and a short-sleeved shirt; 2) a metabolic rate of 1 Met (58.2 W/m²) was assumed which corresponds to the energy produced by a seated person at rest; and 3) the mean radiant temperature was calculated as

$$\bar{T}_r^4 = \sum_{i=1}^N T_i^4 F_{p-i}$$

where \bar{T}_r is mean radiant temperature, T_i is the temperature of surface i , and F_{p-i} is the view factor from a person to surface i . The thermodynamic data used in the PMV calculation are averages over some appropriate zone. When using a well-mixed air model, one commonly has a single value - the room/zone average. The CFD-based model provides additional local information: assigned numbers of local zones are indicated in Figure 2.3.2. Initially, the feedback temperature sensor (thermostat) was assumed to measure the room-averaged temperature in order to compare the well-mixed model to the CFD coupled model. Figure 2.3.7 shows time histories of responses to external temperature, solar load and occupancy for one day in July. The room-averaged temperature and heat extraction-rate for the well-mixed model and for the CFD-coupled model are in reasonable agreement. The variation in the average room temperature is due to the use of a proportional controller, such that higher cooling loads lead to higher zone temperatures. The fact that the average temperatures and extraction rates are similar for the well-mixed and CFD-coupled models would seem to imply that a well-mixed model is a reasonable approach for determining the zone loads. However, it is not possible to use the average room temperature for feedback control. Furthermore, the well-mixed model does not provide any information about spatial variations in comfort conditions.

In fact, Figure 2.3.8 shows that there are significant spatial and time variations in environmental conditions within the space on this July day. Figure 2.3.8 displays profiles of local temperature, humidity ratio, velocity magnitude and mean radiant temperature for the well-mixed room model

and three locations in the room for the CFD-coupled model: 1) the average of the five occupied zones nearest the south window (zones 1, 5, 10, 15, and 20 in Figure 2.3.2) labeled as oz 15 in Figure 2.3.8, 2) the local occupied zone 2 which is on the west end of the second row in Figure 2.3.2 and 2.3.3) the local occupied zone 18 which is near the back of the room away from the windows. The zones nearest the window have significantly higher air and mean radiant temperatures due to solar gains. In addition to having lower gains, zone 18 also has higher air velocities because of closer proximity to an air diffuser; both factors leading to significantly lower air temperatures. The well-mixed model results in environmental indices that are within the middle of the values determined for the CFD-coupled model. However, this is because the average room temperature was used for feedback control for the coupled model which would not be implemented in practice.

Figure 2.3.9 shows results for the same day with a thermostat that uses the average of the zones nearest the south windows (zones 1, 5, 10, 15, and 20 in Figure 2.3.2). Note that by sensing this warmer zone temperature, the peak temperatures in all of the other local zones are diminished by 2 to 3 °C compared to control based on room average temperature. Furthermore, since the controller manipulates supply air mass flow rate and its temperatures based on the (warmer) zone conditions, the temperatures of all zones except for the zones near the window are much lower than that for well-mixed model. This leads to an increased heat extraction rate for the CFD-coupled model compared to the well-mixed model as shown in Figure 2.3.10. Figure 2.3.11 demonstrates the importance of thermostat location on the overall comfort as represented using PMV. The right plot shows PMV for the sensor located near the south window that was used for the results presented in Figure 2.3.9 and Figure 2.3.10. In this case, the conditions are slightly warm near the window during the middle of the day but cold in other locations. Moving the thermostat away from the windows to zone 2 (see Figure 2.3.2) improves comfort in most of the space except near the windows where the conditions become quite warm.

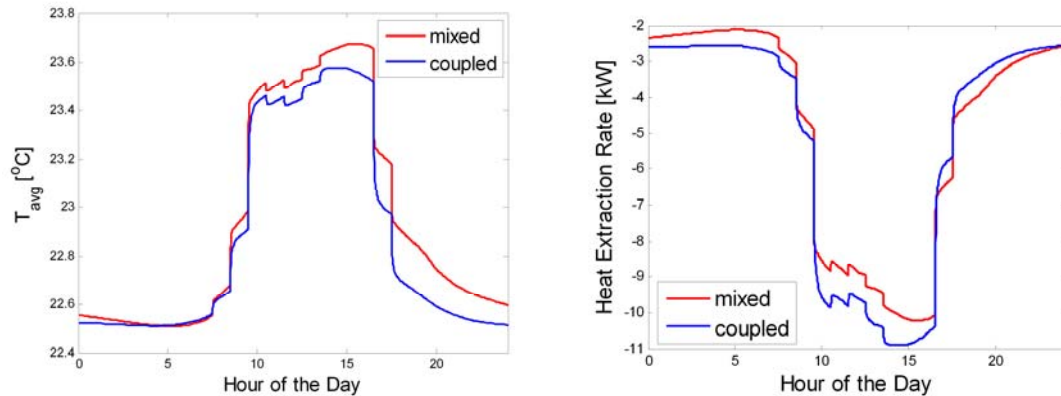


Figure 2.3.7 Profiles of average room air temperature and heat extraction rate for well-mixed and CFD-coupled zone air model using room-averaged air temperature for feedback control.

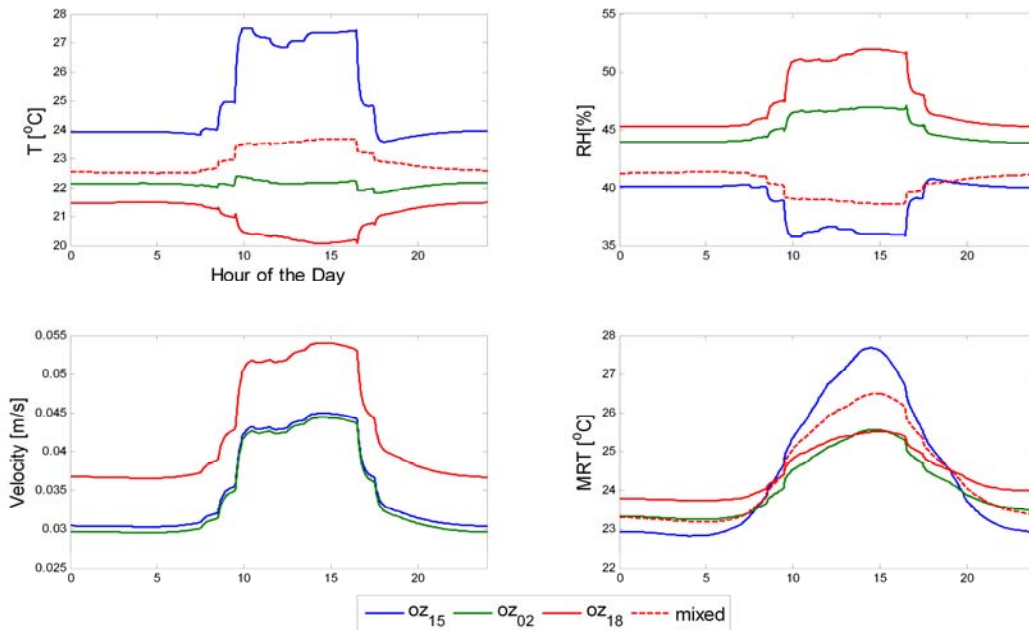


Figure 2.3.8 Indoor environmental metrics based on feedback control using average room temperature

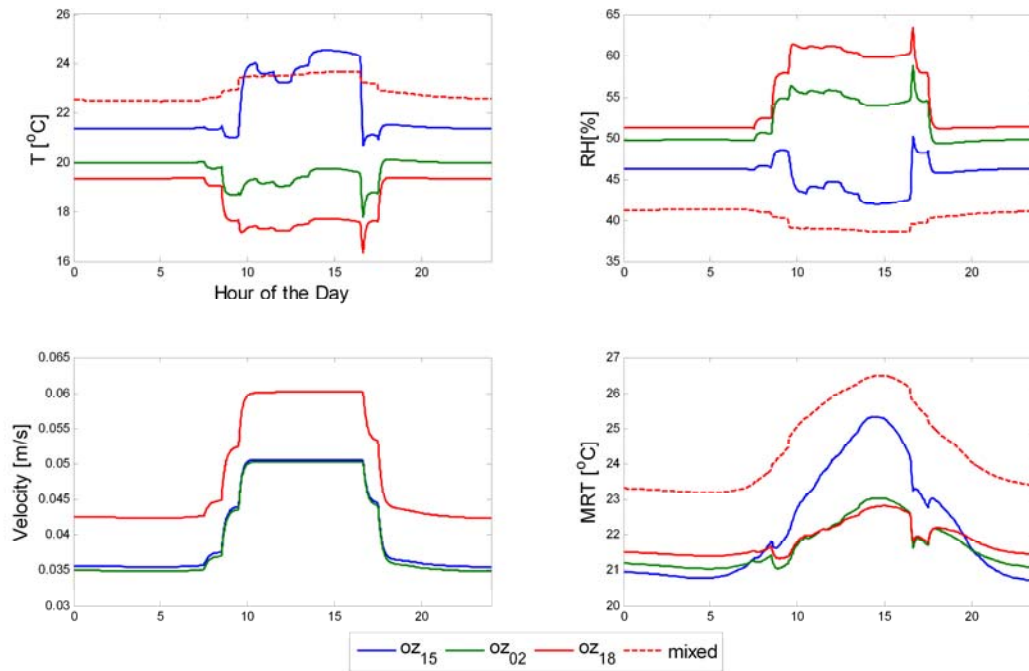


Figure 2.3.9 Indoor environmental metrics based on feedback control using the average of zones 1, 5, 10, 15, and 20 (oz 15, CFD-coupled model) as compared with well-mixed model

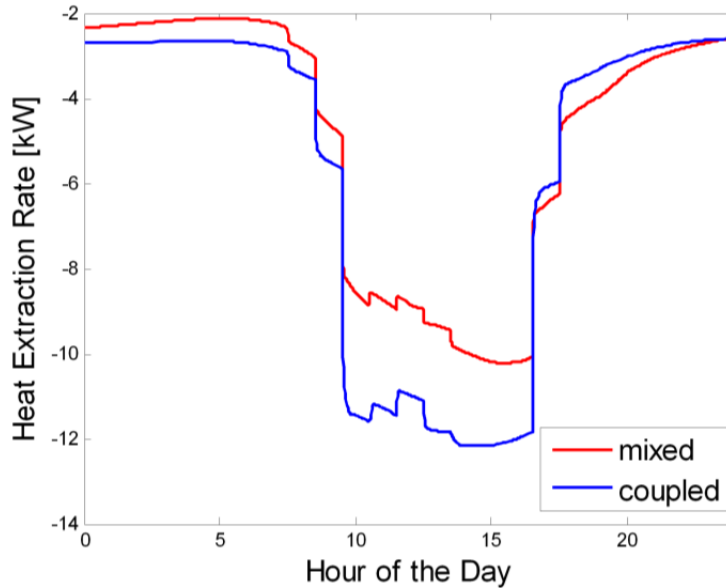


Figure 2.3.10 Heat extraction rate based on feedback control using the average of zones 1, 5, 10, 15, and 20 (oz 15, CFD-coupled model) as compared with well-mixed mode

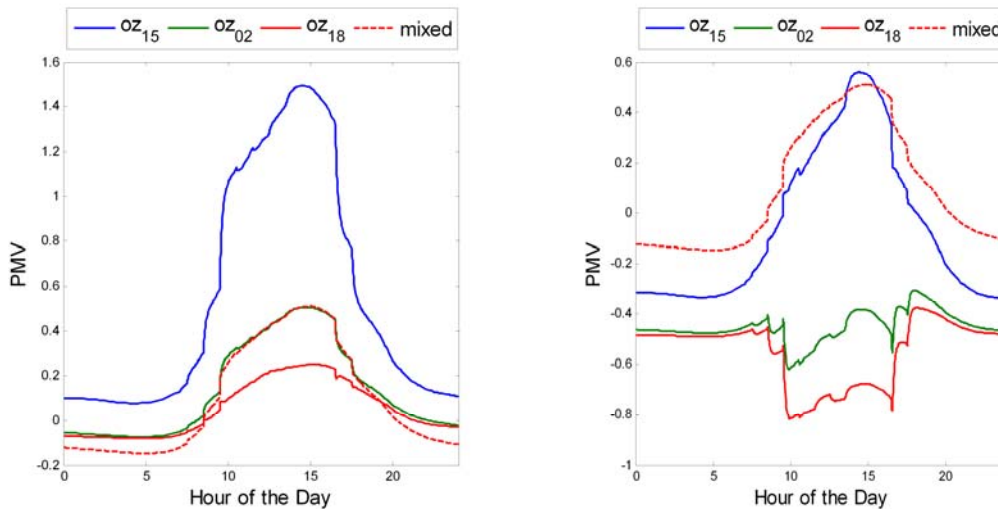


Figure 2.3.11 Comparison of PMV variations for well-mixed model with CFD-coupled model assuming feedback based on zone 2 (left plot) and the average of zones 1, 5, 10, 15, and 20 (right plot)

2.3.5 Conclusions

This section presented a unique approach for coupling a detailed energy load model with an indoor air model that provides spatial comfort information for a zone. The coupled model includes a reduced-order building envelope model that is generated from a detailed representation that considers all of the important energy flows. The indoor-air model is based on CFD data. The model captures some dynamic behavior of the Dirichlet-to-Neumann map and describes the response of surface heat fluxes to surface temperatures. This feature enables coupling of the indoor-air model to the building envelope dynamics. Additionally, the indoor-air model encodes the dynamic behavior of environmental quality metrics at specified locations of

interest. With this enhanced modeling capability we are interested in studying control schemes that are energy efficient and maintain human comfort. An initial case study was performed for a zone that has significant solar gains and where significant spatial variations in comfort conditions were observed. This study illustrated the importance of thermostat location and the need for detailed indoor air modeling when considering this type of building zone.

2.4 Inverse Model for Building Envelope and Equipment

This section focuses on inverse modeling techniques for both envelope and equipment as well as the application to an existing building—Building 101 of the Navy Shipyard at Philadelphia, PA.

2.4.1 Envelope inverse model

2.4.1.1 Inverse model structure

A simplified whole building model that was developed by Chaturvedi and Braun (2002) is shown in the figure below. In this representation, all of exterior walls are combined into a single exterior wall with an external boundary condition that includes the total incident radiation on all wall surfaces. Solar radiation that is transmitted through windows is assumed to be absorbed equally on two sides of an interior wall presentation. The interior wall also captures the effects of floors between stories of a multi-story building. An additional ground element is included to capture ground coupling dynamics. Internal radiative gains are assumed to be distributed with an even flux to walls and ceiling, whereas convective internal gains go directly to the zone air. A pure resistance is included to capture the effects of heat transfer across low-mass elements, such as windows or due to infiltration.

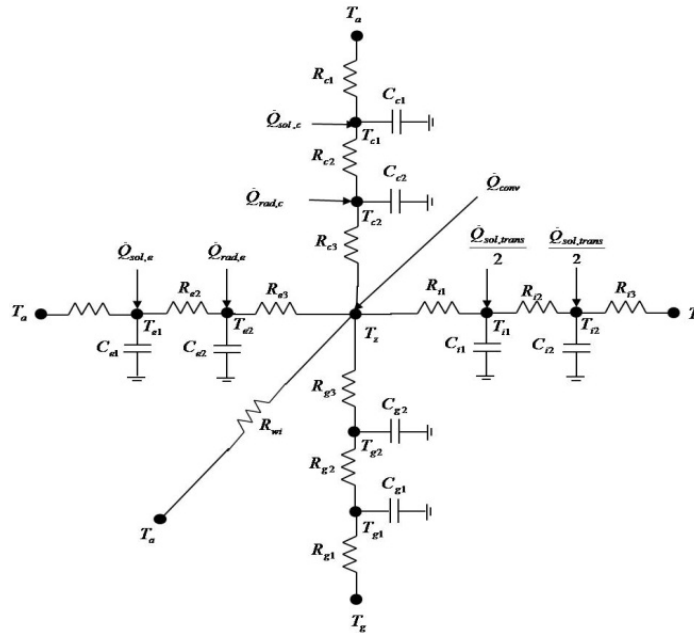


Figure 2.4.1 Thermal network for a single zone building model.

Applying an energy balance to each node in the network, a state-space representation can be established for this simplified model structure:

$$\frac{d\mathbf{x}_b}{dt} = \mathbf{A}_b \mathbf{x}_b + \mathbf{B}_b \mathbf{u}_b$$

$$\mathbf{Y}_b = \mathbf{C}_b \mathbf{x}_b + \mathbf{D}_b \mathbf{u}_b$$

where \mathbf{Y}_b is the output, which can be either cooling load (zone air temperature is input) or zone air temperature (cooling load is input). The state vector \mathbf{x}_b contains all the temperature nodes in the network and input vector \mathbf{u}_b includes boundary temperatures, solar radiation and internal heat gains.

For a fixed set of parameter values, the methodology of Seem et al. (1989) can be used to solve the state-space representation, and to predict cooling load or zone air temperature of the building as a transfer function of the input and state variables. The performance of the model can be evaluated in terms of how well the output (or prediction) matches the actual data (baseline). A commonly used criterion for the deviation of prediction from baseline is least-square error:

$$J_{b,\theta} = \sqrt{\frac{\sum_{k=1}^{N_{train}} (y_{b,k} - y_{actual,k})^2}{N_{train} - 1}}$$

where

$y_{b,k}$ = output (either $\dot{Q}_{b,k}$ or $T_{b,k}$) at time k ;

$y_{actual,k}$ = baseline output at time step k ;

So the formulation of our parameter estimation problem can be written as:

$$\theta^* = \arg \min_{\theta \in \Omega} (J_{b,\theta})$$

where Ω is the search region for the parameter values in the estimation process. This search region is determined according to the information available about the zone. This information can be obtained via several means, such as by requesting a survey from the building administrator or by looking at the blueprint of the building. Generally speaking, the less information we have about the building, the bigger the search region is for the optimization. When the search region is big, the estimation process could more easily converge to a local optimum. So some preprocessing is necessary in obtaining a good initial guess to improve the chances of obtaining a global optimal point. A robust and efficient training methodology is described in Cai and Braun (2012).

2.4.1.2 Multi-zone building inverse model

This section focuses on the application of this inverse modeling approach to a multi-zone case study that is based on the Navy Shipyard Building 101 located in Philadelphia, PA. Building 101 is a three-floor building divided into three main sections: north wing, south wing and middle section. There are ten zones in the north wing that are served by one air-handling unit (AHU). Our case study for this section is focused on three zones that are on the second floor in the north wing, which are labeled as Z8, Z2 and Z3 in the floor layout in Figure 2.4.2.

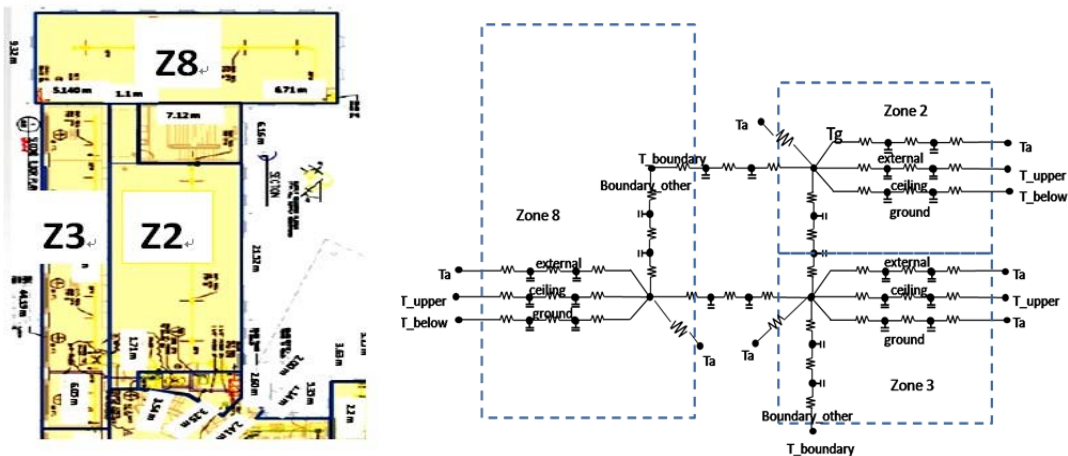


Figure 2.4.2 Floor layout and thermal network for three zones in Building 101.

Figure 2.4.2 also shows the thermal network of the three zones that are to be studied. This thermal network is built up based on the single-zone thermal network shown in Figure 2.4.1. But there are several modifications that are made to each of the zones. For all zones in this specific case study, there are no internal walls so the internal wall branches are taken out. But each zone has additional coupling wall(s) and boundary walls so related branches are inserted. The transmitted solar radiation is applied to the floor instead of the internal wall. In the single-zone thermal network, internal radiative gains are applied to the ceiling and external wall in an area-weighted manner while in the three-zone network, these gains are assumed to go to ceiling and floor equally just for simplicity. In this initial study, all zones that are coupled to these three zones are assumed to have a fixed temperature of 22°C, which include all coupled zones in the 1st and 3rd floors as well as the stair space and lobby for the 2nd floor. As a result of this assumption, all adjacent walls (excluding adjacent floors and ceilings) that are exposed to the same air temperature can be lumped into one boundary wall for a specific zone. For example, zone 2 is adjacent to stair space and lobby through west and east walls respectively and these two adjacent walls are lumped as one wall subject to the same boundary condition. This lumping approach would reduce the size of the estimation problem significantly.

TRNSYS Simulation Results:

Figures 2.4.3 and 2.4.4 show TRNSYS simulation results for a three-day period (650th to 722nd hours of the year) for this building located at Philadelphia, PA. This period is used to present all testing results for the rest of this section. Figure 2.4.3 shows zone-wise temperatures and ambient temperature and Figure 2.4.4 shows all energy inputs to the three zones. Cooling setpoints are 29°C during unoccupied periods and 26°C in the occupied period. Heating setpoints are 15°C in the unoccupied period and 20°C for occupancy. These simulation results are during the winter time so there is heating for all three zones. Zone 2 has a window facing east while zone 3 has a larger window facing west, so peaks of solar radiation are occurring during morning time for zone 2 and in the afternoon for zone 3. Zone 8 has windows and walls with all of the four orientations so the solar radiation has longer effects for zone 8 compared to the other two zones. But due to the larger external wall area, zone 8 has more coupling to ambient temperature so it needs more heating during occupied periods. Zone 3 has only heating for the presented interval, but it actually has cooling for some days even in the winter time because of solar radiation transmitted through the large window on the west wall. Zone 2 and zone 3 have only heating for the whole simulation period (first 1000 hours of the year).

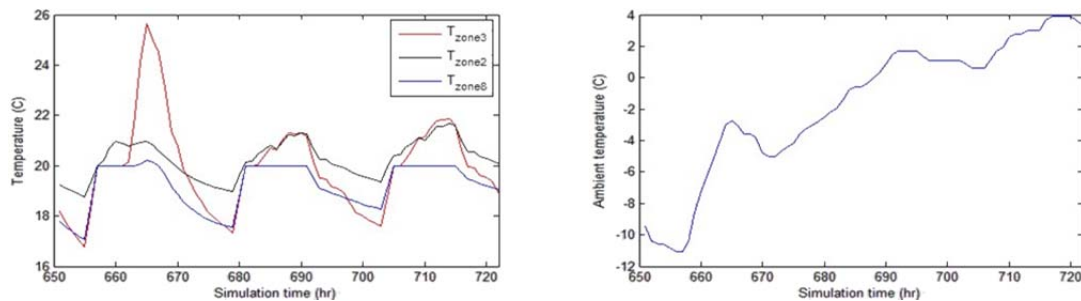


Figure 2.4.3 Air temperatures for three zones and ambient.

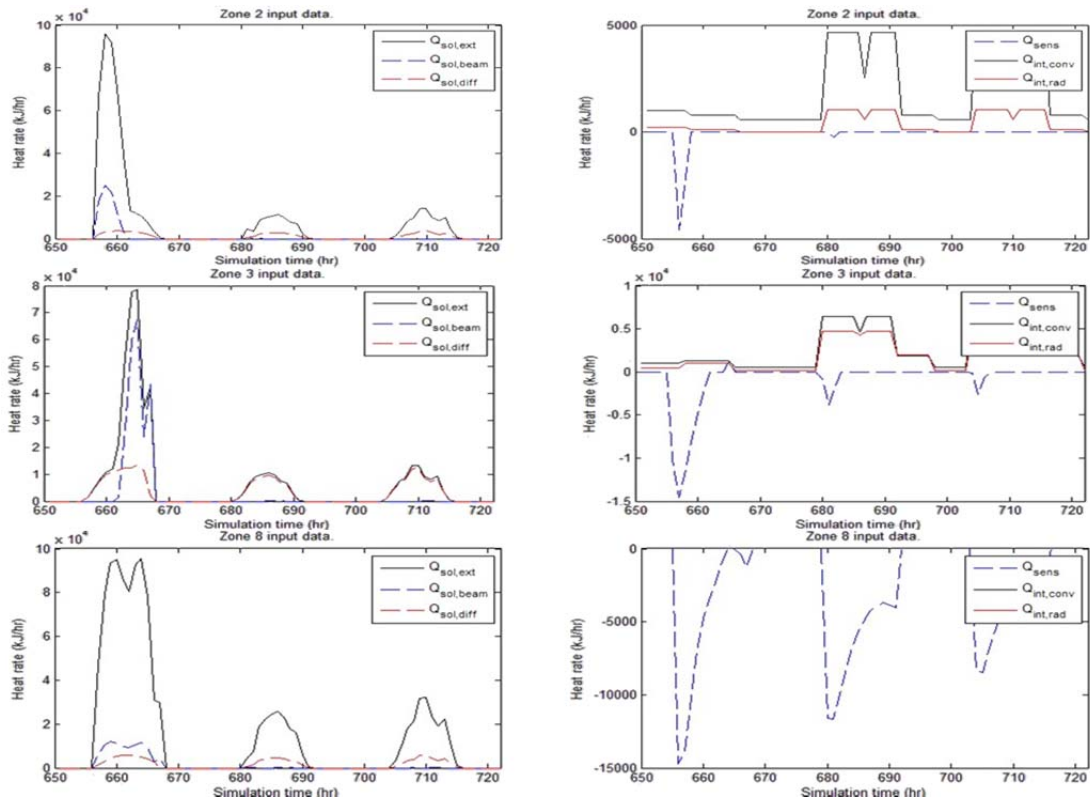
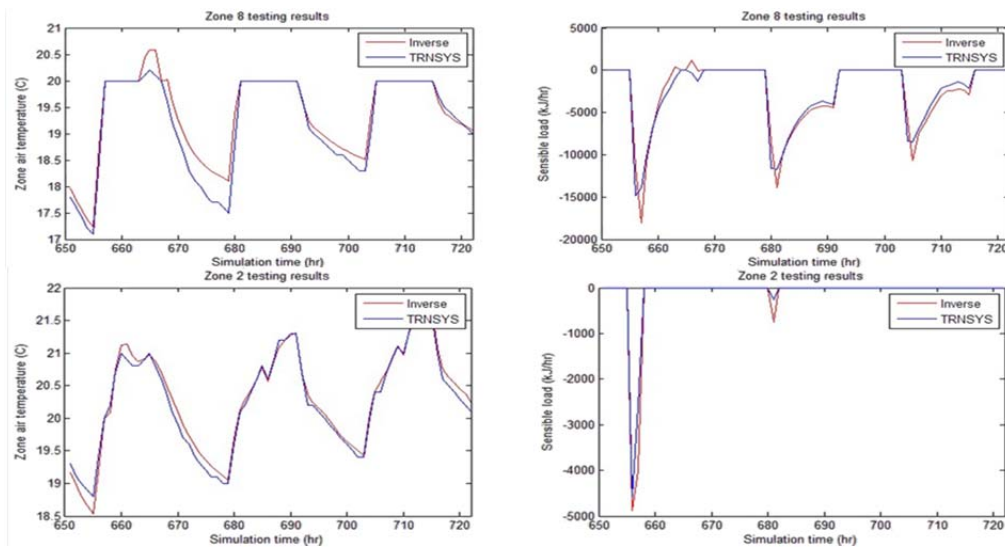


Figure 2.4.4 Solar radiation, internal heat gains and sensible heating or cooling of zones.

Zone-Wise Training:

Applying the inverse modeling techniques described above, each zone model can be trained independently with the other two zone temperatures being boundary conditions. Results during the testing period are shown in Figure 2.4.5 for the three zones. The predictions are reasonable but this training approach results in different zone-to-zone coupling parameters for each of the individual zone models which leads to an overall energy imbalance for the three zones considered together.



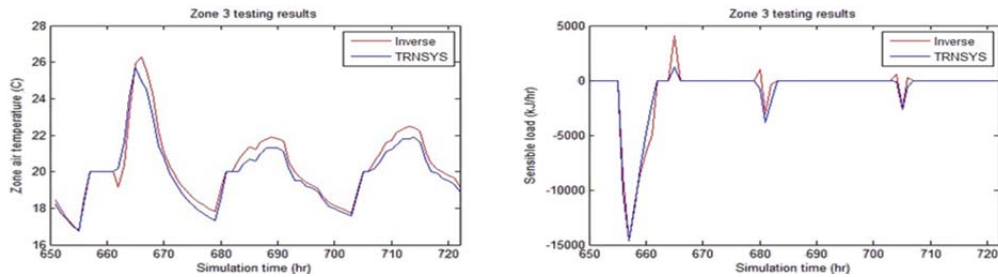


Figure 2.4.5 Zone air temperature predictions from zone-wise trained model and TRNSYS model.

Multi-Zone Coupled Training:

In order to capture unique zone-to-zone coupling factors, a coupled multi-zone structure should be used and estimation should be performed for this coupled problem. Figure 2.4.2 shows a coupled thermal network for the three zones. In the coupled training process, all wall temperature nodes along with zone air nodes are combined into a single state vector. Each iteration of the training process requires the solution of a relatively large state-space model as compared with three separate solutions for three smaller problems with zone-wise training. This increases the computational requirement for each iteration. Also, the algorithm for parameter estimation is applied to a much larger dimensional search space (approximately three times larger for this case study) as compared with three separate smaller parameter estimation problems. The resultant estimation problem becomes very difficult to solve using the previously described solver. Even using 100 multi-start points, the errors of the estimated model are significantly larger than those for zone-wise training. This is undoubtedly because the parameter estimation procedure is determining a local minimum.

Multi-Zone Heuristic Training

The zone-wise training approach is not able to provide a single set of zone-to-zone coupling parameters but provides reasonable predictions and is computationally tractable. The multi-zone coupled training method determines unique coupling factors, but it leads to a large model structure and high-dimensional estimation problem, which is not easy to solve using the proposed training techniques. Therefore, a heuristic training scheme was investigated that combines elements of both training approaches.

If the inter-zonal heat transfer is relatively small compared to other heat transfer paths, then zone-wise training can lead to zone models that are close to the optimum except for the coupling parameters. This is the basis for the heuristic strategy depicted in Figure 2.4.6 for a two-zone case. First, the individual zone models are trained assuming fixed coupling factors based on initial guesses. The zone model parameters are then used as fixed values for training the coupling parameters. These estimated coupling parameter values are then plugged back into the lower level zone-wise training process to tune the non-coupling parameters. The iterative process continues until satisfactory results are reached. This approach reduces the computation requirements and improves final model results.

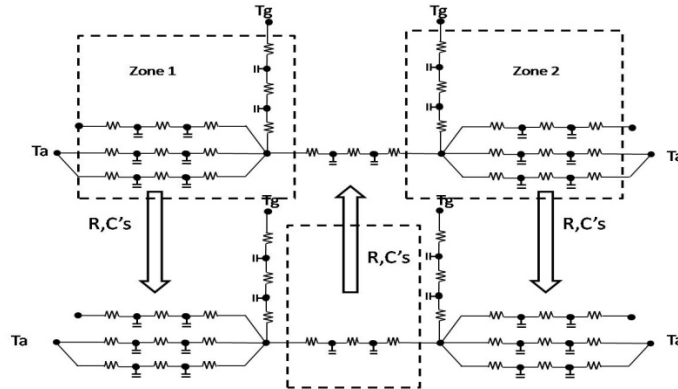


Figure 2.4.6: A two-zone heuristic training scheme illustration.

Table 2.4.1 shows comparisons of RMS errors associated with the training period for the three methods. The heuristic approach provides a single set of coupling factors. The overall accuracy is better than the coupled training approach and similar to the zone-wise training that utilizes separate coupling factors for each zone.

Table 2.4.1: Model performance (temperature prediction RMS error in °C and load prediction relative RMS error in %) comparison for different training processes.

		Zone 8	Zone 2	Zone 3
Zone-wise training	Temperature	0.23	0.174	0.51
	Load	4.42	2.03	4.28
Coupled training	Temperature	0.477	0.456	0.794
	Load	4.15	4.3	7.6
Heuristic training	Temperature	0.27	0.36	0.57
	Load	4.10	2.20	5.6

2.4.1.3 Inverse model from measured data

Fairly detailed measurements were available for the three zones on the 2nd floor, north wing of Building 101. Figure 2.4.7 shows the three zones with pink background color. This is slightly different from Figure 2.4.2 because zone 8 is now a physically separate zone (icon lab) and not coupled with zone 3. Also there is a conference room on the west of this zone.

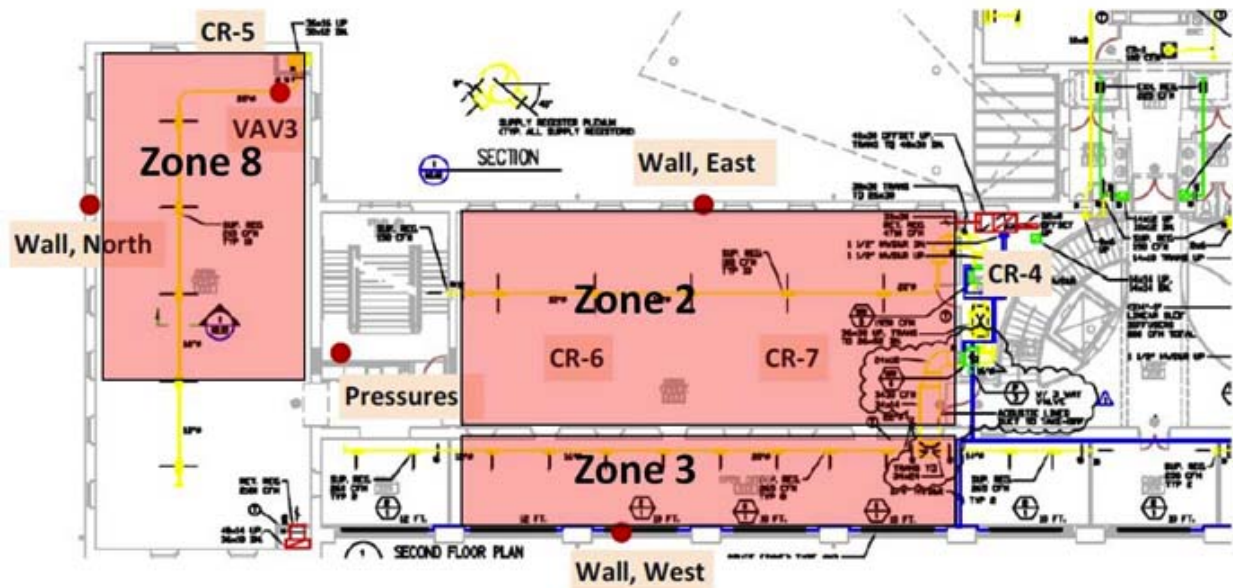


Figure 2.4.7 Zoning of the three zones on 2nd floor, north wing.

The training data set was collected in the following way:

Zone air temperature—for each zone, there were several temperature sensors and the averaged value was taken for each zone.

Sensible cooling—this was calculated using VAV box flow and temperature measurements along with return air temperature measurements. However, VAV3 provides supply air to both the icon lab and a small conference room and relative cooling loads were estimated based on floor area ratios.

Solar flux—solar flux measurements were available for the north, east and west walls.

Internal gains from occupants—there was an occupancy counter for the 2nd floor of the north wing. The spatial occupancy distribution was determined using zone area weighting. Each person was assumed to contribute 100 W internal sensible heat gain with 70% convective and 30% radiative.

Internal gains from lights and other appliances—there were power measurements for lights and other appliances for the whole 2nd floor. The zone internal gains were estimated based on area weighting. Lighting heat gains were assumed to be 70% radiative and 30% convective. For other appliances, heat gains were assumed to be 50% radiative and 50% convective.

Using these measured data, inverse models were established for these three zones. Zone 8 was trained as a separate zone. Zones 2 and 3 were trained simultaneously in a coupled manner. The testing RMSE's of zone 8, zone 3 and zone 2 were 0.56, 0.96 and 0.98 (C) respectively. It is believed that the model for Zone 8 was more accurate because information for initial parameter estimates were obtained from an on-site inspection, whereas the parameters for the other two zones were taken from the inputs to a TRNSYS model developed by UTRC. A lot of actual features were not reflected in the TRNSYS model, e.g., in TRNSYS model of zone 8 there are 9 windows but actually 5 of them are shades that are normally closed at the site.

There were some other uncertainties that could cause inaccurate model estimates. For example,

there was only one temperature sensor on first and third floor so temperatures on these floors were assumed to be identical for use as boundary conditions in the modeling. Also, zonal internal heat gains were estimate using area ratios and total heat gains.

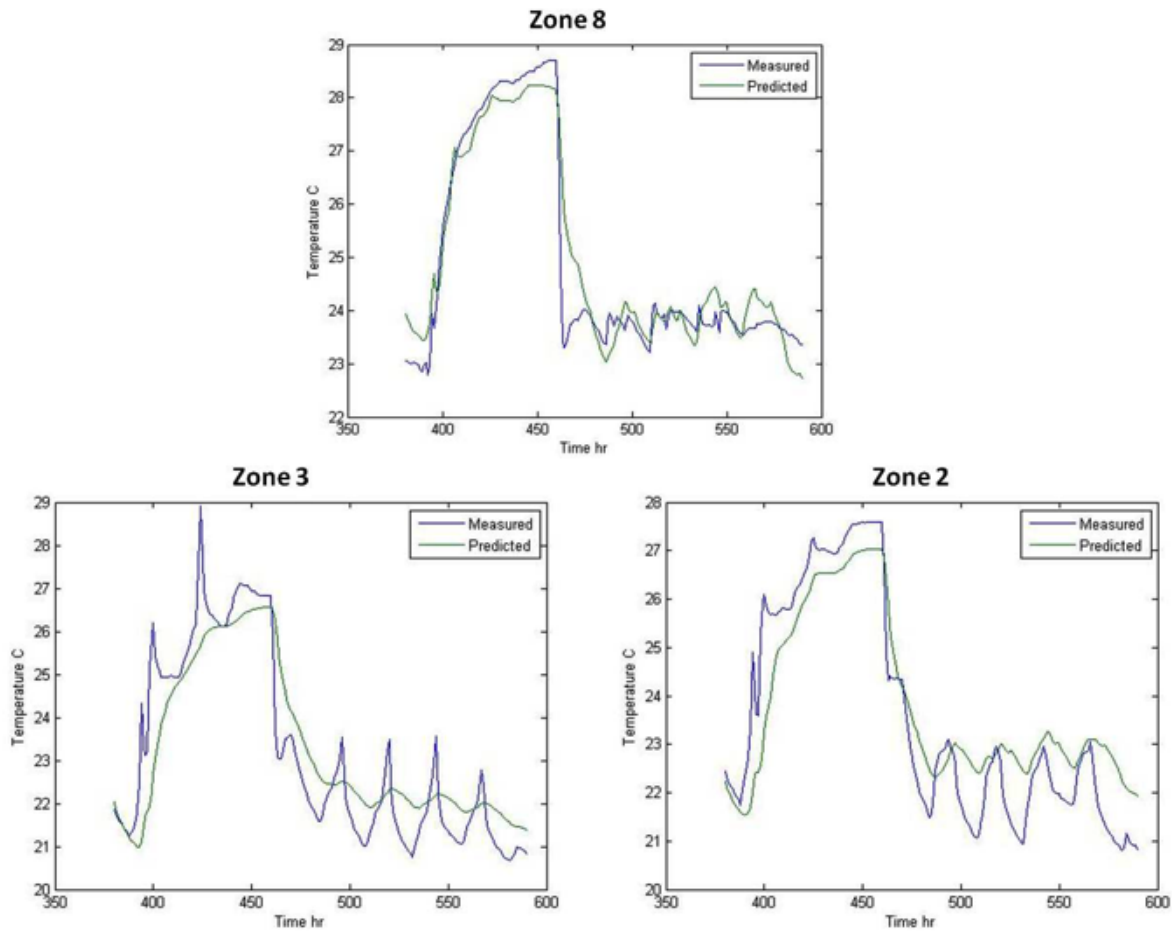


Figure 2.4.8 Performance of estimated model from measured data.

2.4.1.4 Decoupled training approach

Building 101 has a total of 59 zones. Application of the coupled method to obtain an inverse model for this case would be computationally prohibitive because of the high dimensionality of the estimation problem. Therefore, a scalable training method is needed that takes into account weak or non-existent couplings. Based on the initial information that is available about the building to be modeled, a sensitivity analysis can be performed to the large coupled model. From this analysis, a schematic algorithm was developed to identify the weak couplings between all the zones and by eliminating these weak couplings, a large coupled building model can be decoupled into several subgroups.

Our estimator is a least square estimator with an approximate distribution of

$$\hat{\theta} \sim N_p(\theta_0, \Sigma_0)$$

where

$$\Sigma_o = \sigma_o^2 [n\Omega_o]^{-1} \in \mathfrak{R}^{p \times p}$$

$$\Omega_o = \lim_{n \rightarrow \infty} \frac{1}{n} \chi(\theta_o)^T \chi(\theta_o)$$

$$\chi(\theta_o) = \frac{dy}{d\theta_o}$$

and where $\chi(\theta_o)$ is the sensitivity matrix and Ω_o is the Fischer information matrix (FIM). The variance of each parameter is inversely proportional to the diagonal element of this FIM. So the smaller the diagonal element is in FIM, the more confidence there is for the parameter estimate and model output is less sensitive to this parameter. With this in mind, zone coupling strengths are evaluated using

$$\mathbf{IM} = [\Omega_o(i, i): i = 1, \dots, num_para] = [\chi(\theta_o)^T \chi(\theta_o)(i, i): i = 1, \dots, num_para]$$

$$\mathbf{IM_mat} = \begin{bmatrix} \mathbf{IM}_1 \\ \vdots \\ \mathbf{IM}_{10} \end{bmatrix}$$

$$\mathbf{PA_mat} = \begin{bmatrix} \mathbf{PA}_1 \\ \vdots \\ \mathbf{PA}_{10} \end{bmatrix}$$

$$\mathbf{Coup_mat}(i, j) = \mathbf{IM_mat}(i, :) \cdot \mathbf{PA_mat}(j, :).$$

$$\text{where } \mathbf{PA}_i(j) = \begin{cases} 1, & \text{if } j\text{-th parameter belongs to zone } i. \\ 0, & \text{if not.} \end{cases}$$

where $\mathbf{Coup_mat}(i, j)$ is an index of coupling strength between zones i and j . Doing this calculation for the ten zones in the north zone of Building 101 shown in Figure 2.4.9, it was found that the strongest couplings are the pairs of [1,6] [3,5] [2,4] [1,7] [7,9] [2,8] [8,10] [2,10]. These ten zones could then be decoupled into three subgroups as shown in Figure 2.4.10. Previously developed training approaches can be applied to estimate each of the subgroups separately. As a byproduct of this decoupling approach, the non-sensitive parameters can be identified and fixed as the initial guesses, so that dimension of the estimation problem is reduced further and efficiency would be improved. The errors of the estimated model are listed in Table 2.4.2 and reasonably accurate model was obtained.

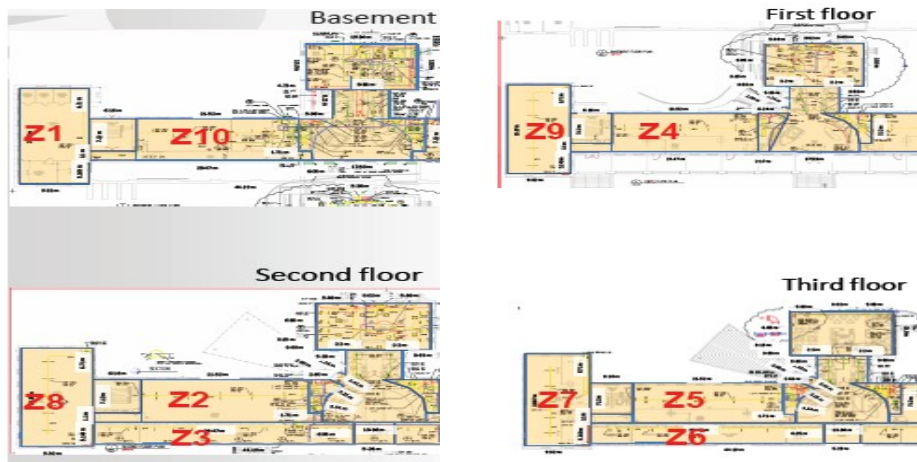


Figure 2.4.9 Floor layout for the ten zones.

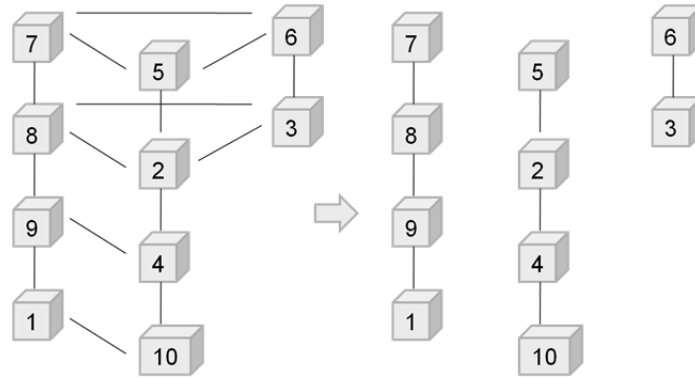


Figure 2.4.10 Decouple the ten zones of Building 101 into three groups.

Table 2.4.2 Testing errors for all the ten zones.

	3	6	2	4	5	7	8	9	10	1
RMSE (C)	0.55	0.53	0.21	0.23	0.26	0.24	0.18	0.42	0.48	0.5

2.4.2 Equipment inverse model

The HVAC system serving the north wing of Building 101 has a multi-stage direct expansion (DX) unit, one heating coil, one variable speed air supply fan and eight VAV boxes. In each VAV box there is a reheat coil to bring the supply temperature up to meet moderate cooling demands. The DX unit has the most significant energy consumption so most of our efforts have focused on developing an appropriate modeling approach for this equipment. Based on these models, optimization was performed to find an optimal control sequence (map). This optimal map could be used for model predictive control studies or implementation.

2.4.2.1 DX unit overview

Figure 2.4.10 is a sketch of the different components in the DX unit. It has two circuits and they were originally designed to be identical. Each circuit has a three-cylinder compressor and two unloaders so there are three stages excluding the off stage for each circuit and the total number of stages is six for the whole unit. There are two evaporators placed in parallel and the air flow across these two evaporators is driven by one supply fan. Each condenser has two fans so there are four stages for the condensers in total. The outlets of the condensers are connected to thermal expansion valves (TEV) to control superheat. Also there is a hot gas bypass from the compressor discharge to the evaporator inlet.

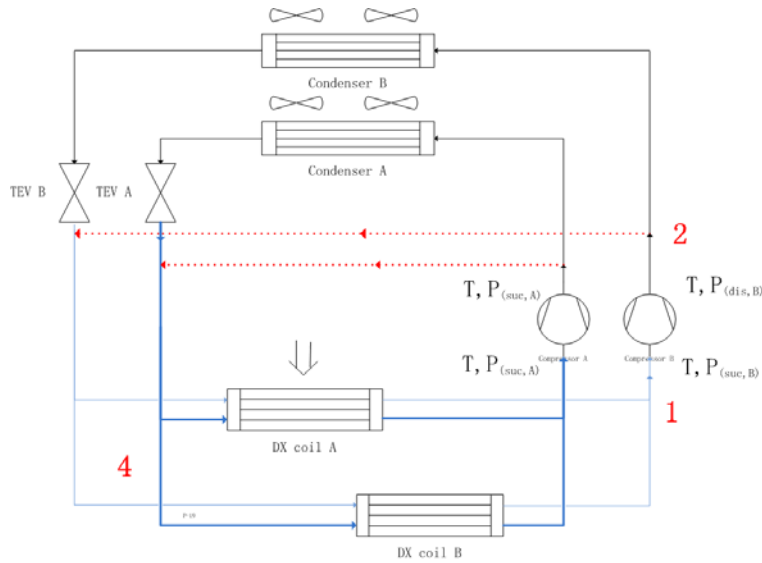


Figure 2.4.10 Sketch of DX unit.

2.4.2.2 Supply fan model

To calculate the AHU supply fan power, we can use a cubic correlation of the flow fraction, which is defined as the actual air flow rate to the nominal value. The nominal air flow rate (V_{rated}) is 20,500 cfm and the allowed minimum air flow fraction (γ) is 50%. To estimate the coefficients, all measured quantities were averaged over a 30-minute period and performance of the resulting model is illustrated in Figure 2.4.11.

$$\gamma = \frac{\dot{V}}{\dot{V}_{rated}}$$

$$P_{fan} = a_0 + a_1\gamma + a_2\gamma^2 + a_3\gamma^3$$

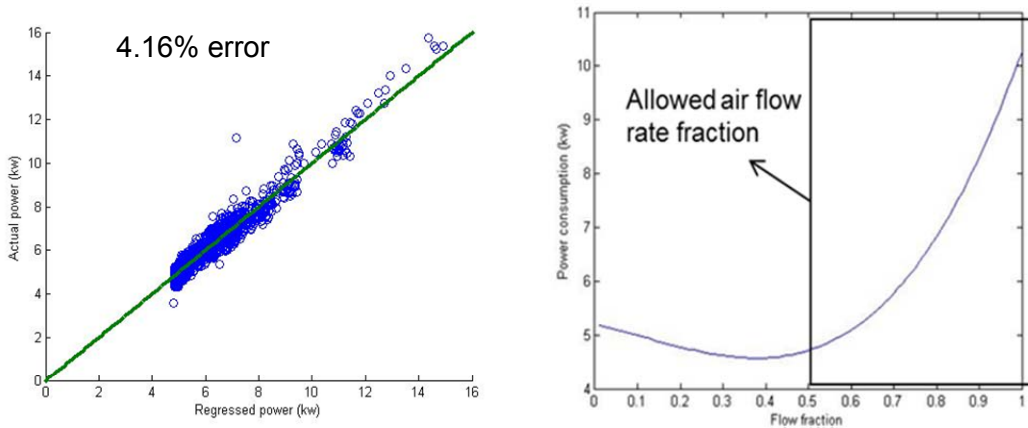


Figure 2.4.11 Supply fan model performance.

2.4.2.3 ASHRAE Toolkit model

The ASHRAE Toolkit model (Brandemuehl, 1993) was implemented in this study as an initial approach for modeling the DX unit. However, some modification was made to capture some of the specific features of this system. In the calculation of total capacity and energy input ratio (EIR, reciprocal of COP), correction factors are used to capture the effects of inlet air wet bulb

temperature for the evaporator ($T_{wb,evap}$), inlet air dry bulb temperature for the condenser (T_{cond}) and air flow rate in the original Toolkit model. In our application, an additional correction factor is considered for representing the staging effect, which appears as the last term correction factor in the following two equations.

$$\begin{aligned}
 q_{tot,evap} &= q_{tot,evap,rated} \cdot f_{cap,T} \cdot f_{cap,Q} \cdot f_{stage} \\
 &= q_{tot,evap,rated} \cdot \left(a_0 + a_1 T_{wb,evap} + a_2 T_{wb,evap}^2 + a_3 T_{cond} + a_4 T_{cond}^2 + a_5 T_{wb,evap} T_{cond} \right) \\
 &\quad \cdot \left(b_0 + b_1 \frac{V}{V_{rated}} \right) \cdot (c_0 + c_1 \cdot Stage) \\
 EIR &= EIR_{rated} \cdot f_{EIR,T} \cdot f_{EIR,Q} \cdot f_{EIR,stage} \\
 &= EIR_{rated} \cdot \left(e_0 + e_1 T_{wb,evap} + e_2 T_{wb,evap}^2 + e_3 T_{cond} + e_4 T_{cond}^2 + e_5 T_{wb,evap} T_{cond} \right) \\
 &\quad \cdot \left(f_0 + f_1 \frac{V}{V_{rated}} + f_1 \left(\frac{V}{V_{rated}} \right)^2 \right) \cdot (g_0 + g_1 \cdot Stage)
 \end{aligned}$$

To calculate the sensible heat ratio (SHR) for a DX coil, a bypass factor method is used in the Toolkit model, but it only considers a constant air flow rate. To consider varying air flow rate, the effect of air flow on the bypass factor (BF) is considered in the following manner:

$$\frac{UA}{c_p} = h_0 \cdot (\dot{m})^{h_1} \Rightarrow BF = e^{-NTU} = e^{-\frac{UA}{\dot{m}c_p}} = \exp\left(-\frac{h_0 \cdot (\dot{m})^{h_1}}{\dot{m}}\right) = \exp\left(-h_0 \cdot (\dot{m})^{h_1-1}\right)$$

The empirical coefficients (h_0 and h_1) were estimated for the DX coil serving the north wing of Building 101 using the calculated capacity, EIR and heat transfer coefficient from measured data. The DX system compressors cycle at fairly high frequency (period is approximately 5 minutes), so averaged quantities were calculated and used in the regression, with an averaging window of 30 minutes. Due to this averaging operation, the compressor stage number ($Stage$) was taken as a continuous variable from 0 to 6. The figure below shows the training results and a reasonably accurate model was obtained.

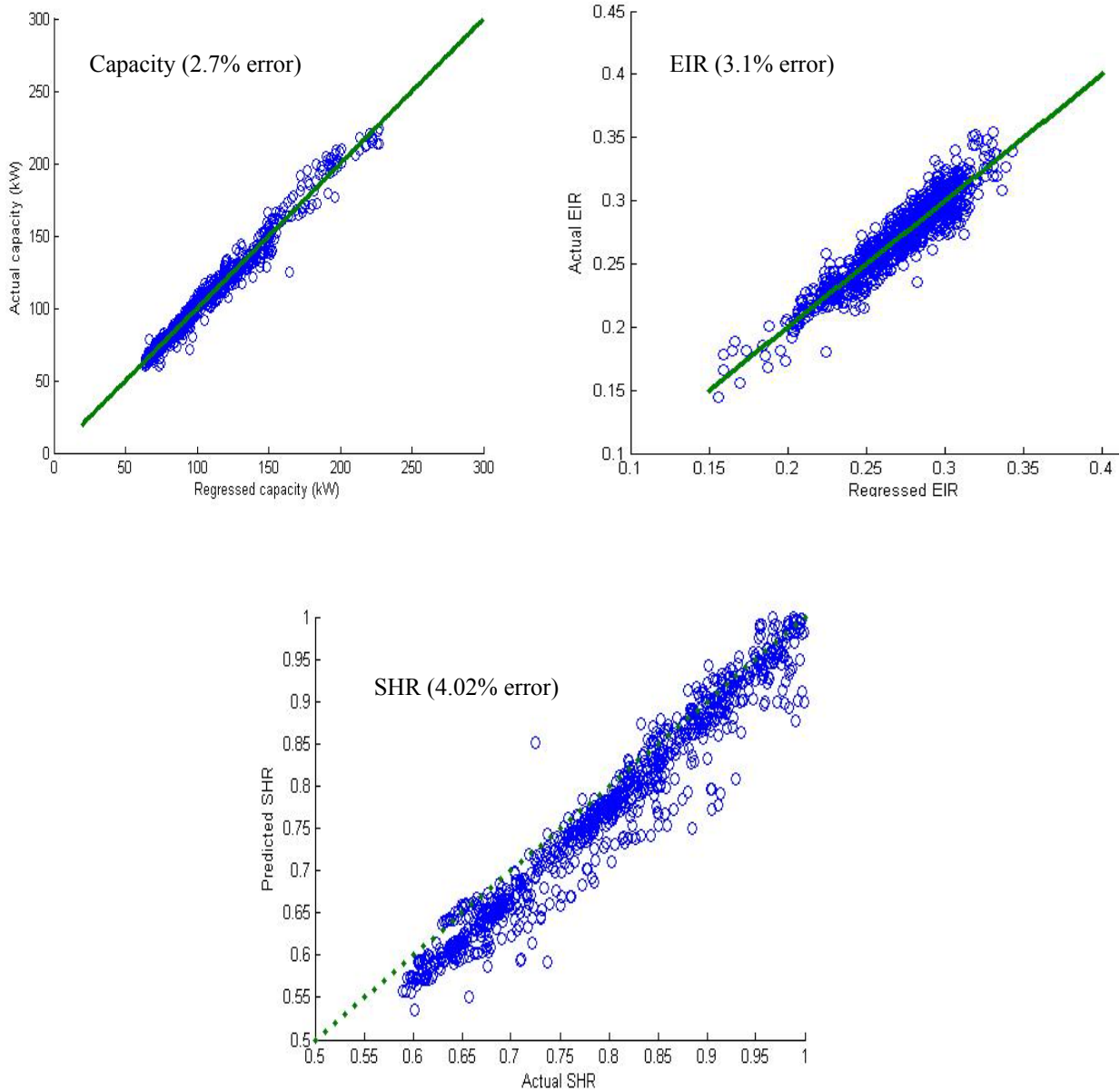


Figure 2.4.12 Comparison of predicted and measured capacity, EIR and SHR.

2.4.2.4 Toolkit model based optimization

The developed DX unit model takes ambient and indoor air conditions, supply air flow rate and compressor stage number as inputs and outputs total power consumption (compressor power plus supply fan power) as well as outlet air condition. To meet a given sensible cooling load there is only one degree of freedom, which can be manipulated by controlling supply air temperature setpoints. Optimization was performed to find the optimal map for any specific operation condition and required sensible cooling load. This optimization problem can be formulated as follows:

$$T_{lvg,opti} = \arg \min_{T_{lvg}} P_{tot} \left(\overline{T_{wb,evap}}, \overline{T_{cond}}, \overline{Q_{sen}}, T_{lvg} \right)$$

$$\text{satisfying} \begin{cases} SHR < SHR_{max} \\ V_{min} < \dot{V} < V_{max} \\ Stage \in [0, 6] \\ T_{min} < T_{lvg} < T_{max} \end{cases}$$

In this formulation, the over-lined variables, like the ambient conditions and required sensible load (Q_{sen}) are given beforehand. SHR_{max} is the allowed maximum sensible heat ratio which corresponds to a minimum dehumidification level. This value can also be set beforehand. For our system, the allowed minimum and maximum air flow rates are $V_{min}=10250$ cfm and $V_{max}=20500$ cfm. The leaving air temperature setpoint T_{lvg} is the optimization variable. Figure 2.4.13 provides a visualization of the power consumption variation with respect to the supply air temperature for a specific case with specified external variable values. The on-site supply air temperature setpoint is constant at 14.1 C and the corresponding power consumption for the specified conditions is 38.52 kW. Looking at the total power curve we see that increasing the supply air temperature would reduce total power consumption since latent load is reduced. If $SHR_{max}=0.85$ is given then the optimal supply air temperature setpoint would be 15.2 C and the corresponding power for these conditions would be 31.03 kW, which is approximately a 19% energy saving. In addition, increasing supply air temperature would also reduce the reheat, if any. So there could be even greater energy savings potential.

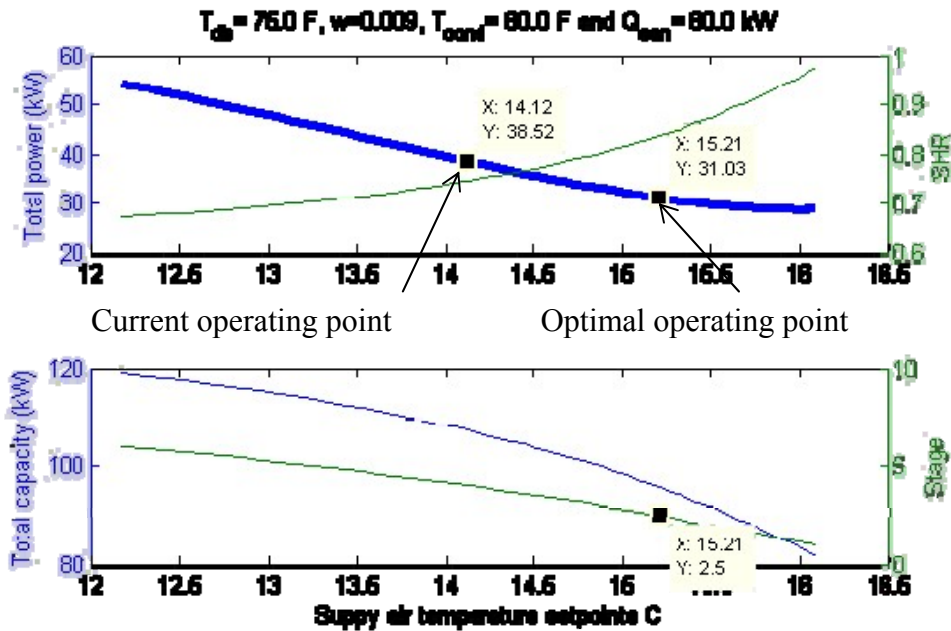


Figure 2.4.13 DX model outputs with respect to supply air temperature (T_{db} , w : dry bulb temperature and humidity ratio of the air entering cooling coil; Q_{sen} : required sensible load).

According to the capacity plots in Figure 2.4.13, there would be a capacity drop from 80 kW to 0 if the stage number transitioned from 1 to 0. The slope of capacity to stage number is much smaller at higher stage numbers. This phenomenon can also be seen from the plotted surface of capacity to air flow rate and stage number in Figure 2.4.14. This unrealistic behavior happens

because in the training data set the stage number is greater than 2.5 most of the time. As a result, there is no confidence in the model predictions at low stage numbers.

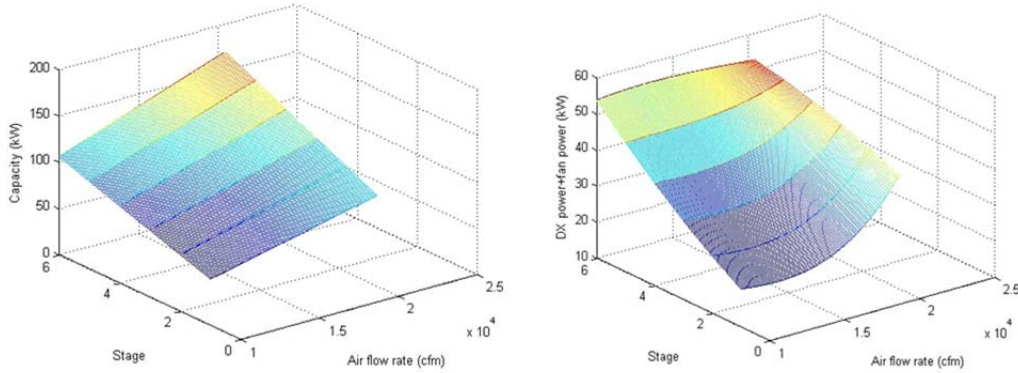


Figure 2.4.14 Visualization of capacity and total power for Toolkit model.

2.4.2.5 Gray-box model

The ASHRAE Toolkit is a black-box model for calculating the total power consumption and capacity and extrapolating performance is not guaranteed. As a result, there is not much confidence in the optimization results that were determined in the previous section using this Toolkit model. To solve this problem more physically-based models were developed at the component level and then coupled together to form an integrated gray-box model. The parameters of the component models were estimated from measured data.

Compressor:

The compressor models for mass flow rate and power consumption are given as follows:

$$\dot{m}_{ref} = \left\{ 1 - c_1 \left[\left(\frac{P_{dis}}{P_{evap}(1-\Delta p)} \right)^{1/k} - 1 \right] \right\} \cdot \frac{V \cdot RPM}{v_{suc} \cdot 60} = \eta_V \cdot C \cdot Stage \cdot \rho_{suc}$$

$$P_{comp} = \dot{m}_{ref} \cdot \frac{k}{k-1} \cdot p_{evap}(1-\Delta p) \cdot v_{suc} \left[\left(\frac{P_{dis}}{P_{evap}(1-\Delta p)} \right)^{\frac{k-1}{k}} - 1 \right] \cdot \eta_{comb}^{-1}$$

$$= Stage \cdot \eta_V \cdot C \cdot \frac{k}{k-1} \cdot p_{evap}(1-\Delta p) \left[\left(\frac{P_{dis}}{P_{evap}(1-\Delta p)} \right)^{\frac{k-1}{k}} - 1 \right] \cdot \eta_{comb}^{-1}$$

$$\eta_{comb} = c_2 P_{evap} / P_{evap,max} + c_3 Stage / 3 + c_4$$

$$k = C_p / C_v(T_{suc}, P_{suc})$$

As a reference for the actual compressor performance, an ideal isentropic process (Threlkeld, 1962) is used in this formulation. With this assumption, a polytropic compression exponent n is taken as the ratio of the constant pressure to constant volume specific heats k . The empirical parameters c_1 to c_4 are estimated from measured data. The parameter c_1 is an effective clearance volume ratio that influences the volumetric efficiency of the compressor as a result of re-

expansion of the gas prior to the suction valve opening. This re-expansion process also depends on the ratio of the discharge to suction pressure. In addition to these parameters, the compressor mass flow rate depends on the rated displacement volume (V), RPM and suction density (ρ_{suc}). Jähnig (1999) pointed out that the compressor overall energy efficiency (η_{comb}) has significant dependence on the evaporating pressure. For our system the number of operating compressor stages is also a dominant variable. A linear form was assumed for the dependence of combined efficiency on evaporating pressure and stage number. Evaporating pressure and stage number have significantly different scales so normalization was performed for these two quantities, where $P_{evap,max}$ is the maximum evaporating pressure for the measured data and the maximum stage number is 3.

Since we only had measurements for the compressor power and no information was available for the refrigerant mass flow rate, all four parameters were estimated simultaneously in the compressor power (P_{comp}) formulation. It was seen from measured data that the isentropic efficiency was relatively constant and close to 0.8. From measured data, the superheat was taken to be a constant 10 C. The training root mean square errors for power predictions were 5.2% for compressor A and 1.8% for compressor B. The sets of parameters have different estimated values for these two compressors but the models have similar trends. Visualization of the model outputs with respect to different inputs are provided in Figure 2.4.15. The surfaces with white background color are plotted from the compressor map provided by the manufacturer. From these plots it can be seen that the estimated model of compressor B is a good match to the rated performance but there is significant deviation for compressor A. It appears the compressor A is not performing well compared to its original performance.

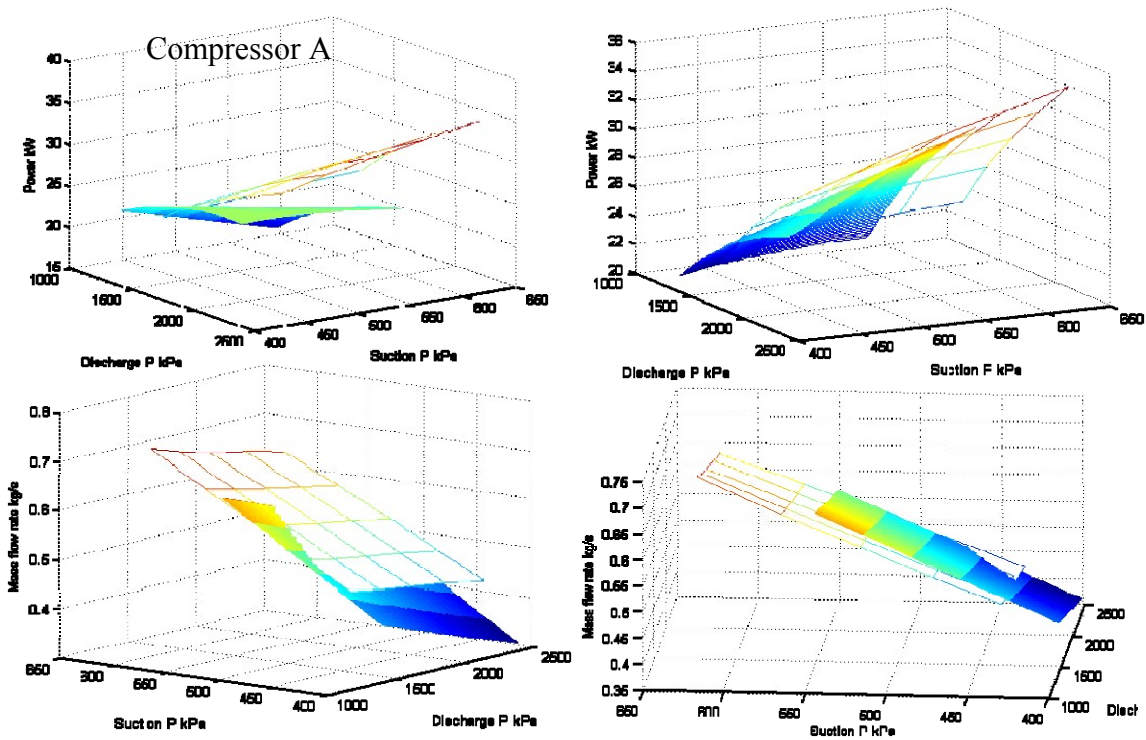


Figure 2.4.15 Comparisons of estimated compressor model to the rated compressor map.

Evaporator:

The effectiveness method was applied to model the evaporator. There are two DX cooling coils and the inlet air conditions are assumed to be identical for these two coils but inlet refrigerant conditions can be different. The heat transfer conductance (UA) is correlated with the air side (\dot{m}_{air}) and refrigerant side (\dot{m}_r) flow rates, with g_2 to g_5 being the correlation coefficients that need to be estimated. There is moisture removal for this cooling coil, so air enthalpies are considered in calculating the total capacity. $h_{air,in}$ is the inlet air enthalpy and $h_{air}[P]$ is the saturated air enthalpy when an air temperature equal to the refrigerant saturated temperature at pressure P . Also we assume the two cooling coils have the same geometric and physical properties so that the parameter sets have identical values for the two coils. The trained total capacity had a root mean square error of 5.8%.

$$Cap = \varepsilon_A \dot{m}_{air} (h_{air,in} - h_{air}[P_A]) + \varepsilon_B \dot{m}_{air} (h_{air,in} - h_{air}[P_B])$$

$$\varepsilon_{A(B)} = 1 - e^{(-Ntu)} = 1 - e^{-\frac{UA_{A(B)}}{\dot{m}_{air}}}$$

$$\frac{1}{UA_{A(B)}} = g_2 (\dot{m}_{air})^{g_3} + g_4 (\dot{m}_{r,A(B)})^{g_5}$$

Condenser fan:

There are two condensing coils and for each coil there are two fans. We had measurements for the number of operating fans ($Stage_{cond, fan}$) but no direct measurements of air flow rates ($\dot{m}_{a,cond}$). In order to calculate the heat exchanger conductance, information about the air flow rate was necessary. The air flow was estimated from an energy balance on the condensers with the condenser heat rejection determined from an overall energy balance on the DX unit. The air mass flow for each condenser was correlated with fan staging using the following form.

$$\dot{m}_{a,condA(B)} := c_0 + c_1 \cdot Stage_{cond, fan, A(B)} + c_2 \cdot Stage_{cond, fan, A(B)}^2$$

Where c_0 to c_2 are the correlation coefficients and $Stage$ is the number of operating condensing fans for one condensing coil. The coefficients were assumed to be identical for the two coils. The training result had a RMSE of 12%. Figure 2.14.16 shows outputs for condenser air flow rate as a function of fan staging. The rated air flow rate is 8.7 kg/s for each unit, which matches the model output at full load.

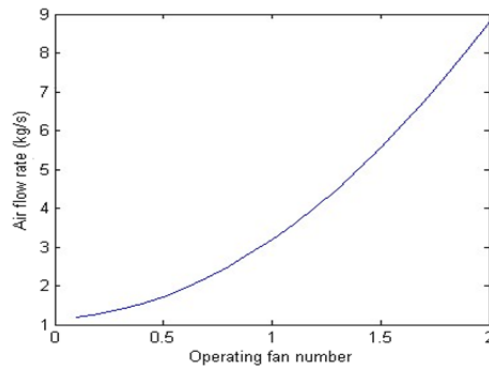


Figure 2.4.16 Variation of air flow rate to the number of operating condensing fans.

Condenser capacity:

Similar to the evaporator model, an effectiveness method was also applied to calculate the heat transfer rate for the condenser. However, the condensing coil is always dry so temperature difference is used instead of enthalpy difference when calculating capacity. $T_{r,cond}$ is the condensing temperature and $T_{air,in}$ is inlet air temperature. Again, the parameters were assumed to be identical for the two coils. The trained model had a RMSE of 9% for total condenser capacity.

$$Cap = \sum_{A,B} \varepsilon_{A(B)} \dot{m}_{air} (T_{r,cond,A(B)} - T_{air,in})$$

$$\varepsilon_{A(B)} = 1 - e^{-Ntu} = 1 - e^{-\frac{UA_{A(B)}}{\dot{m}_{air}}}$$

$$\frac{1}{UA_{A(B)}} = g_2(\dot{m}_{air})^{g_3} + g_4(\dot{m}_{r,A(B)})^{g_5}$$

Thermal expansion valve (TEV):

Thermal expansion valves are used in the current system to regulate the refrigerant mass flow rate for the purpose of maintaining a constant superheat. Mathematical models for a TEV can be found in Broersen (1982) and James (1987). We assume the bulb temperature has slower dynamics than that of the compressor inlet temperature, which makes it reasonable to apply a quasi-static model, i.e., the bulb temperature is always equal to the compressor inlet temperature. In this case, the mass flow rate through the TEV can be calculated as:

$$\dot{m}_r = (c_1 + c_2 \cdot P_b + c_3 \cdot P_{evap}) \sqrt{\rho_{in} (P_{cond} - P_{evap})}$$

where P_b is the saturated pressure of the refrigerant at bulb temperature and ρ_{in} is the refrigerant inlet density (saturated liquid density at the evaporating pressure). To estimate the coefficients, mass flow rate was back calculated using the condenser capacity and enthalpy difference across condenser. The RMSE of the estimated model was 14.5% for refrigerant mass flow rate.

Integrated model:

Table 2.4.3 shows the error of the estimated models for each component. Although errors are relatively large for the condenser fan and TEV models, the integrated model behavior is not that sensitive to these components.

Table 2.4.3 Error for each component in the system.

	A	B
Compressor (power)	5.1 (%)	1.8
Condenser fan (cap)	12.5	
Condenser (cap)	9	
TEV (mass flow)	14.5	14.5
DX coil (cap)	5.8	

Figure 2.4.17 provides a flow chart for the integrated model. The double-underscored variables

are external inputs (boundary conditions). The underscored variables, discharge and suction pressures (P_{dis} , P_{suc}), are internal variables that need to be solved iteratively.

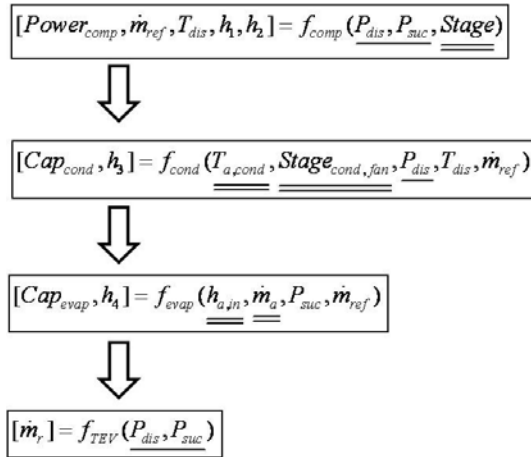
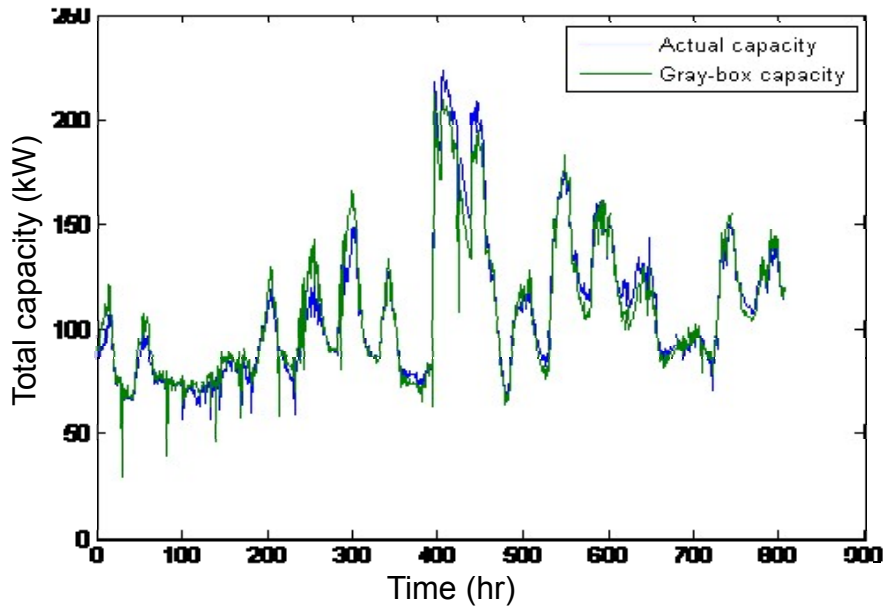


Figure 2.4.17 Flow chart of the integrated model.

Figure 2.4.18 demonstrates that the integrated model predicts both DX unit cooling capacity and compressor power consumption reasonably well. The RMSE's are 5% for capacity and 6% for compressor power.



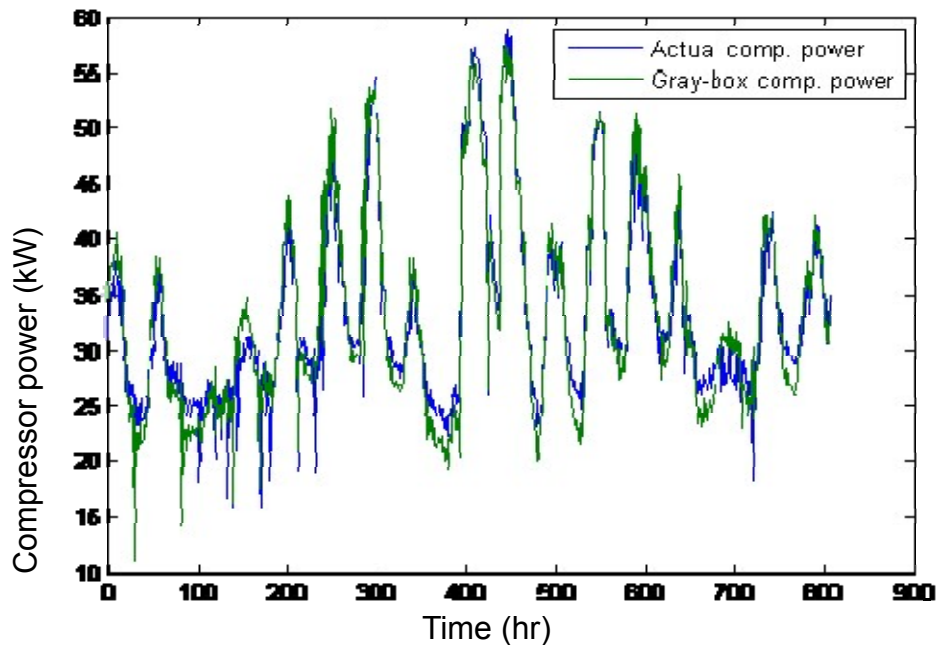


Figure 2.4.18 Comparisons of the predicted capacity and compressor power to the actual values

2.4.2.6 Comparison of Toolkit and gray-box models

Figure 2.4.19 shows capacity and compressor power variation with respect to stage number and supply air flow rate for the Toolkit and gray-box models. As previously mentioned, the Toolkit model predictions do not make sense for low stage numbers because capacity and power do not approach zero as stage number goes to zero. However, the gray-box model does not have this problem and the estimated capacity falls off quickly as the stage number approaches zero. For the compressor power prediction, the gray-box model indicates that the power is mostly dominated by stage number and air flow rate has a small influence. The trend is similar for the gray-box model except at low stage numbers where the air flow dependence becomes artificially high. In region where data were available for training, agreement between the two models is very good for both capacity and power consumption.

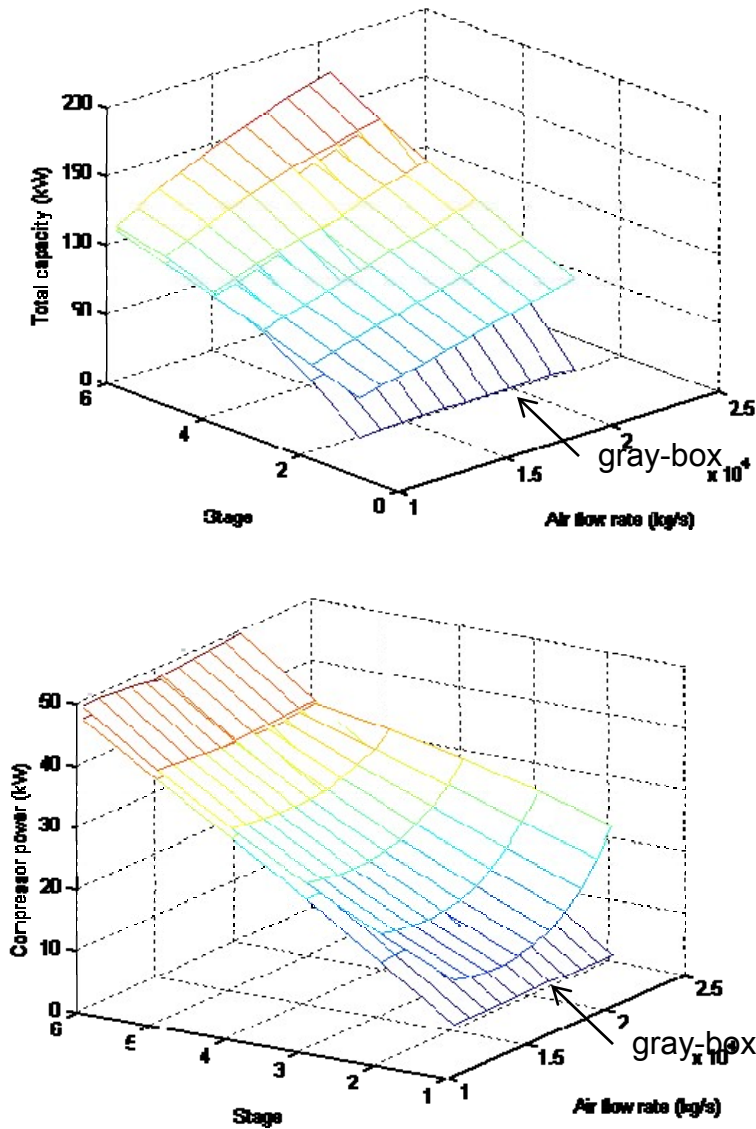


Figure 2.4.19 Comparison of Toolkit and gray-box models.

2.4.2.7 Gray-box model based optimization

The gray-box model has better extrapolating performance but it is computationally inefficient because an iterative process is needed to calculate the internal variables. When generating the optimal map, the computational burden is significant. To improve the efficiency, we implemented a modified Toolkit model but used gray-box model outputs as the training data. To capture the nonlinearities with respect to stage number and air flow rate, more terms are added to the Toolkit model correlation and as a consequence more coefficients have to be estimated. In this situation normalization is important to avoid rank deficiency. The trained model shows good agreement with the gray-box model, with a maximum deviation less than 2%.

Optimization was then performed on the gray-box model as well as the modified Toolkit model and example results are shown in Figure 2.4.20. The resulting optimal operating conditions are slightly different (supply air temperature is 15.6 C for gray-box model and 15.4 for Toolkit model). The calculated energy saving potential is 16.4% using the gray-box model and 20.2%

using the Toolkit model.

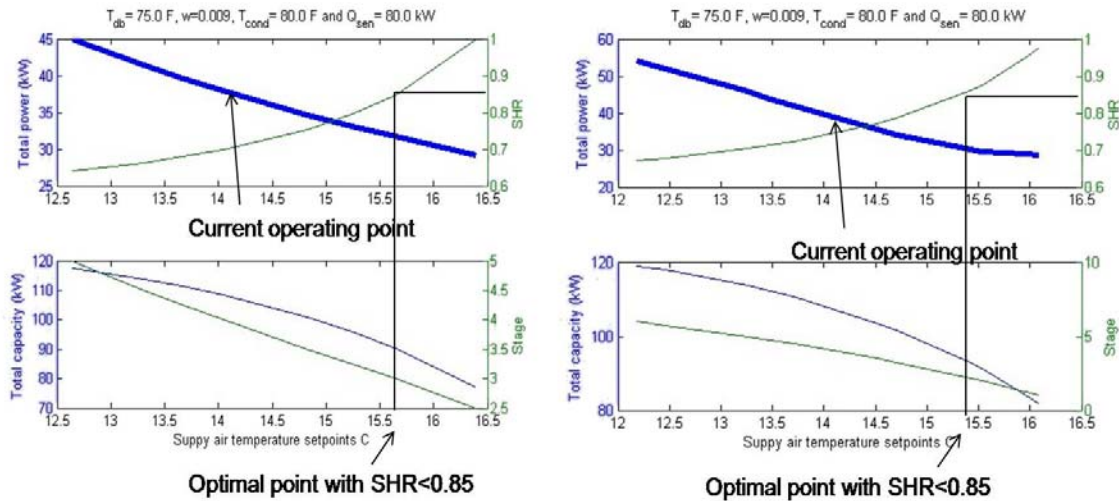


Figure 2.4.20 Optimization results. Left: gray-box model. Right: Toolkit model.

2.4.3 References

1. Chaturvedi, N. and Braun, J.E., 2002, "An inverse gray-box model for transient building load prediction", *HVAC&R Research*, Vol. 8, No. 1, pp. 73-99.
2. Seem, J.E., S.A. Klein, W.A. Beckman, and J.W. Mitchell, 1989, "Transfer functions for efficient calculations of multi-dimensional heat transfer", *Journal of Heat Transfer-Transactions of the ASME* 111(1):5-12.
3. Cai, J. and Braun, J.E., 2012, "Efficient and Robust Training Methodology for Inverse Building Modeling", *SimBuild 2012 5th National Conference of IBPSA-USA*.
4. Brandemuehl, M.J., S. Gabel, and I. Andresen. 1993. HVAC2 Toolkit: Algorithms and Subroutines for Secondary HVAC System Energy Calculations. Atlanta, GA: ASHRAE, Inc.
5. Threlkeld, J.L. 1962. *Thermal environmental engineering*. Englewood Cliffs, NJ: Prentice-Hall.
6. Dagmar Jähmig, 1999. "A Semi-Empirical Method for Modeling Reciprocating Compressors in Residential Refrigerators and Freezers".
7. P. M. T. Broersen, "Control with a thermostatic expansion Valve", *Int. Journal of refrigeration*, Vol. 5, pp. 209-212, 1982.
8. K. A. James and R. W. James, "Transient analysis of Thermostatic Expansion Valve for refrigeration system evaporators using mathematical models", *Trans. Inst M C*, Vol. 9, 1987.

2.5 Data-Driven Model

This section presents the development of control-oriented models for the thermal zones in buildings. Low-order state-space models are identified from the designed input-output responses of thermal zones with disturbances from ambient conditions and internal heat gains. A high-fidelity TRNSYS model of an office building was used as a virtual testbed to generate data for system identification, parameter estimation, and validation of the proposed model structures. This section concludes with evaluations of the state-space model in terms of model accuracy for predictive control design.

Our case study is focusing on the north-wing of Building 101 served by Air Handler Unit 3 (AHU). The HVAC system includes a direct expansion (DX) coil for cooling and a gas-fired boiler for heating. The AHU is connected to 8 VAV boxes downstream with reheat coils. The 8 VAV boxes serve a total of 10 zones, in which VAV #1 and VAV #8 serve zones 1 & 10 and zones 8 & 9, respectively. There is only one supply fan to satisfy the flow rate requirements from all the VAV boxes.

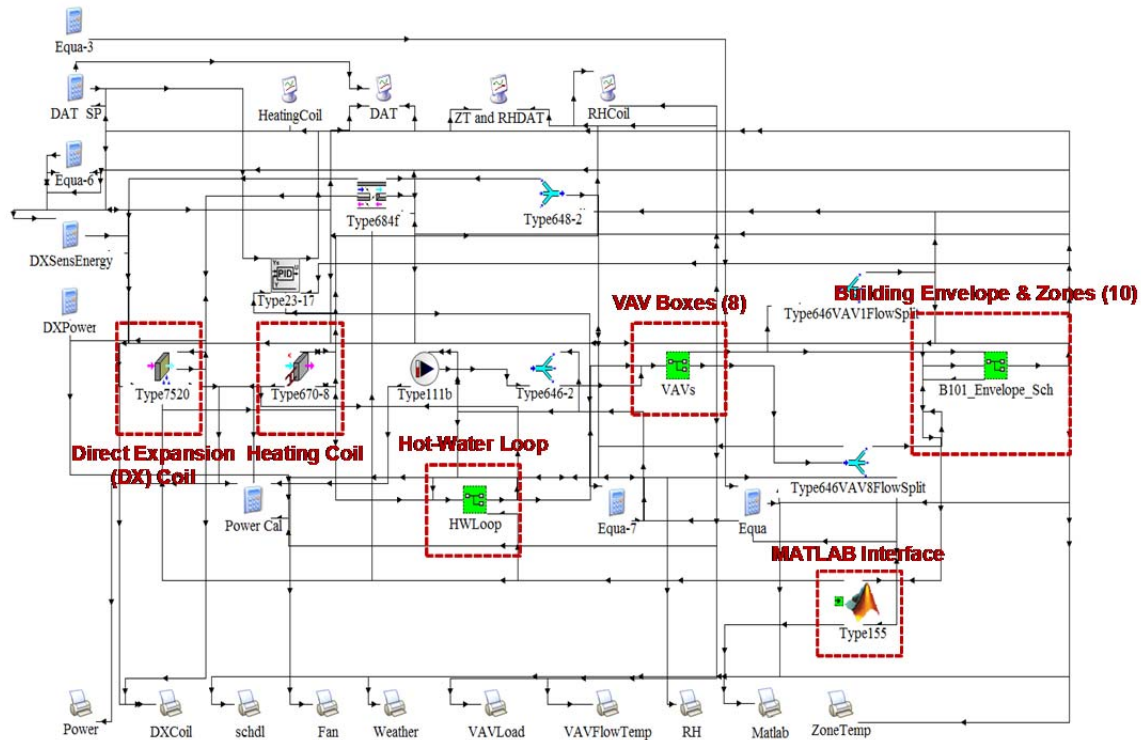


Figure 2.5.1 Screenshot of TRNSYS model for north-wing of Building 101

2.5.1 HVAC Equipment Model

For supervisory level building control and optimization, we assume that the dynamics associated with HVAC equipment is much faster compared to the dynamics from building envelope and zones. Thus, the HVAC equipment model can be treated as quasi-steady state within the time scale of interest. The following presents the HVAC equipment model employed in this study.

2.5.1.1 Fan Model

The power of the supply fan is modeled as a performance map as a function of the fan control signal:

$$P_{fan} = P_{rated}(a_0 + a_1\gamma + a_2\gamma^2) \quad (2.5.1)$$

Where P_{rated} is the rated fan power, γ is the supply fan control signal normalized to [0-1], a_0 , a_1 , a_2 are coefficients determined based on historical data (i.e., March and April in 2012) from Building 101. The parameter values are summarized in Appendix 2.5 (Table A.2.5.1). The temperature rise across the supply fan is modeled as:

$$T_{fan,out} = T_{DX,out} + \frac{P_{fan}(\eta_m + (1-\eta_m)f_{motorloss})}{\gamma\dot{V}_{tot,max}\rho_{air}c_{pa}} \quad (2.5.2)$$

where $T_{DX,out}$ is the air temperature after the DX coil before the supply fan. All other parameters and their values are listed in the Appendix 2.5 (Table A.2.5.2).

2.5.1.2 DX Coil Model

The DX coil model is also modeled as a performance map based on design information. In particular, the coefficient of performance (COP) is modeled as a function of the partial load ratio (PLR):

$$COP = a_0PLR^4 + a_1PLR^3 + a_2PLR^2 + a_3PLR \quad (2.5.3)$$

$$PLR = 100 \cdot \frac{Q_{airtot}}{Q_{airmax}} \quad (2.5.4)$$

The parameter values are listed in the Appendix 2.5 (Table A.2.5.3) and the COP map is shown in Figure A.2.5.1. The maximum air-side heat transfer Q_{airmax} is obtained from the design information (see Table A.2.5.3). The total air-side heat transfer Q_{airtot} is determined by:

$$Q_{airtot} = Q_{sen}/SHR \quad (2.5.5)$$

where Q_{sen} is the air-side sensible heat transfer:

$$Q_{sen} = \dot{m}_{sa} \cdot c_{pa} \cdot (T_{mix} - T_{DX,out}) \quad (2.5.6)$$

where Q_{sen} is the air-side sensible heat transfer, \dot{m}_{sa} is the air mass flow rates across the DX coil, c_{pa} is the specific heat of moist air, T_{mix} is the mixed air temperature before the DX coil, and $T_{DX,out}$ is the air temperature after the DX coil.

The sensible heat ratio (SHR), defined as the ratio of air-side sensible heat transfer to the total heat transfer, is determined based on a regression fit. The data used for calibration and validation are obtained from the Building 101 TRNSYS model.

$$SHR = a \cdot \omega_{mix}^b \quad (2.5.7)$$

where a and b are coefficients determined from the regression fit.

$$\omega_{mix} = \alpha_{oa}\omega_{oa}(RH_{oa}, T_{oa}) + (1 - \alpha_{oa})\omega_{ret}(RH_{ret}, T_{ret}) \quad (2.5.8)$$

where α_{oa} is the outdoor air fraction. ω_{oa} , ω_{ret} , ω_{mix} are the humidity ratios of outdoor air, return air, and mixed air, respectively. RH_{oa} , RH_{ret} , RH_{mix} are the relative humidity of outdoor air, return air, and mixed air, respectively. T_{oa} , T_{ret} , T_{mix} are the temperatures of outdoor air, return air, and mixed air, respectively. α_{oa} is the outdoor air fraction.

Finally, a constraint based on the maximum cooling capacity of the DX coil is added to the MPC formulation:

$$\max(T_{mix} - T_{DX,out}) = \frac{SHR \cdot Q_{airmax}}{\dot{m}_{sa} c_{pa}} \quad (2.5.9)$$

2.5.1.3 VAV Box Model

A VAV box typically includes a damper to adjust the air flow rate and a reheat coil to adjust the hot water flow rate in order to meet the cooling or heating demands from the zone. In the TRNSYS model, there are two individual PID feedback control loops in each VAV that commands the air flow setpoint and reheat valve position, respectively. For supervisory control, it is assumed that the air flow setpoint can be met by the local PID controller and thus the characteristics from damper position to the actual air flow rate are not considered. However, since the reheat valve position is assumed to be our controlled variables in the optimization problem, a model is need to account for the relationship between reheat valve position to the VAV discharge air temperature is needed. The maximum design air and hot water flow rates are summarized in the Appendix 2.5 (Table A.2.5.4) for each VAV box.

An existing heat exchanger model (Type670) from the TESS Library (TESS) is adopted as the reheat coil model in our study. The heat transfer of the reheat coil is determined based on effectiveness and a theoretically maximum possible heat transfer.

$$Q_{max} = C_{min} \cdot (T_{HWS} - T_{fan,out}) \quad (2.5.10)$$

where the minimum heat capacitance C_{min} is defined as:

$$C_{min} = \min(\dot{m}_{hw} C_{pw}, \dot{m}_{vav,air} C_{pa}) \quad (2.5.11)$$

From the simulation data generated by the TRNSYS model, we observed that the water-side heat capacitance is nearly always smaller than that of the air-side. The following assumption is made in order to avoid “if-else” scenarios in the optimization:

$$C_{min} \cong \dot{m}_{hw} C_{pw} \quad (2.5.12)$$

where \dot{m}_{hw} is the hot water mass flow rate in a given reheat coil and C_{pw} is the specific heat of water. The actual water-side heat transfer across the VAV reheat coil is given by:

$$Q_{RH} = \varepsilon Q_{max} \quad (2.5.13)$$

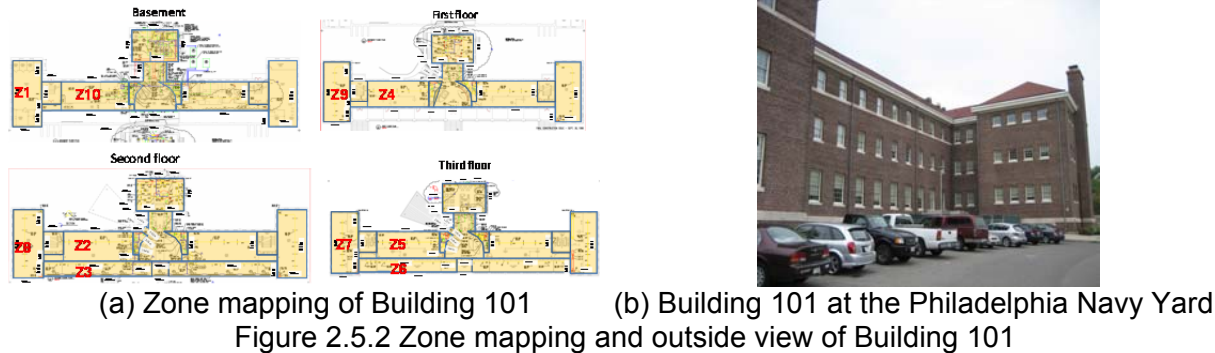
where ε is the effectiveness of the reheat coil and it is assumed to be a constant in the TRNSYS model. The temperature rise across the VAV box could thus be determined as:

(2.5.14)

where T_{air} is the air temperature after the supply fan given in Eq. 2.5.2.

2.5.2 Case Study 1: Building 101 Simulation Study

Figure 2.5.2(a) shows the floor map and zone mapping for the north-wing of Building 101. Figure 2.5.2(b) shows the outside view of Building 101 at the Philadelphia Navy Yard.



2.5.2.1 Model Development: System Identification

System identification typically requires an iterative procedure involving the following steps:

- 1) Selection of input and output signals.
- 2) Functional tests to excite system dynamics within certain input frequencies of interest.
- 3) Selection of model formats and parameter estimation.
- 4) Validation of models based on an independent data set.

Until the model reaches an acceptable accuracy, the above steps may be repeated for an incremental improvement of the model accuracy.

For the building model, we considered the control inputs of VAV supply air flow rate setpoints and zonal supply temperature with ambient temperature as measured disturbances. The outputs of the model are zone air temperatures. Although solar radiation and internal gains were not included as measured disturbances, the responses of the zones to these inputs are significantly slower in comparison to VAV supply conditions. However, this may limit the ability of the model to look ahead over longer time intervals and to properly consider the effects of energy storage within the building mass. Note that for a MPC implementation, an additional model is needed to compute the VAV supply air temperature from the supply air flow and reheat valve position. For simplicity, the same sampling time was used for all the zones. Step response tests were first conducted to evaluate the dominant time scale of the system, the sampling time (3 minutes) was then chosen to ensure that there are at least 4-10 samples within the rise time of the step response (Åström and Wittenmark, 1997).

In the early development, solar radiation was included as an input. However, it was found that the effect of solar radiation on the dynamic response of the zones was quite small and not included in the final model. This may not be the case for other buildings or if longer time horizon predictions are desired. Figure 2.5.3 shows the input (flow setpoints and valve positions) and output signals (zone temperature) selected in the system identification experiments.

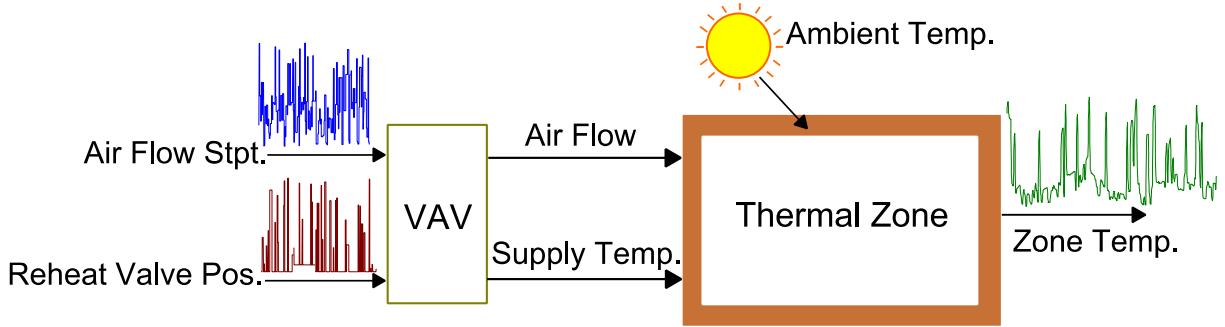


Figure 2.5.3 Input and output signals employed in system identification

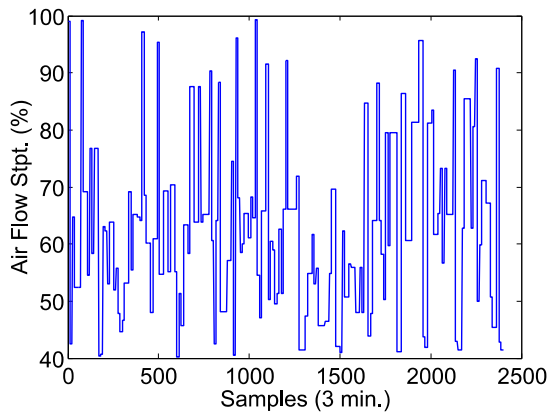
The linear state-space model for zone temperature dynamics is given by

$$\hat{x}(k + 1) = A\hat{x}(k) + Bu(k) \tag{2.5.15}$$

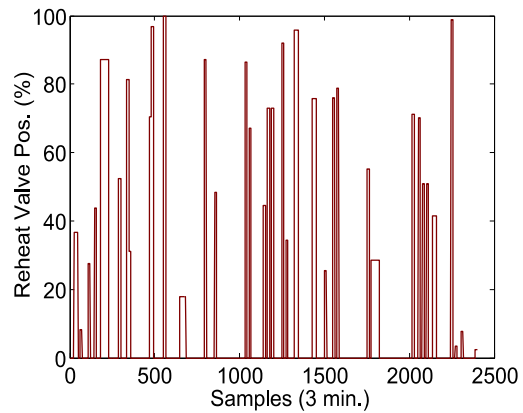
$$\hat{T}_{model}(k) = C\hat{x}(k) + Du(k) \tag{2.5.16}$$

where k is the current time step, \hat{x} is the state vector, u is the input vector, \hat{T}_{model} is the predicted zone temperature, and A, B, C, D are system matrices. The convective coupling between zones was not considered in the current TRNSYS model and thus the state-space models, but the importance of this coupling will be considered in our future studies. We considered a scalable approach to train the model in a semi-automatic fashion. A simultaneous zone model training structure was established to inject signals and perform identification experiments for all zones. The data was collected and converted to specific format that is consistent with the MATLAB System Identification Toolbox (Ljung and Singh, 2012).

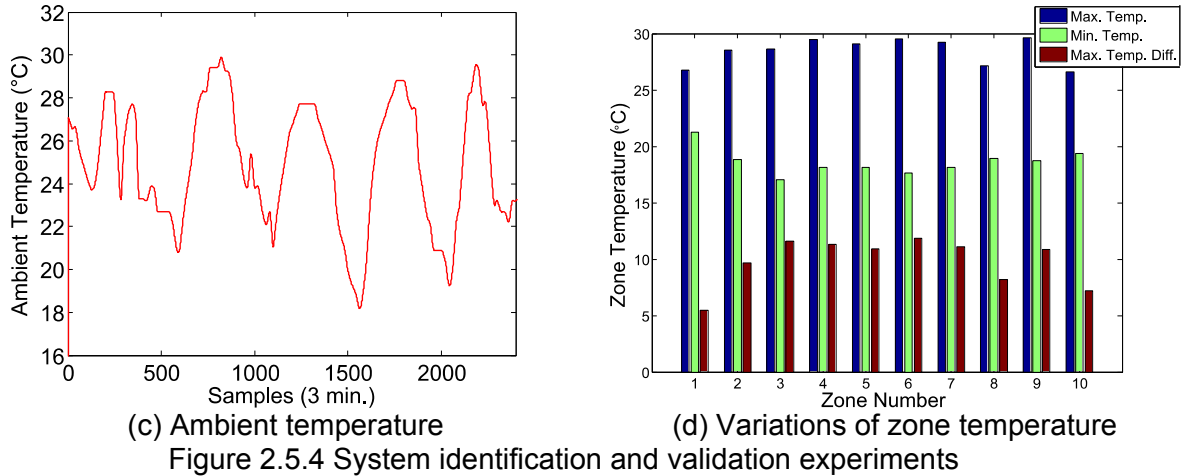
Figure 2.5.4(a) and 2.5.4(b) show the excitation signals for supply air flow setpoint and reheat coil valve position, respectively. The ambient temperature profile during the functional test period is shown in Figure 2.5.4(c). Figure 2.5.4(d) shows the maximum temperature, minimum temperature and maximum temperature difference of each zone during the functional tests. Most of the zones had a zone temperature variation larger than 10°C (18°F), which is credited to the full-range input signals employed in the identification experiments.



(a) Excitation signals for air flow setpoints



(b) Excitation signals for reheat valve position



Our preliminary study suggested that a low-order (3rd order) ARX model identified¹ with the same training data and the same number of inputs could not predict the zone dynamics well when the magnitude of excitation was large, and it only worked well for a small range of operation (Li et al., 2012). More details about the ARX model is described in the Appendix 2.5. Example validation results are shown in Figure 2.5.5(a) for an ARX trained for zone 5. Through a trial-and-error process, we selected the low-order state-space model as it yielded superior performance over the ARX model for the full-range of input signals. Figure 2.5.5(b) provides validation results for the low-order state-space model of zone 5, which has significant better performance compared to the ARX model predictions shown in Figure 2.5.5(a).

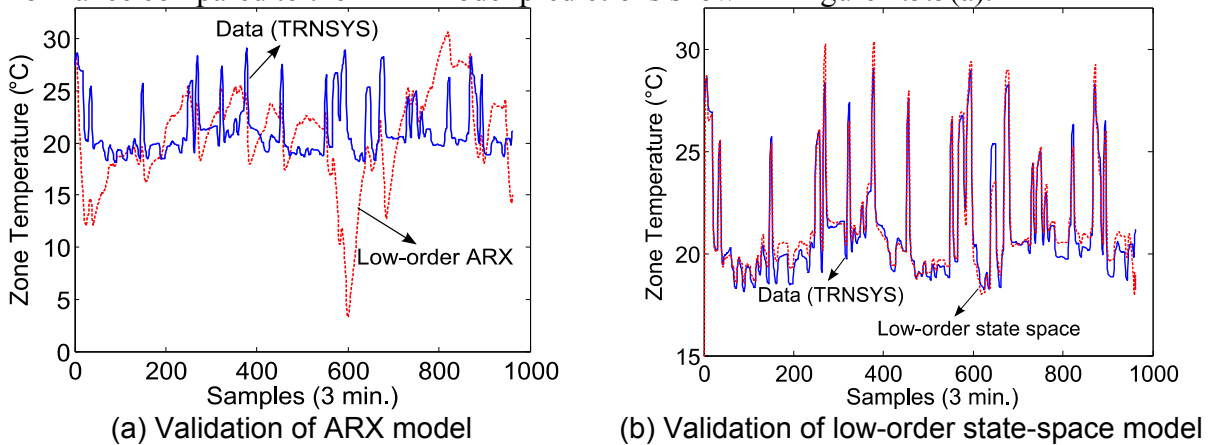


Figure 2.5.5 Comparisons of performance of low-order ARX and low-order state-space model under large excitations

2.5.2.2 Model Development: State Estimation

In order to use the state-space model for online control, the initial states at each times step should be estimated. Since we opted for a data-driven approach, the states have no physical meaning and it would be difficult to guess their actual values. Alternatively, one could consider the system to start from an equilibrium condition, but the initial transients of system states will be large since it is expected that the initial states are not zero.

¹ The ARX model was identified based on least-squares estimation method implemented in the MATLAB System Identification Toolbox.

To tackle this problem, we applied a linear Luenberger observer for the purpose of state estimation. The outputs from the TRNSYS model (i.e., virtual test bed) were assumed to be the “measured” values. The observer equation is given by

$$\hat{T}_{model}(k) = C\hat{x}(k) + Du(k) \quad (2.5.17)$$

$$\hat{x}(k + 1) = A\hat{x}(k) + Bu(k) + L(T_{trnsys}(k) - \hat{T}_{model}(k)) \quad (2.5.18)$$

For a given zone, the observer gain L was determined based on an offline optimization that minimizes the sum of squared errors.

$$L = \operatorname{argmin}_L \sum_{i=1}^{N_{obs}} (T_{trnsys}(i) - \hat{T}_{model}(i))^2 \quad (2.5.19)$$

where N_p is the model prediction horizon in MPC, and N_{obs} is the number of historical data points used in the optimization to obtain L , and T_{trnsys} is zone temperature “measured” from the TRNSYS model. Figure 2.5.6 shows the block diagram for the signal flows among the TRNSYS model, state observer, and MPC controller. More detailed procedures for the implementation and algorithm execution during MPC operation are shown as a flow chart in the Appendix 2.5 (Figure A.2.5.2).

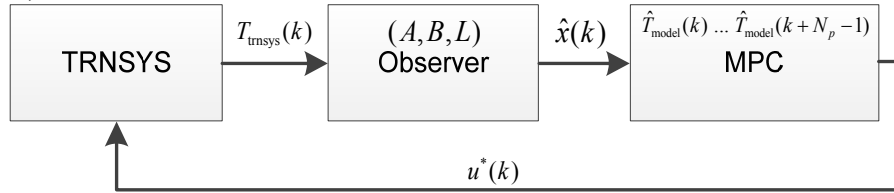


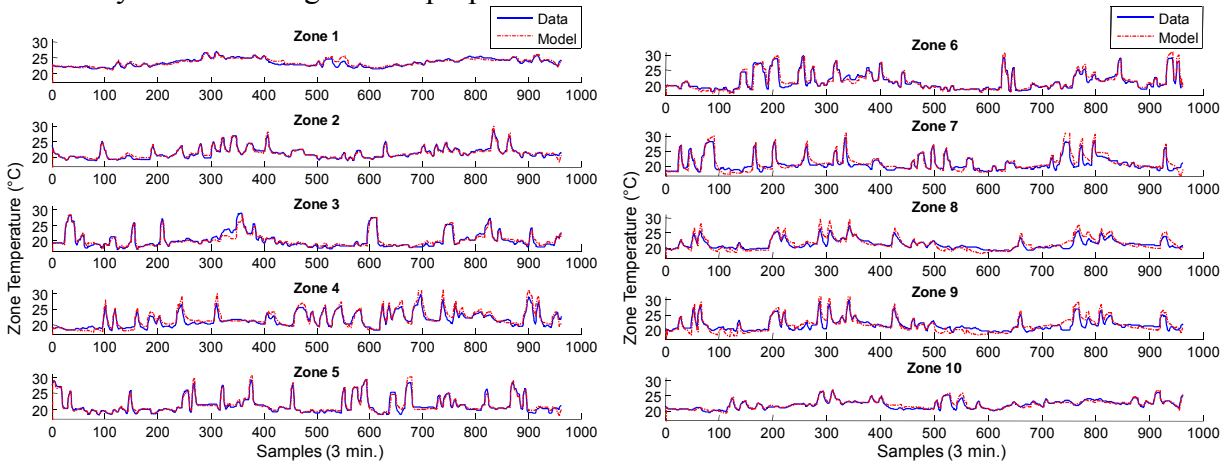
Figure 2.5.6 Block diagram of signal flows among TRNSYS, observer, and MPC

2.5.2.3 Simulation Results

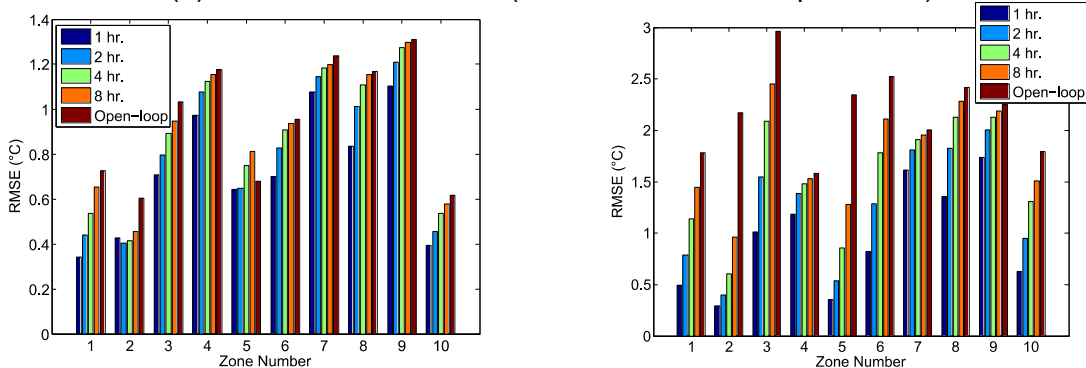
For system identification and validation, we performed functional tests during the 1st week of August using virtual weather data from 2011 (Weather Analytics, 2012). Data from the first three days was used for model identification, and data from the last two days was used for model validation. Figure 2.5.7(a) shows comparisons of 2nd order state-space model predictions with data for all 10 zones served by AHU3 based on validation data. To evaluate the effectiveness of model performance for MPC implementation, Figure 2.5.7(b) and 2.5.7(c) show comparisons of root mean squared error (RMSE) for the 10 zones with predictions of 1 hr., 2 hr., 4 hr., 8 hr., and open-loop scenarios based on functional test and TRNSYS baseline input-output data, respectively. The scenarios for predicting 1 hr., 2 hr., 4 hr., and 8 hr. ahead were realized by reinitializing the system states every 1hr., 2 hr., 4 hr., and 8 hr., respectively. The open-loop scenario did not involve any reinitialization of system states.

Note that we performed very aggressive functional tests (see Figure 2.5.4) to fully excite the system dynamics with predictive results in Figure 2.5.7(b) that appear to be quite good for control design. For the additional model validation results in Figure 2.5.7(c), baseline feedback controllers were implemented within the TRNSYS testbed that adjusted air flow rates or reheat

valve to maintain zone temperature setpoints². The TRNSYS zone air flow rates and supply air temperatures were then fed into the simplified model to determine the zone temperature responses that were compared with TRNSYS zone temperatures. Overall errors in the zone temperature predictions for this test case are presented in Figure 2.5.7(c). This control input scenario is much different than that employed during the model training periods shown in Figure 2.5.4(a) and 2.5.4(b). Overall, the model yielded much worse results for both short-term and long-term predictions than those presented in Figure 2.5.7(b). The degraded model performance under this validation scenario is probably due to the fact that the effects of solar radiation and internal loads become more important relative to the control inputs (zone supply air flow rate and temperature); as compared with the validation scenarios based on functional test data. Future study will be conducted to address the aforementioned limitations. In particular, better models may be needed to approach optimal MPC performance in the presence of variable utility rates and demand charges because longer prediction horizons are required. Uncertainty analysis for internal and solar heat gain predictions should be carried out before these gains are added as inputs to the predictive model. Future study will be conducted to address this problem and the uncertainty estimation algorithms proposed in Section 3.5.2.1 will be considered.



(a) Zone model validation (functional tests, 2 hr. prediction)



(b) RMSE with input-output data from functional tests (c) RMSE with baseline input-output data
 Figure 2.5.7 Validation results for 10 zones in Building 101

² The baseline controller will either adjust VAV reheat valve position with minimum supply air flow setpoint when the zone temperature is below a prescribed heating setpoint or adjust supply air flow setpoint with reheat valve closed when the zone temperature is above a prescribed cooling setpoint. The supply air flow setpoint will be kept as minimum with reheat valve closed if the zone temperature could be maintained between the heating and cooling setpoints (i.e., no feedback control).

2.5.3 Case Study 2: UTRC L Building Testbed

In addition to B101 simulation study, we have further investigated data-driven modeling approach with the low-order state-space model format based on real-building data from UTRC L Building Testbed. The same set of model inputs with Building 101 case study were adopted (see Figure 2.5.3), which include supply air flow rate setpoint, supply air flow temperature, and ambient temperature. The excitation signals during the functional tests are presented in the Appendix 2.5 (Figure A. 2.5.3). Preliminary study indicates that the uncertainties of internal heat gains play an important role to the responses of zone temperature. The model inputs were selected based on the specific needs of our MPC strategy where a relative short prediction horizon is adopted for the purpose of minimizing energy consumption rather than energy cost. The model should include uncertainty estimations and predictions due to variations in zone loads if a longer prediction horizon is needed.

Since MPC is operated in closed-loop fashion and the system states are initialized based on previous temperature measurements at each time step of the optimization. To evaluate the model quality for a more realistic scenario for MPC operation, we have investigated the model predictions when reinitializing the states every 2 hours. Preliminary studies showed that the zone temperature prediction errors could be maintained within 1°C as shown in Figure 2.5.8. However, we have experienced some challenges of having a robust and consistent model performance for different validation scenarios and time periods.

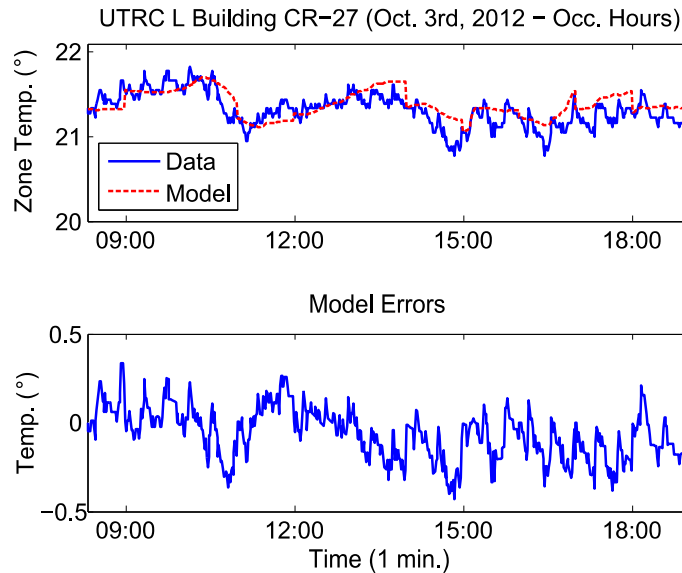


Figure 2.5.8 Validation results of low-order state space model with 2 hr. state reinitialization using regular operation data

To further investigate the modeling approach and improve the model quality, we are considering augmenting the uncertainty estimations to the existing low-order state-space model. The uncertainty estimations would account for the lumped effects of internal heat gains from occupancy, lighting, equipment, and coupling between zones, etc. However, we realize that it would be very difficult to accurately estimate the uncertainty propagations in the predictive control framework, especially when relevant measurements are not available to generate some time-varying profiles that could be helpful in the predictions. Future study will be conducted to

address the issues of uncertainty estimations and propagations for the internal heat gains and their impact to the zone temperature predictions with real-building data.

2.5.4 Conclusions

We have investigated data-driven modeling approaches for MPC in buildings and have demonstrated that reasonable model accuracy for zone temperature predictions could be obtained with low-order state-space models with full-range excitation signals to the dynamic system in the absence of any feedback control. The results were not nearly as good when using control inputs from baseline control² of zone temperature, particularly for longer prediction horizons. Additional work is necessary to assess the utility of the proposed modeling approach within MPC implementations compared to alternative modeling approaches that include internal gains and solar radiation as inputs, particularly for longer-term prediction horizons needed to account for building thermal mass effects. Future work will include an investigation of the modeling approaches and accuracy for Building 101 at the Philadelphia Navy Yard in 2013 using real-time measurements.

2.5.5 References

1. ASHRAE. 2009. ASHRAE Handbook-Fundamentals. Atlanta: American Society of Heating Refrigeration and Air Conditioning Engineers, Inc., pp. 19.1.
2. Åström, K. J., Wittenmark, B. 1997. Computer-Controlled Systems: Theory and Design. 3rd ed. Prentice Hall. Upper Saddle River, NJ. pp. 194.
3. Bacher, P., & Madsen, H. 2011. Identifying suitable models for the heat dynamics of buildings. *Energy and Buildings*, 43(7): 1511-1522.
4. Braun, J. E. 2003. Load control using building thermal mass. *Journal of Solar Energy Engineering*, 125, 292.
5. DOE. 2010. Buildings Energy Data Book. Available: <http://buildingsdatabook.eren.doe.gov/>.
6. EEB HUB. 2012. Available: <http://www.eebhub.org/>.
7. Kim, D., Braun, J. E., 2012, Model-based predictive control for buildings with decoupling and reduced-order modeling. 2nd International High Performance Buildings Conference at Purdue, July 16 – 19, 2012, West Lafayette, IN.
8. Klein, S. A. 1976, TRNSYS: A transient simulation program. Eng. Experiment Station, 440 pages.
9. Li, P., Baric, M., Narayanan, S., and Yuan, S. 2012. A simulation-based study of model predictive control in a medium-sized commercial building. 2nd International High Performance Buildings Conference at Purdue, July 16 – 19, 2012, West Lafayette, IN.
10. Ljung, L., Singh, R. Version 8 of the Matlab System Identification Toolbox. *System Identification*. 16(1): 1826:1831, 2012.
11. Ma, J., Qin, J., Salsbury, T. and Xu, P. 2012. Demand reduction in building energy systems based on economic model predictive control. *Chemical Engineering Science*, 67(1): 92-100.
12. Oldewurtel, F., Parisio, A., Jones, C. N., Gyalistras, D., Gwerder, M., Stauch, V., Lehmann, B., Morari, M. 2012. Use of model predictive control and weather forecasts for energy efficient building climate control. *Energy and Buildings*, 45: 15-27.
13. Prívvara S., Cigler J., Váňa Z., Oldewurtel F., Sagerschnig C., Žáčková E. 2012a. Building modeling as a crucial part for building predictive control. *Energy and Buildings*, Available online 18 October 2012, ISSN 0378-7788, 10.1016/j.enbuild.2012.10.024.
14. Prívvara S., Váňa Z., Žáčková E., Cigler J. 2012b. Building modeling: Selection of the most appropriate model for predictive control. *Energy and Buildings*, 55: 341-350.
15. Qin, S. J., Badgwell, T. A. 2003. A survey of industrial model predictive control technology. *Control Engineering Practice*, 11(7): 733-764.

16. Sun, J., Reddy, A. 2005. Optimal control of building HVAC&R systems using complete simulation-based sequential quadratic programming (CSB-SQP). *Building and environment*, 40(5): 657-669.
17. TESS Library Documentation. 2004. TESS Component Libraries v2.0 for TRNSYS v16.x and TRNSYS Simulation Studio, Thermal Energy System Specialists.
18. Wang, S., Ma, Z. 2007. Supervisory and optimal control of building HVAC systems: a review. *HVAC&R Research*, 14(1): 3-32.
19. Weather Analytics. 2012. Available: <http://weatheranalytics.com/>.
20. Zavala, V. M. 2011. Real-time optimization strategies for building systems. preprint ANL/MCS-P1911-0611.

3. Optimal Supervisory Control

3.1 Introduction

In a general sense, optimal supervisory control involves minimization of a cost function (e.g., energy cost) with respect to control setpoints (e.g., chilled water and air supply temperatures) and subject to constraints (e.g., comfort and equipment capacities). More specifically, model predictive control (MPC) involves minimization of an integrated cost (e.g., daily) and employs building and equipment models as key elements in enabling adaptive and predictive control in response to time varying inputs. Generating models, constraints, and appropriate cost functions for a new application can be time consuming and expensive and has been a limiting factor for widespread application of optimal control. The primary goals are to develop and demonstrate a process, tools and algorithms that can significantly reduce the development and commissioning time/cost to implement optimal supervisory control for retrofits in buildings.

3.2 Building 101 Simulation Based MPC Study

In this section we present the details of the control design, implementation and validation in simulation environment for Building 101 in Philadelphia Navy Yard. The intent of this work is to facilitate control algorithm development, implementation and refinement such that we can evaluate the energy management performance associated with the control implementation with respect to the present baseline control in the building. A secondary goal of this work is to implement the supervisory control algorithms, with energy efficiency objectives, that can be deployed in real building control architecture with short commissioning time and seamless integration with the building management system.

The Building 101 model used for this study is implemented in TRNSYS (Klein, 1976) simulation environment and has been developed within the EEB Hub project.

The control strategy selected for evaluation is model based predictive control. This strategy incorporates prediction aspects with the receding horizon principle. This means that at every step the control inputs are selected in an optimal way over a given prediction horizon to maximize a given performance criterion. After every step the initial states of the system used for the prediction are reinitialized based on present measurements from the system.

The MPC has the following advantages.

- it can naturally account for constraints in the control inputs – such constraints are typically present in HVAC equipments and systems
- it will naturally result in a better coordination between the system equipment such that the energy savings opportunity is maximized
- the prediction capability will enable implementation of control inputs that are able to take advantage of the storage capability in the building envelope (or in general any storage capability that is represented in the system models).

In order to evaluate the potential benefits associated with the implementation of selected control algorithm we first selected a tool chain for control implementation. Section 3.2.1 outlines the selection procedure that has been used to identify suitable tool chain that enables control implementation and future developments relative to a scalable control deployment.

3.2.1 Tool Chain Selection

Our objective was to increase the flexibility of the control development tool chain used in BP1 by integrating a modeling and computation tool in the MPC-based design and testing framework that will provide reduction of design-to-commissioning time.

The specifications requirements for the desired tool are:

- include automatic differentiation tools to support overhead computation requirements;
- support interfaces with sophisticated state-of-the-art numerical solvers to provide computation time scalability for larger optimization problems associated with increased complexity of building and HVAC model dynamics;
- has been extensively tested in academic research and industrial settings.

Refined selection criteria are as follows

- Include tools that provide optimization capability (i.e. optimization solvers) suitable for applications in the area of buildings and HVAC systems
- Rapid prototyping with minimal coding efforts – automatic differentiation tools available
- Ease of integration with
 - o Building management system (BMS) through HUB software services platform
 - o Simulation environment for energy performance evaluation (i.e., TRNSYS)
- Flexibility to easily change
 - o The optimization problem formulation
 - o Dynamical models that characterize the building and HVAC dynamics
- Reliable, supported and tested in industrial applications
- Cost

The following table outlines the tool chain options that have been considered for selection.

Table 3.2.1: Tool chain options for optimization based control development

	Option 1	Option 2	Option 3
Solver	IPOPT	IPOPT	TOMLAB solvers
Automatic differentiation tool for gradient, jacobian, hessian computation	AMPL	ADOL-C	TOMLAB
Optimization problem formulation language	High level mathematical language	Problem formulation code in C++	High level mathematical language
Problem scale	Well tested on large scale problems	Performance on large scale problems is not verified	Well tested on large scale problems
Integration with optimization solvers	Integrated with multiple solvers	Requires C++ code to interface with solvers	User interface and Integrated solvers
Flexibility to fast prototyping and testing of design control performance	Allows fast prototyping and testing	Code has to be developed if changes are made in the problem specification	Allows fast prototyping and testing

		– slow prototyping and testing	
Integration	Default data transfer through files results in communication overhead	Tight integration results in fast communication	Available functionality to support information transfer
Coding language	AMPL (mathematical description)	C++	
Cost	4000\$/license	Free, open source	~12000\$/license

Based on the comparative study of the available tools, assessment presented in Table 3.2.1, we selected for integration A Modeling Language for Mathematical Programming (AMPL (Fourer et al., 1987)) to be used as an optimization platform.

Figure 3.2.1 describes the functional structure of the optimization tool. This structure allows for a fast and efficient computation of optimization solution, due to integration with automatic differentiation tools (to compute online the value of the Gradient (G), Hessian (H) and Jacobian (J) matrices needed by the optimization solver) and solvers (e.g. IPOPT), and offers the flexibility to extensions , fast implementations and evaluations of performance for different problem formulations.

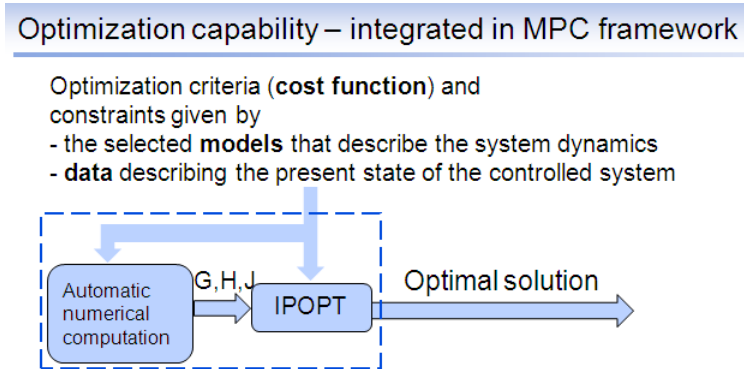


Figure 3.2.1 Structure of selected optimization tool to be included in MPC framework

3.2.2 Description of Selected Tool Chain

Figure 3.2.2 illustrates the software architecture for optimization-based building control which integrates

- TRNSYS as a virtual testbed,
- MATLAB[®] (MATLAB, 2012) as a data acquisition and organization interface and
- AMPL[®] for solving optimization based control problem.

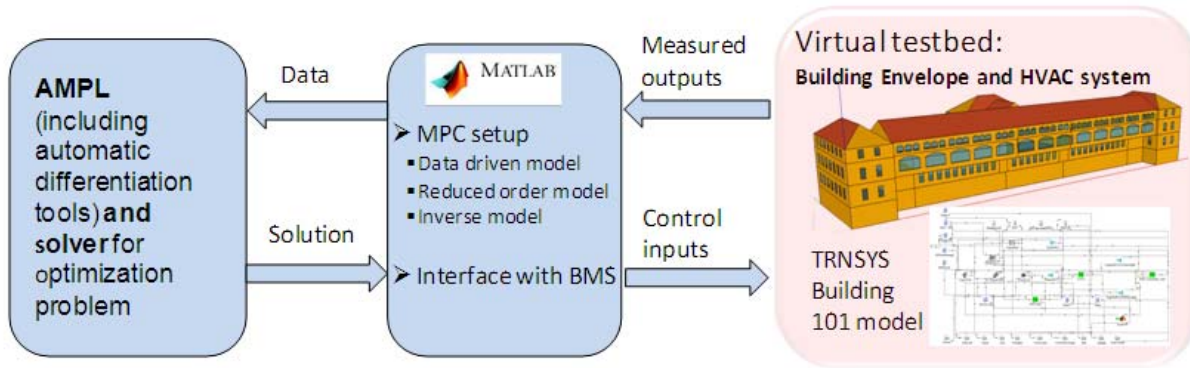


Figure 3.2.2 Integrated tool chain for optimization based building control algorithm development, testing and performance evaluation in simulation

Developed at Bell Laboratories, AMPL is a comprehensive and powerful algebraic modeling language for linear and nonlinear optimization problems, in discrete or continuous variables. AMPL's flexibility and convenience render it ideal for rapid prototyping and model development, while its speed and control options make it an especially efficient choice for repeated production runs.

The integration of AMPL in the control development framework leads to:

- increased development flexibility to reduce design-to-commissioning time and
- computation time scalability to larger optimization problems associated with increased complexity of building and HVAC model dynamics.

The closed loop designed for optimization based energy management for building and HVAC equipment with can be described by the following operation steps that are executed *at every sampling step*

- Read data from the installed building and equipment sensors and store values in the BMS
- Use available services platform (middleware) to
 - o communicate with the BMS,
 - o retrieve data and
 - o organize data according to the requirements specified by the input interface defined by the optimization platform (AMPL and solver)
- Call optimization solver to solve the specified optimization problem
- Use available services platform to
 - o post-process the optimization solution and
 - o communicate the supervisory control setpoints back to the BMS
- BMS implements the received setpoints for supervisory control and the computed actuation for the HVAC actuators.

When integrating this functionality with a building simulation environment the role of the building dynamics, sensors and actuators and local equipment control is taken by a building simulation. Specifically, in the developments outlined in the following sections of the EEB Hub project report we used TRNSYS to simulate the building envelope and HVAC equipment dynamics, sensors, actuators and local controllers, i.e. we used the TRNSYS simulation of the building as a *virtual testbed*.

In a simulation environment the role of the services platform is taken by MATLAB which serves as an interface between the TRNSYS virtual testbed and the AMPL tool that implements the optimization based control algorithm.

3.2.3 Development of Control Algorithm

In this section we outline the development, implementation and the elements of the optimization-based control algorithm.

3.2.3.1 Considerations on HVAC System Architecture and Selection of Decision Variables

The HVAC architecture in Building 101 is AHU + VAV configuration. The control variables are as follows.

- VAV damper position, DP – we assume a one to one mapping between damper position and mass air flow at the VAV outlet
- VAV valve position, RHV – we assume a one to one mapping between valve position and water flow through the available VAV reheat coils. This ideal assumption can be relaxed in practice by selecting VAV discharge air setpoint, as that can be controlled by the valve actuator using a local equipment controller.
- AHU discharge air temperature setpoint, T_{DA}^{SP} .

Figure 3.2.3 presents a schematic representation of the integration of building and HVAC system models with the MPC algorithm. Specifically, the MPC algorithm receives “measurements” of the zone temperatures and outside air temperature (uncontrolled disturbance) and uses optimization tools to calculate the control inputs based on an internal representation of the system dynamics, i.e. building and HVAC equipment models.

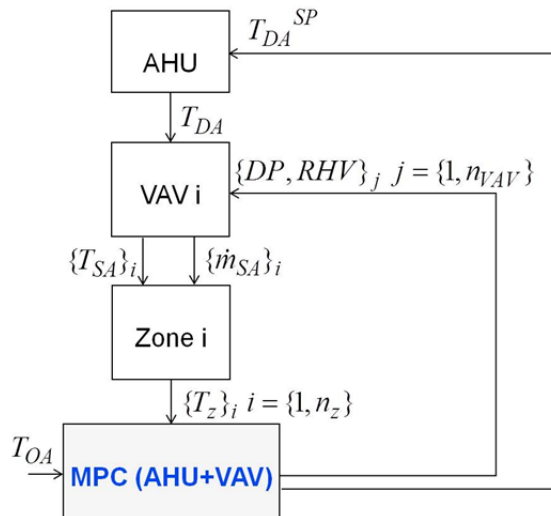


Figure 3.2.3 Control integration with building system

3.2.3.2 Cost Function Selection and Formulation of Constraints

The control objective considered herein is to minimize energy consumption used for air conditioning such that the occupant’s thermal comfort is satisfied. These are conflicting objectives which would place the optimal solution in a saddle point.

The control variables are calculated at every sample time step such that, over the prediction horizon, the following power cost function is minimized.

$$P_{total} = 3P_{fan}(\dot{m}_{sa}) + 3\frac{P_{cooling}(\dot{m}_{DA}, T_{DA})}{COP_{DX}} + \frac{1}{\eta_{boiler}} \sum_{i=1}^{n_{VAV}} P_{reheating}(\dot{m}_{sai}, T_{sai}) \quad (3.2.1)$$

The first term in Eq. 3.2.1 represents the power consumption of the AHU fan, the second term represents the power consumption associated with cooling, while the third term represents the power consumption associated with reheat at the VAV box level. The coefficients “3” for electricity consumption and “1” for steam consumption are determined based on the general assumption for converting primary energy source to electricity and steam, respectively. Using the selected tool chain, the optimization problem can be easily modified to include the demand charge, different pricing for the various energy sources, or real-time utility price. An example AMPL code for cost function and constraints implementation is provided in the Appendix 3.2 (Figure A.3.2.1).

The requirement associated with occupancy comfort most often is expressed in the form of hard constraints on zone temperatures. For example one would say that zone temperature must be larger than lower bound and smaller than the upper bound in the comfort zone. This way of posing constraints should not be transferred directly to the specification of the optimization problem as it often leads to the optimization solver being unable to find feasible solution. In order to avoid such situations, and pose the optimization problem such that it will always allow for feasible solution, we integrate the zone temperature constraints requirements (and the limited available control authority) in the cost function. To achieve this we define:

- A slack variable that describes the distance between the zone temperature comfort band and the measured/predicted value of the zone temperature
- A slack variable that describes the variation between two consecutive values of control inputs

We integrate the slack variables in the cost function that defines the optimization objective. In order to ensure that maintaining comfort will have a large priority over the energy consumption terms we use a large weight on the comfort term. This will lead to enforcing that occupancy comfort will be met and the optimization solution will have a high tolerance to energy consumed to maintain comfort. Slack variables defined on zone temperature will become equal to zero when (predicted) zone temperature is within the prescribed comfort bounds.

3.2.3.3 Selection and Calibration of Models for Optimization Based Supervisory Control Decision

The dynamics of the system, namely building thermal dynamics and HVAC equipment dynamics, are included in the optimization problem as constraints. This means that while predicting and optimizing the system behavior, the system dynamics will have to be satisfied. In order to determine these constraints one needs to spend an effort to find suitable models that can capture and represent the system dynamics as observed in the controlled plant (building and HVAC). In this section we present an outline on the required models and modeling approach that we selected for MPC based controller design.

For MPC implementation two models are required

- Zone thermal model

- HVAC equipment models

Engineering practice provides evidence that the zone thermal model is characterized by large time constants relative to those that describe the HVAC equipment. Given the effective time scale separation we decided to use dynamical models for representing the zone thermal dynamics and use quasi-steady state performance maps to capture the behavior of the HVAC equipment. We outline next the procedures that we used to select and calibrate the building and HVAC equipment models.

In this simulation based study, the zone thermal model has been obtained using system identification procedure on data acquired from the TRNSYS virtual testbed. When transitioned to practice, this procedure will only change at the level of data acquisition. To support computational efficiency but not sacrifice prediction accuracy we went through a procedure of down selection of models for zone thermal dynamics such that model complexity is reduced but the prediction accuracy is still maintained.

The standard procedure for estimation of zone model parameters from data is outlined in Figure 3.2.4.

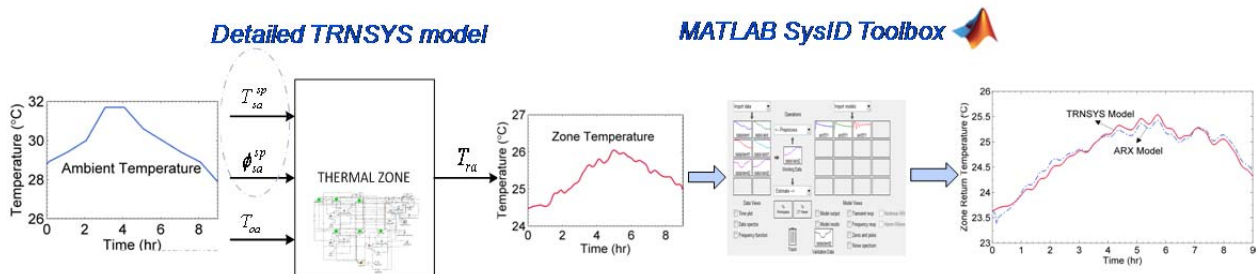


Figure 3.2.4 Procedure for estimation of zone thermal model from data measurements

The control inputs for the zone thermal model are the two decision variables,

- supply air flow setpoint of each VAV and
- reheat valve position of each VAV

as well as the main disturbance (typically measured in the building) that affects the zone thermal dynamics

- the temperature of outside ambient air.

If measurements of solar and internal gains are available they could be included too as inputs of the zone thermal model. In order to evaluate the potential for energy savings in case that the model based predictive control algorithm is implemented on a simple, reduced cost, building control retrofit we currently did not assume available information related to the building internal load or solar load. The online estimate of lumped internal load for predictive-based controller design is an ongoing effort through the BP3.

For the HVAC equipment we considered static curve models that can capture the performance of the equipment during steady state operation, i.e. around a given operating point described by the specified setpoints from the supervisory controller. The following models have been included in the MPC problem formulation. Please refer to Section 2.5 for more details.

- DX coil COP model – defines the coefficient of performance (COP) of the DX coil equipment given the percentage thermal load that the coil must satisfy³;
- VAV reheat coil model – defines the value of the supply air temperature to the zone given the supply air temperature received from AHU and the mass air flow.
- Fan performance curve for energy consumption given mass air flow.

We note that in order to achieve a control design that can take advantage of the storage capacity available in the building envelope and that can minimize the energy consumption used by the HVAC equipments, the system models must capture only the dynamics that are relevant to equipment coordination and thermal storage in the building envelope.

3.2.4 Simulation Study

In this subsection we present the control results that have been obtained and discuss the performance assessment of the control implementation.

3.2.4.1 Simulation Scenario

Simulation studies were conducted to evaluate the effectiveness of the proposed centralized MPC controller. The high-fidelity TRNSYS model was adopted as our virtual testbed. A summer period was considered for the case study. A TRNSYS simulation was performed over five weekdays in the first week of August, 2012. Similar to the study of the data-driven modeling approach, the virtual weather data from 2011 (Weather Analytics, 2012) was used in the simulation.

Figure 3.2.5 shows the ambient temperature and relative humidity profiles during the simulation test week. The internal loads from each zone are assumed to come from the occupancy, lighting and plug, etc, as shown in Figure 3.2.6. Note that the internal load profiles (occupancy, lighting, and plug) are assumed to be the same for each day during the test week (weekdays).

³ Note that the COP of our current DX coil model is assumed to be a function of the thermal load only, which may not be sufficient enough to represent the actual system operation. Future study will adopt a more realistic gray-box model developed by the Purdue team and validated with measurement data.

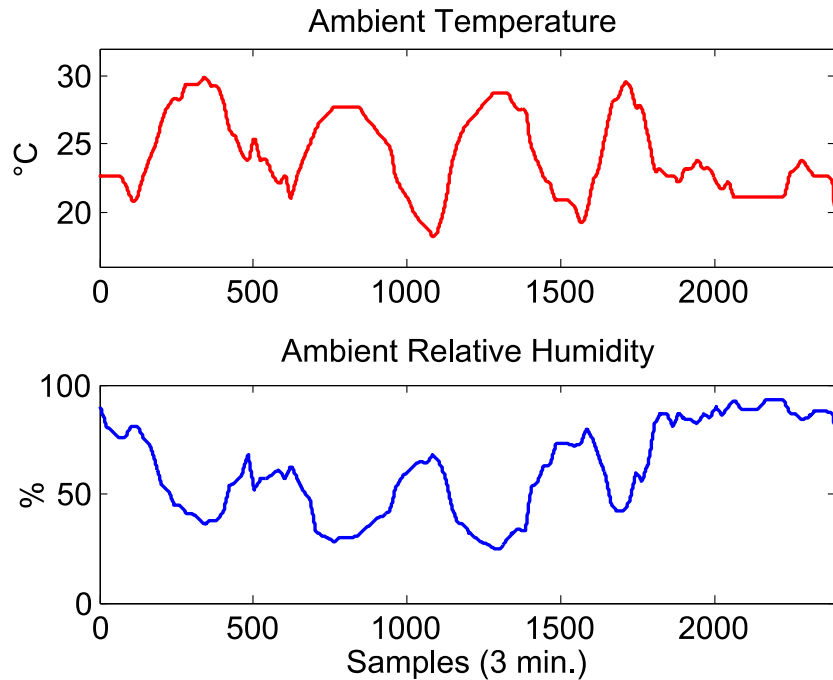


Figure 3.2.5 Ambient temperature and relative humidity of the test week

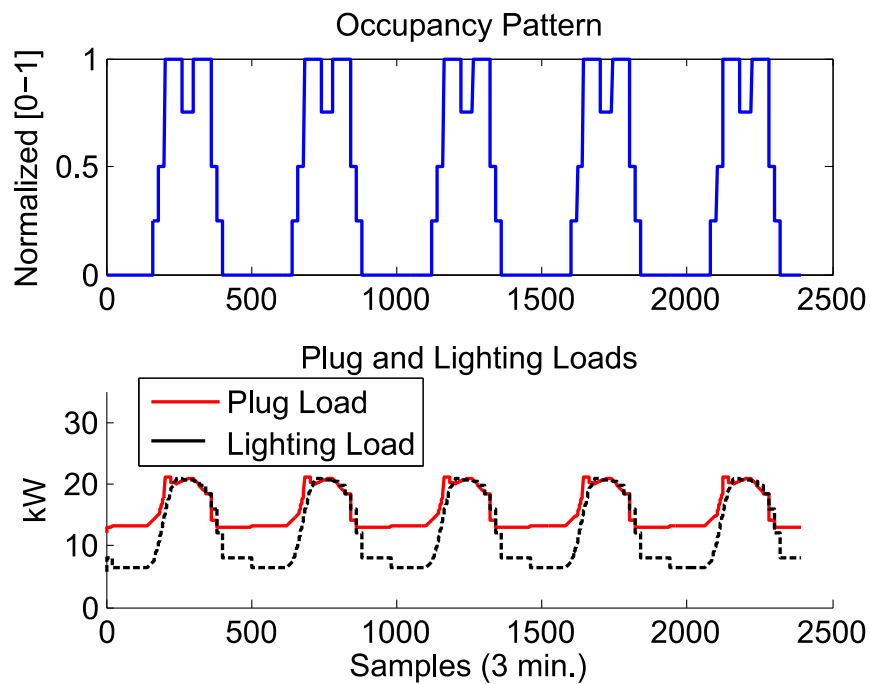


Figure 3.2.6 Occupancy pattern (normalized), lighting, and plug loads

3.2.4.2 Simulation Results

Figure 3.2.7 presents the temperature profile of each zone controlled by the baseline and the MPC, respectively. As can be observed, the centralized MPC controller is trying to regulate the temperature in each zone tightly around the upper bound of the thermal comfort region (dashed lines in Figure Figure 3.2.7) and meanwhile exploiting the trade-offs of DX coil discharge air

temperature (DAT) setpoint, VAV flow rate setpoint, and VAV reheat coil valve positions to optimize the combined energy-and-comfort based costs.

As described in Section 2.5, the baseline controller will either adjust VAV reheat valve position with minimum supply air flow setpoint when the zone temperature is below a prescribed heating setpoint or adjust supply air flow setpoint with reheat valve closed when the zone temperature is above a prescribed cooling setpoint. The supply air flow setpoint will be kept as minimum with reheat valve closed if the zone temperature could be maintained between the heating and cooling setpoints (i.e., no feedback control).

By comparison, as shown in Figure 3.2.8, the MPC controller is taking advantage of the integrated subsystem information and coordinating the control setpoint of VAV air flow setpoint, reheat coil valve position, and DX DAT setpoint to regulate the zone temperature tightly around the upper bound of the comfort interval, and meanwhile exploiting subsystem level trade-offs to optimal the overall HVAC system performance in terms of energy savings.

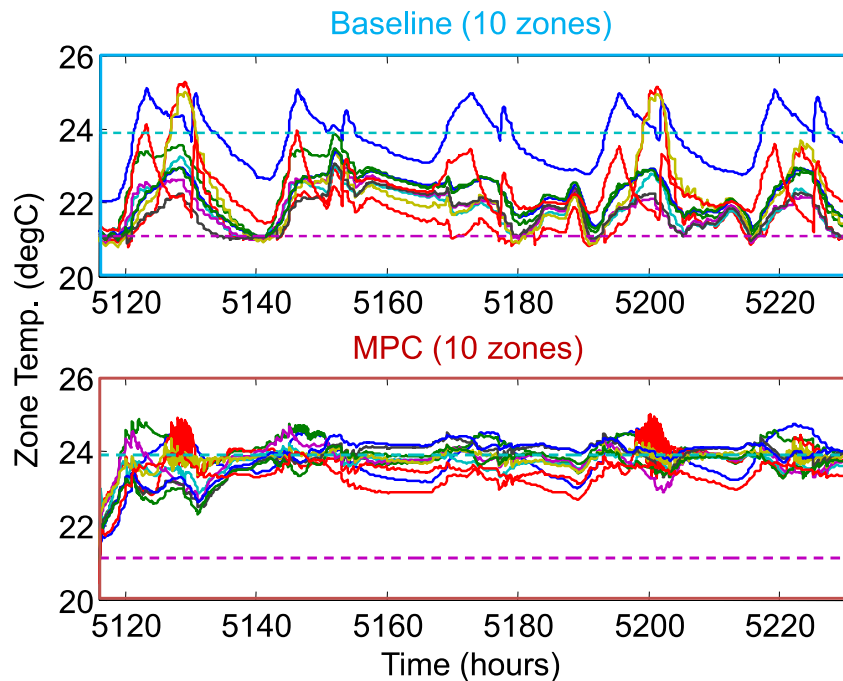


Figure 3.2.7 Comparisons of zone temperature profiles between baseline and MPC

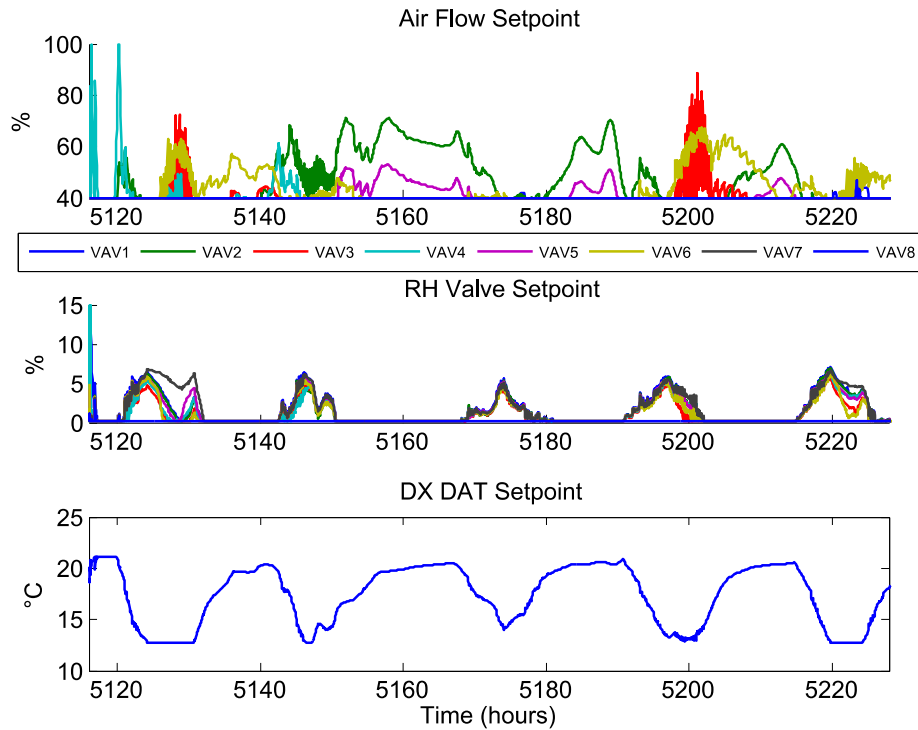


Figure 3.2.8 Controlled variables from MPC

Figure 3.2.9 shows comparisons of energy consumption breakdowns between the baseline control and the MPC. The system with the proposed MPC strategy demonstrated ~17.5% energy savings for the HVAC system. It can be observed that most of the energy savings come from reduced electrical energy savings for the compressors within the DX unit.

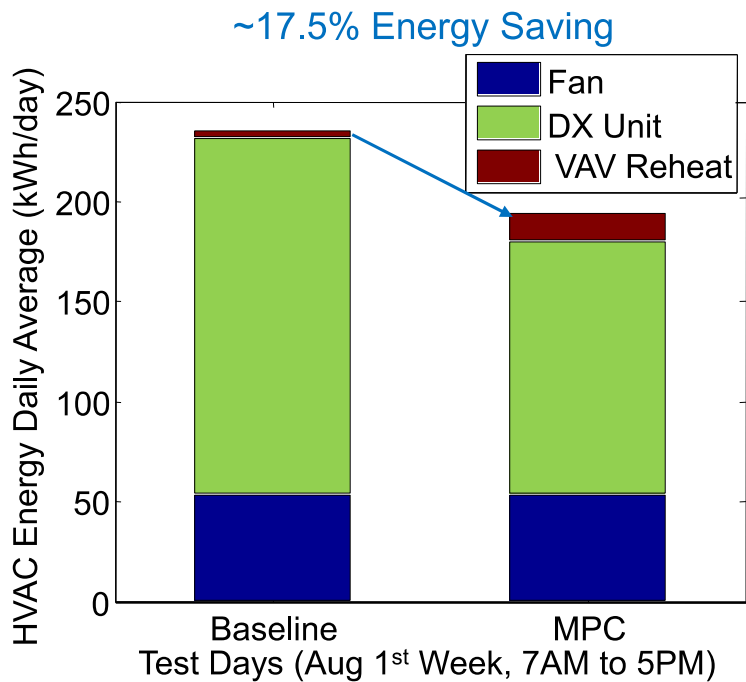


Figure 3.2.9 Comparisons of energy consumption breakdown between baseline and MPC

Figure 3.2.10 illustrates the main reasons for energy savings brought by the MPC. Compared to the baseline control, the discharge air temperature (DAT) setpoint is higher during the whole test week, which brought significant savings for the direct expansion (DX) unit power, as shown in the lower subplot of Figure 3.2.10.

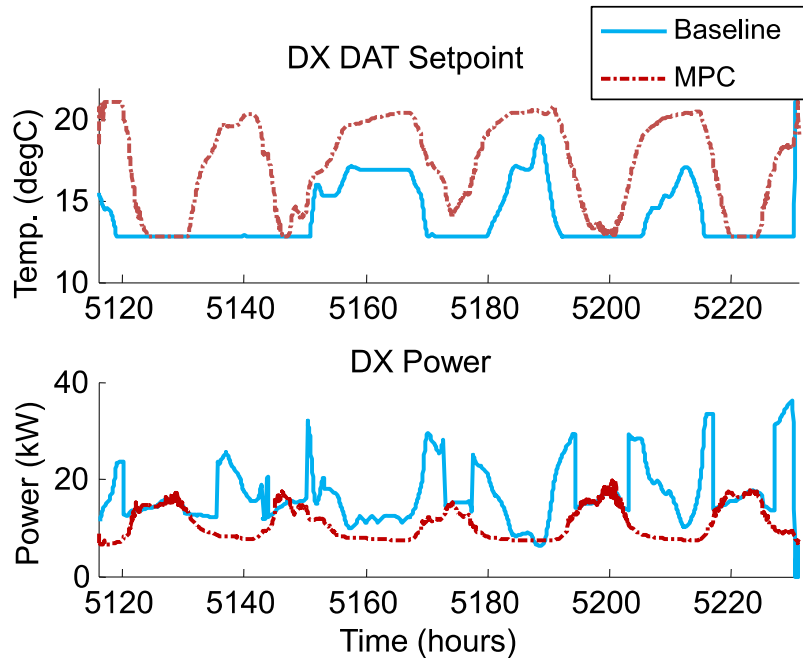


Figure 3.2.10 Comparisons of DAT setpoints and DX unit power between baseline and MPC

3.2.5 Conclusions and future work

In this case study, we have demonstrated an effective and efficient tool chain for optimization-based control development and implementation, as well as the effectiveness of centralized MPC control strategy through its application to a multi-zone building system with a central HVAC and multiple VAV boxes (w. reheat coils). In particular, we have evaluated the effectiveness of our proposed low-order state-space model, which demonstrated superior performance in the closed-loop control scenarios with a relative short prediction horizon of one hour. With our high-fidelity virtual testbed, we demonstrated a promising overall HVAC energy savings of $\sim 17.5\%$ and observed that most energy savings come from the DX coil unit. This study can be further extended and a few suggestions for future study are summarized as follows:

- Real-building demonstration of Building 101 in 2013 Q1.
 - The BMS upgrade of Building 101 will be completed by January 2013. After this, we will evaluate the effectiveness of the proposed MPC controller for real-building scenarios.
- MPC performance with uncertain internal load profiles.
 - Currently, the internal load (occupancy, lighting, plug, etc.) profiles are assumed to be exactly the same for each day. However, such assumption is not valid for real-building case study. We will study the effect of such uncertainties and possibly their prorogations in the prediction range of interest and evaluate their impact to the MPC controller performance.

- MPC Performance Analysis using B101 ROM – to evaluate the benefits of longer prediction horizons.
 - In BP2 UTRC implemented MPC for the linear B101 - ROM developed by the team from Purdue. The implementation has been done in MATLAB[®]/Simulink[®] environment in order to evaluate the performance potential of the MPC strategy coupled with the reduced order model of the building envelope dynamics. Based on the results the UTRC team provided the following recommendations.
 - 1) ROM must be obtained after reducing the fast dynamics of the building to steady state behavior; this will allow for a MPC formulation with lower sampling rates.
 - Maintaining the fast dynamics in the ROM leads to the requirement of fast sampling rates and large number of steps in the MPC prediction horizon and longer time for obtaining the optimization solution.
 - Note: for control implementation it is required that solution computation time must be smaller than the sampling rate.
 - 2) Lower sampling rates are needed in order to
 - take advantage of the building envelope as a storage and
 - allow for MPC computation time in case of longer prediction horizons (if possible > day).

3.2.6 References

1. Klein, S. A. 1976. TRNSYS: A transient simulation program. Eng. Experiment Station, 440 pages.
2. Fourer, R., Gay, D. M., Kernighan, B. W. 1987. AMPL: A mathematical programming language. AT&T Bell Laboratories.
3. MATLAB. 2012. Available: <http://www.mathworks.com/products/matlab/>.
4. Weather Analytics. 2012. Available: <http://weatheranalytics.com/>.

3.3 Purdue Living Lab Simulation Based MPC Study

The computational cost of applying model-based predictive control (MPC) grows significantly with increasing complexity of the system causing issues in the real-time implementation and feasibility of MPC. The objective of this study was to develop an efficient approach for MPC in order to enable practical implementation for multi-zone buildings where there are significant degrees of freedom for system supervisory control variables, including both plant and multi-zone air temperatures set points. A method that decouples the plant and building analyses was investigated since the plant dynamics occur on a relatively small time scale compared to the dynamics of the building. Also, a state-space transformation-based technique was applied to determine a reduced-order model that is more amenable to control optimization. Results are presented for some case studies using a simulation test bed.

3.3.1. Introduction

For the last two decades there has been a growing interest in applying Model-based Predictive Control (MPC) for reducing electrical energy usage and costs for operation in buildings. For instance, experimental tests showed that up to 10% of the electrical energy could be saved for a relatively lightweight building through dynamic control when utilizing thermal storage inherent within the building mass (F.B. Morris et al, 1994).

Many approaches have been suggested for taking thermal comfort into account for the MPC problem. Examples of comfort level metrics include zone air temperature, mean radiant temperature and relative humidity. Comfort metrics can be either introduced explicitly into the objective function resulting in a multi-objective optimization problem or implicitly in the state/output constraints. One simple approach is to introduce linear or quadratic penalty functions into the objective function so that the costs increase when the comfort conditions (e.g., temperature) deviate from given acceptable comfort ranges. Sometimes the acceptable thermal comfort levels are treated as constraints. Other comfort level metrics that incorporate the important indoor environmental parameters are the predicted mean vote (PMV) and percent people dissatisfied (PPD). In this study, Fanger's PPD model is used to express the complex nature of thermal discomfort. This model can be included in the objective function or implicitly as a constraint.

An important issue in terms of applying MPC is that the computational cost grows significantly with increasing complexity of the system. By neglecting plant dynamics, a method which decouples the plant and building analyses can be applied to reduce the computational cost. This approach was introduced by J.E. Braun (1990) and was investigated by M. Kararti et al. (1995) for the evaluation of optimal control for ice storage systems. It can also be found in several other works, including L. Lu et al. (2005), K.F. Fong et al. (2006), and A. Kusiak et al. (2010). In the current paper, plant and building decoupling is utilized to enable MPC for buildings.

To further tackle the computational cost issue, we propose to use model-order reduction as described by D. Kim and J.E. Braun (2012) to characterize the building dynamics. Most of the previous strategies to handle complex building thermal networks for optimal control are based on system identification methods. Data-driven black box models, which rely on experimental data or simulation results from a physical model, can lead to unrealistic and non-interpretable predictions (J. Casillas et al. 2003). Furthermore, one of the most important and difficult problems in system identification is to choose the "best" model among a set of candidate models,

which necessarily requires a “model validation” process (L. Ljung, 1999). Typically up to 80% of the time for determining a model is spent on this step. The approach presented in this paper for generating a reduced-order building model is based on a physical description and may lead to a more reliable model that is more easily obtained.

3.3.2. *Simulation Methods*

The main assumptions adopted in this study are summarized as follows.

- In the cost function, we only consider the electrical power consumption from fans, pumps, and chillers, but not from other sources such as lighting and electric heaters.
- Forecasts of weather and internal loads are assumed to be perfect.
- Constant convective heat transfer coefficients at the interior surfaces are assumed.
- Relative humidity and CO₂ level of the zone are not considered.
- Local controllers are ideal such that all feedback controllers follow set-points exactly unless limited by capacity.
- The plant operation is quasi-static and contains no dynamics. For this case study, the plant-side energy storage effects are assumed to be negligible compared to the building thermal mass effects. A careful investigation of the accuracy and validity of this assumption will be considered in the future.
- Only time-of-use energy charges are considered with no demand charges.

Objective Function of Model Predictive Control

For this study, the cost of electricity is assumed to vary with time but in the absence of any demand charges. The utility cost is given by

$$Utility = \sum_{k=0}^{N-1} R_k \times P_k \times \Delta t$$

where $R[k]$ is the electric rate [\$/kWh] for any time step k and $P[k]$ is the power consumption for the HVAC system at that time step.

In this study, Fanger’s PPD model (1967, 1980) is used to express the complex nature of thermal discomfort. PPD is the percent people dissatisfied and Fanger’s model uses predicted mean vote (PMV) as the input to this model. The PMV model that uses six input variables: zone air temperature, relative humidity, relative air velocity, mean radiant temperature, activity level, and insulation value of the clothing. PMV values range from -3 (cold), to +3 (hot) with zero as the desirable value. The PMV-PPD model is widely used and accepted for design and field assessment of comfort conditions.

The objective function used in this study is expressed as

$$J = \sum_{k=0}^{N-1} R_k P_k \Delta t$$

with the constraints

$$\begin{cases} PPD_k \leq 10, & k \in OfficeHour \\ PPD_k < 30, & else \end{cases} \quad (3.3.1)$$

The value 10 comes from the ASHRAE Fundamentals and corresponds to a PMV range of ± 0.5 . The value of 30 is chosen to correspond to “slightly warm” or “slightly cool” according to the PMV index.

The evaluation of PPD requires solving nonlinear algebraic equations, which could be a burden for the MPC problem. Therefore, in an effort to reduce computational cost, a regression method is adopted. The independent variables are zone air temperature and mean radiant temperature, which together determine the PPD value for the assumptions previously specified. The regression model is as follows

$$PPD = \beta_0 + \beta_1 T_z + \beta_2 T_{MRT} + \beta_3 T_z^2 + \beta_4 T_{MRT}^2 + \beta_5 T_z \times T_{MRT} + \beta_6 T_z^3 + \beta_7 T_{MRT}^3 + \beta_8 T_z^2 \times T_{MRT} + \beta_9 T_z \times T_{MRT}^2 \quad (3.3.2)$$

Figure 3.3.1 shows that the regression model tracks the Fanger's predictions of PPD over the input range of interest. The scattered points represent the Fanger's values and the continuous color map indicates the regression-based model.

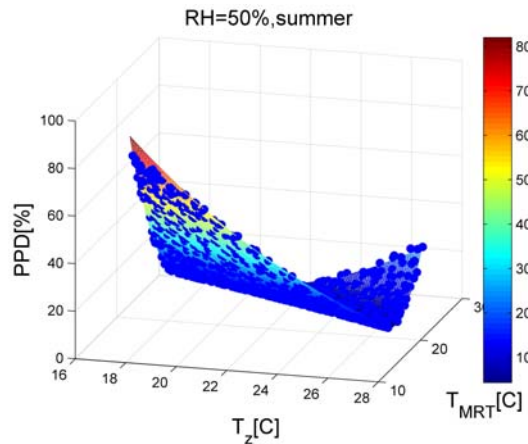


Figure 3.3.1 PPD comparison between regression and Fanger's model results (50% RH, less than 0.2 m/s air velocity, 0.5clo and unit Met)

Plant Decoupling Approach

A schematic of the simple cooling plant considered in this case study is shown in Figure 3.3.2. It contains an outdoor air (OA) damper, cooling coil, chiller, cooling tower and pumps. The model assumes that the components in the system operate at quasi-steady state. In this study, variable-speed cooling tower fans, pumps and supply air fans were considered. Heat transfer through air ducts and pipes are neglected and zone loads are met by control of the supply air to the space (termed mechanical ventilation). The plant equipment models and performance characteristics are based on representations from EnergyPlus and are described in a later section.

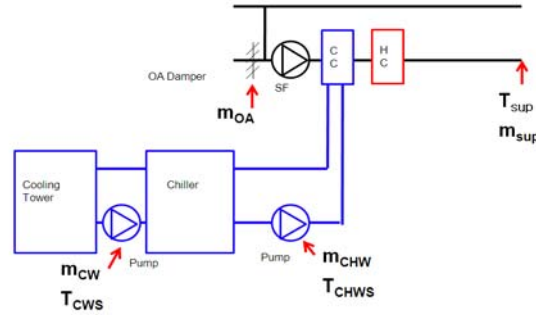


Figure 3.3.2 Schematic diagram of the considered cooling plant

The MPC controller provides set points to the local controller of the HVAC system based on zone air temperature, mean radiant temperature and predictions of weather data and internal sources. The number of setpoints that need to be determined by the optimizer of the MPC has a large effect on the computational requirements and feasibility of implementation. The concept employed here to solve this problem is to decouple the building and plant system. If the dynamic behavior of the plant is neglected, then the optimal set of cooling plant setpoints is not affected by any past information but only depends on current conditions. Therefore, an optimal plant map can be generated as a function of zone air temperature (T_{zone}), outdoor air temperature (T_{OA}), ambient relative humidity (RH), and mechanical cooling at the zone (Q_{vent}) and used as a lookup table for the MPC algorithm to determine the tracking of zone cooling that takes optimal use of the building dynamics. This is the strategy that is proposed and employed within this case study. The plant optimization problem involves finding the optimal set-points that give minimum power consumption for a given heat extraction rate, T_{zone} , T_{OA} and RH at any given time or $\min Power(m_{OA}, m_{sup}, m_{CW}, T_{CHWS}, T_{CWS}, T_{OA}, RH, T_{zone}, Q_{vent})$

with respect to

$$\begin{bmatrix} m_{OA} \\ m_{sup} \\ m_{CHW} \\ m_{CW} \\ T_{CHWS} \\ T_{CWS} \end{bmatrix} \text{ s.t. } \left\{ \begin{array}{l} A \leq m_{OA} \leq B \\ C \leq m_{sup} \leq D \\ E \leq m_{CHW} \leq F \\ G \leq m_{CW} \leq H \\ L \leq T_{CHWS} \leq M \\ \max(T_{CHWS}, T_{wb}) \leq T_{CWS} \leq N \end{array} \right. \quad (3.3.3)$$

The optimal plant solution then can be mapped in terms of the input variables according to

$$P^* = P_{\min}(T_{OA}, RH, T_{zone}, Q_{vent}) \quad (3.3.4)$$

The bounds of A to N in equation 3.3.3 are defined by the HVAC system. The MPC wants to find a trajectory for Q_{vent} rather than a single point value while the optimal map provides optimal plant set points at any time given conditions for T_{zone} , T_{OA} , RH and Q_{vent} . There are several difficulties in obtaining an optimal look-up table. The objective function for HVAC plants may be non-convex and contains several nonlinear algebraic equations; it is difficult to generate

proper constraints; and there may be several discrete modes of operation that cause discontinuities. In particular, the design variables must be in a feasible region in the optimization process. For example, the supply air temperature must be greater than the chilled water supply temperature by an amount dictated by the capacity of the coil and operating conditions. These types of constraints are difficult to handle without validated models for each of the components. A global optimization algorithm with an interior barrier method was employed in this study for the plant optimization. The validity of the results was tested by considering limiting cases with known solutions, such as when the only plant power is associated with the chiller.

Cooling Plant Model

The variable-speed cooling tower fans and pumps are modeled with a cubic relationship between power consumption and flow rate (pump and fan affinity law). For the VAV fan used to supply air flow to the zone, the fan power is modeled as outlined in ASHRAE 90.1.

$$P_{fan} = a_0 + a_1 PLR_{fan} + a_2 PLR_{fan}^2 + a_3 PLR_{fan}^3 \quad (3.3.5)$$

At this point in our study, latent energy removal effects are neglected for the cooling coil. Also, heat gains to air ducts and pipes are neglected. The effectiveness-NTU method is used for the cooling coil to determine the limiting heat transfer rate.

$$\epsilon = 1 - \exp\left[\frac{1}{C_r} NTU^{0.22} \{ \exp[-C_r NTU^{0.78}] - 1 \}\right] \quad (3.3.6)$$

where C_r is the ratio of the minimum to maximum capacity rate (F.P. Incropera and D.P. Dewitt 2001). Energy and mass balance equations are then used to determine temperatures, cooling coil load (Q_{CCL}) and chiller load (Q_{CHL}).

The empirical model employed in EnergyPlus is used to determine chiller cooling capacity, energy efficiency, and power consumption as a function of chilled water supply temperature, condenser water supply temperature, and part-load ratio (M. Hydeman and K.L. Gillespie 2002). The cooling tower model is also referred to EnergyPlus and represents a York cooling tower.

Reduced-Order Building Model

A reduced-order building envelope model was built based on the procedure described by D. Kim and J.Braun (2012) and summarized here. A finite-volume formulation is used to describe the heat conduction through walls. For any outside wall belonging to an individual zone, a heat balance equation is applied considering convective heat, solar radiation and long wavelength interactions. The radiosity method is utilized to express the net flux under the assumption that the walls are gray, diffuse and opaque. The long-wave interaction terms were linearized and fixed convective heat transfer coefficients were assumed to build up a linear time invariant state-space form for the building thermal network. A balanced truncation method is applied to the representation to generate a reduced-order model. An important feature of the state-space transformation method is that the reduced-order model preserves most of the properties of the original system such as dynamic response, observability/controllability and stability. The final form of the reduced-order building system is shown below.

$$\begin{aligned} \dot{x} &= Ax + B_w w + B_u u \\ y &= Cx \end{aligned} \quad (3.3.7)$$

The controllable input, u , includes the heat extraction/addition rate to the zone air and the possibility of having a heat source inside a building material. It could represent mechanical ventilation, an electric heater, chilled beams or radiant heating /cooling. For this case study, it is assumed that only mechanical ventilation is available as the controllable input. w represents several uncontrollable terms, including the heat flow due to solar radiation, long-wave interaction between sky/ground and exterior walls and uncontrollable internal heat gains due to occupants and so on. The output y is chosen to be the zone air and mean radiant temperatures that are inputs to the PPD model. Surface weighted average temperatures are used to approximate the mean radiant temperature.

MPC Controller Setup

The MPC problem for the case study considered here is expressed as

$$\begin{aligned}
 u, v = \arg \min \quad & \sum_{k=0}^{N-1} R_k P(y_k, w_k, u_k, v_k) \Delta t \\
 \text{s.t.} \quad & \begin{cases} x_{k+1} = Ax_k + B_w w_k + B_u u_k \\ y_k = Cx_k \\ PPD(y_k) \leq 10, k \in \text{OfficeHour} \\ PPD(y_k) < 30, \text{ else} \\ f(y_k, w_k, u_k, v_k) = 0 \\ g(v_k) \leq 0 \end{cases}
 \end{aligned} \tag{3.3.8}$$

where v represents all the set-points in the quasi-static HVAC plant for this study:

- flow rate of supply air and outdoor air
- flow rate and temperature of chilled water
- flow rate and temperature of condenser water

The arguments of the minimum are the vector input sequences of u and v , i.e.,

$$\{u[k|k], u[k+1|k], \dots, u[k+N_p+1|k]\}$$

and

$$\{v[k|k], v[k+1|k], \dots, v[k+N_p+1|k]\}$$

In words, the goal is to find the optimal trajectories that minimize the energy costs while keeping the thermal comfort level within specified bounds.

For each prediction time step, $k \in [0, N-1]$, PPD is calculated using the regression model. The power consumption of the plant is a function of the cooling load, room air temperature, and ambient conditions and is represented as $f(y_k, w_k, u_k, v_k) = 0$. To handle nonlinearities associated with the plant model, a Sequential Quadratic Programming (SQP) optimization algorithm is used to solve the optimal control problem.

3.3.3. Case Study Results

The zone considered in this case study is the Purdue Living Lab #1 that is part of the building shown Figure 3.3.3. Some parameters employed in the modeling include:

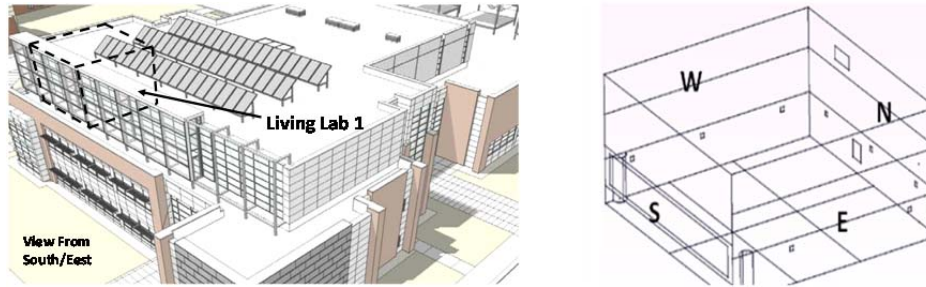


Figure 3.3.3 Purdue Living Laboratory schematic

- The size of the building: 32 ft for width and depth and 14.5 ft height. The south window area is 130 ft².
- The materials for wall construction consist of concrete, insulation board, stucco, gypsum board, and double glazed windows.
- The east, north walls and floor are adjacent to other rooms that are assumed to be at fixed zone air temperatures of 22 °C.
- TMY2 weather data in Indianapolis for the summer season (July/1 to July/31) is used.
- 17.77 W/m²-K and 3.05 W/m²-K are used for convective heat transfer coefficient at the outside and inside surfaces, respectively.
- 65 Watt per person, 230 Watt per computer and 20 Watt/m² are assigned for the internal gains during the office hours (7am ~ 6pm).
- 20 persons with 20 computers occupied the space during office hours.
- Electricity rates of 0.04 \$/kWh for office hours (7am ~ 6pm) and 0.02 \$/kWh for other times are employed.

The baseline state-space model was applied to the Living Laboratory zone and then model-order reduction was performed. The baseline model employed 201 states and the model order was reduced to 10 states with about a factor of four reduction in the computational requirements. Figure 3.3.4 shows a comparison of zone temperature variation with a PID controller in place for the baseline and reduced-order models. The zone temperature responses are very similar and lead to near identical time variations in zone loads. More detailed analyses will be performed in future work to better understand any limitations of the reduced-order model for this case study.

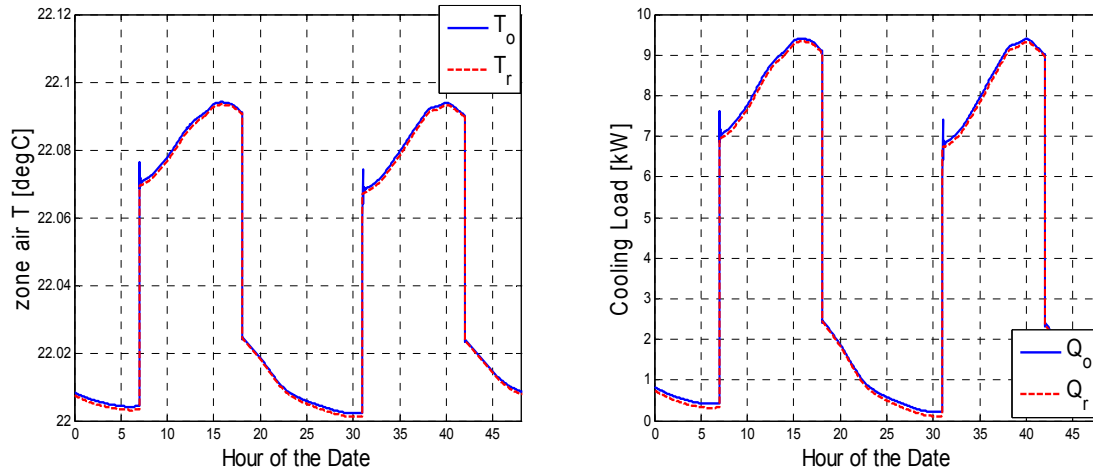


Figure 3.3.4 Example model comparisons between baseline (full-order) state-space and reduced-order models under PID control on July 22nd and 23rd (T_o and Q_o are zone air temperature and load for baseline state-space model, T_r and Q_r are zone air temperature and load for reduced-order model)

The cooling plant was scaled to meet the peak load requirements for the Living Laboratory zone and an optimal cooling plant model was generated which was used within the MPC formulation for this case study. The MPC optimization algorithm generates an optimal sequence of $\{u[k], u[k+1], \dots, u[k+N_p-1]\}$ over a prediction horizon $[k, k+N_p]$ and only the first part of the sequence, $u[k]$, is applied to the building model. For the next time $k+1$, the same procedure is applied with the initial guesses of the pre-calculated $\{u[k+1], u[k+2], \dots, u[k+N_p-1]\}$. A 24-hour prediction horizon was used to capture the usage of thermal mass in the building structure and a 15-minute prediction time step was adopted.

Figure 3.3.5 shows sample MPC results for a day in July. The time-of-use energy charges provide incentive for the MPC to apply precooling prior to the occupied period. The optimal trajectory satisfies the constraints of PPD within 10% during occupied hours and 30% during unoccupied hours. After precooling prior to occupancy, the PPD is maintained at the upper limit of 10% to minimize energy consumption since the high energy rates are coincident with the occupied period. This level of PPD corresponds to a zone air temperature setpoint during occupancy of around 25 C for summer clothing levels. It is interesting to note that the difference between the zone air and mean radiant surface temperatures reaches a maximum at the occupied period due to precooling. Further, the mean radiant temperature is always lower than the zone air temperature during occupancy implying that energy storage in the wall surfaces is acting to reduce the load. This difference tends towards zero by the end of occupancy implying that the MPC is attempting to make full utilization of the energy storage. Another interesting point is that the optimal zone air temperature peaks at the beginning of the occupied period and decreases over time. This is a result of the use of PPD as the cost constraint. The lower mean radiant temperature at the beginning of occupancy allows use of a higher zone temperature to achieve the same comfort level as compared with the higher mean radiant temperatures experienced later in the day. Higher zone air temperature setpoints lead to energy savings because of reduced loads.

It is also interesting to note that precooling includes both mechanical and ventilation precooling because the ambient temperature is lower than the zone temperature prior to occupancy but not cool enough to provide the level of cooling needed to minimize total daily operating costs. Plant power consumption peaks near the end of occupancy because of the higher ambient temperature.

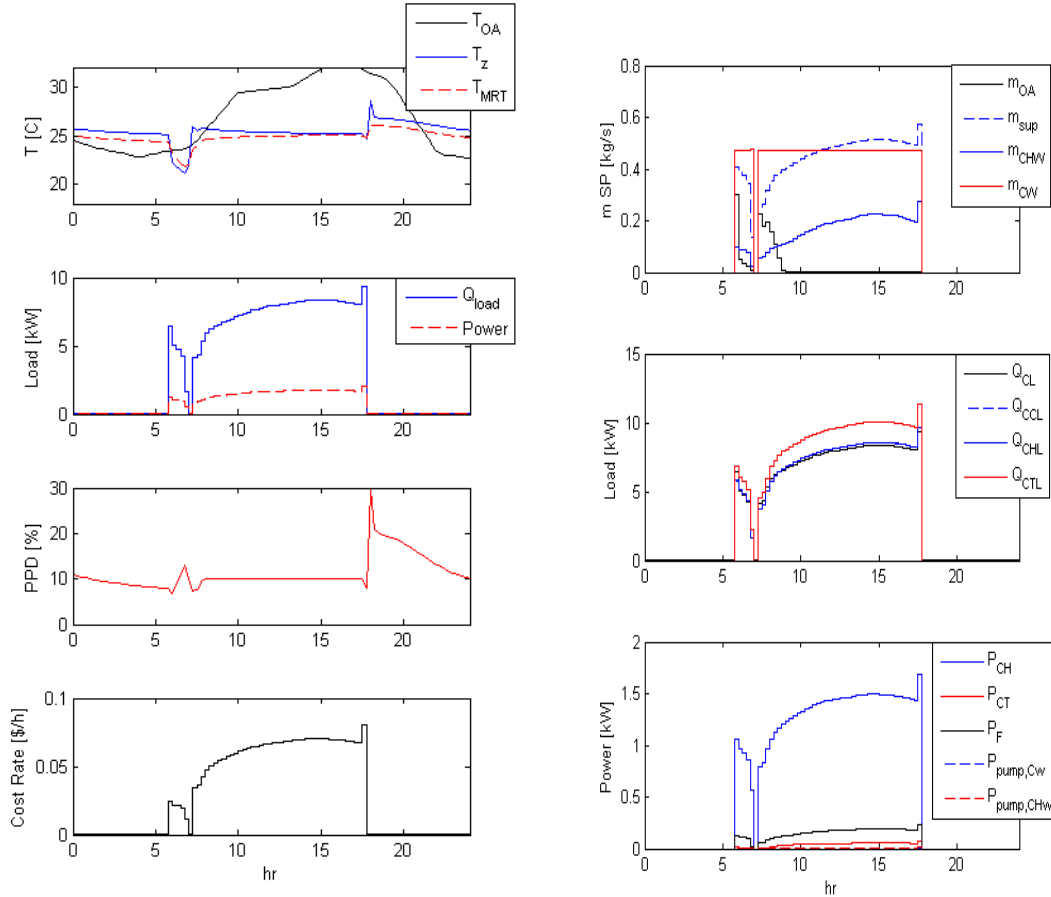


Figure 3.3.5 Example MPC results for July 22

3.3.4. Conclusions

The objective of the case study outlined in this paper is to provide a means for implementing MPC in buildings where there are significant degrees of freedom in terms of HVAC supervisory control variables. We have avoided making assumptions that are solely based on reducing the computational load but that would affect the accuracy of the results, such as constant plant COP of plant and or only including air temperature in thermal comfort evaluations and constraints. A method which decouples the plant and building analyses is utilized based on the fact that the dynamics of the plant occur on a relatively small time scale compared to the dynamics of the building. For a 24-hour time horizon with 15-minute time steps, this approach reduces the number of optimization variables from 671 (7 plant control variables, 24-hour prediction horizon with 15-minute time steps) to 96. Also, a state-space transformation-based technique is applied to determine a reduced-order model that is more amenable for controller design and optimization.

3.3.5. References

1. ASHRAE Fundamentals, 2005
2. Braun, J.E., 1990, A Reducing energy costs and peak electrical demand through optimal control of building thermal mass, *ASHRAE Transactions*
3. Casillas, J., Cerdón, O., Herrera, F., Magdalena, L., 2003 , Interpretability issues in fuzzy modeling, vol. 128 of Studies in Fuzziness and Soft Computing, *Springer*
4. Energy plus, Engineering reference Fanger, P.O., 1967, Calculation of thermal comfort: Introduction of a basic comfort equation, *ASHRAE Transactions* 73(2):III.4.1.
5. Fanger, P.O., Bahidi, L., Olesen, B.W., Langkilde, G., 1980, Comfort limits for heated ceilings, *ASHRAE Transactions*, 86.
6. Fong, K.F., Hanby, V.L., Chow, T.T., 2006, HVAC system optimization for energy management by evolutionary programming, *Energy Build*, 38(3): p220-31
7. Hydeman, M., Gillespie, K.L., 2002. Tools and Techniques to Calibrate Electric Chiller Component Models. *ASHRAE Transactions*, AC-02-9-1.
8. Incropera, F.P., Dewitt, D.P. , 2001, Fundamentals of Heat and Mass Transfer, *John Wiley & Sons*
9. Krarti, M., Brandemuehl, M.J., Henze, G.P., 1995, Evaluation of Optimal Control for Ice Storage Systems, Final Project Report for *ASHRAE* 809-RP
10. Kelman, A., Borrelli, F., 2011, Bilinear Model Predictive Control of a HVAC System Using Sequential Quadratic Programming *18th IFAC World Congress*
11. Kusiak, A., Li, M., Tang, F., 2010, Modeling and optimization of HVAC energy consumption, *Applied Energy*, 87 3092-3102
12. Kim, D., Braun, J.E, 2012, Reduced-Order Modeling for Building Controls' Development, *2012 International High Performance Buildings Conference at Purdue*, Purdue University
13. Lu, L., Cai, W., Xie, L., Li, S., Soh, Y.C., 2005, HVAC system optimization in building section. *Energy Build* 2005, 37(1):11-22
14. Morris, F.B., Braun, J.E., Treado, S.J., 1994, Experimental and simulated performance of optimal control of building thermal storage, *ASHRAE Transactions*, vol.100, No.1
15. Ma, Y., Anderson, G., Borrelli, F., 2011, A Distributed Predictive Control Approach to Building Temperature Regulation, *American Control Conference*
16. Wang, S., 1998, Dynamic Simulation of a Building Central Chilling System and Evaluation of EMCS On-Line Control Strategies, *Building and Environment*, Vol. 33, No. 1, pp. I-20

3.4 MPC Approaches and Algorithms

As noted by Rawlings and Mayne (Rawlings and Mayne 2009):

“Model predictive control has its roots in optimal control. The basic concept of MPC is to use a dynamic model to forecast system behavior and optimize the forecast to produce the best decision – the control move at the current time”

The successful implementation of this idea requires a dynamic mathematical model that can simulate the future behavior of the system with acceptable accuracy. In particular, it may be necessary to incorporate estimates of the future disturbances applied to the system. Secondly, we must be able to ‘solve’ the resulting optimal control problem quickly and accurately so that the required control value is available in a timely way. Thus, it is of interest to study the underlying control problem(s) and their numerical solution.

3.4.1 Optimal Control Formulations

In this section we consider several optimal control formulations for energy/cost-efficient cooling of a simple, single-zone room. To focus ideas we consider a scenario with

- exterior wall
- *thermal storage*- high thermal capacitance features of the building interior
- *room air* - temperature, occupied zones

A notional view of the room is shown in Figure (3.4.1); thermal energy storage is modeled in the solid circles which depict the

- wall interior temperature (T_i)
- storage temperature (T_s)
- room-air temperature (T_a)

Four energy exchange mechanisms are modeled:

1. conduction through the exterior wall from T_i to T_a
2. radiant exchange between T_i and T_s
3. convection from T_i to T_a
4. convection from T_s to T_a

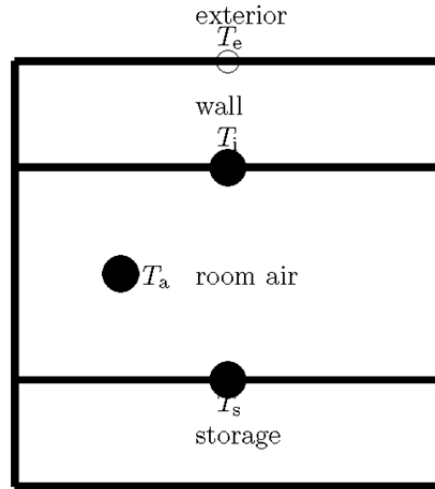


Figure 3.4.1 Notional View of Single Zone

In summary, with the linearized model for radiant exchange the dynamics of our system can be written as

$$\dot{\mathbf{z}}(t) = \mathbf{f}(t, \mathbf{z}(t), u(t)) = \mathbf{A} \mathbf{z}(t) + \begin{bmatrix} \frac{kA}{C_i \Delta} T_e(t) \\ 0 \\ \frac{-C(u(t))}{C_a} \end{bmatrix}, \quad (3.4.1)$$

where

$$u(t) \in \Omega = \{0\} \cup [u_{\min}, u_{\max}], \quad \text{and} \quad \mathbf{z}(t) = \begin{bmatrix} T_i(t) \\ T_s(t) \\ T_a(t) \end{bmatrix}. \quad (3.4.2)$$

In Equation (3.4.1) $C(u)$ (the cooling rate for a given power input) is modeled as

$$C(u) = \text{cop}(u) \times u, \quad u \in \Omega = \{0\} \cup [\underline{U}, \bar{U}], \quad 0 < \underline{U} \leq \bar{U}.$$

Here the function $\text{cop}(u)$ represents the *coefficient of performance* and is a given positive function of the applied power (u). Additional details of the model are discussed in the Appendix 3.4. In the next section we formulate an optimal control problem for these dynamics.

Optimal Control Problem

Whereas the primary focus of our optimization study is minimal energy use, to avoid trivialities it is necessary to place some restrictions on the temperature histories. To this end we formulate a discomfort metric, namely

$$D = \int_0^{t_f} c(t) \Psi(T_a(t), T_{\min}, T_{\max}) dt ,$$

where

$$\Psi(T, T_{\min}, T_{\max}) = \begin{cases} (T - T_{\min})^2 & T < T_{\min} \\ (T - T_{\max})^2 & T > T_{\max} \\ 0 & \text{otherwise,} \end{cases}$$

and where c is a *zero-one* function, the characteristic function of the occupied time interval.

In formulating the power cost we admit time-varying power rates and define our cost-functional as

$$J[u] = \mu_p \int_0^{t_f} r(t) u(t) dt + \mu_D D , \quad (3.4.3)$$

where $r > 0$ is a given function specifying the time-varying cost of power. The parameters $\mu_p, \mu_D > 0$ admit a trade-off of the power-cost and discomfort metrics.

We anticipate that the exterior wall temperature T_e , the power-rate r , and the characteristic function c will be given over a 24 hour period and that the parameter $\mu_p, \mu_D > 0$ are given. We take $t_f = 24$ (h) and seek *periodic boundary conditions* $\mathbf{z}(0) = \mathbf{z}(t_f)$ and a control function u to minimize the cost (3.4.3) subject to the dynamics (3.4.1 – 3.4.2).

Affine cop(u)

We consider a case wherein

$$\text{cop}(u) = \alpha + \beta u \quad \alpha, \beta > 0.$$

Analysis (see the Appendix 3.4) shows that optimal controls are *bang-bang* and

$S(t) = \left(\hat{\lambda}_a^{\text{crit}} - \frac{\hat{\lambda}_a(t)}{r(t)} \right)$ is a *switching function* with

$$u^*(t) = \begin{cases} 0 & \text{if } S(t) > 0 \\ 1 & \text{if } S(t) < 0 \end{cases}$$

where

$$\hat{\lambda}_a^{\text{crit}} = \frac{\hat{\mu}_p}{r(t) C(1)} > 0 .$$

Quadratic cop(u)

We now consider a case wherein

$$\text{cop}(u) = \alpha + \beta u + \gamma u^2$$

with data specifications:

- $\text{cop}(0) = \alpha > 0$

- $\max_{[\underline{U}, \bar{U}]} \text{cop}(u) = v > \alpha$
- $\arg \max \text{cop} = \ell, \quad 0 < \underline{U} < \ell < \bar{U}.$
- $C'(u)|_{u=\bar{U}} = \text{cop}(\bar{U}) + \bar{U} \text{cop}'(u)|_{\bar{U}} > 0$

From these specifications we find that:

$$\beta = \frac{2(v - \alpha)}{\ell} > 0 \quad \text{and} \quad \gamma = \frac{-(v - \alpha)}{\ell^2} < 0.$$

Analysis of this case reveals that optimal controls can take the value zero (control off), or take a value in the range $[\ell, \bar{U}]$. It is never optimal to choose a control on the range $[\underline{U}, \ell)$ (see the Appendix 3.4).

Computational Approaches:

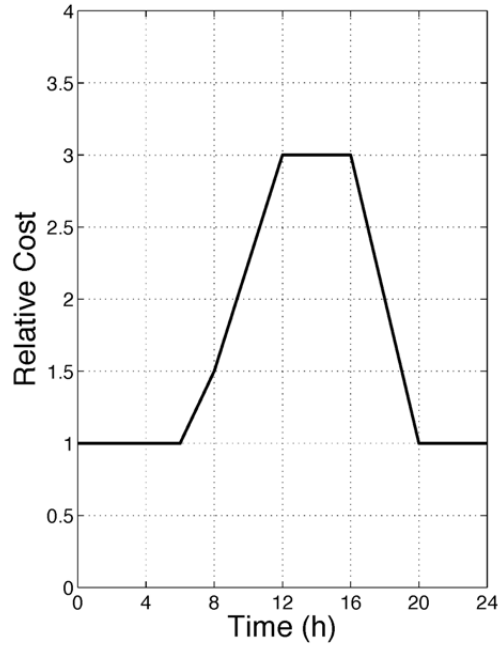
NLP Formulation (Affine cop)

The Maximum Principle has revealed that an optimal control takes only the values in $\{0, \bar{U}\}$. We assume there are N (a finite-number) of switches (*i.e.* no chattering junctions). Of course, we do not know the value N . As described in the Appendix 3.4, we assume that on the initial and final sub-arcs the optimal control has the same value ($u^* = 0$) and the number of switches (N) is even.

With this structure in mind we formulate a (family of) finite-dimensional nonlinear programming problem(s) (NLP) wherein the unknowns are the initial states and the switching times, the cost functional is J (3.4.3) and the equality constraints are the periodic boundary conditions, *viz:* $\mathbf{z}(t_f) - \mathbf{z}(0) = 0$. The parameter of the family of problems is N . We numerically solve the initial-value problem (3.4.1 - 3.4.2 with the initial states), alternating between cooling-off ($u^*(t) = 0$) and cooling-on ($u^*(t) = \bar{U}$) sub-arcs as specified by the switching times. For this purpose it's important to ensure the switching times are monotone increasing; we impose a minimum separation time between consecutive switch times. In the NLP setting this is realized as a set of $(N - 1)$ linear inequalities.

Two Cooling Periods: $N = 4$

As an instance of an NLP formulation, we consider a problem with four switch points. The NLP problem has seven variables and three equality constraints (periodicity of the temperatures - T_i, T_s, T_a). The variation of power-cost with time-of-day is shown in Figure 3.4.2

Figure 3.4.2 Power Cost function ($r(t)$)

A **Matlab** code was implemented and the *active-set* algorithm of **fmincon** (MATLAB, 2012) was used to *solve* the NLP problem. The NLP problem was numerically challenging; perhaps reflecting some issues in the dynamic model (comments later). We imposed a heavy weight on the *discomfort metric* (D);

$$\mu_p = 1 \quad \text{and} \quad \mu_D = 1. \times 10^{04} .$$

The electrical power was limited to 20 w and produced a maximum cooling of 140 w which reduces the air temperature at $2.7^\circ\text{C}/h$. The thermal capacitance of the air is relatively small, with $\frac{C_i}{C_a} \approx 9$ and $\frac{C_s}{C_a} \approx 10$. We conjecture that the relatively low control authority makes the periodicity requirements on T_s and T_i particularly challenging.

One result is shown in Figure 3.4.3. The (solid) black line represents the 'exterior' temperature (T_e); this is part of the problem data. The (dash-dot) red box defines the 'comfort constraint - the zone-air temperature (T_a - the (solid) red-line) is supposed to be in the box during the 'occupied time' ($7.5 \leq t \leq 18.5$). This specification is also problem data. The (solid) blue line is the interior wall temperature (T_i); it is conductively coupled to the exterior temperature. The (solid) green line is the temperature of the *storage mass* (T_s). Note that whereas the state histories T_i and T_s are smooth, the history of T_a is only piecewise smooth since it is explicitly driven by the (discontinuous) control.

At $t = 0$, the interior wall temperature (T_i) is the highest so it begins to decrease, while the storage wall temperature (T_s) is lowest and begins to increase. The air, initially at an intermediate temperature, exchanges energy with both of these elements and begins a slow

decrease. At $t = 03:32$ the control comes on and continues until $t = 07:16$; T_a is reduced to near the comfort lower bound at $T = 22^\circ\text{C}$. T_i , and T_s are also decreased toward local minima. As the exterior temperature (T_e) rises the other temperatures are driven upward until at $t = 13:05$ when T_a approaches the upper comfort bound. A second cooling period begins and lasts until 20:34. Lastly, with the cooling off and the exterior temperature decreasing the variables T_i , T_s and T_a return to their initial values. Cooling uses 224 wh of energy and the power-cost is 0.4242 (units). The *discomfort metric* is quite small; $D \approx 1. \times 10^{-09}$. Decreasing the weight μ_D by several orders of magnitude has little effect on the state/control histories. With $\mu_D \approx 1$ the state T_a begins to exceed the upper bound T_{\max} .

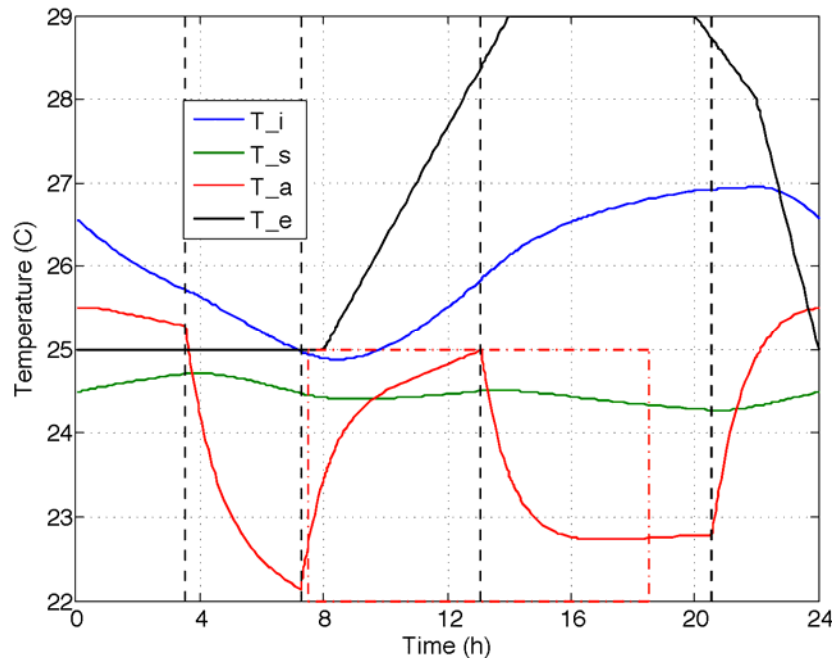


Figure 3.4.3 Temperature histories with two cooling periods

Five Cooling Periods: $N=10$

Cases for three and four cooling periods are included in the Appendix 3.4. The results from the Four Cooling Period case were used to initialize a case with five cooling periods. In this case the final cooling period begins after the occupied period (see Figure 3.4.4) during the period of lowest power-cost (see Figure 3.4.2). Note that the (red) T_a trajectory passes through the upper-right corner of the comfort-constraint box. If the 8th switch (off at $t = 17:28$) had been a little earlier, the zone-air temperature would have exceeded the upper-comfort bound; if it had occurred a little later additional high-cost cooling would have been applied. This result is perhaps from a different family of local minima than was seen in the earlier cases. It must be noted, however, that due to the minimum-switch-time constraint, the N -family of NLP problems are not nested. Thus, for example, an $N = 8$ solution can not be trivially made feasible for an $N = 10$ problem.

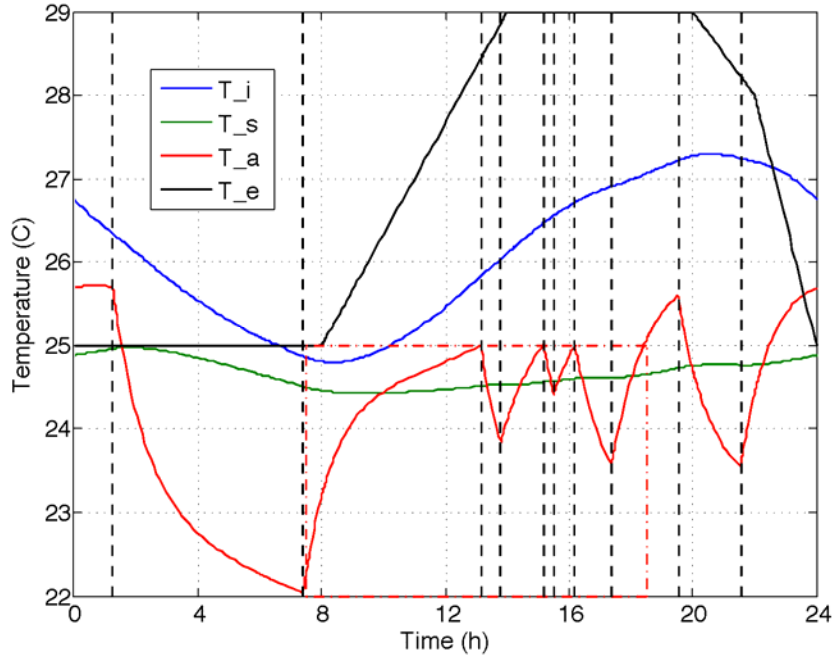


Figure 3.4.4 Temperature histories with five cooling periods

Summary

The performance attained in the four cases is summarized in Table 3.4.1; switch times are summarized in the Appendix 3.4. We see that the additional cooling periods lead to sequentially lower power-costs but that the trend in energy-used is not monotonic. In these numerical results none of the minimum-time-spacing constraints were active.

There is no claim that the NLP *solutions* presented here are actual minimizers. The optimizer stopped because the changes in the NLP parameters or the cost functional were sufficiently small (10^{-04}). We have not verified that any of the candidate switching sequences actually satisfy the Minimum Principle.

Table 3.4.1 Summary of Results

Cooling Periods	Power-Cost	Energy Used (wh)
2	0.4241	224.1
3	0.3561	224.6
4	0.3246	217.0
5	0.2819	203.9

NLP Formulation: Quadratic COP

For this discretization we impose a grid on the time axis; each state is approximated as a continuous, piecewise linear function whereas each control is a piecewise constant. A simple case is shown in Figure 3.4.5.

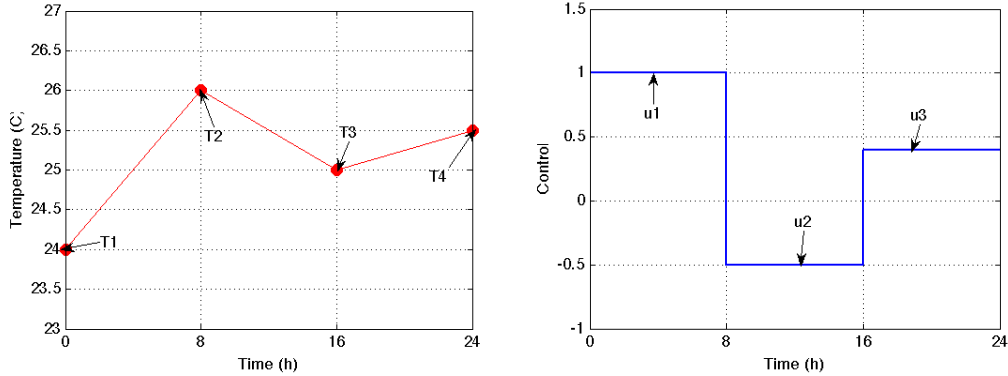


Figure 3.4.5 Generic State (Temperature) and Control Discretization

The NLP unknowns are the state values at the nodal points, and the control values on the intervals. The differential equations (3.4.1 – 3.4.2) are (approximately) enforced by the 2nd order implicit midpoint rule. Details and some numerical results are given in the Appendix 3.4.

Max u

We study an open-loop optimal control problem for energy efficient cooling of a simple room. The goal is to provide insights for the development of an implementable control scheme based on a Model Predictive Control strategy. In this version the cost function includes a term

$$F(\max_t u(t))$$

that is, a term depending on the peak value of the control. To study this problem the upper-bound on the control is no longer part of the problem data, but is an unknown to be determined as part of the solution process. Analysis of this problem is included in the Appendix 3.4. In lieu of an explicit specification of the upper bound \bar{U} we find a necessary optimality condition:

$$F'(\bar{U}) = \int_0^{t_f} \dot{\lambda}_{\bar{U}}(t) dt = \int_{t|u^*(t)=\bar{U}} \left[\mu_p r(t) - \frac{\lambda_a(t)}{C_a} \frac{C'(\bar{U})}{\ell} \right] dt. \quad (3.4.4)$$

Equation (3.4.4) is the optimality condition for the control bound \bar{U} .

Modeling of external disturbance

As the name implies, Model Predictive Control requires a model for the future behavior of the system including, where appropriate, the behavior of any external loads. We have studied the use of an *Internal Model* to characterize important unknown heating loads. The discussion is framed in terms of the single-zone model (Fig 3.4.1)) modified to include an exogenous *solar load* on the *storage mass*. Details are in the Appendix 3.4.

Our objective is to construct an estimate for the solar load based on measurements/ observations of $T_e, q_w,$ and y_{noisy} . To this end we create an *augmented system* consisting of the original closed-loop system with three states augmented with an additional state(s) that model the solar load. According to the *Internal Model Principle* (Francis and Wonham 1975) the dynamic description of the augmented state should be compatible with the expected behavior of the disturbance. Our first model is the simplest.

First-order lag:

In this case the additional state (s_d) satisfies the ODE

$$\tau \dot{s}_d(t) = -s_d(t)$$

where $\tau > 0$ is selected so that the system is stable, but not too stable. We're thinking that the disturbance is constant, but not too constant! This formulation has been used by O'Neill et al., 2010 in a multi-zone building. To formulate the associated Kalman filter we must specify noise covariances on all of the states, including S_d .

Second-order oscillator:

Given the periodic nature of the solar disturbance, it might be preferable to choose an oscillatory model for the disturbance, viz

$$\ddot{s}_d(t) + 2\zeta \omega_n \dot{s}_d(t) + \omega_n^2 s_d(t) = 0.$$

Here we could exploit the known (nominal) period for the solar input, i.e. $\omega_n = \frac{2\pi}{24\text{h}}$.

We must also specify a value for the damping ratio $0 \leq \zeta \leq 1$.

Kalman filter

For each model we construct a Kalman filter for the appropriately augmented system. The filter requires four inputs:

- 1) the cooling load (q_u) provided to the system,
- 2) the external wall temperature (T_e) applied to the system,
- 3) the noisy measurement of the *storage temperature* (T_s), and
- 4) the noisy measurement of the *zone-air temperature* (T_a).

First-order lag:

The measured (noisy) values for the *storage and zone-air temperatures* along with the filtered values are shown in Figure 3.4.6 The transient in the filtered value from its initial-value 24C takes about 8 hours but then tracking is reasonable.

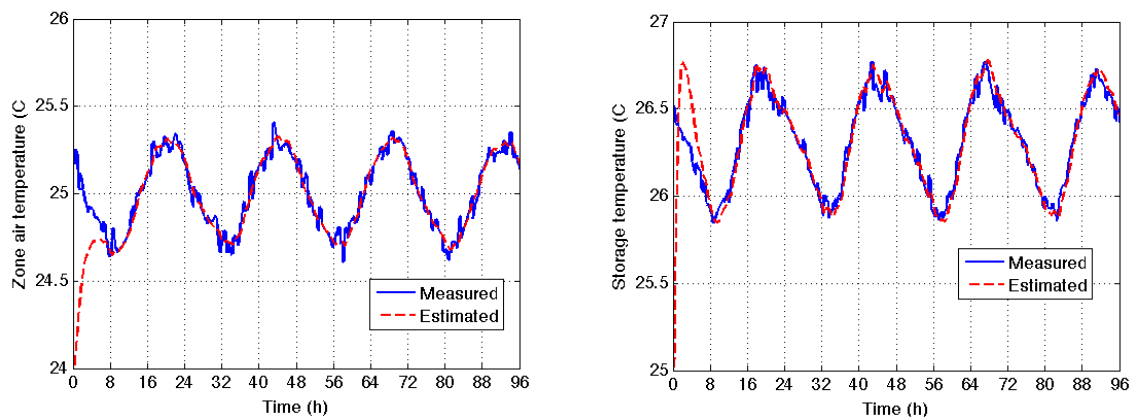


Figure 3.4.6 Sensed and Estimated Temperatures, Storage (left) and Zone-air (right)

Our main result, the tracking of the solar-load, is displayed in Figure 3.4.7. Here we see that in addition to the initial transient, there is a lag between the true and the estimated values. It may be that additional tuning (e.g. adjusting the process noise value) can improve the results.

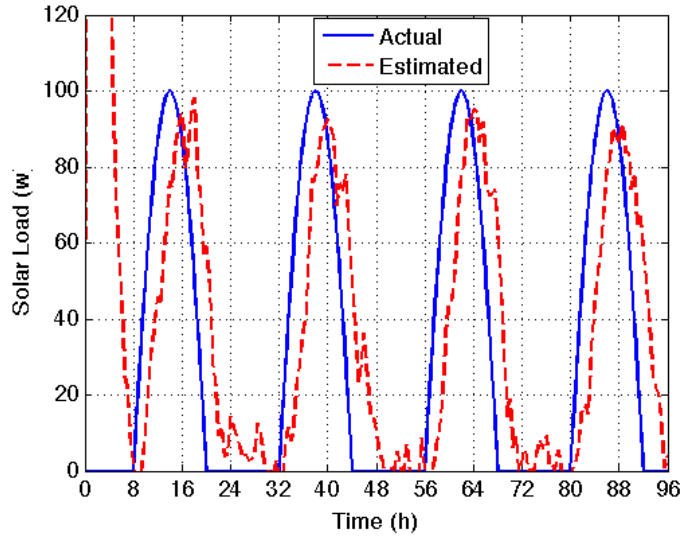


Figure 3.4.7 Actual and Estimated Solar Loads (First-order model)

Second-order oscillator:

Here again we did some modest tuning of the parameters (process noise for the pair (\hat{s}_d, s_d)). In this case (see Figure 3.4.8) there is a substantial initial transient but the eventual tracking is much improved over the first-order case. The results for smoothed estimates of T_s and T_a are indistinguishable from the first-order case (Figures 3.4.6).

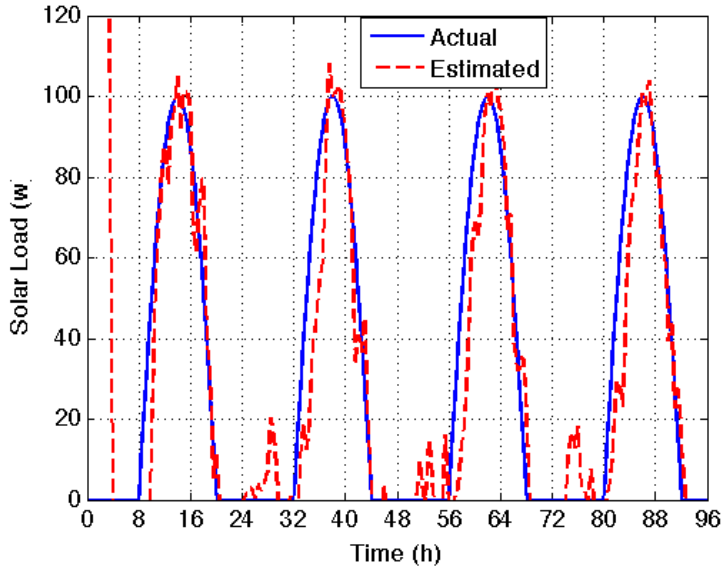


Figure 3.4.8 Actual and Estimated Solar Loads (Second-order model)

Conclusions:

This preliminary study demonstrates that it is feasible to reconstruct unknown disturbance inputs based on measured data. Note that we do require an accurate model of the system, including the

vector that characterizes how the disturbance affects the system dynamics. Note that we have assumed that the *external temperature* (T_e) is known exactly.

Using a first-order disturbance model results in a lag between the actual and the predicted solar loads. A second-order disturbance model produces better ultimate tracking, albeit with a large initial transient. *The Internal Model Principle* [Francis – op.cit.] suggests the use of higher-order models that better reflect the expected behavior of the disturbance. This extends the approach used in (O'Neill et al., 2010)

Reference

1. J.B.Rawlings and D.Q.Mayne, Model Predictive Control: Theory and Design, Nob Hill Publishing, Madison, WI, 2009
2. MATLAB. 2012. The MathWorks, Optimization Toolbox, <http://www.mathworks.com/help/optim/index.html>
3. B.A. Francis and W.M.Wonham, The internal model principle for linear multivariable regulators, Applied Mathematics Optimization, 2 (1975), no. 2, 170 - 194.
4. Z. O'Neill, S. Narayanan, and R. Brahme. 2010. Model-based thermal load estimation in buildings, Proceedings of the Fourth National Congress of the International Building Performance Simulation Association, August 2010, 474 – 481.

3.4.2 Comparative Evaluation of MPC Strategies for Purdue Living Lab Case Study

Model predictive control (MPC) is increasingly being viewed as a practical solution for building heating, ventilation and air-conditioning (HVAC) systems control [1], [2]. The ability to incorporate information such as weather forecasts and occupancy profiles in real time decisions makes MPC approaches highly attractive in this regard. However, the complexity of building models can make such approaches infeasible for all but the smallest buildings. Hence, some simplifying assumptions are usually made when formulating the MPC problem for building controls. The different assumptions and simplifying techniques lead to different control strategies or solvers. If the underlying assumptions are too different, comparison of the performance of the solvers is no longer straightforward. Hence there is a need for a common benchmark applicable to all solvers that can rank solvers based on their “optimality”. Such a benchmark would ideally be a critical part of a tool chain for designing implementable optimal control solutions in buildings. Additionally, such a benchmark can also help evaluating the benefits of retrofitting buildings.

The current study aims to provide one such benchmark. We use a Purdue Living Lab based single zone case study to rank some promising MPC control strategies based on the savings in energy costs provided while maintaining occupant thermal comfort. A setback based strategy is used to provide the baseline operating costs from which the savings are measured. Additionally, computational complexity involved in the solvers is also compared. This is done with the view of studying scalability and real time implementation feasibility of the solvers. We begin with describing the case study used to compare the solvers.

3.4.2.1 Purdue Living Lab single zone case study.

For the purpose of this study, a simplified 12-dimensional state-space model of the Purdue Living Lab VAV room was used as the common test case. The model was obtained by applying energy balances at suitably chosen points inside the room and the walls. The non-linear model thus obtained captured all the transients due to heat extraction and solar radiation. Details of the modeling procedure are reported in [3]. For application in model predictive approaches, the non-linear model was simplified. After linearization, discretization and appropriate model order reduction techniques [3], the model may be expressed in the form

$$\begin{aligned}x_{t+1} &= Ax_t + Bu_t + Fw_t \\ T_t &= Cx_t,\end{aligned}\tag{3.4.2.1}$$

where A, B, C and F represent the system matrices of reduced dimension obtained via model order reduction and t denotes the discrete time instant. The state vector x_t represents a transformed vector containing information about the temperatures of the wall and air nodes. The controllable inputs (rate of heat extraction kW) are denoted by the vector u_t . Vector w_t denotes the exogenous (uncontrollable) inputs acting on the envelope (solar radiation, ground radiation). The output matrix C provides the linear relation between the states and the outputs. For the Living Lab model, the zone air temperature T_z and the mean radiant temperature T_{rad} were assumed to be available as the output i.e. $T_t = [T_z, T_{rad}]_t^T$.

The exogenous input w_t captures 16 uncontrollable variables whose complete data was assumed to be known. For simulations, this data was extracted from Indiana TMY2 weather data

(available for every 10 min intervals) corresponding to July 2010 (summer). The state space model was discretized with a time step of 10 minutes assuming zero order hold. The choice of the time step was motivated by the resolution of the weather data available. Additionally, the internal gains due to occupants and equipment were modeled proportional to the occupancy profile depicted in Fig. 3.4.2.1. Peak occupancy (24 occupants) corresponded to an internal gain of 6 kW. Utility rates were assumed to follow a time-of-day pricing with peak price being 0.15\$/kWh from 10 am to 3 pm and 0.5 \$/kWh during off peak times.

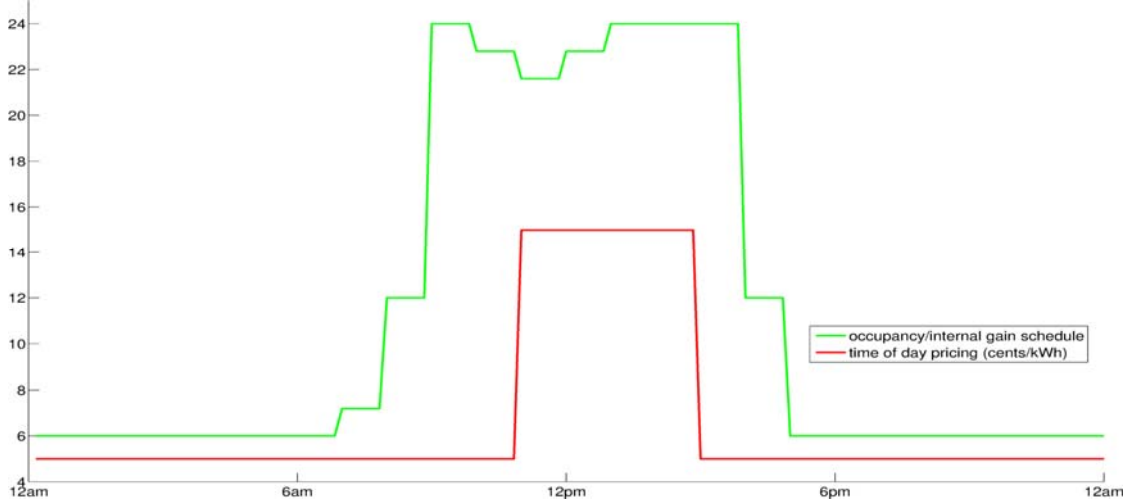


Figure 3.4.2.1 Schedule of occupancy and utility pricing.

A quasi-static approach was used in modeling the Air Handling Unit (AHU) and cooling plant supplying cool air to the room. This was motivated by the need to reduce the large number of controllable variables available on the plant side. Under certain simplifying assumptions such as constant efficiency and pressure ratios, the power consumption of the different components (namely coils, fans and pumps) were modeled using empirical models. The total power consumption of the plant was generated by summing up the individual consumptions and had the following form

$$P = f(\dot{m}_{vent}, T_{vent}, T_z, T_{OA}, RH).$$

Here \dot{m}_{vent} and T_{vent} represent the flow rate and the temperature of the air supplied by the AHU, while T_z and T_{OA} denote the room air temperature and the ambient temperature respectively. RH stands for the relative humidity of the ambient air. Noting that the controllable variables \dot{m}_{vent} and T_{vent} together affect the room dynamics in (3.4.2.1) via the rate of heat extraction u , we can relate the AHU operating power to the heat extraction rate using a lookup table of the form

$$P^*(u, T_z, T_{OA}, RH) = \min_{u=g(\dot{m}_{vent}, T_{vent})} f(\dot{m}_{vent}, T_{vent}, T_z, T_{OA}, RH).$$

The lookup table $P^*(u, T_z, T_{OA}, RH)$ gives the minimum power consumption of the AHU when supplying a heat extraction rate of u at zone temperature T_z , ambient temperature T_{OA} and RH humidity level. Using this optimal map reduces the degrees of freedom (\dot{m}_{vent}, T_{vent} to u) available in controlling the room dynamics. This leads to a reduction in the search space when searching for optimal plant operation. Also, the lookup table in effect decouples the optimal control of the room dynamics and the problem of choosing the plant set points. It should be noted

that there is an implicit assumption of the plant components having much smaller time constants compared to the zone dynamics to justify the usage of a quasi-static model. Further details on the plant modeling are given in [4].

Computing the energy costs incurred due to an optimal trajectory is relatively straight forward. From the lookup table P^* described above, it is possible to compute the dollar costs of energy corresponding to a control trajectory u as follows

$$J = \sum r_t P^*(u; T_z, T_{OA}, RH)_t .$$

Here r_t denotes the time-of-day price in dollars per unit power per time step and $P^*(\cdot)_t$ refers to the computed power consumption at time t . We assume that the complete information of the ambient conditions is known and the zone temperature T_z is available from the room dynamics as component of the output $T_t = Cx_t$. Using the above relation it is possible to compute the actual energy costs incurred by the trajectory generated by any particular solver. We ignore the peak demand costs in this study, to simplify computation.

3.4.2.2 MPC optimization strategies

Model predictive control involves forecasting the system trajectories, over a prediction horizon L , and making an optimal decision based on the prediction [5]. The first step of the optimal decision is applied to the system and the process repeated with an updated forecast. Assuming complete information of exogenous inputs w_t in (1), the predicted trajectories at time t under a control input trajectory $u_{t|t}, u_{t+1|t}, \dots, u_{t+L-1|t}$ are described by

$$\begin{aligned} x_{t+k+1|t} &= Ax_{t+k|t} + Bu_{t+k|t} + Fw_{t+k|t} \\ T_{t+k|t} &= Cx_{t+k|t}, \quad x_{t|t} = x_t, \quad k = 0, 1, \dots, L-1, \end{aligned} \quad (3.4.2.2)$$

where the subscript $k + t|t$ is used to denote the predicted value at time $k + t$ formed by propagating the initial value at time t . The model predictive control problem can be formulated using the predicted trajectories to define an optimization problem over the look ahead horizon L as follows.

$$u^* = \arg \min \sum_{k=0}^{L-1} J_k(x_{t+k|t}, u_{t+k|t}) \quad (3.4.2.3)$$

J_k represents the cost incurred at k steps into the future. The optimization problem is constrained by the dynamics in (3.4.2.2). Out of the resulting optimal input sequence $u_{t|t}^*, u_{t+1|t}^*, \dots, u_{t+L-1|t}^*$, only the first input $u_{t|t}^* = u_t^*$ is applied to the system in (3.4.2.1) and the trajectories are predicted with x_{t+1} as the initial condition. A major challenge in applying model predictive approaches to buildings is the computational complexity presented by optimization at every time step. As the cost functions J_k need not be convex, one needs to resort to numerical optimization. Additionally, the dimension of the search space grows linearly with the prediction horizon L as the length of the trajectory to be optimized grows.

Hence, some approximations are usually made to facilitate real-time computation. We describe three different MPC strategies (solvers) based on the approximations made and compare the performance in terms of the benchmark cost function when applied to the Living Lab case study.

We begin by describing a non MPC night time setback based strategy which is used to obtain the baseline costs of operating the AHU in a conventional way.

Conventional Control

For the Living Lab model described, a nighttime setback strategy was simulated as a conventional baseline strategy. The control law was determined in order to maintain the zone air temperature at a set-point of 26°C during working hours (6am -6pm). During the night, the zone air temperature is allowed to float to a maximum of 30°C. Time-of-day pricing was hence ignored during the control generation. The results of a 3 day simulation are depicted in Fig. 3.4.2.2.

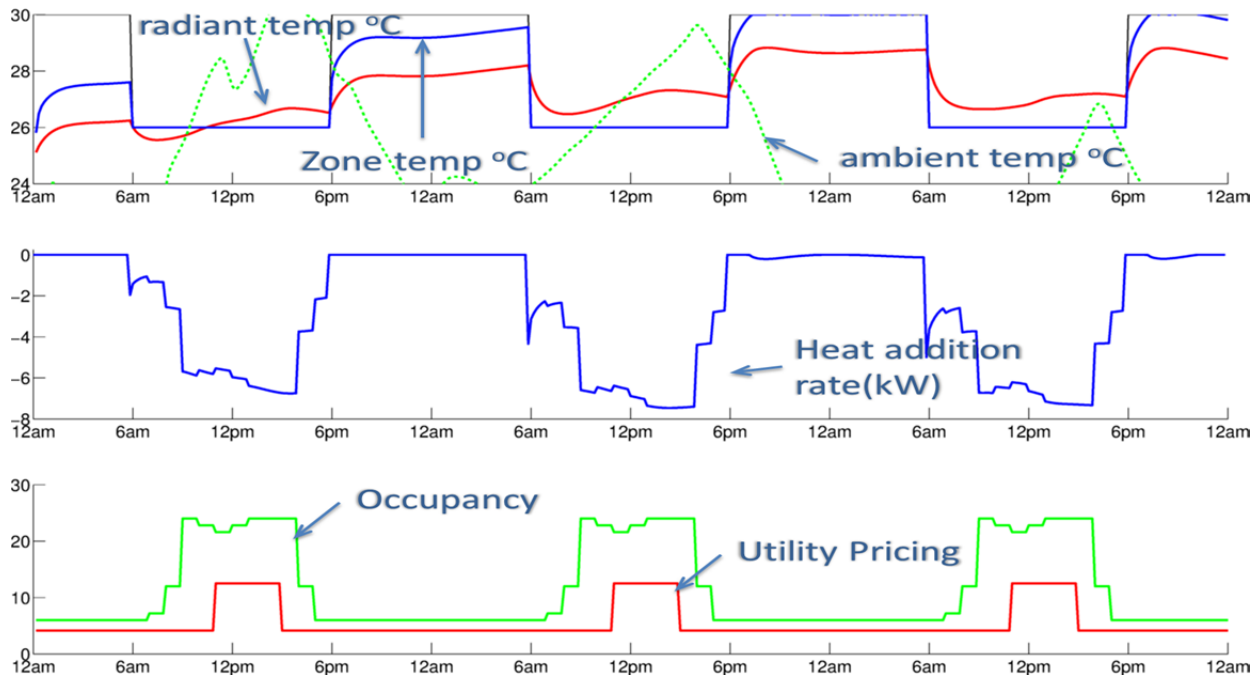


Figure 3.4.2.2 Trajectories under conventional control.

Evaluating the power costs for the obtained control trajectory yields a mean of 1.409\$ operating costs per day for this three-day period. This result quantifies the baseline metric which can be improved by using MPC based approaches. The conventional control strategy has negligible computational complexity as there is no optimization involved at any time.

Quadratic Programming (QP) based MPC

In general, solving the optimization problem in (3.4.2.3) can be intractable in real time due to the non-convex nature of the cost functions J_k . However by approximating the cost function using quadratics enables us to use highly efficient quadratic programming based numerical optimization routines. In particular, the linear nature of the constraints involved in the problem such as constraints due to dynamics (3.4.2.2) and constraints on the output (temperature thresholds) makes quadratic programming (QP) [6] an attractive choice for optimization. In order to apply quadratic programming based MPC to the case study, we obtain local quadratic approximations of the lookup table $P^*(u, T_z, T_{OA}, RH)$ in terms of the control input u , parameterized for various values of T_z, T_{OA}, RH . The fits generated for the case study were

sufficiently close to the actual value. Fig. 3.4.2.3 depicts the closeness of a typical quadratic fit.

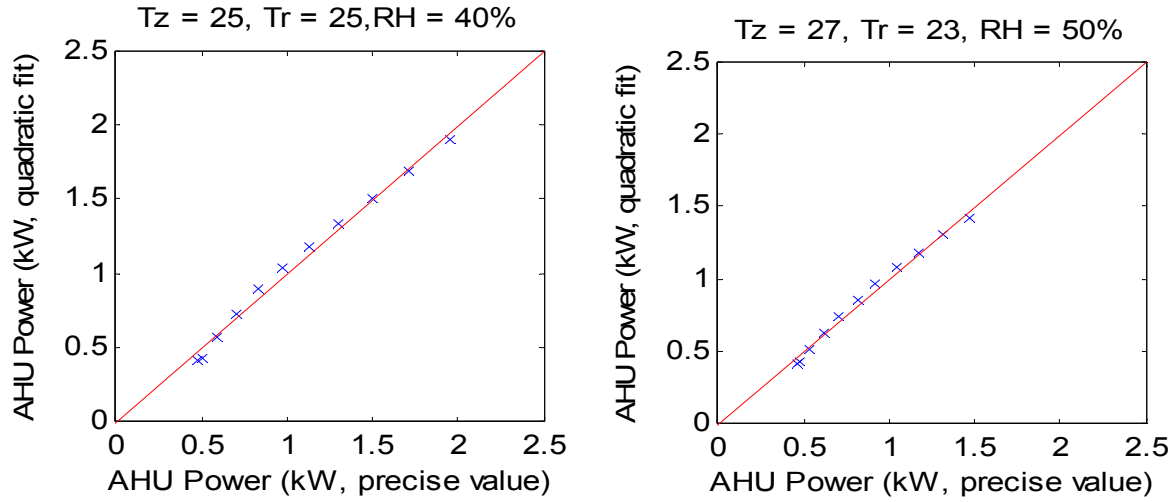


Figure 3.4.2.3 Quadratic Fits vs. Actual Power consumption

Using the quadratic fits, we can express the total power costs over the look ahead horizon as the quadratic

$$\sum_k (x_{t+k|t}, u_{t+k|t}) = \sum_t r_t u_{t+k|t}^T Q_k(x_{t+k|t}, T_{OA}, RH) u_{t+k|t}.$$

Here Q_k are in general positive definite matrices of appropriate dimension obtained from the quadratic fitting of the lookup table. The dependence of the fit on T_z is modeled via the state variable x_t . Observing that the power consumption is only weakly dependent upon the zone temperature due to its low variance over the look ahead horizon, we can further choose Q_k independent of $x_{t+k|t}$ without affecting the cost function appreciably. Using this approximation allows us to obtain a closed form Hessian of the cost function independent of the control law and facilitates using quadratic programming based solvers.

QP based solvers can handle only linear and interval constraints. Hence we express the occupant comfort in terms of a temperature interval. During the occupied hours (6am – 6pm) we constrain the zone temperature to lie within a band of $25^{\circ}C - 27^{\circ}C$. This is almost comparable with the setback strategy used for the conventional controller. To express this constraint as a linear function of the control inputs, we use (3.4.2.2) to obtain

$$\begin{aligned} \begin{bmatrix} x_{(t+1|t)} \\ \vdots \\ x_{(t+L|t)} \end{bmatrix} &= \begin{bmatrix} A \\ A^2 \\ \vdots \\ A^L \end{bmatrix} x_t + \begin{bmatrix} B & 0 & \dots & 0 & 0 \\ AB & B & \dots & 0 & 0 \\ \vdots & \vdots & \ddots & B & 0 \\ A^{L-1}B & A^{L-2}B & \dots & AB & B \end{bmatrix} \begin{bmatrix} u_{(t+1|t)} \\ \vdots \\ u_{(t+L|t)} \end{bmatrix} \\ &+ \begin{bmatrix} F & 0 & \dots & 0 & 0 \\ AF & F & \dots & 0 & 0 \\ \vdots & \vdots & \ddots & F & 0 \\ A^{L-1}F & A^{L-2}F & \dots & AF & F \end{bmatrix} \begin{bmatrix} w_{(t+1|t)} \\ \vdots \\ w_{(t+L|t)} \end{bmatrix} \\ \begin{bmatrix} x_{(t+1|t)} \\ \vdots \\ x_{(t+L|t)} \end{bmatrix} &= \begin{bmatrix} C & 0 & \dots & 0 \\ 0 & C & \dots & 0 \\ \vdots & \vdots & \ddots & \vdots \\ 0 & \dots & 0 & C \end{bmatrix} \begin{bmatrix} x_{(t+1|t)} \\ \vdots \\ x_{(t+L|t)} \end{bmatrix} \end{aligned} \quad (3.4.2.4)$$

Since $w_{t+k/t}$ is assumed to be completely known over the lookahead interval we can express interval constraints on $T_{t+k/t}$ as linear constraints on $u_{t+k/t}$. Constraints on the heat extraction rate imposed by the AHU capacity are also assumed to be interval constraints ($u_{t+k/t} \in [u^{min}, u^{max}]$). Using the closed form Hessian and the constraint formulation, we simulate the model predictive control strategy using a lookahead horizon of 24 hours. The results of the simulation are shown in Fig. (3.4.2.4).

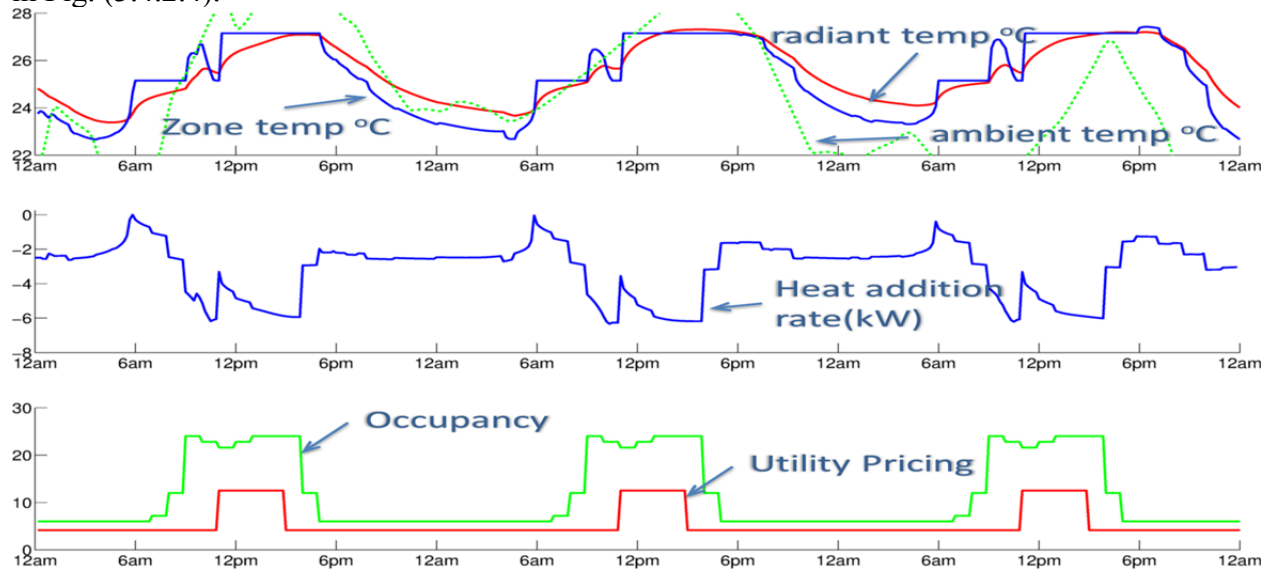


Figure 3.4.2.4 Trajectories under QP based MPC

The results indicate that the QP based solver utilizes a precooling based strategy in response to the variation in utility rates. Precooling can be observed during the interval from 6am to 10am when the utility rates are at their off peak prices (0.05\$/kWh). During the peak period, the controller drives the temperature to the maximum comfortable value (27°C) while using the energy storage from the precooling period initially. This explains the drop in cooling rate occurring around 10am. The mean operating costs over 3 days were evaluated to be 1.278 \$/day or a savings of 9.3% over the conventional setback strategy. On an Intel Core2Duo 2.1Ghz computer, the average time taken to calculate the optimal control law for one look-ahead horizon is 4.65 seconds. Note that this time is much smaller than the discretization interval of 10 mins indicating the feasibility of real time computations for this case.

Move Blocking based MPC solver

MPC strategies face growing computational costs with increasing dimension of the state space and the look-ahead horizons. Hence most MPC strategies do not scale well to multi-zone buildings. To further reduce the computational complexity involved in the QP solver, we introduce the concept of move blocking. Move blocking [7] refers to the reduction in the degrees of freedom (number of control inputs to be optimized) by restricting a fixed number of changes in the control inputs. For instance, the QP solver described above had 144 degrees of freedom (1 control input per 10 min for 24 hours look ahead) to be optimized over every look ahead. Using a move blocking approach one can decrease the computational load by constraining the control input to remain fixed for certain time steps. Fixing the control input changes to occur every 2 hrs instead of 10 mins yields a 12 degree of freedom solver which can be solved in much less time

than the original problem at the cost of optimality. The results of such a solver (12 degree of freedom) are presented in Fig. 3.4.2.5. The mean energy costs over 3 days are computed to be 1.306\$/day. It is observed that the controller is suboptimal to the QP solver presented previously. However, the average time per decision is reduced to 0.65 seconds.

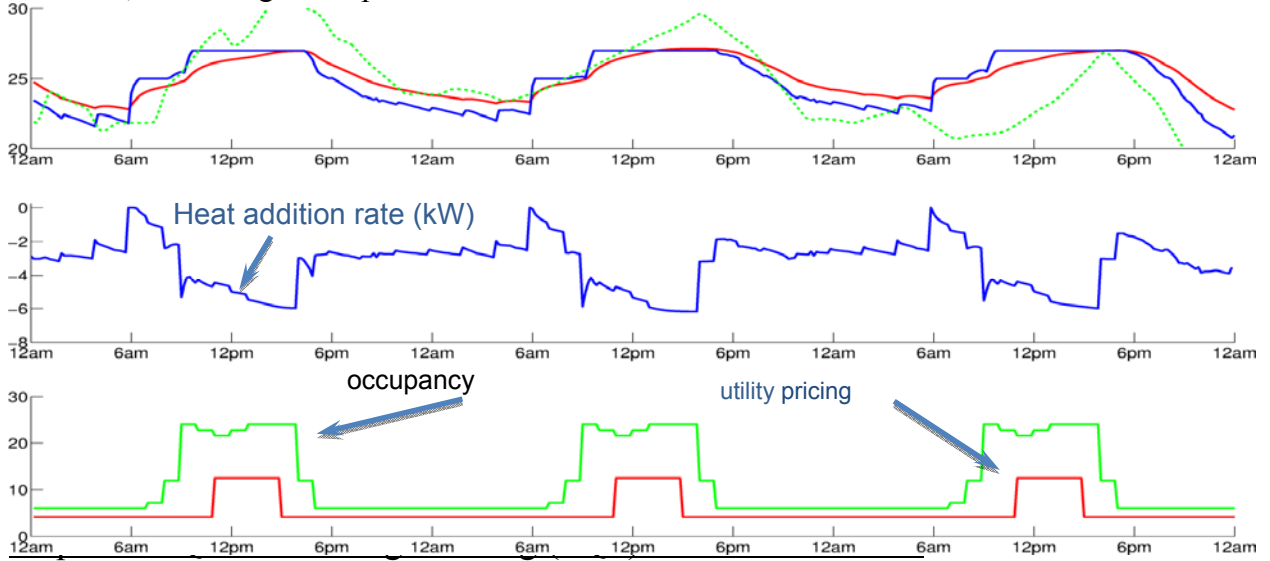


Figure 3.4.2.5 Trajectories under move blocking based MPC

The QP solver described previously approximates the nonlinear energy cost function with a quadratic in order to make the computation of the optimal control tractable. Sequential quadratic programming (SQP) extends that idea by iteratively approximating the cost function as a quadratic and the search direction is chosen to be the corresponding minimizer. SQP involves multiple numerical computations of the cost function Hessian. This can be prohibitively expensive when the cost function evaluation is time-consuming. SQP can also handle nonlinear constraints via linearization thus allowing for better comfort metrics such as PPD or PMV. Following the development in Section 3.3.2, we incorporate a PPD based constraint in the problem formulation. The MPC problem at time t was formulated with the cost function as

$$\min \sum_{k=0}^{L-1} J_k \text{ subject to}$$

$$PPD_{t+k|t} \leq \begin{cases} 10\% & \text{from 6am to 6pm} \\ 30\% & \text{otherwise} \end{cases}$$

where, the constraint on PPD prioritizes comfort during occupied periods while allowing for less conservative cooling requirements during other times. Additional factors for computing PPD such as occupant clothing and activity levels are chosen so that the 10% PPD corresponds closely to the $25^{\circ}C - 27^{\circ}C$ comfort interval. Computing the PPD involves solving a nonlinear algebraic equation and hence is computationally demanding. To facilitate computing, a cubic regression model was developed for expressing the PPD in terms of the zone air temperature and the mean radiant temperature. Similarly, the lookup table P^* was also represented using a global quadratic

$$P^*(u; T_z, T_{OA}, RH) = [u, T_z, T_{OA}, RH]^T P [u, T_z, T_{OA}, RH] + P_0.$$

The MPC problem is numerically solved using the SQP solver with the cost J_k being approximated using the global quadratic fit. Further details of the SQP solver are presented in [4]. Results of the simulation of the SQP solver for the case study are presented in Fig. 3.4.2.6. For the case study it is observed that the solver has issues with widely fluctuating control law. This phenomenon is due to the convergence of the solutions to local minima and will be investigated in the future. The mean operating costs are 1.300\$/kWh with a mean decision time of 4.55 seconds.

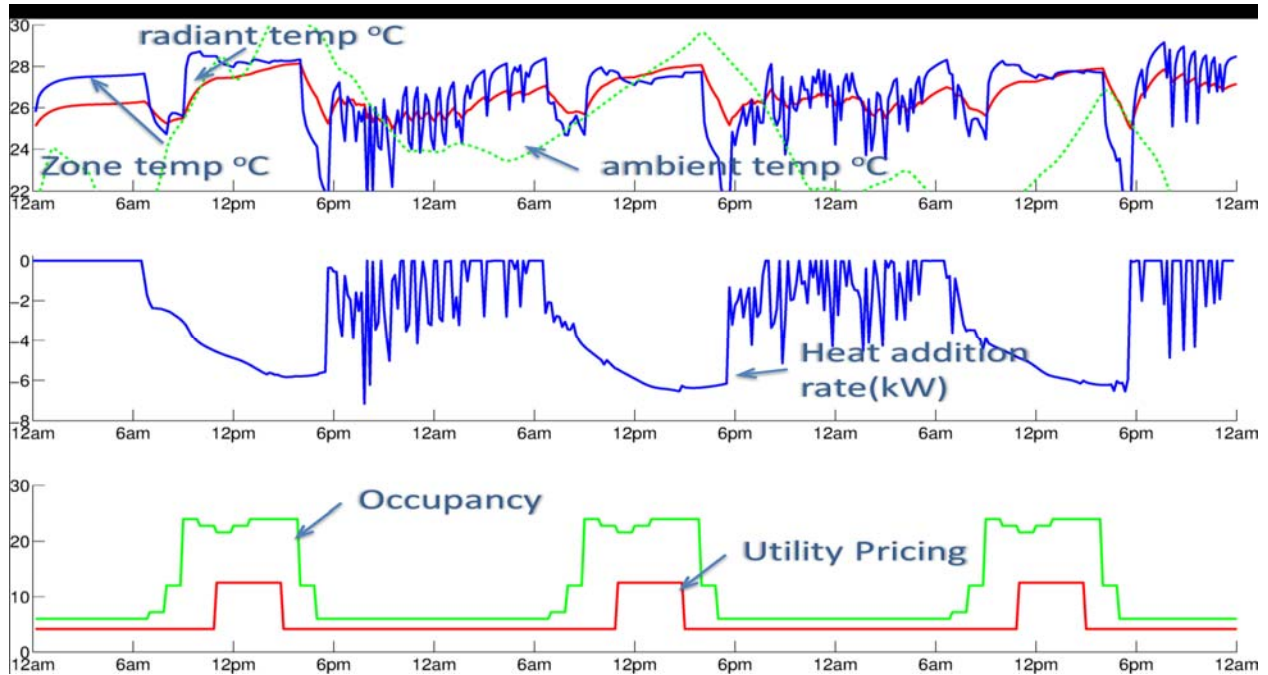


Figure 3.4.2.6 Trajectories under SQP based control- Convergence to local minima

Table 3.4.2.1: Comparison of MPC solvers

<i>Solver</i>	<i>Mean AHU Energy Costs (per day)</i>	<i>Computational Costs(sec/decision) Intel Core2Duo 2.1Ghz</i>
Conventional(Setback based)	1.409 \$ (baseline)	Realtime (no optimization involved)
Quadratic Programming (QP)	1.278 \$ (9.3 % saving)	4.5 sec (24 hour lookahead)
Move blocking (12 degrees of freedom)	1.306 \$ (7.3 % saving)	0.65 sec (24 hour lookahead)
Sequential Quadratic programming based solver	1.300 \$ (7.7 % saving)	4.55 sec (24 hour lookahead)

3.4.2.3 Summary

Table 3.4.2.1 summarizes the performance of the solvers studied. We observe greater than 9% savings compared to conventional setback control when using MPC based algorithms. The higher running cost of the conventional controller is expected as no provision is made for time of day pricing. The feasibility of operating the MPC in real time is also established from the computation runtimes. It must be noted that the scaling to a multi-zone building will result in an exponential increase in the computation burden due to the increase in the degrees of freedom. This can be alleviated to some extent using move blocking based approaches as suggested from the decrease in computational time at the cost of suboptimal savings.

3.4.2.4 Comments

We have formulated a preliminary tool chain to compare the efficacy of any MPC based control strategy in terms of the energy and implementation costs. Another dimension for comparison of the MPC strategies is occupant thermal comfort. Comparing MPC solvers consistently over their performance in occupant comfort would require a quantification of occupant discomfort. Though metrics such as PMV and PPD as used in the SQP solver are available, integrating them into the cost function poses some problems. First, there is no uniform way to scale the relative importance of energy costs and discomfort penalty. This can lead to different tradeoffs and control trajectories. Some empiricism is required in this regard. One interesting method is to study the change in occupant productivity with thermal discomfort. One study in this area is [8] where the variation of the productivity in office environments with PMV is formulated. Second, integrating discomfort metrics in the cost function invariably leads to more nonlinearity thus affecting the convergence of the solvers themselves. Further work is required in this area to avoid such issues.

3.4.2.5 Conclusions

Based on the results, we conclude that there is a scope for savings using model predictive control in buildings. We have a preliminary toolkit to compare the efficacy of other algorithms. Additional criteria that can be incorporated for comparing solvers include their performance in terms of occupant comfort and their sensitivity to inaccurate forecasts and models. Future directions include comparing other strategies in multiple and more varied scenarios.

3.4.2.6 References

1. V. Zavala, J. Wang, S. Leyffer, E. Constantinescu, M. Anitescu, and G. Conzelmann, "Proactive energy management for next-generation building systems," in *Proc. IBPSA-USA SimBuild 2010*, 2010.
2. Y. Ma, F. Borrelli, B. Hencsey, B. Coffey, S. Bengesa, and P. Haves, "Model predictive control for the operation of building cooling systems," in *Proc. American Control Conference (ACC), 2010*. IEEE, 2010, pp. 5106–5111.
3. D. Kim and J. Braun, "Reduced-order building modeling for application to model-based predictive control," in *Proc. IBPSA-USA SimBuild 2012*, 2012.
4. D. Kim and J. Braun, "Model-based predictive control for buildings with decoupling and reduced-order modeling," in *Proc. 2nd International High Performance Building Conference*, 2012.
5. J. Maciejowski, *Predictive control: with constraints*. Pearson education, 2002.
6. J. Nocedal and S.J. Wright, *Numerical Optimization* (2nd ed.). Berlin, New York:Springer Verlag 2006.
7. R. Cagienard, P. Grieder, E. Kerrigan, and M. Morari, "Move blocking strategies in receding

- horizon control,” *Journal of Process Control*, vol. 17, no. 6, pp. 563–570, 2007.
8. P. Roelofsen, “The impact of office environments on employee performance: The design of the workplace as a strategy for productivity enhancement,” *Journal of Facilities Management*, vol. 1, no. 3, pp. 247–264, 2002

3.5 Scalable and Cost Effective Implementation of Optimal Building Control

3.5.1 Introduction and Motivation

During the BP2, while developing and evaluating the technical approach we noted the following challenges associated with the potential implementation of a control retrofit using the MPC algorithmic approach

- High commissioning cost – due to time required for model selection and calibration
- Maintenance of the control solution – due to the fact that the model parameters can exhibit high variability for different operating points
- Computational scalability – large computation power and time required

To alleviate the above mentioned difficulties, UTRC proposes an approach that can be implemented and tested as part of the efforts planned for BP3. The proposed approach has been developed based on the divide and conquer idea, and makes use of optimization tools to achieve optimal coordination between the HVAC equipment. Specifically, the proposed approach may use the following sequence of decisions at different levels in the hierarchy:

- For each zone using available measured data one computes current expected demand (to compensate for the effects of the thermal load disturbances) based on a
 - o Simplified nominal model of thermal zone dynamics and
 - o Online uncertainty/load estimation
- Propagate the expected optimal air conditioning demand (heating or cooling) as a request to the AHU level where decision will be made on using optimization on the AHU (air flow and discharge air temperature),
- Given the received discharge air temperature received from AHU, at the VAV level an optimization problem can be again solved to provide optimal zone inputs supply air flow and supply air temperature.
- Demand for energy can be further propagated to cooling/heating plant level where a new optimization based control problem can be formulated and solved.

Preliminary results and insights are outlined in subsection 3.5.2.

The features that will characterize the hierarchical control approach are summarized as the following

- Hierarchical architecture: amenable for parallel and distributed implementation,
- Minimal modeling efforts of building envelope,
- Adaptive to model parameters/load variations.

The implementation of the hierarchical control architecture will result in an overall increased scalability of the control development and deployment, and increased robustness to unmeasured and uncertain disturbances. This will ultimately translate into reduced control commissioning time and will allow for continuous adaptation of a control strategy to respond to continuously variable loads associated with changing weather conditions, occupant behavior, etc. Additionally, enabled by the hierarchical approach to building control, the control retrofit strategy will become highly scalable to implementation on a heterogeneous set of buildings.

The hierarchical architecture offers high flexibility to integration with model based predictive control approach that has been developed in BP1 and BP2 to exploit the advantages offered by prediction coupled with the storage capability offered by the building envelope.

3.5.2 Preliminary Study on the Hierarchical Control Architecture

3.5.2.1 Zone Level Models and Online Uncertainty Estimation

We propose the following model for zone temperature dynamics

$$mc \frac{dT}{dt} = \dot{m}_{sa} c (T_{sa} - T) + w(\dot{m}_{sa}, T, T_{sa}, T_{oa}, \dots) \quad (3.5.1)$$

This simplified first order dynamical model for the individual zone temperature dynamics includes a nominal part, which can be accurately determined, and an uncertain part comprising the model uncertainties and disturbances, including the internal load. The effect of un-modeled dynamics and that of the un-measured input loads is captured by the uncertainty term, denoted by w . This term aggregates all unknown heat gains/losses in the zone as well as model uncertainty. The uncertainty term can be estimated online using receding horizon maximum likelihood estimation formulation.

Two uncertainty estimation algorithms have been considered.

- The first algorithm is an uncertainty observer that requires continuous-time implementation, i.e. ODE numerical integration methods, and provides strong guarantees on bounded estimation error.
- The second algorithm is an optimization-based moving horizon estimator which solves a least-square problem over the data history in order to estimate uncertainty in dynamics. The least-square algorithm operates in discrete-time and is more suitable for implementation in commercial digital HVAC control hardware. However, the least-square algorithm does not provide theoretical guarantees on estimation error bounds.

Future study will be conducted in BP3 to refine the approach to uncertainty estimation and propagation for the internal heat gains and their impact to the zone temperature predictions with real-building operational data.

3.5.2.2 Optimal Control for Zone Temperature

Given the model for zone temperature described by Eq. 3.5.1 coupled with the online uncertainty estimation procedure, for every zone one needs to design control policies to select $T_{sa}(T, w)$ and $\dot{m}_{sa}(T, w)$ such that the constraint on zone temperature is satisfied $T \in [T_{min}, T_{max}]$. Equation 3.5.2 describes the optimization problem that can be solved to provide optimal control solution for the two decision variables $T_{sa}(T, w)$ and $\dot{m}_{sa}(T, w)$.

$$\begin{aligned} & \min_{T_{sa}^r, \dot{m}^r, T^r} \alpha \dot{m}^r + \beta \dot{m}^r (T_{sa}^r - T_{da}) \\ \text{subj. to: } & (T - T^r) (c \dot{m} (T_{sa}^r - T) + \hat{w}) + q(T - T_{sa}^r)^2 \leq 0, \\ & T_{min} \leq T^r \leq T_{max} \end{aligned} \quad (3.5.2)$$

One notes that the system dynamics are included in the constraint specification, and that the cost function to be optimized penalizes the mass air flow to the zone and the reheat energy. This formulation offers the user selection capability for the two weights that define the balance between electrical energy spent at the fan level to generate the required air flow and the energy spent for reheat. A next step to evaluate the performance of this decision is to incorporate performance curves associated with the fan and reheat coil.

Figure 3.5.1 presents the obtained optimal decision maps for supply air temperature setpoint and supply mass air flow setpoint for a zone, calculated at the VAV level, given a fixed discharge air temperature provided at the level of the AHU. The figures show the values of the optimal control inputs setpoints with respect to the value of the estimated uncertainty and the value of the measured zone temperature.

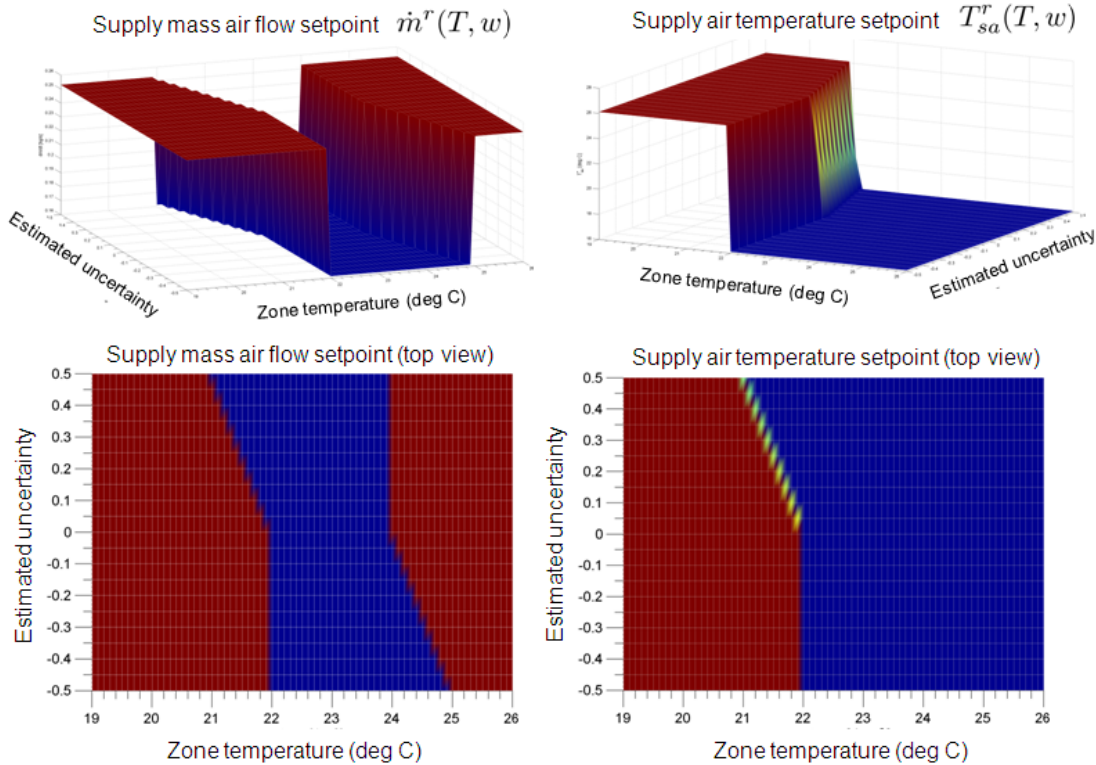


Figure 3.5.1 Optimal decision maps for supply air temperature setpoint and supply mass air flow setpoint at the VAV level

The preliminary results indicate that the on a local level one can optimally calculate the supervisory control setpoints that will result in zone temperature control with minimal energy consumption. We note that these preliminary results, calculated using optimization, present a similar switching pattern with the VAV control inputs often observed in common practical implementations. In fact one notes that the calculated optimal control inputs present a on/off behavior and the switching boundary, correlated with the zone thermal comfort setpoint band of [21.1, 23.89] deg C, can be optimally selected based on the value of the estimated uncertainty and the present zone temperature measurement.

3.5.2.3 Software Architecture Design to Enable Scalable Implementation and Deployment, and Fast Commissioning Of Optimal HVAC Control Algorithms

In order to have a scalable deployment of the control algorithms an important future task has to consider development of software architecture that will support integration between different control and estimation modules making use of the services offered by the software platform that provides middleware between selected control algorithms and the BMS. This control architecture

must also allow seamless integration between control algorithms and building and equipment models.

Following a natural hierarchical architecture of a building, an object-oriented control framework was defined. The software framework provides class definition for common HVAC components like zones, VAVs and AHUs and defines communication interface between them and data-acquisition and actuation middleware. This development framework will be further refined, by defining standardized interfaces between software objects representing models and algorithms, to support seamless integration of building envelope, equipment and load prediction models (from a building models library) with the developed optimization based control algorithms. This effort will enable fast commissioning of the building control for different building types and allow performance evaluation and comparison of different control approaches in the real-building systems.

3.5.3 Automatic Differentiation

The combination of nonlinear model predictive control (NMPC) algorithms, described above, with automatic differentiation (AD) algorithms to accurately compute the required derivative information provides a robust computational platform for control design⁴. While a few commercially available AD implementations are available in MATLAB. However these do not provide differentiation of many basic functions, including most matrix functions, which are important in engineering and control applications. This includes solutions to ordinary differential (algebraic) equations, eigenvalue problems, Lyapunov or Riccati equation solvers, matrix factorizations, among scores of important functions. In many cases, the underlying algorithms are not available to implement third party differentiation algorithms, or the algorithms themselves are not differentiable due to algorithmic choices such as conditional statements (max/min, abs, etc.) or adaptivity (quadrature and ODE solvers). Thus, to build an AD tool that works for the largest number of (control) engineers, we have implemented new algorithms that provide the best possible estimate of the derivative when it is defined, and provide consistent one-sided derivatives when the derivative itself is not defined.

For example, many algorithms have a non-differentiable implementation even when the underlying mathematical problem is differentiable. Our strategy is to implement numerically consistent derivatives when feasible, but to develop new algorithms to compute derivatives when the underlying algorithms are not available. To this point, most relevant MATLAB functions have been implemented for differentiation with respect to a single parameter (efficiently handling multiple parameters through forward and reverse modes of AD are planned for BP3. We note that our new algorithms take the approach of avoiding numerically generated non-differentiability by approximating the derivative of the mathematical problem instead of the derivative of the approximation to the mathematical problem. For example, for the ODE functions, the output is not differentiable when parametric changes affect the time step selection algorithm (which is nearly every case since the interesting problems occur when the parameter affects the solution output). We provide examples of a few of the new algorithms we have developed in the Appendix 3.5.

⁴ Cao and Al-Seyab, Nonlinear model predictive control using automatic differentiation, European Control Conference, 2003.

3.5.4 State Estimation from Sensed Data (Optimal Sensor Placement)

Our objective is to develop and demonstrate a process, tool, and algorithms that will significantly reduce the development and commissioning time/cost to implement advanced building control algorithms for retrofits by automating model and control law generation. The BP2 deliverable is the Demonstration of prototype building control algorithms that provide guaranteed performance with robustness margins for whole building solutions. In order to accomplish this, one must deal with the fact that not all states are available for measurement (*partial state output*) and hence some form of state estimation must be used. Thus, a state estimator must be considered if there is any hope of quantifying the robustness of realistic model predictive controllers. Sensor types and locations *greatly* impact the quality of these estimators.

It is well known that the performance of MPC deteriorates because of the estimation error. In order to study and quantify the robustness an output feedback MPC, it is necessary to choose a suitable strategy for the state estimation. We focus on the Kalman Filter (KF) since it is the most popular tool used in modern control and there is a rigorous proof of the stability with error bounds. Recently, new (local) error estimates have been obtained for the Extended Kalman Filter (EKF) which will be essential for Nonlinear MPC (NMPC) that is the basis for the Task 4.2 work. To illustrate the potential practical benefits of the sensor location tool, consider the results obtained on the test room below.

The test case is a suite with one zone devoted to a bed area and the remaining zones are bath and dressing areas as depicted in Figure 3.5.2 below. There are two inlet diffusers and one outflow return vent, which is the only outflow when the door is closed.

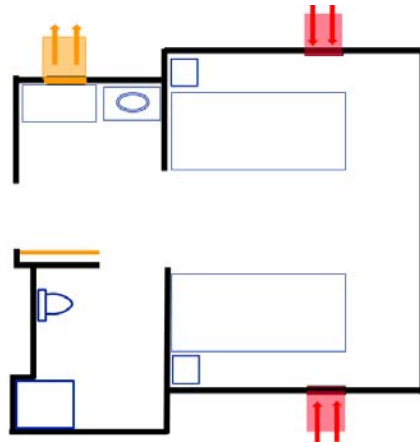


Figure 3.5.2 A three zone suite problem with airflow

It is important to note that the air flow through the room can have a tremendous impact on sensing and control. In particular, if one were to assume a “well mixed flow” and formulate the sensor location problem, then the “optimal location” would in general not be valid for more realistic room operation. Figure 3.5.3 shows the advection velocity field $v(\bar{x})$ for the cases with the door open and closed. In the test problem here, clearly the flow is not well mixed in either case. However, the flow in the room to the right has similar a structure and one might guess that if one limits the sensor location to the bed area, then the optimal location will not change dramatically. This indeed is true as demonstrated in the numerical example below.

The estimation error is based on employing a Kalman Filter for state estimation and given by

$$\mathcal{J}(\bar{\mathbf{q}}) = \mathbb{E} \left(\int_0^{+\infty} \|z_e(s, \bar{\mathbf{q}}) - z(s)\|^2 ds \right) = Tr(\Sigma(\bar{\mathbf{q}})), \quad (3.5.3)$$

where $\bar{\mathbf{q}}$ is the sensor location, $\mathbb{E}(\mu)$ denotes the expected value of the random variable μ and $Tr(\Sigma(\bar{\mathbf{q}}))$ denotes the trace of the state estimation covariance operator $\Sigma = \Sigma(\bar{\mathbf{q}})$. Consequently, the optimal sensor location problem is to find an optimal location $\bar{\mathbf{q}}^{opt}$ such that $\mathcal{J}(\bar{\mathbf{q}}) \triangleq Tr(\Sigma(\bar{\mathbf{q}}))$ is minimized.

To illustrate the range of values for the cost function $\mathcal{J}(\bar{\mathbf{q}}) = Tr(\Sigma(\bar{\mathbf{q}}))$, we assume that there is only one sensor and that the sensor can only be placed on a wall in the bedroom area on the right side of the suite. The spatial variation starts with the sensor located on the intersection of the upper wall in the bed area with the room divider on the left of the bed area. As $\bar{\mathbf{q}}$ moves along the upper wall to the right, down the right wall and back to the left of the lower wall, the cost $\mathcal{J}(\bar{\mathbf{q}}) = Tr(\Sigma(\bar{\mathbf{q}}))$ is computed and plotted. It is important to note that one does not have to make assumptions about where the disturbance is located. In particular, by setting the suite disturbance to be

$$\eta(t, \bar{\mathbf{x}}) = [\mathcal{G}w(t, \cdot)](\bar{\mathbf{x}}) = \iiint_{\Omega} \delta_{\epsilon}(\bar{\mathbf{x}} - \bar{\mathbf{y}})w(t, \bar{\mathbf{y}})d\bar{\mathbf{y}} \approx w(t, \bar{\mathbf{x}}), \quad (3.5.4)$$

where $\delta_{\epsilon}(\bar{\mathbf{x}})$ is an approximation of the Dirac delta function, the disturbance operator is approximately the identity. This particular choice of disturbance means that we are assuming the minimal information about the spatial location and intensity of the random field.

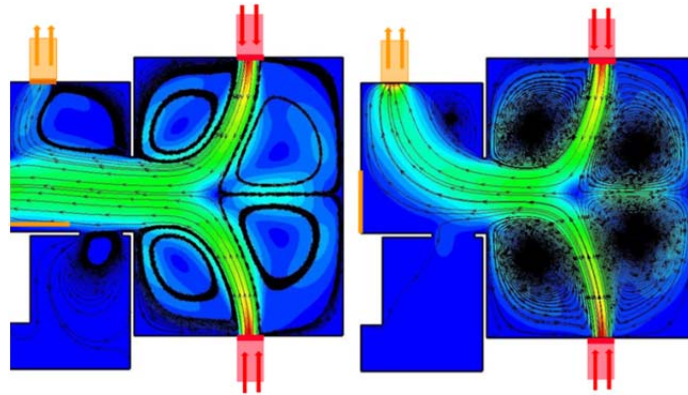


Figure 3.5.3 Flow through the suite problem: door open and closed

In Figures 3.5.4 and 3.5.5 we plot the values of $\mathcal{J}(\bar{\mathbf{q}}) = Tr(\Sigma(\bar{\mathbf{q}}))$ as the sensor location $\bar{\mathbf{q}}$ moves around the wall in the right room. Here, “upper” refers to the upper wall, “right” refers to the right wall, “lower” is the bottom wall, and “left” is the left wall of the bed area. Note that we also computed the cost $\mathcal{J}(\bar{\mathbf{q}}) = Tr(\Sigma(\bar{\mathbf{q}}))$ for the case where the sensor is placed in the opening between the bed area and the left zone of the suite even though there is no wall there.

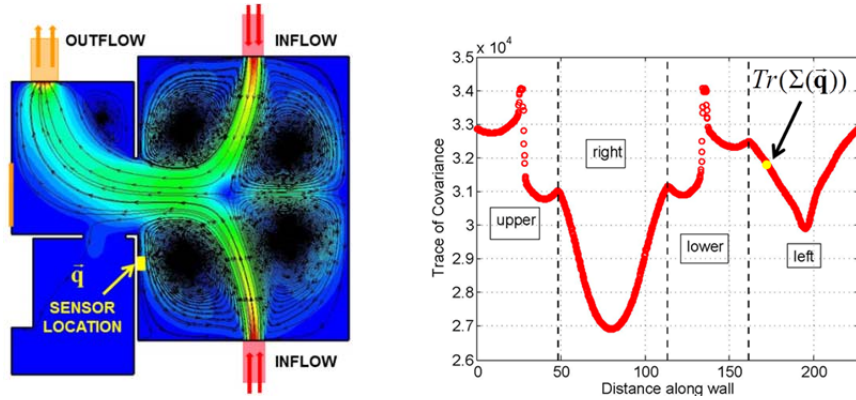


Figure 3.5.4 Plot of the cost $\rho(\bar{\mathbf{q}}) = Tr(\Sigma(\bar{\mathbf{q}}))$ and a sensor location on lower left wall

Observe that the optimal location is in the middle of the right wall and the absolute estimation error is approximately $\rho(\bar{\mathbf{q}}^{opt}) \approx 2.68 \times 10^4$ which should be expected since the error is computed over all time and nothing is assumed about the location and intensity of the disturbances. The important point is that by placing a sensor in the optimal position, the total estimation error can be reduced by nearly 30% compared to the worst placement near the inlet vents. Also observe that as the sensor location moves across the inlet vents, there is sharp jump in the cost $\rho(\bar{\mathbf{q}}) = Tr(\Sigma(\bar{\mathbf{q}}))$. Elsewhere, the cost is relative smooth which implies a gradient based optimization scheme should work well if one avoids placing a sensor on inlet vents. In fact, the Matlab™ optimization toolbox easily found the global minimum for this test problem.

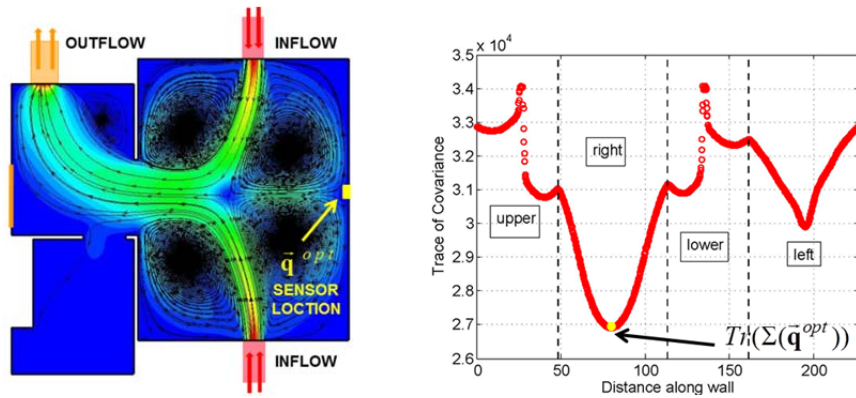


Figure 3.5.5 The optimal location on right wall and the plot of the Cost $\rho(\bar{\mathbf{q}}) = Tr(\Sigma(\bar{\mathbf{q}}))$

As noted above, the case where the door is open is similar to the closed door case and the optimal location is essentially the same. However, as shown in Figure 3.5.6 below the absolute estimation error is approximately $\rho(\bar{\mathbf{q}}^{opt}) \approx 3.54 \times 10^4$ which implies the state estimator is less accurate when the door is open.

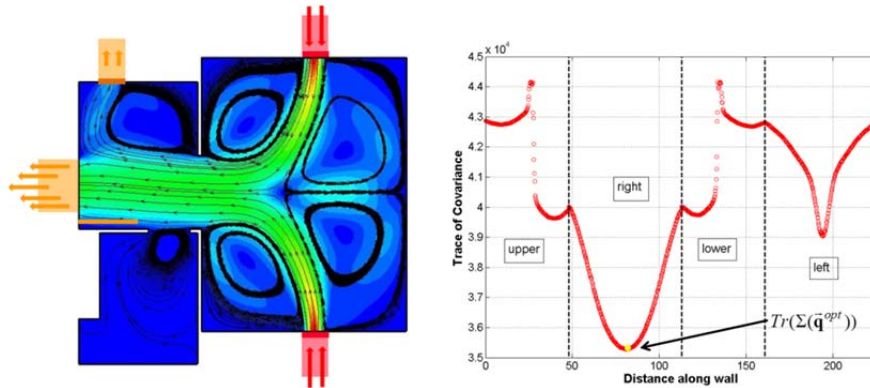


Figure 3.5.6 Plot of the cost $J(\bar{q}) = Tr(\Sigma(\bar{q}))$ for the open door case

We have developed an approach and initial computational tool to address the problem of optimally locating sensors to minimize the mean square error between a temperature field and an estimated temperature field based on localized sensed output alone. This is important since measurements in typical building systems often come from sensors that are spatially distributed and provide accurate measurements only in (small) local regions. We focused on the Kalman filter since it is optimal for a fixed sensor type and location. The Kalman filter is a powerful tool for state estimation needed in the development of practical feedback and MPC controllers when only partial sensed information is available. In addition, the basic method can be applied to problems where robustness of the controller is essential. Since buildings are highly uncertain dynamical systems, placing sensors for robust control and optimality of performance is a key to the operation of future high performance buildings. Early testing indicates that multi-grid like algorithms can be employed to reduce design cycle times by 10X. Expanding this tool to address multi-sensor types and locations will make it useful for practical implementation by several user groups.

4. Summary and Future Work

Significant progress was made in developing and demonstrating tools that could be used to provide a scalable and cost effective platform for generation of site-specific optimized controls for buildings. Accomplishments in the BP2 have included 1) development of control-oriented models along with case study demonstration results, which covers reduced-order and inverse (data-driven) models for building envelope, indoor air, and HVAC equipment; 2) development, comparisons and implementation of MPC approaches and algorithms along with case study results, which covers simulation-based studies for both Building 101 and the Purdue Living lab; and 3) scalable and cost effective implementation of optimal building control, which covers preliminary study on the hierarchical control architecture, state estimation from sensed data and efficient algorithms for optimal control with meaningful cost models. In the following sections, an executive summary is provided for these accomplishments.

The collaborative effort in the BP2 will continue in the BP3 and will involve further development and application of the tools. There are three collaborative activities in this subtask. UTRC is focusing on implementation and demonstration for a centralized solution in Building 101 and West Chester University. Purdue is addressing automatic model generation and evaluating the benefits of distributed versus centralized solutions. VT is tackling some of the numerical approaches for obtaining models and solving the optimization problems. This subtask will start to categorize optimal control strategies for different building and systems types with potential energy savings range. This will facilitate building owners, operators and energy managers to screen, identify and select the appropriate strategies for their buildings

Appendix

Appendix 2.2

Fitting the Data: the Iterative Rational Krylov Algorithm

We have developed a novel two-stage method for designing reduced-order models for indoor air environments. Our method does not require access to internal dynamics and produces a reduced-model directly from input/output measurements. In the first step of method, input-output data is obtained by subjecting each input of interest to a step-like change and the outputs are sampled. This simulation is achieved using FLUENT. By differentiating the output samples using finite differences, impulse response data (Markov parameters) are obtained. We then form a large-scale block-Hankel matrix whose entries are the Markov parameters obtained by numerical simulation. The common data-driven model reduction methods would simply apply Partial Realization^{A1} or the Eigenvalue Realization Algorithm (ERA)^{A2} to this Hankel matrix to extract the reduced-model directly. However, these approaches would suffer from the fact that they would not make use of the data to its fullest extent. Instead, we apply partial realization and/or ERA to obtain an intermediate-order model which makes use of the available data as much as possible.

This intermediate model is not our final model since its order is usually quite large, around 3000. However, what this intermediate model now presents is a state-space realization, allowing us to further reduce it *optimally* using optimal projection-based model reduction techniques. This is in contrast to reducing the data directly without an optimal reduction search. In this second-stage of our approach, we employ interpolatory optimal H_2 model reduction method, known as Iterative Rational Krylov Algorithm (IRKA)^{A3}. IRKA is numerically effective requiring only linear solves; thus can be easily applied to intermediate model to reduce it optimally. The (optimal) reduced-model of this second stage is our final data-driven model for the underlying input/output dynamics. We have applied this two-stage reduction method to Purdue Radiant Room and obtained a very accurate match of the full-order input/output data.

Stage-1

Let $\mathbf{G}_{FOM}(z) = \sum_{k=1}^{\infty} \mathbf{g}_k z^{-k}$ be the expansion around $s = \infty$. Construct

$$\mathbf{L} = \begin{bmatrix} \mathbf{g}_1 & \mathbf{g}_2 & \cdots & \mathbf{g}_N \\ \mathbf{g}_2 & \mathbf{g}_3 & \cdots & \mathbf{g}_{N+1} \\ \vdots & \vdots & \cdots & \vdots \\ \mathbf{g}_N & \mathbf{g}_{N+1} & \cdots & \mathbf{g}_{2N-1} \end{bmatrix}, \quad \mathbf{M} = \begin{bmatrix} \mathbf{g}_2 & \mathbf{g}_3 & \cdots & \mathbf{g}_{N+1} \\ \mathbf{g}_3 & \mathbf{g}_4 & \cdots & \mathbf{g}_{N+2} \\ \vdots & \vdots & \cdots & \vdots \\ \mathbf{g}_{N+1} & \mathbf{g}_{N+3} & \cdots & \mathbf{g}_{2N} \end{bmatrix}$$

$$\mathbf{Z} = \begin{bmatrix} \mathbf{g}_1^T & \mathbf{g}_2^T & \cdots & \mathbf{g}_N^T \end{bmatrix}^T, \quad \text{and} \quad \mathbf{T} = \begin{bmatrix} \mathbf{g}_1 & \mathbf{g}_2 & \cdots & \mathbf{g}_N \end{bmatrix}.$$

Let $\mathbf{L} = \mathbf{Y}\mathbf{O}\mathbf{X}^T$, be the SVD of \mathbf{L} with $\text{rank}(\mathbf{L}) = k$. Then,

^{A1} A.J.Mayo and A.C.Antoulas. A framework for the solution of the generalized realization problem. Linear Algebra and Its Applications, 2007.

^{A2} S.Y. Kung. A new identification and model reduction algorithm via singular value decomposition. Proc. 12th Asilomar Conf. Circuits, Syst. Comput., 1978.

^{A3} S. Gugercin, A.C. Antoulas, and C.A. Beattie. "\$\mathcal{H}_2\$ model reduction for large-scale linear dynamical systems". SIAM Journal on Matrix Analysis and Applications, 2008.

$$\mathbf{G}(z) = \mathbf{C}(z\mathbf{E} - \mathbf{A})^{-1}\mathbf{B},$$

where

$$\mathbf{E} = \mathbf{Y}_k^T \mathbf{L} \mathbf{X}_k, \quad \mathbf{A} = \mathbf{Y}_k^T \mathbf{M} \mathbf{X}_k, \quad \mathbf{B} = \mathbf{Y}_k^T \mathbf{Z}, \quad \mathbf{C} = \mathbf{T} \mathbf{X}_k.$$

is our intermediate reduced-model.

Stage-2

In the second-stage of the methods, we apply projection-based optimal model reduction method IRKA^{A3} to further reduce the intermediate model $\mathbf{G}(z) = \mathbf{C}(z\mathbf{E} - \mathbf{A})^{-1}\mathbf{B}$ and obtain our final reduced model. A sketch of IRKA is given below:

Algorithm: **Iterative Rational Krylov Algorithm (IRKA)**

1. $\mathbf{G}(z) = \mathbf{C}(z\mathbf{E} - \mathbf{A})^{-1}\mathbf{B}$.
2. Choose initial interpolation points $\{s_1, \dots, s_r\}$; and tangential directions $\{\mathbf{b}_1, \dots, \mathbf{b}_r\}$ and $\{\mathbf{c}_1, \dots, \mathbf{c}_r\}$; all three sets chosen are closed under conjugation.
3. Construct

$$\mathbf{V}_r = [(\mathbf{s}_1\mathbf{E} - \mathbf{A})^{-1}\mathbf{B}\mathbf{b}_1, \dots, (\mathbf{s}_r\mathbf{E} - \mathbf{A})^{-1}\mathbf{B}\mathbf{b}_r].$$

$$\mathbf{W}_r = [(\mathbf{s}_1\mathbf{E} - \mathbf{A})^{-T}\mathbf{C}^T\mathbf{c}_1, \dots, (\mathbf{s}_r\mathbf{E} - \mathbf{A})^{-T}\mathbf{C}^T\mathbf{c}_r].$$
4. until convergence
 - a. $\mathbf{A}_r = \mathbf{W}_r^T \mathbf{A} \mathbf{V}_r$, $\mathbf{E}_r = \mathbf{W}_r^T \mathbf{E} \mathbf{V}_r$, $\mathbf{B}_r = \mathbf{W}_r^T \mathbf{B}$, and $\mathbf{C}_r = \mathbf{C} \mathbf{V}_r$.
 - b. Compute $\mathbf{A}_r \mathbf{x}_i = \hat{\lambda}_i \mathbf{E}_r \mathbf{x}_i$ and $\mathbf{y}_i^* \mathbf{A}_r = \hat{\lambda}_i \mathbf{y}_i^* \mathbf{E}_r$ with $\mathbf{y}_i^* \mathbf{E}_r \mathbf{x}_i = \delta_{ij}$ where \mathbf{y}_i^* and \mathbf{x}_i are left and right eigenvectors associated with $\tilde{\lambda}_i$
 - c. $s_i \leftarrow \frac{1}{\tilde{\lambda}_i}$, $\mathbf{b}_i^T \leftarrow \mathbf{y}_i^* \mathbf{B}_r$ and $\mathbf{c}_i \leftarrow \mathbf{C}_r \mathbf{x}_i$, for $i = 1, \dots, r$.
 - d. Construct

$$\mathbf{V}_r = [(\mathbf{s}_1\mathbf{E} - \mathbf{A})^{-1}\mathbf{B}\mathbf{b}_1, \dots, (\mathbf{s}_r\mathbf{E} - \mathbf{A})^{-1}\mathbf{B}\mathbf{b}_r].$$

$$\mathbf{W}_r = [(\mathbf{s}_1\mathbf{E} - \mathbf{A})^{-T}\mathbf{C}^T\mathbf{c}_1, \dots, (\mathbf{s}_r\mathbf{E} - \mathbf{A})^{-T}\mathbf{C}^T\mathbf{c}_r].$$
5. $\mathbf{A}_r = \mathbf{W}_r^T \mathbf{A} \mathbf{V}_r$, $\mathbf{E}_r = \mathbf{W}_r^T \mathbf{E} \mathbf{V}_r$, $\mathbf{B}_r = \mathbf{W}_r^T \mathbf{B}$, $\mathbf{C}_r = \mathbf{C} \mathbf{V}_r$.
6. $\mathbf{G}_r(z) = \mathbf{C}_r(z\mathbf{E}_r - \mathbf{A}_r)^{-1}\mathbf{B}_r$.

The reduced model in Step 6, i.e. $\mathbf{G}_r(z) = \mathbf{C}_r(z\mathbf{E}_r - \mathbf{A}_r)^{-1}\mathbf{B}_r$, is the final reduced-model of our two-stage reduction methodology.

Appendix 2.5

Data-Driven Model

Table A.2.5.1 Coefficients for supply fan power in Eq. 2.5.1

Parameter	Value
a_0	1.0842
a_1	-3.1077
a_2	3.2201

Table A.2.5.2 Parameters for air temperature across supply fan in Eq. 2.5.2

Parameter	Value
η_m	0.93
$f_{motorloss}$	1
$\dot{V}_{tot,max}$	12.2531 (kg/s)

Table A.2.5.3 Parameters for the DX coil model

Parameter	Value
a	0.0008029
b	-1.508
a_0	-6.27e-7
a_1	1.41e-4
a_2	-1.14e-2
a_3	0.378
Q_{airmax}	8.2157e5 (kJ/hr)

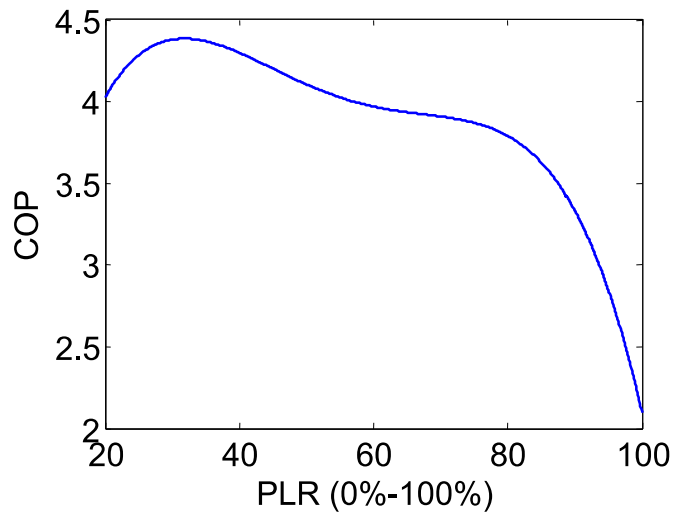


Figure A.2.5.1 COP map of the DX coil as a function of the PLR

Table A.2.5.4 Max VAV supply air and hot water flow rates

VAV Number	Max. Air Flow Rate (kg/hr)	Max. Water Flow Rate (kg/hr)
1	3860	388
2	3962	399
3	6969	701
4	5588	562
5	4775	480
6	4734	476
7	4978	501
8	9245	930

ARX Model for Building 101 Case Study

A standard ARX (Auto-Regressive with exogenous input) model structure can be described by:

$$y(t) + \sum_{i=1}^{n_y} a_i y(t-i) = \sum_{i=1}^{n_u} \sum_{j=1}^{n_{bj}} b_j u_i(t-j), \quad (\text{A.2.5.1})$$

where y denotes model outputs and u_i , $i = 1, \dots, n_u$ are model inputs. Structure of the model, i.e. the set of values n_a , n_{b1} , n_{b2} and n_{b3} for each zone, is selected based on the algorithms implemented in the MATLAB System Identification Toolbox. An initial guess for the model order is obtained using the Akaike's information criterion (AIC) and further updated with several iterations to improve the quality of the data fitting and transient responses of the model.

For the results shown in Figure 2.5.5(a), the coefficients of matrix A and B in Eq. A.2.5.1 are given by:

$$A = [1 \quad -1.7542 \quad 0.85752 \quad -0.091517],$$

$$B = \begin{bmatrix} 0 & 0.060779 & -0.096404 & 0.024017 \\ 0 & -0.49965 & 0.84993 & -0.18496 \\ 0 & 2.174 & -4.2875 & 2.127 \end{bmatrix}.$$

The model inputs associated with the above B matrix are supply air temperature, supply air flow setpoint, and ambient temperature, respectively.

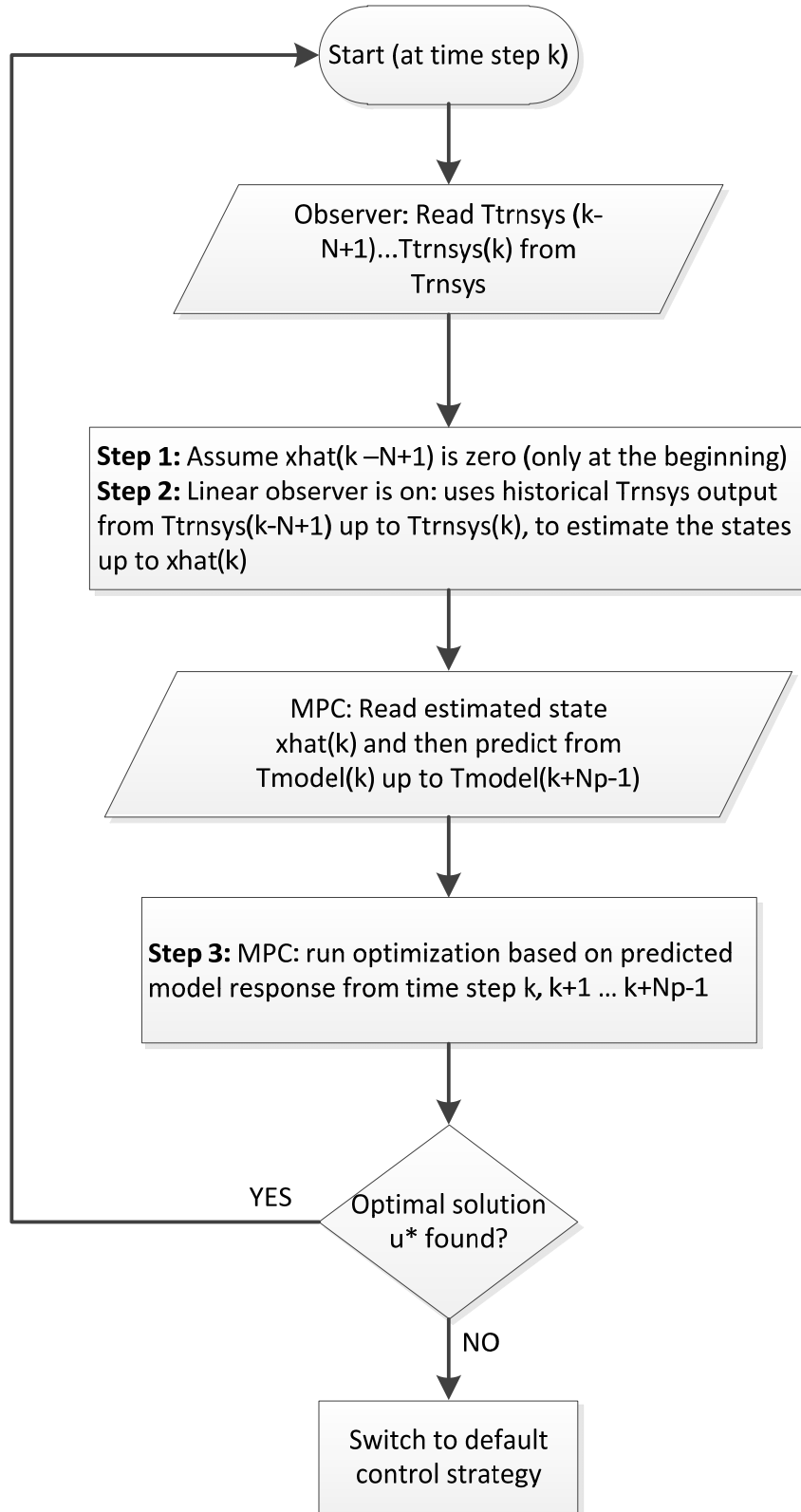
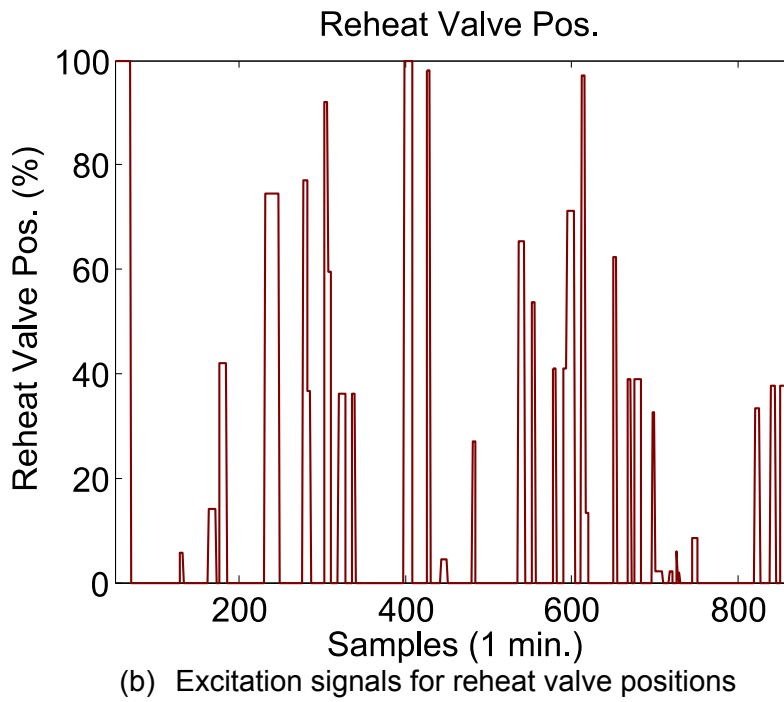
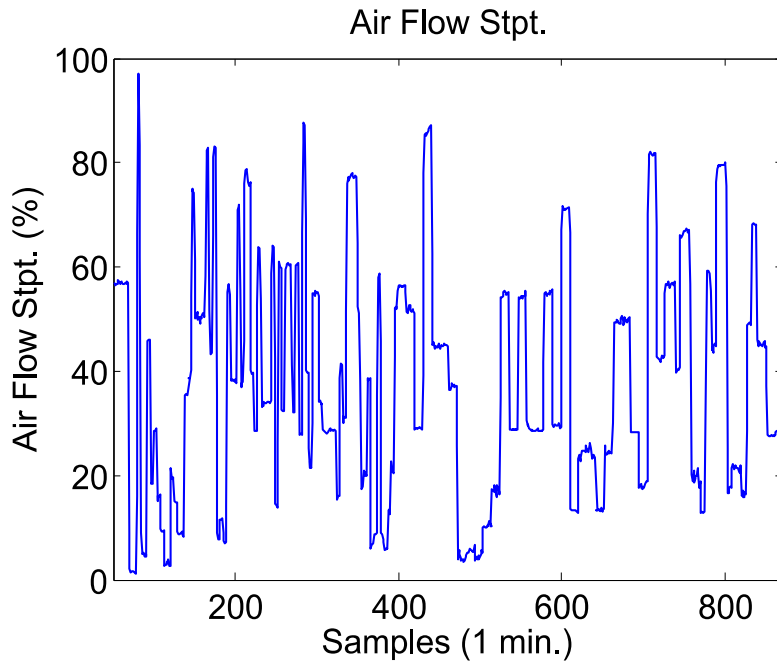
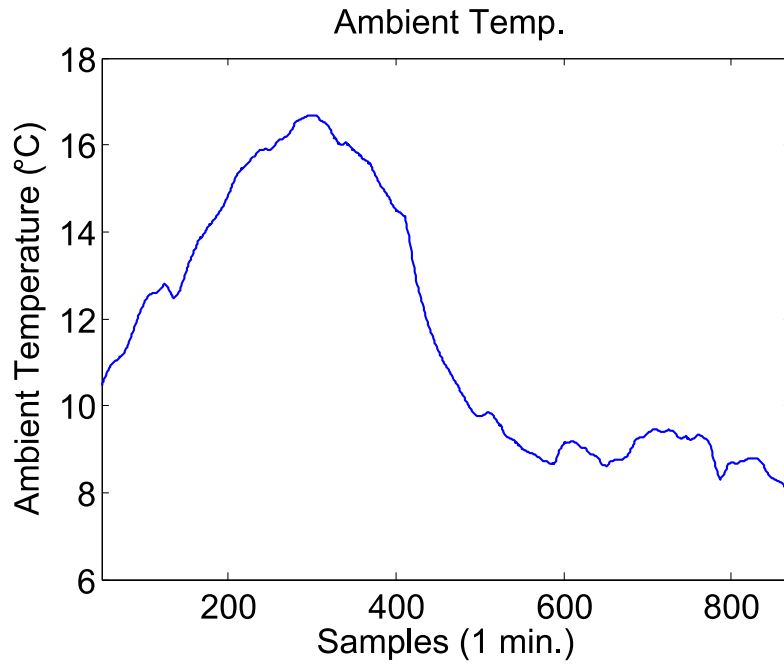


Figure A.2.5.2 Flow chart of MPC operation with state observer and its interactions with the TRNSYS model





(c) Ambient Temperature

Figure A.2.5.3 Input signals for system identification of zones in UTRC L Building testbed (Data: Nov. 25, 2011; Room: CR27)

Appendix 3.2

Building 101 Simulation Based MPC Study

Cost Function

$$\begin{aligned}
 & \sum\{z \text{ in } 1 \dots nz, i \text{ in } 1 \dots N\} \left(\begin{aligned}
 & 5000 * s[z,i] * s[z,i] + \text{Penalty on comfort violations} \\
 & 500 * s2[z,i] * s2[z,i] + \\
 & 5 * du[z,1,i] * du[z,1,i] + \text{Penalty on variations of control inputs} \\
 & 100 * du[z,2,i] * du[z,2,i] + \\
 & 1 * cpa * (u[z,1,i] - DAT[i]) * u[z,2,i] * (maxflowZone[z]/3600) / (VAVcoi1_eff^{0.78}) + \\
 & \sum\{i \text{ in } 1 \dots N\} (3 * (cpa * DX[i] * (\sum\{z \text{ in } 1 \dots 8\} u[z,2,i] * (maxflowVAV[z]/3600)))) / (0.1 + DX_COP[i]) + \\
 & \sum\{i \text{ in } 1 \dots N\} (3 * Pfan[i]); \text{Fan energy}
 \end{aligned} \right)
 \end{aligned}$$

VAV energy ←
DX coil energy ←

Constraints

Bounds on decision variables

```

param DAT_min;
param DAT_max;

var DAT {j in 1 .. N} >= DAT_min, <= DAT_max ;
    
```

Zone temperature dynamics (state-space model)

```

subject to zone_temp_est_init {z in 1..nz}:
y[z,1] = sum{m in 1..ns} C[z,m] * xhat0[z,m,1];

subject to state_const_init {z in 1..nz, m in 1..ns}:
xhat[z,m,2] = sum{n in 1..na} A[z,m,n] * xhat0[z,n,1] + sum{l in 1..nc} B[z,m,l]*u[z,l,1] + B[z,m,nc+1]*w[1];

subject to zone_temp_est {z in 1..nz, j in 2..N}:
y[z,j] = sum{m in 1..ns} C[z,m] * xhat[z,m,j];

subject to state_const {z in 1..nz, m in 1..ns, j in 2..N}:
xhat[z,m,j+1] = sum{n in 1..na} A[z,m,n] * xhat[z,n,j] + sum{l in 1..nc} B[z,m,l]*u[z,l,j] + B[z,m,nc+1]*w[j];
    
```

Figure A.3.2.1 Example AMPL code for Building 101 MPC case study

Appendix 3.4

As noted by Rawlings and Mayne^{A1}:

“Model predictive control has its roots in optimal control. The basic concept of MPC is to use a dynamic model to forecast system behavior and optimize the forecast to produce the best decision – the control move at the current time”

The successful implementation of this idea requires a dynamic mathematical model that can simulate the future behavior of the system with acceptable accuracy. In particular, it may be necessary to incorporate estimates of the future disturbances applied to the system. Secondly, we must be able to ‘solve’ the resulting optimal control problem quickly and accurately so that the required control value is available in a timely way. Thus, it is of interest to study the underlying control problem(s) and their numerical solution.

In this Section we consider several optimal control formulations for energy/cost-efficient cooling of a simple, single-zone room. To focus ideas we consider a scenario with

- exterior wall
- *thermal storage*- high thermal capacitance features of the building interior
- *room air* - temperature, occupied zones

A notional view of the room is shown in Figure (3.4.1); thermal energy storage is modeled in the solid circles which depict the

- wall interior temperature (T_i)
- storage temperature (T_s)
- room-air temperature (T_a)

Four energy exchange mechanisms are modeled:

1. conduction through the exterior wall from (T_i) to T_a
2. radiant exchange between (T_i) and T_s
3. convection from (T_i) to T_a
4. convection from T_s to T_a

^{A1} J.B.Rawlings and D.Q.Mayne, Model Predictive Control: Theory and Design, Nob Hill Publishing, Madison, WI, 2009

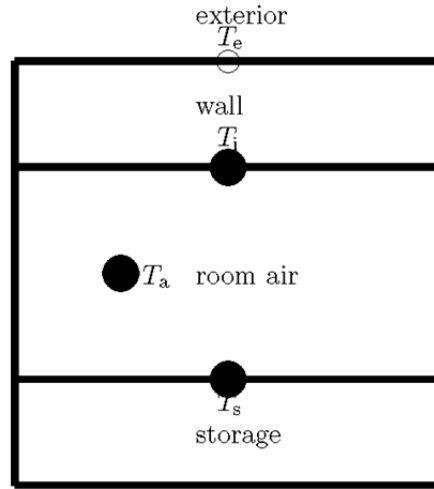


Figure A3.4.1 Notional View of Single Zone

Four energy exchange mechanisms are modeled:

- 1) q_{cond} - conduction through the exterior wall from T_i to T_e
- 2) q_{rad} - radiation from T_i to T_s
- 3) q_{conv_i} - convection from T_i to T_a
- 4) q_{conv_s} - convection from T_s to T_a

With these energy-exchange mechanisms, the *lumped* dynamic model is

$$C_i \frac{dT_i}{dt} = -(q_{\text{cond}} + q_{\text{rad}} + q_{\text{conv}_i})$$

$$C_s \frac{dT_s}{dt} = (q_{\text{rad}} - q_{\text{conv}_s})$$

$$C_a \frac{dT_a}{dt} = (q_{\text{conv}_i} + q_{\text{conv}_s} - C(u))$$

where the C_k values ($k \in \{i, s, a\}$) are thermal capacitances, and $C(u)$ is the cooling delivered to the room-air using electrical input power u .

The conduction term is given by a simple one-dimensional model as

$$q_{\text{cond}} = \frac{kA}{\Delta} (T_i - T_e).$$

Radiant exchange between the two interior surfaces is modeled as

$$q_{\text{rad}} = \sigma A \left(\frac{\epsilon_i \epsilon_s}{\epsilon_i + \epsilon_s - \epsilon_i \epsilon_s} \right) (T_i^4 - T_s^4).$$

If the surface temperatures are reasonably close, the radiant exchange can be approximated by the linear model

$$q_{\text{rad}} = \sigma A \hat{T}^3 \left(\frac{\epsilon_i \epsilon_s}{\epsilon_i + \epsilon_s - \epsilon_i \epsilon_s} \right) (T_i - T_s),$$

where \hat{T} is a suitable mean temperature. Finally, the convection terms are given by

$$q_{\text{conv}_k} = (hA)_k (T_k - T_a), \quad k \in \{i, s\}$$

In summary, with the linearized model for radiant exchange the dynamics of our system can be written as

$$\dot{\mathbf{z}}(t) = \mathbf{f}(t, \mathbf{z}(t), u(t)) = \mathbf{A} \mathbf{z}(t) + \begin{bmatrix} \frac{kA}{C_i \Delta} T_e(t) \\ 0 \\ \frac{-C(u(t))}{C_a} \end{bmatrix}, \quad (\text{A.3.4.1})$$

where

$$u(t) \in \Omega = \{0\} \cup [u_{\min}, u_{\max}], \quad \text{and} \quad \mathbf{z}(t) = \begin{bmatrix} T_i(t) \\ T_s(t) \\ T_a(t) \end{bmatrix}. \quad (\text{A.3.4.2})$$

The specific structure of the \mathbf{A} -matrix may be deduced from the previous discussion. In the next section we formulate an optimal control problem for these dynamics.

Optimal Control Problem

Whereas the primary focus of our optimization study is minimal energy use, to avoid trivialities it is necessary to place some restrictions on the temperature histories. To this end we formulate a discomfort metric, namely

$$D = \int_0^{t_f} c(t) \Psi(T_a(t), T_{\min}, T_{\max}) dt, \quad (\text{A.3.4.3})$$

where

$$\Psi(T, T_{\min}, T_{\max}) = \begin{cases} (T - T_{\min})^2 & T < T_{\min} \\ (T - T_{\max})^2 & T > T_{\max} \\ 0 & \text{otherwise,} \end{cases}$$

and where c is a *zero-one* function, the characteristic function of the occupied time interval. With $T_{\min} = T_{\max}$, the function Ψ is a quadratic that penalizes variation in room-air temperature, and with $T_{\min} < T_{\max}$ there is a finite *comfort range* with zero quadratic penalty.

In formulating the power cost we admit time-varying power rates and define our cost-functional as

$$J[u] = \mu_p \int_0^{t_f} r(t) u(t) dt + \mu_D D, \quad (\text{A.3.4.4})$$

where $r > 0$ is a given function specifying the time-varying cost of power. The parameters $\mu_p, \mu_D > 0$ admit a trade-off of the power-cost and discomfort metrics.

We anticipate that the exterior wall temperature T_e , the power-rate r , and the characteristic function c will be given over a 24 hour period and that the parameter $\mu_p, \mu_D > 0$ are given. We take $t_f = 24$ (h) and seek *periodic boundary conditions* $\mathbf{z}(0) = \mathbf{z}(t_f)$ and a control function u to minimize the cost (A.3.4.4) subject to the dynamics (A.3.4.1 – 3.4.2).

Necessary Conditions

We apply the *Minimum Principle*^{A2 A3} to our problem and begin by defining the variational Hamiltonian

$$H(t, \lambda_0, \lambda_z, \mathbf{z}, u) = \left\langle \begin{pmatrix} \lambda_0 \\ \lambda_z \end{pmatrix}, \begin{pmatrix} f_0(t, \mathbf{z}, u) \\ \mathbf{f}(t, \mathbf{z}, u) \end{pmatrix} \right\rangle = \langle \lambda_z, \mathbf{A}\mathbf{z} \rangle + \lambda_a \frac{C(u)}{C_a} + \lambda_0 (\mu_p r(t) u + \mu_D c(t) \Psi(T_a)) \quad (\text{A.3.4.5})$$

where $z \in \mathbb{R}^3$ is given in display A.3.4.2 and the adjoint vector λ_z is defined similarly.

The *Minimum Principle* requires that the scalar $\lambda_0 \geq 0$; we assume that $\lambda_0 \neq 0$ and normalize the adjoint system with the choice $\lambda_0 = 1$.

Adjoint System

Evolution of the adjoint (λ_z) is governed by the inhomogeneous linear system:

$$\dot{\lambda}_z(t) = -\mathbf{A}^T \lambda_z(t) - \begin{bmatrix} 0 \\ 0 \\ \mu_D c(t) \frac{\partial \Psi}{\partial T_a} \end{bmatrix} \quad (\text{A.3.4.6})$$

^{A2} G. Leitmann, *The Calculus of Variations and Optimal Control*, Plenum Press, 1981.

^{A3} L.S. Pontryagin, V.G. Boltyanski, R.V. Gamkrelidze, and E.F. Mischenko, *The Mathematical Theory of Optimal Processes*, Wiley-Interscience, 1962.

Optimality

We consider that part of the variational Hamiltonian that depends (explicitly) on the control (u). Since the electrical power cost function $r(t)$ and the thermal capacitance of the air (C_a) are positive, we factor these out

$$\hat{H}(u) \stackrel{\Delta}{=} \left(\frac{C_a}{r(t)} \right) H_{\text{cont}}(u) = \underbrace{(\mu_p C_a)}_{\stackrel{\Delta}{=} \hat{\mu}_p \geq 0} u - \underbrace{\left(\frac{\lambda_a(t)}{r(t)} \right)}_{\stackrel{\Delta}{=} \hat{\lambda}_a(t)} C(u), \quad (\text{A.3.4.7})$$

where $C(u)$ (the cooling rate for a given power input) is modeled as

$$C(u) = \text{cop}(u) \times u, \quad u \in \Omega = \{0\} \cup [\underline{U}, \bar{U}], \quad 0 < \underline{U} \leq \bar{U}. \quad (\text{A.3.4.8})$$

Here the function $\text{cop}(u)$ represents the *coefficient of performance* and is a given positive function of the applied power (u). In the following we scale the units of input-power so that $\bar{U} = 1$; thus the time-varying weight (r) in the cost-functional is the cost of *maximum power*.

The *Minimum Principle* requires that we characterize the value(s) of the control that minimize \hat{H} over the set Ω . Since \hat{H} is continuous and the domain Ω is compact minimizers exist; since \hat{H} is smooth there are four possibilities to consider for *extremal control* (u^*):

1. $u^* = \underline{U}$, which requires that $\frac{\partial \hat{H}}{\partial u} \Big|_{u_{\min}} \geq 0$,
2. $u^* = 1 = \bar{U}$, which requires that $\frac{\partial \hat{H}}{\partial u} \Big|_1 \leq 0$,
3. $u^* = u_{\text{int}}$ occurs at an interior point with $\frac{\partial \hat{H}}{\partial u} \Big|_{u_{\text{int}}} = 0$ and $\frac{\partial^2 \hat{H}}{\partial u^2} \Big|_{u_{\text{int}}} \geq 0$
4. $u^* = 0$ \$, that is, the isolated point in Ω - zero power.

Affine cop(u)

We consider a case wherein

$$\text{cop}(u) = \alpha + \beta u \quad \alpha, \beta > 0.$$

To examine the possibilities we consider graph(s) of $\hat{H}(u)$ for generic values of $\mu_p, \alpha, \beta, \underline{U}$ and for several values of $\hat{\lambda}_a$ (see Figure A. 3.4.2)

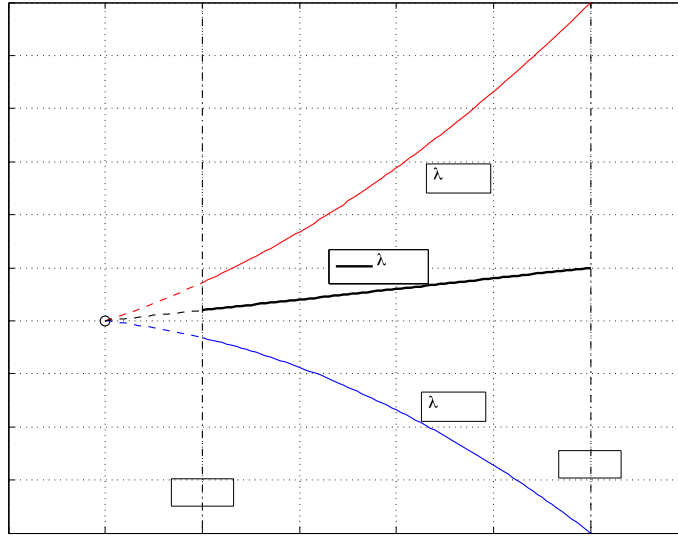


Figure A.3.4.2 Graphs of $\hat{H}(u)$ for several $\hat{\lambda}_a$ values

We note that *interior minimizers* are not feasible, since $u_{\text{int}} < 0 < \underline{U}$. Furthermore, there is a critical value of $\hat{\lambda}_a = \hat{\lambda}_a^{\text{crit}}$ such that for $\hat{\lambda}_a > \hat{\lambda}_a^{\text{crit}}$ the upper bound, $u = \bar{U} = 1$ provides a global minimizer for $\hat{H}(u)$, and for $\hat{\lambda}_a < \hat{\lambda}_a^{\text{crit}}$ the value $u = 0$ provides a global minimizer. This critical value is

$$\hat{\lambda}_a^{\text{crit}} = \frac{\hat{\mu}_p 1}{r(t) C(1)} > 0.$$

Optimal controls are *bang-bang* and $S(\lambda_a) \triangleq \left(\hat{\lambda}_a^{\text{crit}} - \frac{\lambda_a}{r(t)} \right)$ is a *switching function* with

$$u^*(t) = \begin{cases} 0 & \text{if } S(\lambda_a(t)) > 0 \\ 1 & \text{if } S(\lambda_a(t)) < 0. \end{cases} \quad (\text{A.3.4.9})$$

Quadratic cop(u)

We now consider a case wherein

$$\text{cop}(u) = \alpha + \beta u + \gamma u^2$$

with data specifications:

- $\text{cop}(0) = \alpha > 0$
- $\max_{[\underline{U}, \bar{U}]} \text{cop}(u) = v > \alpha$
- $\arg \max \text{cop} = \ell, \quad 0 < \underline{U} < \ell < \bar{U}.$
- $C'(u)|_{u=\bar{U}} = \text{cop}(\bar{U}) + \bar{U} \text{cop}'(u)|_{\bar{U}} > 0$

From these specifications we find that:

$$\beta = \frac{2(v-\alpha)}{\ell} > 0 \quad \text{and} \quad \gamma = \frac{-(v-\alpha)}{\ell^2} < 0.$$

The final specification guarantees that $C(u)$ is an increasing function for $u \leq \bar{U} = 1$. Clearly, it would not make sense to use more power if it produced less cooling.

For current purposes, as well as later discussion, it's useful to exploit the general structure of the variational Hamiltonian (A.3.4.5) and to interpret the $\arg \min H$ -operation geometrically. The control (u) dependent part of the variational Hamiltonian (A.3.4.5) is

$$H_c(u) = \left\langle \begin{pmatrix} \lambda_0 \\ \lambda_a \end{pmatrix}, \begin{pmatrix} \mu_p r(t) u \\ \frac{-C(u)}{C_a} \end{pmatrix} \right\rangle = r(t) \left\langle \begin{pmatrix} \lambda_0 \\ \frac{\lambda_a}{r(t)C_a} \end{pmatrix}, \begin{pmatrix} \mu_p u \\ -C(u) \end{pmatrix} \right\rangle.$$

The vector on the right in this inner-product is the (augmented) state-rate and captures the time-rates of the control-dependent parts of the cost function and the state. Since $r(t) > 0$ it can be safely factored. The locus of admissible points is shown in Figure 3.4.3. Note that the other terms in the variational-Hamiltonian are independent of the control and do not affect the $\min - H$ operation.

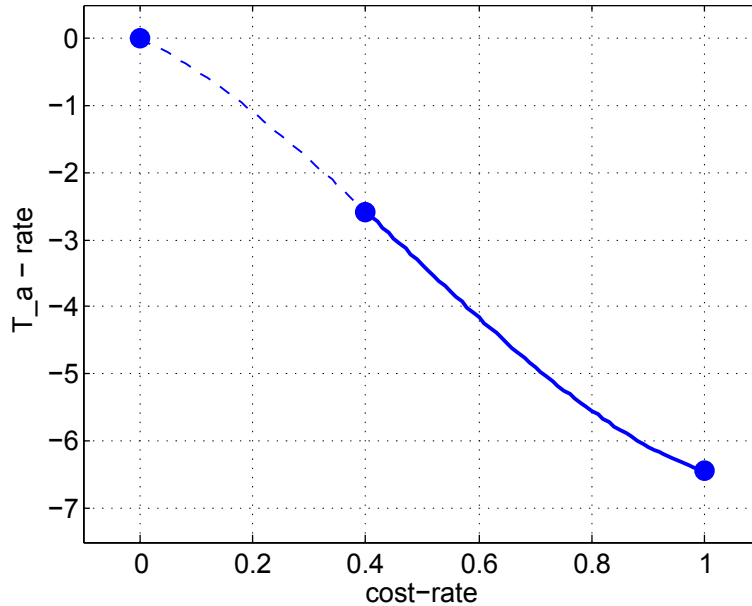


Figure 3.4.3 Velocity set

Next, consider a fixed vector with components $\begin{pmatrix} 1 \\ \hat{\lambda}_a \end{pmatrix}$, where $\hat{\lambda}_a \triangleq \frac{\lambda_a}{r(t)C_a}$ (see Figure

A.3.4.4).

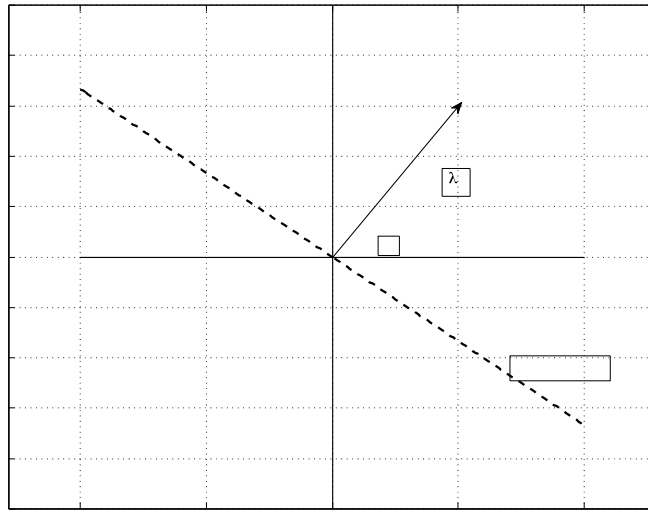


Figure A.3.4.4 Adjoint vector in state-rate space

The orthogonal complement $\{\hat{\lambda}_a\}^\perp$ is the subspace of vectors orthogonal to (the span of) $\hat{\lambda}_a$, and for points in this subspace we have $H_c = 0$. Any translation of this subspace along the $+\hat{\lambda}_a$ direction has $H_c(u) = \chi$, a positive real, whereas any translation along the opposite direction is a set of points with negative real values for the function H_c .

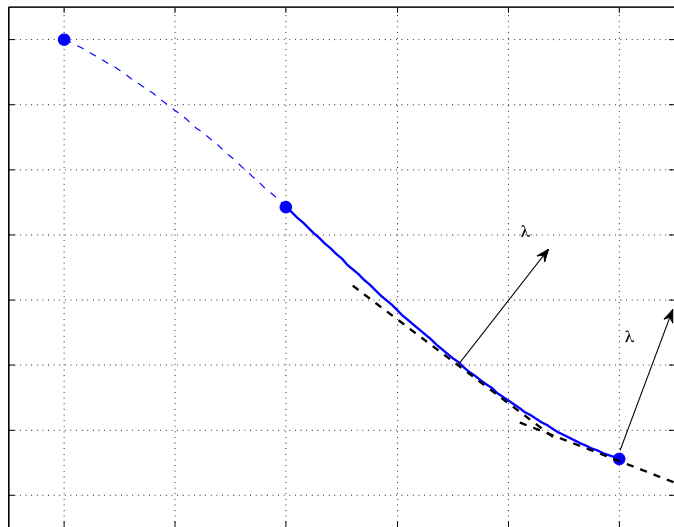


Figure A.3.4.5 Adjoint vector and velocity set

The ideas underlying Figures A.3.4.3 & A.3.4.4 are combined in Figure A.3.4.5. From this analysis we find there are two critical values of $\hat{\lambda}_a$:

$$\hat{\lambda}_a^1 = \frac{\mu_p}{\alpha + 2\beta\ell + 3\gamma\ell^2} > 0,$$

and

$$\hat{\lambda}_a^{\text{II}} = \frac{\mu_p}{\alpha + 2\beta + 3\gamma} = \frac{\mu_p}{C'(u)|_{u=\bar{U}=1}} > 0$$

The results of the $\min H$ -operation are

$$u^*(t) = \begin{cases} 0 & \text{if } \hat{\lambda}_a(t) < \hat{\lambda}_a^{\text{I}} \\ u_{\text{int}} & \text{if } \hat{\lambda}_a^{\text{II}} \leq \hat{\lambda}_a(t) \leq \hat{\lambda}_a^{\text{I}} \\ 1 & \text{if } \hat{\lambda}_a^{\text{II}} < \hat{\lambda}_a(t), \end{cases}$$

where

$$u_{\text{int}} = \left(\frac{-\beta}{3\gamma} \right) + \sqrt{\left(\frac{\beta}{3\gamma} \right)^2 + \frac{\mu_p - \hat{\lambda}_a \alpha}{3\gamma}}.$$

Transversality

For our periodic boundary condition on the state, the transversality conditions^{A4} are:

$$\lambda_z(t_f) = \lambda_z(0). \quad (\text{A.3.4.10})$$

Computational Approaches: Affine cop(u)

The combined state/adjoint system along with the periodic boundary conditions on (\mathbf{z}, λ_z) constitute a boundary-value in six dependent variables. In principle, one could try to use a *shooting method* (for multiple shooting see Stoer and Bulirsch^{A5}). However, the Hamiltonian structure of the state-adjoint system implies that the combined eigenvalues occur in symmetric pairs about the *imaginary axis*. Indeed, for typical system parameters we find the eigenvalues of the state/adjoint system are:

$$\sigma = \pm 0.015 / h, \pm 0.153 / h, \pm 19.579 / h.$$

For the fastest growing of these over the time interval $[0, 24h]$ the growth is

$$\exp(19.579 / h \times 24h) > 10^{204} !$$

While a *parallel-shooting* approach may mitigate the computational sensitivity, it seems that any approach based on solving the boundary-value problem *ab initio* is likely to be a challenge.

NLP Formulation (Affine cop)

The Maximum Principle has revealed that an optimal control takes only the values in $\{0, \bar{U}\}$. We assume there are N (a finite-number) of switches (*i.e.* no chattering junctions). Of course, we do not know the value N . Since the switching function depends on the adjoint (λ_a) and since the adjoint variables satisfy a periodic boundary condition, we further assume that on the initial and final sub-arcs the optimal control has the same value ($u^* = 0$) so that

$$S(\lambda_a(0)) = S(\lambda_a(t_f)) < 0, \text{ and the number of switches } N \text{ is even.}$$

^{A4} J.L. Speyer, Periodic Optimal Flight, Journal of Guidance, Control, and Dynamics, (19) 1996, 745-755.

^{A5} J.Stoer and R.Bulirsch, Introduction to Numerical Analysis, Springer-Verlag, 1992, Chap. 7

With this structure in mind we formulate a (family of) finite-dimensional nonlinear programming problem(s) (NLP) wherein the unknowns are the initial states and the switching times, the cost functional is J (3.4.4) and the equality constraints are the periodic boundary conditions, viz: $\mathbf{z}(t_f) - \mathbf{z}(0) = 0$. The parameter of the family of problems is N . We numerically solve the initial-value problem (A.3.4.1 and A.3.4.2 with the initial states), alternating between cooling-off ($u^*(t) = 0$) and cooling-on ($u^*(t) = \bar{U}$) sub-arcs as specified by the switching times. For this purpose it's important to ensure the switching times are monotone increasing; we impose a minimum separation time between consecutive switch times. In the NLP setting this is realized as a set of $(N - 1)$ linear inequalities.

A *solution* that emerges from this sequence of NLP problems can be tested by the Minimum-Principle analysis. This becomes computationally feasible because with the switching points known one can formulate conditions on the costate $\lambda_z(0)$. Such an approach was demonstrated^{A6}.
%

Two Cooling Periods: $N = 4$

As an instance of an NLP formulation, we consider a problem with four switch points. The NLP problem has seven variables and three equality constraints (periodicity of the temperatures - T_i, T_s, T_a). The variation of power-cost with time-of-day is shown in Figure A.3.4.6

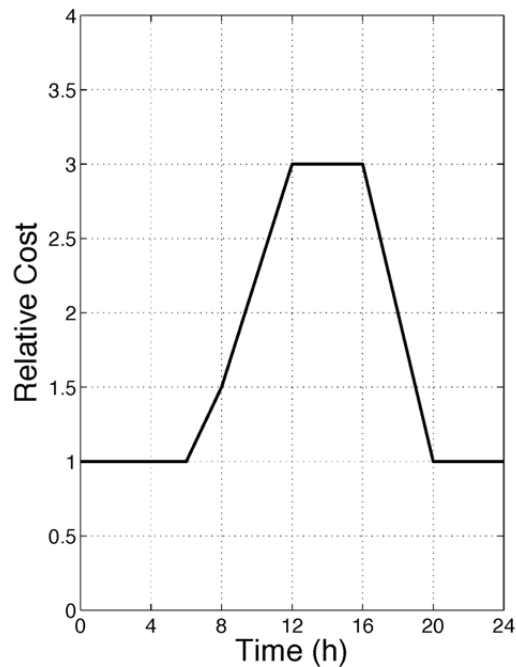


Figure 3.4.6 Power Cost function $(r(t))$

^{A6} J.Z.Ben-Asher, J.A.Burns, and E.M.Cliff, Time optimal slewing of a flexible structure, Journal of Guidance, Control, and Dynamics, (15) 1992, 360 - 367.

A **Matlab** code was implemented and the *active-set* algorithm of **fmincon** [opt_toolbox] was used to *solve* the NLP problem. The NLP problem was numerically challenging; perhaps reflecting some issues in the dynamic model (comments later). We imposed a heavy weight on the *discomfort metric* (D);

$$\mu_p = 1 \quad \text{and} \quad \mu_D = 1. \times 10^{04} .$$

The electrical power was limited to 20 w and produced a maximum cooling of 140 w which reduces the air temperature at $2.7^\circ\text{C}/h$. The thermal capacitance of the air is relatively small, with $\frac{C_i}{C_a} \approx 9$ and $\frac{C_s}{C_a} \approx 10$. We conjecture that the relatively low control authority makes the periodicity requirements on T_s and T_i particularly challenging.

One result is shown in Figure A.3.4.7. The (solid) black line represents the 'exterior' temperature (T_e); this is part of the problem data. The (dash-dot) red box defines the 'comfort constraint - the zone-air temperature (T_a - the (solid) red-line) is supposed to be in the box during the 'occupied time' ($7.5 \leq t \leq 18.5$). This specification is also problem data. The (solid) blue line is the interior wall temperature (T_i); it is conductively coupled to the exterior temperature. The (solid) green line is the temperature of the *storage mass* (T_s). Note that whereas the state histories T_i and T_s are smooth, the history of T_a is only piecewise smooth since it is explicitly driven by the (discontinuous) control.

At $t = 0$, the interior wall temperature (T_i) is the highest so it begins to decrease, while the storage wall temperature (T_s) is lowest and begins to increase. The air, initially at an intermediate temperature, exchanges energy with both of these elements and begins a slow decrease. At $t = 03:32$ the control comes on and continues until $t = 07:16$; T_a is reduced to near the comfort lower bound at $T = 22^\circ\text{C}$. T_i , and T_s are also decreased toward local minima. As the exterior temperature (T_e) rises the other temperatures are driven upward until at $t = 13:05$ when T_a approaches the upper comfort bound. A second cooling period begins and lasts until 20:34. Lastly, with the cooling off and the exterior temperature decreasing the variables T_i, T_s and T_a return to their initial values. Cooling uses 224 wh of energy and the power-cost is 0.4242 (units). The *discomfort metric* is quite small; $D \approx 1. \times 10^{-09}$. Decreasing the weight μ_D by several orders of magnitude has little effect on the state/control histories. With $\mu_D \approx 1$ the state T_a begins to exceed the upper bound T_{\max} .

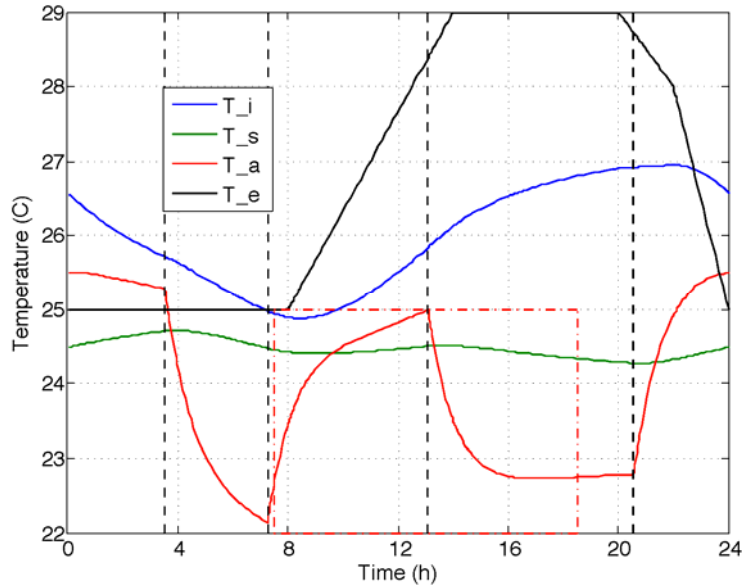


Figure A.3.4.7 Temperature histories with two cooling periods

Three Cooling Periods: N=6

The results from the Two Cooling Period case were used to initialize a case with three cooling periods. As seen in Figure A.3.4.8 T_s begins slightly higher than the previous case, the initial cooling period begins significantly earlier at $t = 01:54$ and continues until $t=07:10$. With the cooling off, the zone-air temperature reaches the upper comfort level at 13:34 and the cooling comes on briefly until 14:01. The zone-air temperature again rises to the upper comfort level and the cooling comes on for the third time at $t=15:16$. The effect of the additional cooling period is to maintain the zone-air temperature near the upper comfort level.

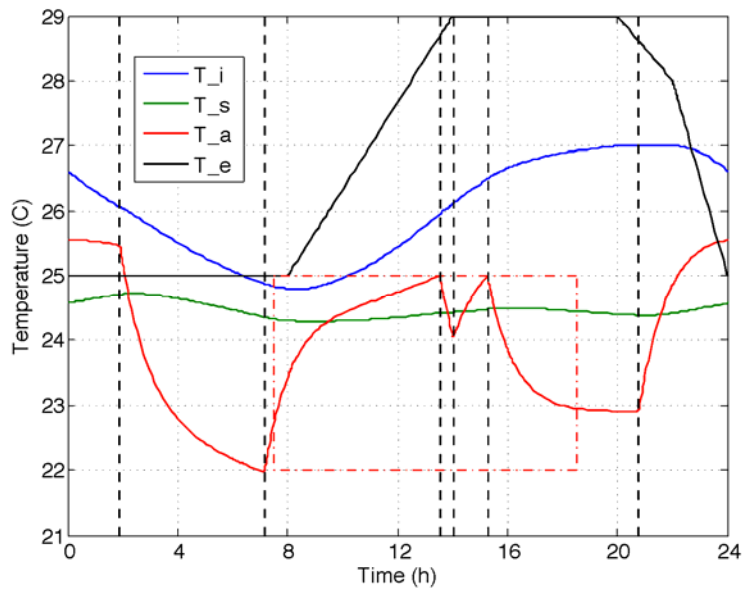


Figure A.3.4.8 Temperature histories with three cooling periods

Four Cooling Periods: N=8

The results from the Three Cooling Period case were used to initialize a case with four cooling periods. Here (see Figure A.3.4.9) the initial cooling period (01:37, 07:16) is slightly modified from the previous case. The 2nd and 3rd cooling periods are brief (approximately 1/2 hour) and effectively maintain the zone-air temperature near the upper comfort level.

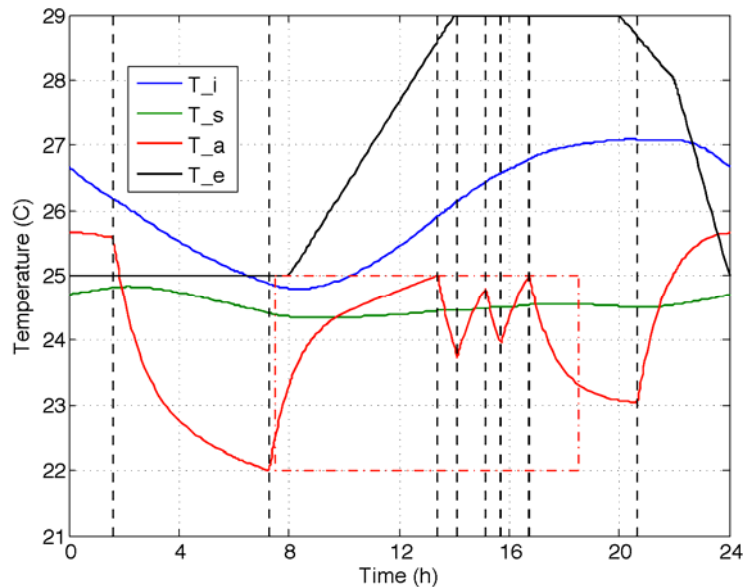


Figure A.3.4.9 Temperature histories with four cooling periods

Five Cooling Periods: $N=10$

The results from the Four Cooling Period case were used to initialize a case with five cooling periods. In this case the final cooling period begins after the occupied period (see Figure A.3.4.10) during the period of lowest power-cost (see Figure A.3.4.6). Note that the (red) T_a trajectory passes through the upper-right corner of the comfort-constraint box. If the 8th switch (off at $t = 17:28$) had been a little earlier, the zone-air temperature would have exceeded the upper-comfort bound; if it had occurred a little later additional high-cost cooling would have been applied. This result is perhaps from a different family of local minima than was seen in the earlier cases. It must be noted, however, that due to the minimum-switch-time constraint, the N -family of NLP problems are not nested. Thus, for example, an $N = 8$ solution can not be trivially made feasible for an $N = 10$ problem.

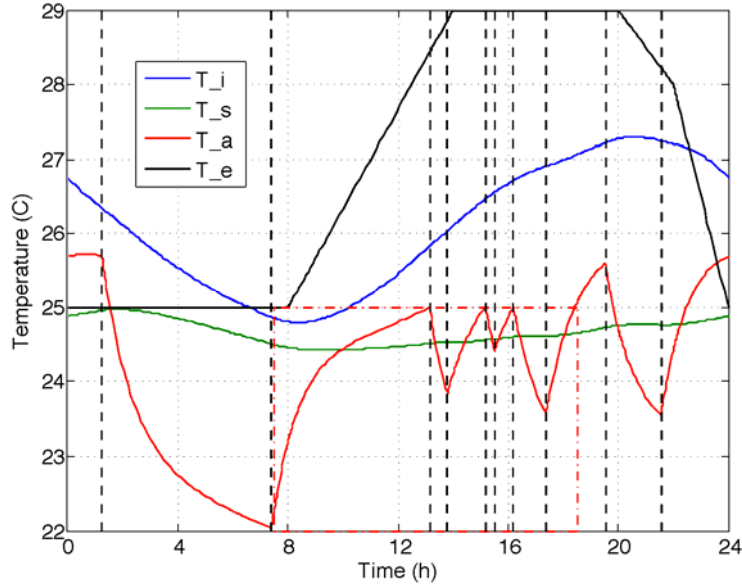


Figure A.3.4.10 Temperature histories with five cooling periods

Summary

The performance attained in the four cases is summarized in Table A.3.4.1; switch times are summarized in Table A.3.4.2. We see that the additional cooling periods lead to sequentially lower power-costs but that the trend in energy-used is not monotonic. In these numerical results none of the minimum-time-spacing constraints were active.

There is no claim that the NLP *solutions* presented here are actual minimizers. The optimizer stopped because the changes in the NLP parameters or the cost functional were sufficiently small (10^{-04}). We have not verified that any of the candidate switching sequences satisfy the Minimum Principle.

Table A.3.4.1 Summary of Results

Cooling Periods	Power-Cost	Energy Used (wh)
2	0.4241	224.1
3	0.3561	224.6
4	0.3246	217.0
5	0.2819	203.9

Table A.3.4.2 Switch Times

Cooling Periods	2	3	4
On	4.221	1.893	1.614
Off	7.248	7.164	7.275
On	NA	13.668	13.414
Off	NA	14.026	14.119

On	NA	15.270	15.148
Off	NA	NA	15.695
On	NA	NA	16.275
Off	20.567	20.777	20.661

NLP Formulation: Quadratic cop

For this discretization we impose a grid on the time axis; each state is approximated as a continuous, piecewise linear function whereas each control is a piecewise constant. A simple case is shown in Figure A.3.4.11.

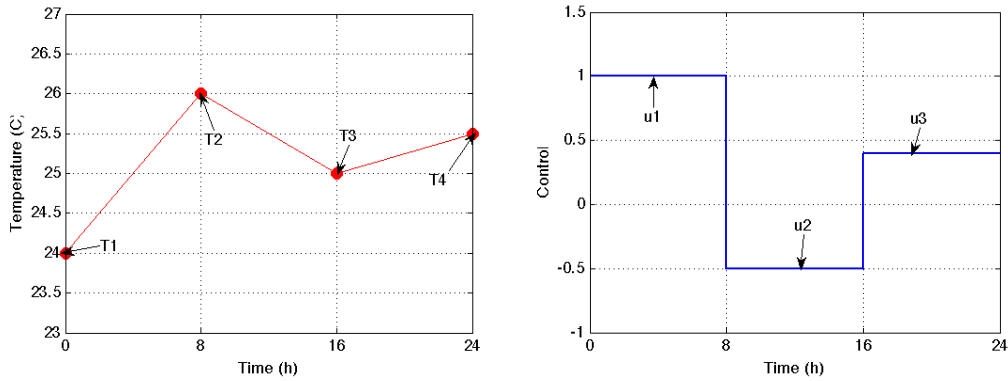


Figure A.3.4.11 Generic state (temperature) and control discretization

The NLP unknowns are the state values at the nodal points, and the control values on the intervals. The differential equations (A.3.4.1 – A.3.4.2) are (approximately) enforced by the 2nd order implicit midpoint rule. Data values at the k^{th} node denoted as $x_k \in \mathbb{R}^n, u_k \in \mathbb{R}^m$. With the state data we can evaluate $\dot{x}(\tau_k)$. Consider one such *panel*:

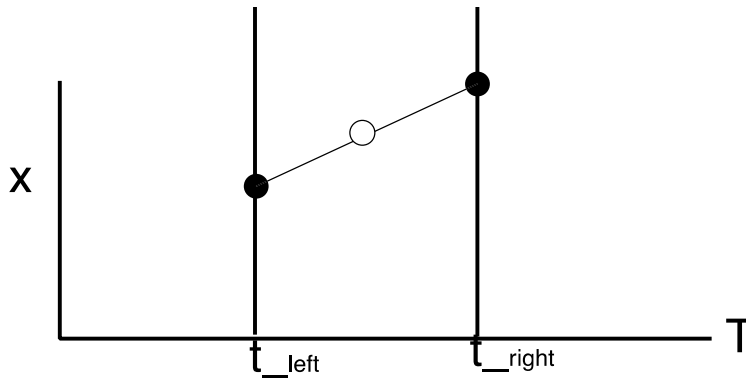


Figure A.3.4.12 Typical panel

The state at the mid-point is the simple average $x_m = (x_{k-1} + x_k) / 2$, whereas the slope is $\dot{x}_c = (x_k - x_{k-1}) / (\tau_k - \tau_{k-1})$. The *defect* is the difference

$$\text{defect} = \frac{x_k - x_{k-1}}{(\tau_k - \tau_{k-1})} - f(t_m, x_m, u_m) \in \mathbb{R}^{N_{\text{states}}}. \quad (\text{A.3.4.11})$$

Forcing the defect in Equation (A.3.4.11) to be zero implements the *implicit mid-point rule* - it is 2nd order accurate. The $N_{\text{states}} \times N_{\text{panels}}$ defects (= 0) are imposed as equality constraints in the NLP problem.

Since the defect constraint at the k^{th} panel depends only on the local states and controls (left and right), the Jacobian of the constraint-function for the NLP problem is sparse. In particular, for the k^{th} constraint we have

$$\begin{aligned} \frac{\partial c_k(Z)}{\partial x_k} &= \frac{I}{(\tau_k - \tau_{k-1})} - \frac{1}{2} \frac{\partial f(t, x, u)}{\partial x} \Big|_m \\ \frac{\partial c_k(Z)}{\partial x_{k-1}} &= -\frac{I}{(\tau_k - \tau_{k-1})} - \frac{1}{2} \frac{\partial f(t, x, u)}{\partial x} \Big|_m \\ \frac{\partial c_k(Z)}{\partial u_k} &= -\frac{\partial f(t, x, u)}{\partial u} \Big|_m \end{aligned}$$

Note that the Jacobian of these constraints is sparse; the constraint C_k depends on the local values of the states and control.

This numerical optimization scheme was implemented using the **Matlab** procedure **fmincon** with the active-set algorithm. The problem data are the same as in the Affine cop case but here we use the quadratic cop model with data $\alpha = 4.0$, $\nu = 7.0$, and $\ell = 18$.

Shown in Figure A.3.4.13 are the resulting state histories for the N=128 case. Note that the NLP problem has 512 unknowns and 384 equality constraints. We see that there are five cooling periods including one at the beginning (approximately [00, 04]) and one at the end (approximately [22, 24]). As in the affine cop case, the control switches in the late afternoon tend to keep the air-temperature near its upper bound, and the zone-air temperature exceeds the upper-bound just as the occupied period ends at 1800 h.

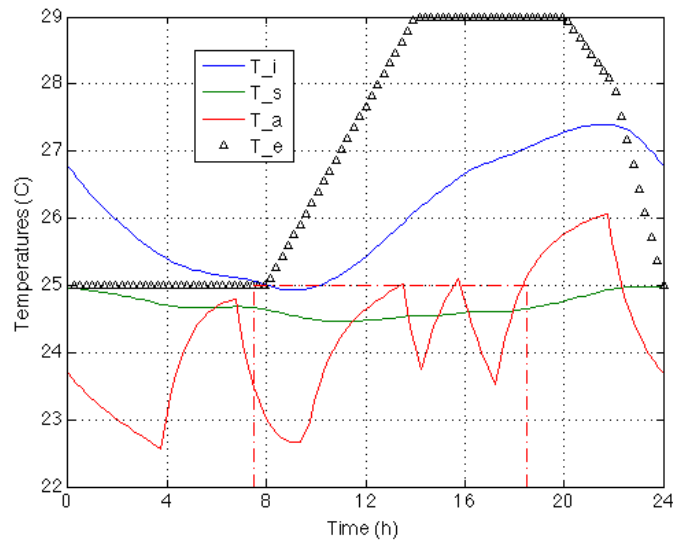


Figure A.3.4.13 State histories for N=128

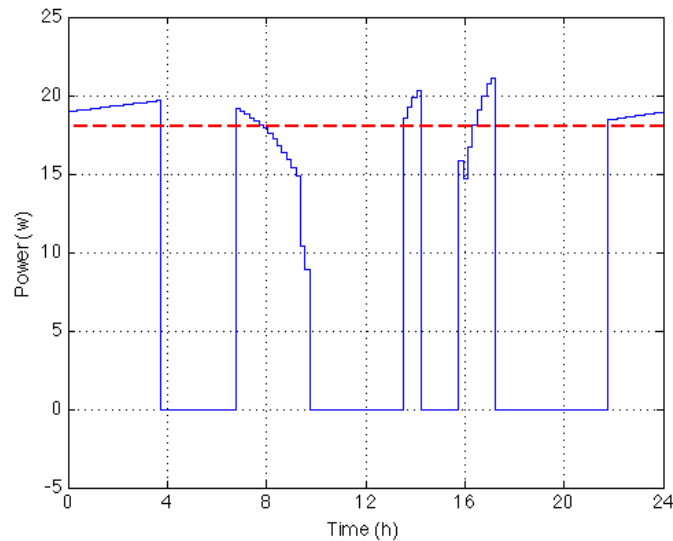


Figure A.3.4.14 Control history for N=128

The corresponding control history is shown in Figure A.3.4.14. The dashed red-line is the power-value for max cop. Recall that our optimal control analysis dictates that optimal controls should never be less that this value. The NLP results display this feature on the first, third and fifth control-on arcs, but not on the second and fourth control-on arcs. At this time we are continuing to study the results.

Max u

We study an open-loop optimal control problem for energy efficient cooling of a simple room. The goal is to provide insights for the development of an implementable control scheme based on a Model Predictive Control strategy. In this version the cost function includes a term

$$F(\max_t u(t))$$

that is, a term depending on the peak value of the control. This model captures a relatively simple version of peak-demand pricing.

In this problem the upper-bound on the control is no longer part of the problem data but is an unknown to be found as part of the problem solution. We transform the problem to a standard optimal control setting by augmenting the unknown (\bar{U}) to the state with trivial dynamics; the upper-bound is now a state-dependent control constraint

$$\dot{\bar{U}} = 0, \quad u(t) - \bar{U} \leq 0. \quad (\text{A.3.4.12})$$

The additional dynamics indicate that \bar{U} is an *unknown constant*. The dynamics of the original states are as given in Equations (A.3.4.1-A.3.4.2), whereas the cost functional (A.3.4.4) is modified to

$$J[u] = F(\bar{U}) + \mu_p \int_0^{t_f} r(t) u(t) dt + \mu_D D. \quad (\text{A.3.4.13})$$

$$H(t, \lambda_0, \lambda_z, \lambda_{\bar{U}}, \mathbf{z}, \bar{U}, u) = \langle \lambda_z, \mathbf{A}\mathbf{z} \rangle - \lambda_a \frac{C(u)}{C_a} + \lambda_0 \left(\mu_p r(t) u + \mu_D c(t) \Psi(T_a) \right) + \nu (u - \bar{U}). \quad (\text{A.3.4.14})$$

The last term in (A.3.4.14) accounts for the state-dependent control constraint; ν is the Valentine multiplier^{A7}. The adjoint system for λ_z is the same as before, whereas for $\lambda_{\bar{U}}$ we have

$$\dot{\lambda}_{\bar{U}} = \nu. \quad (\text{A.3.4.15})$$

On time intervals where $u^*(t) = \bar{U}$, ν follows from $\frac{\partial H}{\partial u} = 0$, namely

$$\nu = \frac{\lambda_a(t)}{C_a} C'(u) - \mu_p r(t), \quad (\text{A.3.4.16})$$

otherwise $\nu = 0$.

The optimality condition is unchanged from the earlier analyses, since the added term in the variational Hamiltonian is zero (one or another of the factors must be zero). The transversality conditions for λ_z are unchanged, whereas for $\lambda_{\bar{U}}$ we have:

$$\lambda_{\bar{U}}(0) = 0, \text{ and } \lambda_{\bar{U}}(t_f) = F'(\bar{U}).$$

Combining with equations (A.3.4.15, A.3.4.16) we have:

$$F'(\bar{U}) = \int_0^{t_f} \dot{\lambda}_{\bar{U}}(t) dt = \int_{t|u^*(t)=\bar{U}} \left[\mu_p r(t) - \frac{\lambda_a(t)}{C_a} \frac{C'(\bar{U})}{\ell} \right] dt. \quad (\text{A.3.4.17})$$

Equation (3.4.17) is the optimality condition for the control bound \bar{U} .

Modeling of external disturbance

^{A7} F.A. Valentine, The Problem of Lagrange with Differential Inequalities as Added Side Conditions, University of Chicago Press, 1937.

As the name implies, Model Predictive Control requires a model for the future behavior of the system including, where appropriate, the behavior of any external loads. We have studied the use of an *Internal Model* to characterize important unknown heating loads. The discussion is framed in terms of a single-zone model.

A simple thermal model for a room includes a number of interacting systems. To focus ideas we consider a (summer) cooling scenario with

- *exterior wall*
- *thermal storage*- high thermal capacitance features of the building interior
- *room air* - temperature, occupied zones

A notional view of the room is shown in Figure A. 3.4.15; thermal energy storage is modeled in the solid circles which depict the

- wall interior temperature (T_i)
- storage temperature (T_s)
- room-air temperature (T_a)

Four energy exchange mechanisms are modeled:

5. conduction through the exterior wall from (T_i) to T_a
6. radiant exchange between (T_i) and T_s
7. convection from (T_i) to T_a
8. convection from T_s to T_a

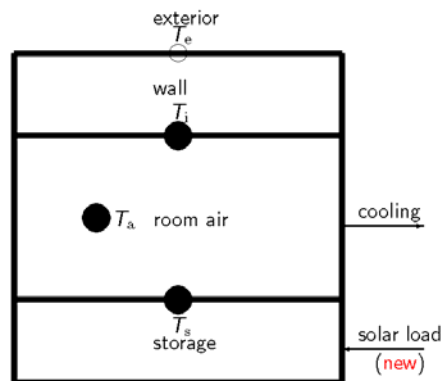


Figure A. 3.4.15 Single zone with solar load

Four energy exchange mechanisms are modeled:

- 1) q_{cond} - conduction through the exterior wall from T_i to T_e
- 2) q_{rad} - radiation from T_i to T_s
- 3) q_{conv_i} - convection from T_i to T_a
- 4) q_{conv_s} - convection from T_s to T_a

With these energy-exchange mechanisms, the *lumped* dynamic model is

$$C_i \frac{dT_i}{dt} = -(q_{\text{cond}} + q_{\text{rad}} + q_{\text{conv}_i})$$

$$C_s \frac{dT_s}{dt} = q_{\text{rad}} - q_{\text{conv}_s} + q_{\text{solar}}$$

$$C_a \frac{dT_a}{dt} = (q_{\text{conv}_i} + q_{\text{conv}_s} - q_u)$$

where the C_k values ($k \in \{i, s, a\}$) are thermal capacitances, and q_u is the cooling delivered to the room-air using electrical input power u .

The conduction term is given by a simple one-dimensional model as

$$q_{\text{cond}} = \frac{kA}{\Delta}(T_i - T_e).$$

Radiant exchange between the two interior surfaces is modeled as

$$q_{\text{rad}} = \sigma A \left(\frac{\epsilon_i \epsilon_s}{\epsilon_i + \epsilon_s - \epsilon_i \epsilon_s} \right) (T_i^4 - T_s^4).$$

If the surface temperatures are reasonably close, the radiant exchange can be approximated by the linear model

$$q_{\text{rad}} = \sigma A \hat{T}^3 \left(\frac{\epsilon_i \epsilon_s}{\epsilon_i + \epsilon_s - \epsilon_i \epsilon_s} \right) (T_i - T_s),$$

where \hat{T} is a suitable mean temperature. The convection terms are given by

$$q_{\text{conv}_k} = (hA)_k (T_k - T_a), \quad k \in \{i, s\}$$

Finally, the disturbance is given by q_{solar} an unknown *solar source* applied to the *storage mass*.

Since our interest here is in estimating exogenous we posit a simple cooling control scheme

$$q_u(t) = K(T_a(t) - T_{\text{ref}})$$

where $K > 0$ and T_{ref} is a specified reference temperature.

A *Simulink* diagram of the model is shown in Figure A. 3.4.16. Note that we have assumed that the zone air temperature is available noise-free.

multi-zone building. To formulate the associated Kalman filter we must specify noise covariances on all of the states, including S_d .

Second-order oscillator:

Given the periodic nature of the solar disturbance, it might be preferable to choose an oscillatory model for the disturbance, *viz*

$$\ddot{s}_d(t) + 2\zeta\omega_n\dot{s}_d(t) + \omega_n^2s_d(t) = 0.$$

Here we could exploit the known (nominal) period for the solar input, *i.e.* $\omega_n = \frac{2\pi}{24\text{h}}$.

We must also specify a value for the damping ratio $0 \leq \zeta \leq 1$.

Kalman filter

For each model we construct a Kalman filter for the appropriately augmented system. The filter requires four inputs:

- 1) the cooling load (q_u) provided to the system,
- 2) the external wall temperature (T_e) applied to the system,
- 3) the noisy measurement of the *storage temperature* (T_s), and
- 4) the noisy measurement of the *zone-air temperature* (T_a).

An (A,B,C,D) model for the filter was constructed for the filter using the **Matlab** routine *kalman*. A *Simulink* diagram of the system with the filter is shown in Figure A.3.4.17.

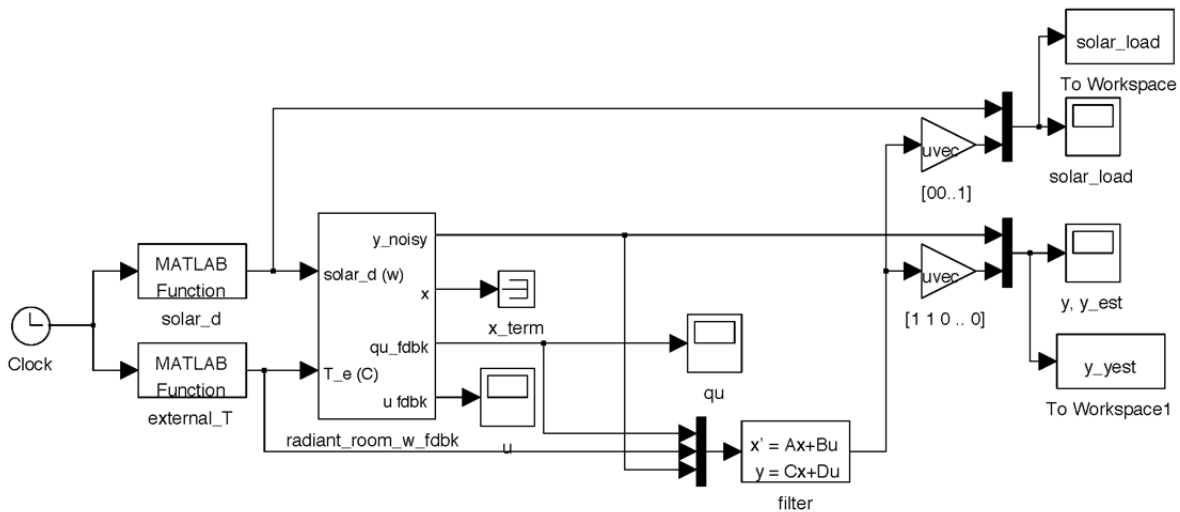


Figure A.3.4.17 Simulink diagram of combined system and filter

The system in Figure A.3.4.16 was run and adjustments were made to the control gain and reference temperature in and to the initial temperatures ($T_i(0), T_s(0), T_a(0)$) to produce reasonable periodic response histories over a 96 hour period. These are shown in Figure A.3.4.18

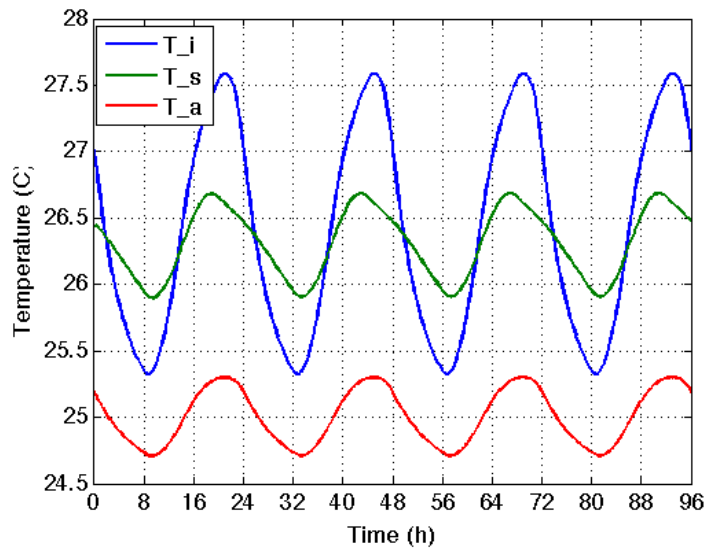


Figure A.3.4.18 Time histories of the (3) states

First-order lag:

The measured (noisy) values for the *storage temperature* along with the filtered values are shown in Figure A.3.4.19. The transient in the filtered value from its initial-value 24C takes about 8 hours but then tracking is reasonable.

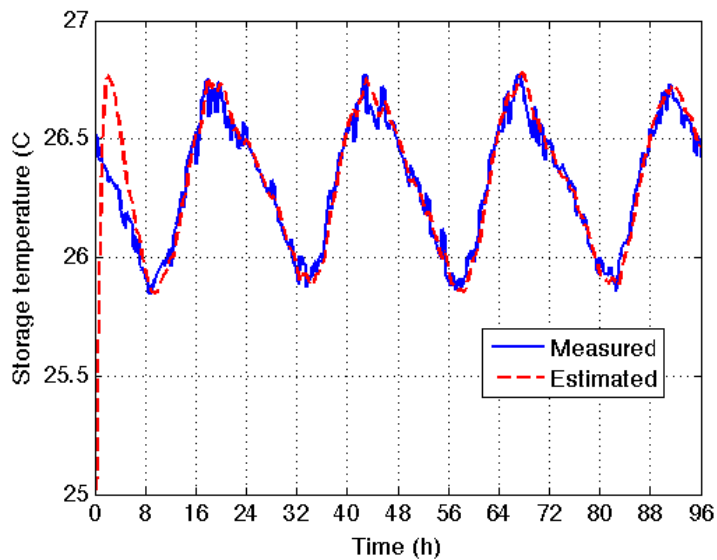


Figure A.3.4.19 Sensed and estimated storage temperatures

Similar results for the *zone-air temperature* are shown in Figure A.3.4.20

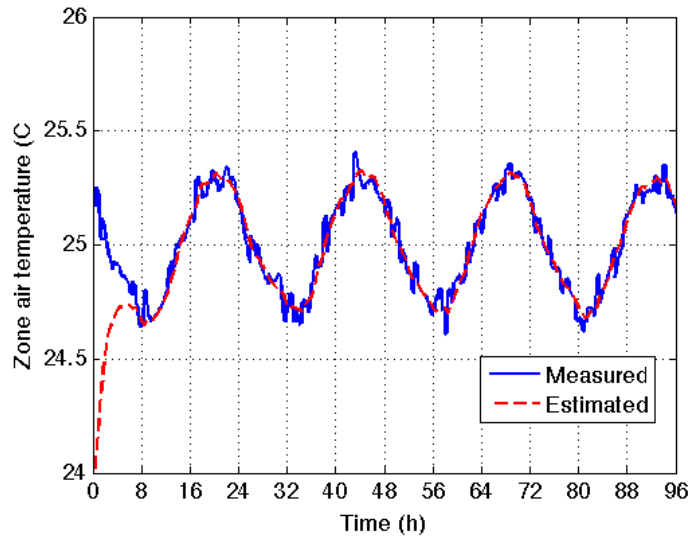


Figure A.3.4.20 Sensed and estimated zone-air temperatures

Our main result, the tracking of the solar-load, is displayed in Figure A.3.4.21 . Here we see that in addition to the initial transient, there is a lag between the true and the estimated values. It may be that additional tuning (*e.g.* adjusting the process noise value) can improve the results.

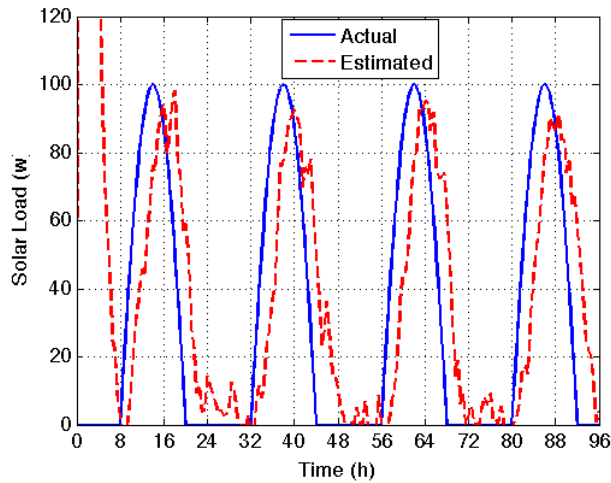


Figure A.3.4.21 Actual and estimated solar loads (first-order model)

Second-order oscillator:

Here again we did some modest tuning of the parameters (process noise for the pair (\dot{s}_d, s_d)). In this case (see Figure A.3.4.22) there is a substantial initial transient but the eventual tracking is much improved over the first-order case. The results for smoothed estimates of T_s and T_a are indistinguishable from the first-order case (Figures A.3.4.19 – A.3.4.20).

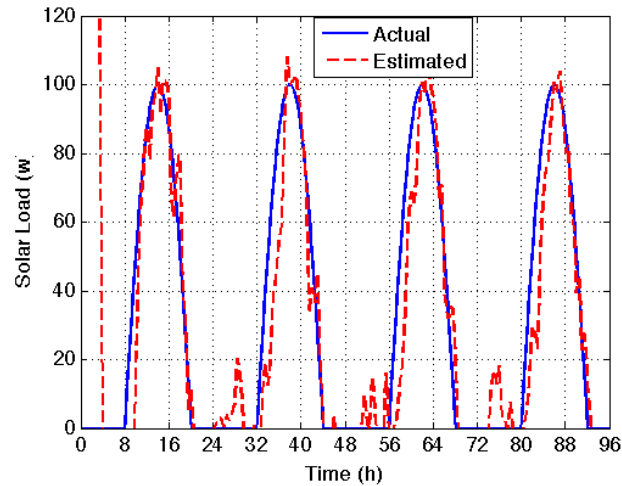


Figure A.3.4.22 Actual and Estimated Solar Loads (Second-order model)

Conclusions

This preliminary study demonstrates that it is feasible to reconstruct unknown disturbance inputs based on measured data. Note that we do require an accurate model of the system, including the vector that characterizes how the disturbance affects the system dynamics. Note that we have assumed that the *external temperature* (T_e) is known exactly.

Using a first-order disturbance model results in a lag between the actual and the predicted solar loads. A second-order disturbance model produces better ultimate tracking, albeit with a large initial transient. *The Internal Model Principle* [Francis – op. cit.] suggests the use of higher-order models that better reflect the expected behavior of the disturbance. This extends the approach used in [O’Neill⁴⁹].

⁴⁹ Z. O’Neil, S. Narayanan, and R. Brahme, Model-based thermal load estimation in buildings, Proceedings of the Fourth National Congress of the International Building Performance Simulation Association, August 2010, 474 – 481.

Appendix 3.5

Automatic Differentiation

We provide some more detail on automatic differentiation (AD) of Matlab functions by considering two matrix functions: the Cholesky factorization algorithm (chol) and the matrix norm function (norm). Differentiating the Cholesky factorization $A = R'R$ leads to the equation

$$R'R + R'\dot{R} = \dot{A}, \quad (1)$$

which can be solved with a variation of the Bartels-Stewart algorithm, column-by-column, for the solution \dot{R} (see Algorithm 1 below). Note that the symmetry of the left hand side of equation (1) implies that \dot{A} must be symmetric for the Cholesky factorization to be differentiable. This is equivalent to the concept that the Matlab function chol is a mapping between the space of symmetric positive definite matrices to the space of upper triangular matrices with positive diagonal entries. As in Lyapunov equations, the definiteness of \dot{A} characterizes the definiteness of \dot{R} .

ALGORITHM 1: Sensitivity of the Cholesky Factorization

Input: A positive definite, Hermitian matrix A and its Hermitian parametric derivative \dot{A} .

Output: The Cholesky factor R and its parametric derivative \dot{R} that satisfies (1).

$$\dot{R}_{11} = \dot{A}_{11} / (2 * R_{11});$$

$$\dot{R}_{1,2:n} = \dot{A}_{1,2:n} - (\dot{R}_{11} / R_{11}) * R_{1,2:n};$$

for $i = 2 \dots n$ **do**

 similarly for each row

end

The remainder of this section discusses the treatment of $\|\cdot\|_2$. There are two challenges here.

Since we need to differentiate the largest singular value, there is the issue of non-differentiability of the maximum function. This is treated by computing the right Dini derivative. The second challenge is in the calculation of derivatives of singular values. This is achieved by first

calculating $\sigma_1 = \|A\|_2$. The calculation of the dominate left and right singular vectors can be found noting that σ_1 is an eigenvalue of a matrix involving A with dominant singular vectors contained in the eigenvectors. Thus, we have the relationship

$$\begin{bmatrix} -\sigma_1 I & A' \\ A & -\sigma_1 I \end{bmatrix} \begin{bmatrix} v_1 \\ u_1 \end{bmatrix} = \begin{bmatrix} -\sigma_1 I & V\Sigma U' \\ U\Sigma V' & -\sigma_1 I \end{bmatrix} \begin{bmatrix} v_1 \\ u_1 \end{bmatrix} = \begin{bmatrix} 0 \\ 0 \end{bmatrix}$$

Now, differentiating $A = U\Sigma V'$ and looking at the (1,1) entry of the matrix equation

$$U' \dot{A} V = U' \dot{U} \Sigma + \dot{\Sigma} + \Sigma \dot{V}' V$$

and using the differentiated orthogonality relationships $u_1' \dot{u}_1 = 0$ and $v_1' \dot{v}_1 = 0$, leads to the formula for the derivative of the norm:

$$\dot{\sigma}_1 = \dot{u}_1' \dot{A} v_1$$